

République Algérienne Démocratique et Populaire  
Ministère de l'Enseignement Supérieur et de la Recherche Scientifique  
École Nationale Polytechnique



المدرسة الوطنية المتعددة التقنيات  
Ecole Nationale Polytechnique

Département de Génie Mécanique  
Laboratory of Green and Mechanical Development



Submitted in fulfillment of the requirements for the degree of State Engineer in Mechanical Engineering

---

Development of a Savonius Wind Turbine Prototype:  
Design and Fabrication of Sandwich Rotor Blades with Gyroid Lattice Core and Hybrid Composite Skins

---

*Ines BENSEGHIR and Meriem Malika AIB*

Presented and publicly defended on : November 30th, 2025

**Composition of the Jury:**

President	Mr. Slimane DJELLAL	MCB	ENP
Supervisor	Mr. Yacine BELKACEMI	MCA	ENP
Co-Supervisor	Mr. Abdelhamid BOUHELAL	MCA	ENP
Co-Supervisor	Mr. Arezki SMAILI	Prof	ENP
Examiner	Mr. Naserddine AMOURA	MCA	ENP
Guest	Mr. Said RECHAK	Prof	ENP





République Algérienne Démocratique et Populaire  
Ministère de l'Enseignement Supérieur et de la Recherche Scientifique  
École Nationale Polytechnique



المدرسة الوطنية المتعددة التقنيات  
Ecole Nationale Polytechnique

Département de Génie Mécanique  
Laboratory of Green and Mechanical Development



Submitted in fulfillment of the requirements for the degree of State Engineer in Mechanical Engineering

---

Development of a Savonius Wind Turbine Prototype:  
Design and Fabrication of Sandwich Rotor Blades with Gyroid Lattice Core and Hybrid Composite Skins

---

*Ines BENSEGHIR and Meriem Malika AIB*

Presented and publicly defended on : November 30th, 2025

**Composition of the Jury:**

President	Mr. Slimane DJELLAL	MCB	ENP
Supervisor	Mr. Yacine BELKACEMI	MCA	ENP
Co-Supervisor	Mr. Abdelhamid BOUHELAL	MCA	ENP
Co-Supervisor	Mr. Arezki SMAILI	Prof	ENP
Examiner	Mr. Naserddine AMOURA	MCA	ENP
Guest	Mr. Said RECHAK	Prof	ENP

République Algérienne Démocratique et Populaire  
Ministère de l'Enseignement Supérieur et de la Recherche Scientifique  
École Nationale Polytechnique



المدرسة الوطنية المتعددة التقنيات  
Ecole Nationale Polytechnique

Département de Génie Mécanique  
Laboratory of Green and Mechanical Development



Mémoire de projet de fin d'études  
pour l'obtention du diplôme d'ingénieur d'état en génie mécanique

**Thème :**

---

Développement d'un prototype d'éolienne Savonius :  
Conception et fabrication de pales en structure sandwich à âme gyroïde et peaux composites  
hybrides

---

*Ines BENSEGHIR et Meriem Malika AIB*

Présenté et soutenu publiquement le : 30 novembre 2025

**Composition du jury :**

Président	M. Slimane DJELLAL	MCB	ENP
Encadrant	M. Yacine BELKACEMI	MCA	ENP
Co-encadrant	M. Abdelhamid BOUHELAL	MCA	ENP
Co-encadrant	M. Arezki SMAILI	Prof.	ENP
Examineur	M. Naserddine AMOURA	MCA	ENP
Invité	M. Said RECHAK	Prof.	ENP

## Acknowledgements

---

*First and foremost, we express our sincere gratitude to Almighty God for granting us the strength and perseverance to complete this work.*

*We extend our deepest appreciation to our supervisors, Dr. Yacine Belkacemi, Prof. Arezki Smaili, and Dr. Abdelhamid Bouhelal, for their invaluable guidance, continuous support, and trust throughout this project. Their expertise, insightful feedback, and availability have been instrumental in shaping this work.*

*Our sincere thanks go to the technical staff and engineers of the department for their unwavering assistance and technical support. We are particularly grateful to Alcadworks team, especially Kelthoum and Aichi, for their valuable contributions and technical expertise. We also thank Mr. Guergueb for his essential help and support.*

*We would also like to acknowledge the faculty members of the Mechanical Engineering Department for their dedication and the knowledge they have imparted throughout our academic journey. Special recognition is due to Dr. Yacine Belkacemi, Head of the Mechanical Engineering Department, for his leadership, encouragement, and for providing the necessary resources that facilitated our project.*

*Finally, we thank all those who, directly or indirectly, contributed to the successful completion of this project.*

*Meriem Malika Aib  
Ines Benseghir*

## Dedications

---

### ***To my parents,***

*For their unwavering support, endless patience, and constant encouragement throughout this journey. I am eternally grateful for their love and guidance that have brought me to this point.*

*To my Aunt Karima for her constant support and encouragements she was my source of hard and honest work i would never reach to this place without her also.*

*And to my brother Anis for all the support and encouragements still many things i will forver be gratefull.*

*With love and gratitude,  
Meriem Malika Aib*

### ***To my parents,***

*For their endless support, understanding, and encouragement throughout this challenging journey. This achievement would not have been possible without their love and belief in me.*

*With deepest gratitude,  
Ines Benseghir*

## ملخص

يعرض هذا العمل تصميم وتصنيع وتقييم دوار توربين رياح من نوع سافونيوس خفيف الوزن، تم تطويره باستخدام بنية شطيرية مكونة من قلب جيوريدي مطبوع ثلاثي الأبعاد وجلود مركبة ذات أساس حيوي. تمثل الهدف في تحسين استجابة الدوار عند سرعات الرياح المنخفضة، مع تقليل الكتلة مع الحفاظ على السلامة البنيوية. تم اعتماد نهج يجمع بين التجربة والنمذجة العددية لتوصيف المادة والتحقق من سلوك الدوار. وقد حقق التصميم النهائي تقليلاً بنسبة 48.6% في الكتلة مقارنة بنظيره المصنوع من PLA، مع الحفاظ على السلامة البنيوية تحت الأحمال التشغيلية، حيث لم تتجاوز التشوهات نسبة 0.05% من ارتفاع الدوار. تؤكد النتائج الإمكانيات الكبيرة للجمع بين المواد المركبة الحيوية وهندسات TPMS في تطوير حلول خفيفة الوزن وعالية الكفاءة الهيكلية.

### الكلمات الدالة :

توربين رياح سافونيوس، مركبات حيوية، شبكة جيوريد، الطباعة ثلاثية الأبعاد، CFD، FSI

## Résumé

Ce travail fait l'objet de la conception, la fabrication et l'évaluation d'un rotor de turbine éolienne Savonius léger, réalisé à partir d'une structure sandwich combinant un noyau gyroïde imprimé en 3D et des peaux composites biosourcées. L'objectif était d'améliorer la réactivité du rotor à faibles vitesses de vent tout en réduisant sa masse et en conservant son intégrité structurale. Une approche expérimentale et numérique combinée a été adoptée pour caractériser le matériau et valider le comportement du rotor. La structure finale a permis une réduction de masse de 48.6% par rapport à un rotor équivalent en PLA, tout en maintenant l'intégrité mécanique sous chargements opérationnels, avec une déformation maximale n'excédant pas 0,05% de la hauteur du rotor. Les résultats confirment le potentiel de l'association des composites biosourcés avec les structures architecturées pour le développement de solutions légères et mécaniquement performantes.

**Mots clés :** éolienne Savonius ; composites biosourcés ; structure gyroïdale ; impression 3D ; CFD ; FSI

## Abstract

This work presents the design, fabrication, and evaluation of a lightweight Savonius wind turbine rotor using a sandwich structure made of a 3D-printed gyroid core and bio-sourced composite skins. The objective was to enhance rotor responsiveness at low wind speeds while reducing mass and maintaining structural integrity. A combined experimental and numerical approach was adopted to characterize the material and validate the rotor behavior. The final structure achieved a 48.6% reduction in mass compared to a PLA equivalent, while maintaining structural integrity under operational loads, with maximum deformation not exceeding 0.05% of the rotor height. The results confirm the potential of combining bio-based composites with TPMS architectures for the development of lightweight, structurally efficient solutions.

**Keywords:** Savonius wind turbine; bio-based composites; gyroid lattice; 3D printing; CFD; FSI

# Contents

■ ■ ■

**List of Tables**

**List of Figures**

**List of Symbols and Abbreviations**

<b>General Introduction</b>	<b>18</b>
<b>1 Introduction and Theoretical Background</b>	<b>23</b>
1.1 Savonius Wind Turbine: Principles and Challenges . . . . .	24
1.1.1 Operational Principles . . . . .	24
1.1.2 Aerodynamic Challenges and Structural Implications . . . . .	26
1.2 Aerodynamic and Structural Analysis: A Coupled Approach . . . . .	29
1.2.1 Principles of CFD Investigations . . . . .	31
1.2.2 Principles of FEA Structural Analysis . . . . .	36
1.3 Date Palm Fiber Characterization for Composite Applications . . . . .	41
1.3.1 Anatomy of Date Palm and Fiber-bearing Parts . . . . .	42
1.3.2 Fiber Extraction Methods . . . . .	50
1.3.3 Treatment and Surface Modification of Plant Fibers . . . . .	52
1.3.4 Mechanical Properties of Date Palm Fibers . . . . .	52
1.4 Date Palm Fiber Polymer Composites . . . . .	54
1.4.1 Matrix Selection: Thermosets vs Thermoplastics . . . . .	55
1.4.2 Epoxy Matrix Composites: Fabrication and Performance . . . . .	57
1.5 Sandwich Structures with Lattice Cores . . . . .	60
1.5.1 Overview of Sandwich Structures . . . . .	60
1.5.2 Evolution of Core Architectures: Toward Additive Manufactured Lattices	60
1.5.3 Lattice Structures: Architectures, Properties, and Applications . . . . .	61
1.5.4 Gyroid Lattices: A Special Class of TPMS Structures . . . . .	62
1.5.5 Sandwich Structures with Lattice Cores: A Synergistic Design . . . . .	64
<b>2 Design Analysis and Realization Methodology</b>	<b>65</b>
2.1 Rotor Design Configuration . . . . .	66
2.1.1 Context and Project Goals . . . . .	66
2.1.2 Kamoji's Experimental Investigations and Findings . . . . .	66
2.1.3 Selected Rotor Configuration . . . . .	67
2.1.4 Wind Tunnel Blockage Effects . . . . .	68
2.1.5 Scaling Calculations for Wind Tunnel Testing . . . . .	70
2.1.6 Structural Analysis and Minimum Constraint Requirements . . . . .	70
2.2 Material Selection and Characterization . . . . .	74

2.3	Rotor Manufacturing and Realization . . . . .	76
2.3.1	Date Palm Fiber Extraction Protocol . . . . .	77
2.3.2	3D Printing Process of the Rotor Components . . . . .	79
2.3.3	Composite Lamination and Rotor Assembly . . . . .	84
2.4	Final Outcome and Performance Assessment . . . . .	87
<b>3</b>	<b>Material Characterization</b>	<b>88</b>
3.1	Background and scope . . . . .	89
3.2	Theory of Homogenization . . . . .	89
3.2.1	Introduction and Motivation . . . . .	89
3.2.2	Fundamental Assumptions and Scope . . . . .	90
3.2.3	Homogenization Workflow . . . . .	90
3.3	Material Characterization Procedure and Results . . . . .	96
3.3.1	Date Palm Fibres (DPF) Characterization . . . . .	96
3.3.2	ABS Characterization . . . . .	101
3.3.3	Sandwich Characterization . . . . .	106
3.3.4	Gyroid Characterization . . . . .	110
<b>4</b>	<b>Rotor Response and Performance Analysis</b>	<b>116</b>
4.1	Experimental Methods . . . . .	117
4.1.1	Wind Tunnel Description . . . . .	117
4.1.2	Wind Tunnel Drive System . . . . .	119
4.1.3	Instrumentation in the Wind Tunnel . . . . .	120
4.1.4	Generator selection criteria . . . . .	123
4.1.5	Calculating Measurement Uncertainty . . . . .	123
4.1.6	Test Procedure . . . . .	124
4.2	Numerical Setup and Methodology . . . . .	126
4.2.1	2D Validation Case Setup . . . . .	126
4.2.2	3D Validation Case Setup . . . . .	134
4.2.3	3D Helical Savonius (S-90) Validation Case . . . . .	137
4.2.4	One-Way Fluid-Structure Interaction (FSI) Simulation . . . . .	139
<b>5</b>	<b>Results and Discussion</b>	<b>143</b>
5.1	Experimental Wind Tunnel Performance . . . . .	144
5.1.1	Measurement uncertainty estimation . . . . .	145
5.2	Numerical Simulation Results . . . . .	147
5.2.1	2D Conventional Savonius Rotor . . . . .	147
5.2.2	Validation of Two-Dimensional Computational Model . . . . .	148
5.2.3	Validation of Three-Dimensional Computational Model . . . . .	149
5.2.4	Quantitative Comparison of Torque Stability for Helical and Conventional Rotors . . . . .	151
5.2.5	Validation of Numerical Model through Power Coefficient Analysis . . . . .	152
5.2.6	Flow Field Visualization and Contour Analysis . . . . .	153
5.2.7	Fluid-Structure Interaction (FSI) Analysis of the Helical Rotor . . . . .	157
	<b>Conclusion</b>	<b>159</b>
	<b>Bibliography</b>	<b>162</b>
	<b>Appendix</b>	<b>172</b>

# List of Tables

...

1.1	Fluid–Structure Interaction (FSI) framework components . . . . .	30
1.2	Physical properties of common natural fibers used in composites . . . . .	45
1.3	Physical properties of date palm fibers from different parts and extraction techniques . . . . .	46
1.4	Summary of surface modification techniques for plant fibers . . . . .	52
1.5	Mechanical properties of common natural fibers used in composites . . . . .	53
1.6	Comparison between mechanical properties of date palm fibers from different parts with different treatment techniques, Adapted from [1]. . . . .	54
1.7	Mechanical properties of date-palm fiber/epoxy composites [2] . . . . .	59
1.8	Flexural properties of date-palm fiber/epoxy composites [3] . . . . .	59
1.9	Roles of sandwich structure components . . . . .	60
1.10	Comparison between traditional and architected lattice cores . . . . .	61
2.1	Configurations of helical Savonius rotors tested . . . . .	66
2.2	Summary of experimental results from Kamoji et al. (2009) for helical Savonius rotor configurations [4]. . . . .	67
2.3	Selected reference configuration adopted for the present study. . . . .	67
2.4	Blockage ratio thresholds and recommended corrective actions [5? ]. . . . .	69
2.5	Comparison between the present scaled model and Kamoji’s reference configuration. . . . .	70
2.6	Input parameters used for aerodynamic and structural analysis. . . . .	71
2.7	Summary of derived aerodynamic and mechanical quantities for the reference gust condition ( $U = 15$ m/s, $C_{t,max} = 0.33$ ). . . . .	73
2.8	Thermal characteristics of candidate 3D-printing materials for the lattice core. . . . .	75
2.9	Optimized Gyroid Core Printing Parameters . . . . .	82
2.10	Rotor Printing Configurations and Results . . . . .	84
2.11	Comparison of final rotor mass and cost with respect to reference rotors. . . . .	87
3.1	Descriptive statistics for fibre bundle diameter ( $n = 11$ ) . . . . .	97
3.2	Mechanical properties of individual palm-date fibre bundles. . . . .	99
3.3	Comparison of average mechanical properties with literature data (Elseify <i>et al.</i> ). . . . .	100
3.4	Nominal dimensions and testing parameters for ISO 527-2 Type 1A specimens. . . . .	102
3.5	Mechanical properties of full-density ABS specimens printed along the X-axis. . . . .	103
3.6	Mechanical properties of full-density ABS specimens printed along the Y-axis. . . . .	104
3.7	Mechanical properties of full-density ABS specimens printed along the Z-axis. . . . .	104
3.8	Constituent material properties used in the micromechanical model. . . . .	106
3.9	Equivalent orthotropic properties of impregnated yarn ( $V_f = 0.55$ ). . . . .	107
3.10	Input parameters for woven composite RVE in <i>ANSYS Material Designer</i> . . . . .	108
3.11	Homogenization results for woven composite under different mesh densities. . . . .	109
3.12	Modeling parameters used for gyroid core homogenization. . . . .	110



3.13	Mesh convergence study for gyroid core homogenization. . . . .	111
3.14	Homogenized elastic properties of the ABS gyroid structure. . . . .	112
3.15	Experimental tensile test results for gyroid specimens along the $z$ -direction. . . .	113
3.16	Homogenized properties of the full sandwich structure. . . . .	114
3.17	Comparison of stiffness-to-weight ratio for different materials. . . . .	115
4.1	Summary of uncertainty rules. . . . .	124
4.2	Geometric parameters of the Savonius rotor used for 2-D validation (adapted from [6]). . . . .	127
4.3	Computational domain geometry specifications. . . . .	128
4.4	Mesh quality metrics and target values used for mesh acceptance. . . . .	129
4.5	Mesh statistics for the 2-D mesh-independence study. . . . .	132
4.6	Geometric parameters for the scaled 3D Savonius rotor validation. . . . .	134
4.7	Mesh statistics for the 3-D mesh-independence study. . . . .	136
4.8	Geometric configuration of helical Savonius rotors (Kamoji et al., 2009). . . .	137
4.9	Computational parameters for validation case. . . . .	138
4.10	Experimental performance targets (Kamoji et al., 2009). . . . .	138
4.11	Comparison of mesh statistics for fluid and structural domains. . . . .	141
4.12	Solver configuration used for the transient structural analysis. . . . .	142
5.1	Experimental wind-tunnel results . . . . .	144
5.2	Tip–speed–ratio uncertainties. . . . .	145
5.3	Electrical-power uncertainties computed from Table 1.1. . . . .	146
5.4	Uncertainty in the power coefficient $C_p$ . . . . .	146
5.5	Statistical analysis of torque variability for the conventional and helical Savonius rotors. . . . .	152
5.6	Critical displacement peak coordinates . . . . .	157
5.7	Summary of main experimental and numerical results. . . . .	159

# List of Figures

■ ■ ■

1	Cumulative wind power capacity worldwide . . . . .	18
2	Comparison between SWT and HAWTs . . . . .	19
3	Estimation of annual number of date palm trees and annual tonnage of date palm byproduct in Algeria. . . . .	20
4	Different parts of date palm byproduct. . . . .	20
1.1	Savonius rotor geometry and main parameters, Adapted from [7]. . . . .	24
1.2	Scheme of the operational principle of Savonius turbine, Adapted from [7]. . . . .	24
1.3	Flows patterns on a Savonius rotor, Adapted from [8]. . . . .	25
1.4	Design Methodology Flowchart. . . . .	26
1.5	Sum of moment cycles on a different stage rotors, Adapted from [8]. . . . .	27
1.6	Turbulent kinetic energy (TKE) contours at TSR of 0.8. . . . .	28
1.7	Variation of Factor of Safety with rotor angle for Savonius rotor with duct augmentation at 4 m/s (adapted from [9]) . . . . .	29
1.8	Boundary conditions and computational domains for (a) 2D and (b) 3D Savonius simulations. Adapted from [10]. . . . .	31
1.9	CFD methodology selection framework based on turbine geometry and boundary conditions. . . . .	32
1.10	Mesh topology around the S-rotor: (a) overview of the discretized domain; (b) near the interface; and (c) prismatic boundary layers. Adapted from [11]. . . . .	33
1.11	Schematic representation of the near-wall boundary layer. . . . .	33
1.12	Classification of turbulence models in ANSYS Fluent. . . . .	35
1.13	Schematic of Finite Element Analysis (FEA) process. . . . .	36
1.14	3D CAD geometry of the rotor model used in the FSI analysis. . . . .	36
1.15	Boundary condition setup for the Savonius rotor [12]. . . . .	37
1.16	ANSYS interface showing pressure load interpolation using <i>Mechanical-Based Mapping</i> between fluid and structural meshes. . . . .	38
1.17	Schematic representation of the partitioned FSI coupling process. Adapted from [13]. . . . .	40
1.18	Schematic representation of date palm morphology. . . . .	42
1.19	Principal date palm fiber sources: spadix stems, leaflets, midribs, and mesh. . . . .	43
1.20	Classification and locations of date palm fiber sources . . . . .	43
1.21	SEM analysis of maguey fibers showing (a) fiber morphology and (b) the instrumentation used. . . . .	44
1.22	Density samples preparation and measurement (adapted from Elseify et al. 2018) . . . . .	45
1.23	Morphological variations in date palm midrib (DPM) fiber cross-sections: (a) vascular bundle and microfibril structure, (b) CT scan showing lumen distribution, (c) C-shaped fibers, (d) flaky fibers resulting from processing, (e) elliptical fibers, and (f) irregular-shaped fibers (Elseify et al., 2020). . . . .	47

1.24	SEM micrographs of date palm midrib fibers in the longitudinal direction: (a, b) untreated fibers showing surface impurities and parenchyma cells; (c, d) NaOH-treated fibers showing partial removal of parenchyma and presence of silica crystals [14]. . . . .	48
1.25	Representative cross-sections of different date palm fiber types . . . . .	48
1.26	Diagram showing the structural arrangement of lignin, hemicellulose and cellulose microfibrils [1]. . . . .	49
1.27	Microstructural organization of plant fibers . . . . .	49
1.28	Chemical composition profile of date palm fibers (% by weight) . . . . .	50
1.29	Yucca fiber extraction methods comparison (adapted from [15]) . . . . .	51
1.30	Schematic of the single fiber tensile test specimen setup according to ASTM D3822, showing the paper frame and the gauge length. . . . .	53
1.31	Classification of polymer matrices for natural fiber composites . . . . .	55
1.32	Thermo-gravimetric degradation of coir, under nitrogen and air atmospheres, at the heating rate of 10 °C min <sup>-1</sup> . . . . .	56
1.33	Schematic of the hand layup process. . . . .	57
1.34	Diagram of Resin Transfer Moulding (RTM) method. . . . .	58
1.35	Filaments winding process. . . . .	58
1.36	Schematic of a sandwich panel. . . . .	60
1.37	Classification of lattice architectures: strut-based vs. surface-based topologies. . . . .	62
1.38	Example of a gyroid unit cell of 40% infill. . . . .	63
1.39	(a) Gyroid sandwich and (b) PUF-filled gyroid sandwich at 20% gyroid core density [16]. . . . .	64
2.1	Helical Savonius rotors tested: (a) with shaft between end plates; (b) and (c) two views of helical rotor without shaft between end plates. . . . .	67
2.2	Solid blockage, <i>Adapted from</i> [17]. . . . .	68
2.3	Wake blockage, <i>Adapted from</i> [17]. . . . .	68
2.4	Combined effects of solid and wake blockage on normalized wind speed along the tunnel axis for a VWAT, <i>Adapted from</i> [17]. . . . .	69
2.5	Half-cylindrical shell cantilever model . . . . .	71
2.6	Material selection workflow for the final rotor configuration. . . . .	74
2.7	Manufacturing workflow for the rotor realization process. . . . .	76
2.8	Fiber Extraction from Date Palm Midribs (developed in this work) . . . . .	78
2.9	Date palm fibers after extraction. . . . .	79
2.10	Fused deposition modeling diagram . . . . .	80
2.11	Illustrations of process parameters . . . . .	81
2.12	nTopology rotor model. . . . .	82
2.13	Observed layer shifting at upper rotor heights . . . . .	82
2.14	Print improvement with reduced speed, but premature failure remains . . . . .	83
2.15	Final printing with support structures . . . . .	84
2.16	Hybrid reinforcement fabric showing date palm fiber yarns integrated with fiber-glass fabric . . . . .	85
2.17	Sequential assembly process of the hybrid Savonius rotor. . . . .	86
3.1	Schematic representation of the material characterization workflow. . . . .	89
3.2	Finite element-based homogenization workflow. . . . .	91
3.3	Different RVE configurations showing fiber–matrix disposition. . . . .	92
3.4	Meshing of representative volume elements (RVE). . . . .	92

3.5	SEM micrographs showing surface morphology of (a) treated and (b) untreated date palm fibres at 250× magnification . . . . .	96
3.6	SEM cross-sections of twelve representative date midrib fibres showing diameter variability. Subfigures (a–l) correspond to individual fibres measured at magnifications ranging from 150× to 250×. . . . .	98
3.7	Experimental setup for single-fibre tensile testing according to ASTM D3822. . . . .	99
3.8	Stress-strain curves for the eleven tested fibre bundles. . . . .	100
3.9	Full-density ABS tensile specimens printed along different orientations. . . . .	101
3.10	ISO 527-2 Type 1A specimen geometry used for uniaxial tensile tests. . . . .	101
3.11	Full-density ABS tensile specimens illustrating characteristic FDM failure modes: interlayer delamination, intralayer separation, and void-induced stress concentrations . . . . .	102
3.12	Stress-strain curves for full-density ABS specimens printed along the X-axis. . . . .	103
3.13	Stress-strain curves for full-density ABS specimens printed along the Y-axis. . . . .	103
3.14	Stress-strain curves for full-density ABS specimens printed along the Z-axis. . . . .	104
3.15	Numerical model setup for woven composite homogenization. . . . .	108
3.16	Finite element setup for gyroid core homogenization. . . . .	110
3.17	Representative homogenization results for the gyroid core. . . . .	111
3.18	Gyroid tensile test specimens oriented along the z-axis. . . . .	112
3.19	Experimental stress–strain curves for gyroid specimens along the z-direction. . . . .	113
3.20	Finite element model of the sandwich structure used for homogenization. . . . .	114
4.1	Closed-circuit wind tunnel at the National Polytechnic School of Algiers. . . . .	117
4.2	Schematic diagram of the ENP closed-circuit wind tunnel (adapted from [18]). . . . .	118
4.3	The airflow through the wind tunnel . . . . .	118
4.4	Electric motor and axial fan assembly (adapted from [18]). . . . .	119
4.5	Main control panel with integrated Variable Frequency Drive (VFD) for fan speed regulation. . . . .	120
4.6	VFD digital interface for controlling and monitoring the fan motor. . . . .	120
4.7	Pitot tube for airspeed measurement. . . . .	121
4.8	KIMO MP200 digital manometer. . . . .	121
4.9	AMPROBE TACH-10 contact/non-contact digital tachometer. . . . .	122
4.10	CROWN CT44052 digital multimeter used for voltage and current measurements. . . . .	122
4.11	Bicycle dynamo (3 W) selected for power generation . . . . .	123
4.12	Rotor assembly mounted . . . . .	124
4.13	Circuit setup used for electrical measurements during testing. . . . .	125
4.14	Savonius rotor cross-section. . . . .	126
4.15	Computational domain layout for 2D simulations (adapted from [19]). . . . .	127
4.16	Mesh generation steps . . . . .	128
4.17	Refined 2D mesh after applying the meshing strategy . . . . .	130
4.18	2D mesh independence study at TSR = 0.8. . . . .	133
4.19	3D geometry of the Savonius rotor. . . . .	134
4.20	Cross-section of the 3D computational domain. . . . .	135
4.21	3D computational domain with named selections. . . . .	135
4.22	3D mesh independence study at TSR = 0.8. . . . .	136
4.23	Local mesh refinement around the Savonius rotor and overlap gap region. . . . .	137
4.24	Surface mesh of the helical Savonius rotor. . . . .	138
4.25	Imported geometry in <i>ANSYS Transient Structural</i> showing suppressed fluid domains. . . . .	139

4.26	Helical rotor assembly with main solid components. . . . .	139
4.27	Material definitions in <i>ANSYS Engineering Data</i> . . . . .	140
4.28	Bonded contact definition between rotor and upper plate. . . . .	140
4.29	Boundary condition setup in the Transient Solver. . . . .	141
4.30	Comparison of mesh discretization between the CFD and structural domains used for one-way FSI coupling. . . . .	141
5.1	Measured power coefficient $C_p$ vs. tip-speed ratio (TSR) with uncertainty bars. .	144
5.2	Instantaneous torque output from 2D CFD simulation at TSR=0.8 . . . . .	147
5.3	Dynamic torque variation with azimuth angle . . . . .	147
5.4	2D CFD validation: Power coefficient vs tip speed ratio . . . . .	148
5.5	2D CFD validation: Torque coefficient vs tip speed ratio . . . . .	149
5.6	3D CFD validation: Power coefficient vs. tip-speed ratio . . . . .	149
5.7	3D CFD validation: Torque coefficient vs tip speed ratio( $\lambda$ ) . . . . .	150
5.8	Normalized torque variation over one revolution. . . . .	151
5.9	Static pressure contours around the rotor blades at two different tip speed ratios (TSR). . . . .	153
5.10	Velocity magnitude contours around the rotor blades. . . . .	154
5.11	Vorticity magnitude contours. . . . .	154
5.12	Vorticity magnitude contours for the 3D Savonius rotor. . . . .	155
5.13	3D velocity field visualization for the Savonius rotor. . . . .	155
5.14	Comparison of vorticity magnitude contours for the helical Savonius rotor at $\lambda = 0.65$ under two different contour scaling ranges. . . . .	156
5.15	Velocity and static pressure contours for the helical Savonius rotor at $\lambda = 0.65$ . .	156
5.16	Total displacement of the helical Savonius rotor as a function of azimuth angle. .	157
5.17	Total deformation contours on the helical Savonius rotor. . . . .	158
5.18	Imported pressure loadings applied on the helical Savonius rotor. . . . .	158
5.19	Mechanized fiber extraction concept . . . . .	160

# List of Symbols and Abbreviations

...

## Latin Symbols

$A$	Rotor area	(m <sup>2</sup> )
$A_s$	Projected frontal area of the rotor	(m <sup>2</sup> )
$A_t$	Cross-sectional area of the tunnel test section	(m <sup>2</sup> )
$B_R$	Blockage ratio	(-)
$C$	Stiffness matrix	(-)
$C_f$	Skin friction coefficient	(-)
$C_p$	Power coefficient	(-)
$C_t$	Torque coefficient	(-)
$C_T$	Torque coefficient	(-)
$D$	Rotor diameter	(m)
$E$	Young's modulus	(Pa)
$F$	Force	(N)
$FoS$	Factor of safety	(-)
$G$	Shear modulus	(Pa)
$H$	Rotor height	(m)
$I$	Second moment of area	(m <sup>4</sup> )
$M$	Torque or moment	(N·m)
$N$	Number of samples or rotational speed	(- or rpm)
$P$	Power	(W)
$p$	Pressure	(Pa)
$R$	Rotor radius	(m)
$Re$	Reynolds number	(-)
$S$	Compliance matrix or shear strength	(- or Pa)

$T$	Torque	(N·m)
$t$	Time or thickness	(s or m)
$U$	Velocity	(m/s)
$u$	Displacement or velocity component	(m or m/s)
$V$	Volume	(m <sup>3</sup> )
$V_f$	Fiber volume fraction	(-)
$W$	Section modulus	(m <sup>3</sup> )
$x, y, z$	Cartesian coordinates	(m)
$y^+$	Non-dimensional wall distance	(-)

## Greek Symbols

$\alpha$	Angle of attack or constant	(° or -)
$\beta$	Twist angle or mode coefficient	(° or -)
$\gamma$	Shear strain	(-)
$\delta$	Deflection or displacement	(m)
$\varepsilon$	Strain	(-)
$\lambda$	Tip speed ratio	(-)
$\nu$	Poisson's ratio or kinematic viscosity	(- or m <sup>2</sup> /s)
$\rho$	Density	(kg/m <sup>3</sup> )
$\sigma$	Stress	(Pa)
$\tau$	Shear stress	(Pa)
$\omega$	Angular velocity or specific dissipation rate	(rad/s or 1/s)
$\xi$	Damping ratio or geometry parameter	(-)
$\Gamma$	Interface boundary	(-)
$\Delta$	Difference or determinant	(-)
$\theta$	Azimuth angle	(°)

## Subscripts and Superscripts

$eff$	Effective
-------	-----------

<i>max</i>	Maximum
<i>min</i>	Minimum
<i>net</i>	Net value
<i>stat</i>	Static
<i>tot</i>	Total
<i>UTS</i>	Ultimate tensile strength
<i>x, y, z</i>	Directional components
1, 2, 3	Principal material directions
+	Positive direction
–	Negative direction



## Abbreviations

LCOE	Levelized Cost of Energy
USD	United States Dollar
IRENA	International Renewable Energy Agency
WWEA	World Wind Energy Association
HAWT	Horizontal Axis Wind Turbine
VAWT	Vertical Axis Wind Turbine
SWT	Savonius Wind Turbine
FSI	Fluid–Structure Interaction
CFD	Computational Fluid Dynamics
FEA	Finite Element Analysis
FVM	Finite Volume Method
URANS	Unsteady Reynolds-Averaged Navier–Stokes
RVE	Representative Volume Element
DPF	Date Palm Fiber
SEM	Scanning Electron Microscopy
FESEM	Field Emission Scanning Electron Microscopy
TPMS	Triply Periodic Minimal Surface
FDM	Fused Deposition Modeling
ABS	Acrylonitrile Butadiene Styrene
PLA	Polylactic Acid
PETG	Polyethylene Terephthalate Glycol
VFD	Variable Frequency Drive
RPM	Revolutions Per Minute
TKE	Turbulence Kinetic Energy
TSR	Tip Speed Ratio
CV	Coefficient of Variation
PBC	Periodic Boundary Conditions
BoI	Body of Influence
AM	Additive Manufacturing

# General Introduction

■ ■ ■

In the context of the worldwide energy transition, wind emerges as the most prominent renewable energy source due to its inherent scalability and a declining LCOE reaching USD **0.033/kWh** globally for onshore wind, according to IRENA 2024 [20], with a total installed capacity exceeding **1,174 GW** for 2024, representing around **10%** of global electricity generation (WWEA, 2024)[21].

Nevertheless, many countries still struggle to harness wind energy effectively due to limited wind

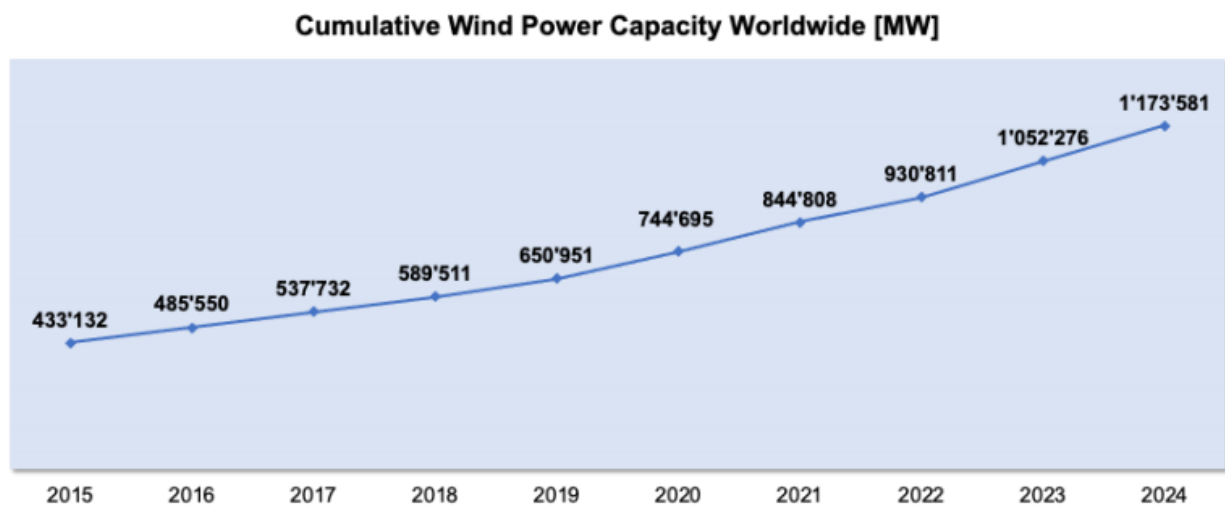


**FIGURE 1** – Cumulative wind power capacity worldwide [21]

resources (low speeds and restricted open areas) or prohibitive costs of conventional horizontal-axis wind turbines (HAWTs). This is where Savonius vertical-axis wind turbines (VAWTs) emerge as a compelling alternative, particularly for urban deployment.

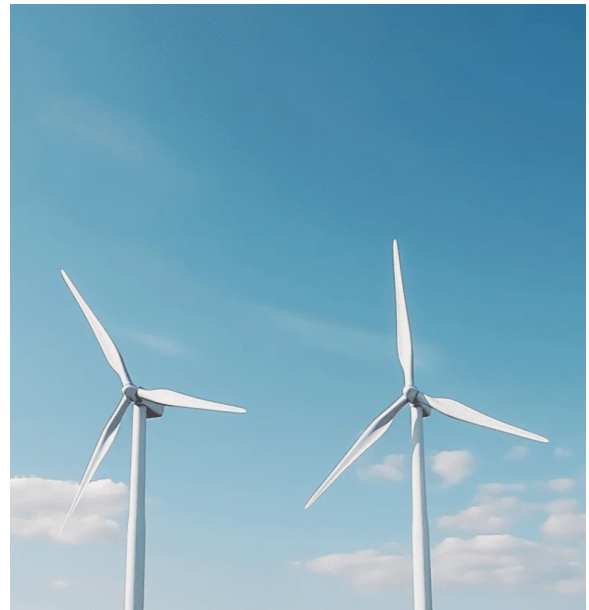
Unlike HAWTs that require precise wind alignment and minimum speeds of 3-5 m/s, Savonius turbines operate omnidirectionally and in low wind speed turbulent environments, achieving self-starting at speeds as low as 2.5 m/s [22]. Their drag-based design eliminates complex yaw and pitch mechanisms, resulting in three key urban-friendly advantages:

- Minimal noise generation, often <35 dB, due to low tip speeds [23]. Thanks to passive airflow and architectural noise reducing features such as S-shaped or helical blades, studies report up to 2.7 dB quieter noise compared to standard designs.
- Compact and modular installation even on rooftops and low towers.
- Significantly lower manufacturing and maintenance costs.

These attributes make Savonius turbines particularly suitable for decentralized or low-wind-speed regions where traditional approaches fail.



(a) SWT



(b) HAWT

**FIGURE 2** – Comparison between SWT and HAWTs

## Problem Statement

Despite their ability to start at low wind speeds, Savonius wind turbines suffer from several structural and dynamic limitations. Torque fluctuations and vibrations are among these, leading to mechanical fatigue and reduced performance stability. In addition, conventional heavy rotors may fail to respond adequately to intermittent, short-duration wind pulses, resulting in missed energy capture opportunities.

A key challenge, therefore, lies in optimizing the rotor's structural configuration to ensure both low rotational inertia, enhancing responsiveness and reducing startup torque, and sufficient mechanical stiffness to maintain integrity and stability under cyclic aerodynamic loading.

## Local Opportunity and Scientific Motivation

In Algeria, pruning of date palm trees generates a significant quantity of agricultural waste each year. According to Almi et al, the number of date palm trees exceeded **18 million** in 2012 [24], resulting in an annual production of more than **8.7 million tonnes** of date palm byproduct residues.

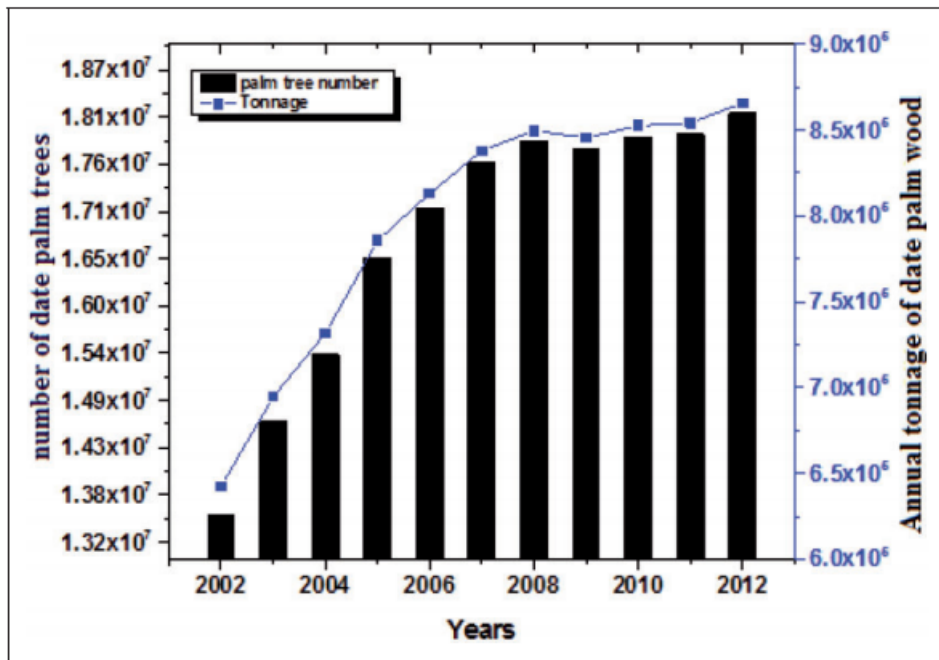


**FIGURE 3** – Estimation of annual number of date palm trees and annual tonnage of date palm byproduct in Algeria. [24]

This biomass primarily consists of lignocellulosic residues which includes petioles, rachis, leaflets, bunches, spathes, and other components.

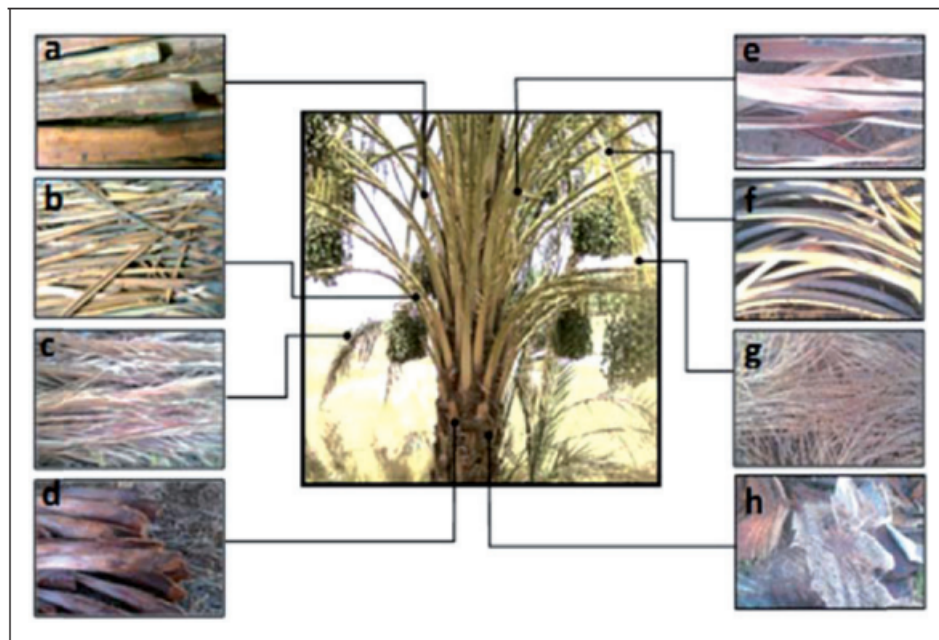


**FIGURE 4** – Different parts of date palm byproduct: (a) Rachis, (b) Thorns, (c) Leaflets, (d) Petiole, (e) Spathe, (f) Bunch, (g) Pedicels, (h) Fibrillium. [24]

The fibers extracted from these date palm residues are not only abundant and low-cost, but also exhibit promising mechanical properties, particularly those derived from midrib. Lobna A. Elseify et al. reported tensile strengths of **500 MPa** and Young's moduli of **16.1 GPa** for midrib fibers of date palm [25], highlighting their suitability as reinforcement in composite materials. Their use aligns with the global shift toward biosourced composites, which aim

to reduce environmental impact, decrease cost, and increase the sustainability of engineered systems. Integrating such material into small-scale renewable energy technologies supports both local valorization and scientific innovation.

## Project Objectives

This project aims to demonstrate a comprehensive approach to sustainable wind turbine development through the following key objectives:

1. **Material Assessment and Processing:** Identify optimal byproducts and develop fiber extraction protocols to obtain sustainable raw materials.
2. **Rotor Configuration and Scaling:** Select the best rotor performance configuration as described by Kamoji et al. (2009), and scale the design for compatibility with wind tunnel testing.
3. **Core Structure Development:** Choose appropriate auxetic materials and fabricate the 3D printed core structure to enhance mechanical properties.
4. **Assembly System Design:** Design and manufacture the turbine assembly components, including endplates and housing, while developing a composite skin application to improve durability and performance.
5. **Performance Validation:** Conduct wind tunnel testing to measure power coefficient and rotation speed, and perform fluid–structure interaction (FSI) analysis to validate experimental results comprehensively.

## Methodological Approach

To address the defined objectives, a structured methodology was adopted throughout the project. The work began with a detailed analysis of the problem and a comprehensive review of the relevant literature on Savonius turbines, bio-based composites, and architected cores. Informed by these findings, solutions were adapted and customized to the specific requirements of the rotor application.

Several design and material options were evaluated based on feasibility, performance potential, and experimental constraints. A preliminary selection was made and the proposed concepts were realized through fabrication and prototyping. Finally, a multi-level performance evaluation was conducted using both numerical simulations (including FSI) and experimental testing to validate the structural and aerodynamic behavior of the system.

## Scientific Contribution and Novelty

This project introduces a novel rotor blade architecture for Savonius wind turbines by combining bio-sourced woven composite skins made from date palm fibers with a 3D-printed gyroid lattice core. While natural fiber composites and architected cores have each been investigated separately, their integration into a sandwich blade specifically for a Savonius VAWT has not been previously reported.

Moreover, the study adopts a sequential homogenization strategy—spanning from fiber scale to full sandwich composite—combined with experimental characterization and fluid–structure interaction simulations. This multi-scale, multi-physics approach offers a comprehensive framework for optimizing both the material and aerodynamic performance of the rotor, thereby advancing the state of the art in sustainable small wind turbine design.

## Report Structure

This report is organized into five chapters, each addressing a critical aspect of the design, realization, and evaluation of the Savonius wind turbine rotor developed using bio-sourced and architected materials. The structure reflects the multidisciplinary nature of the project structural design, material science, advanced manufacturing and numerical simulation.

- **Chapter 1 — Introduction and Theoretical Background:** This chapter establishes the theoretical framework of the study. It begins by reviewing the aerodynamic operating principles of Savonius turbines, focusing on torque asymmetry, low efficiency, and structural constraints. The chapter also introduces fluid–structure interaction (FSI) phenomena and the role of computational fluid dynamics (CFD) and FSI simulations in rotor design. It then explores the characteristics and applications of sandwich structures and architected lattice cores, particularly triply periodic minimal surfaces (TPMS) such as gyroids, as lightweight yet mechanically efficient solutions. A section is dedicated to palm date fibers, summarizing their morphological features, extraction techniques, mechanical properties, and potential for use in bio-based composites.
- **Chapter 2 — Design Methodology and Realization of the Rotor:** This chapter details the complete process of rotor conception and manufacturing. The first part addresses geometric design, aerodynamic modeling, scaling adaptations, and preliminary structural estimations based on analytical tools. The second part describes the material selection strategy and the entire fabrication workflow, including natural fiber treatment, composite skin lamination, gyroid core 3D printing, and final assembly. This chapter serves as a bridge between numerical design logic and practical implementation, ensuring structural feasibility within aerodynamic constraints.
- **Chapter 3 — Material Characterization :** This chapter presents a combined experimental and numerical methodology to determine the equivalent elastic properties of the sandwich material. The mechanical behavior of the woven skin and the gyroid core were each characterized through tensile testing and homogenization simulations. These properties were then integrated to compute the overall stiffness of the full sandwich structure, serving as input for subsequent rotor-scale simulations.
- **Chapter 4 — Rotor Performance Investigation:** The fourth chapter assesses the mechanical and aerodynamic behavior of the assembled rotor under realistic conditions. It combines CFD–FSI simulations and wind tunnel testing to evaluate deformation, load response, and fluid interaction. This analysis serves to validate the suitability of the bio-based sandwich architecture for small-scale wind energy harvesting.
- **Chapter 5 — Results and Discussion :** The final chapter synthesizes the main findings obtained from both simulations and physical testing. It compares expected and observed performance metrics, identifies limitations, and proposes avenues for further optimization. The chapter concludes with a critical evaluation of the rotor’s potential deployment and the scalability of the materials and processes involved.

# Introduction and Theoretical Background

...

## Overview



This chapter establishes the scientific framework of the study, covering Savonius turbine aerodynamics, numerical methods, structural/material strategies, and natural fiber composites. It reviews the state of the art in each area to clarify the research gap and prepare for the design methodology.

## 1.1 Savonius Wind Turbine: Principles and Challenges

### 1.1.1 Operational Principles

The Savonius rotor is a type of vertical axis wind turbine (VAWT), typically with 2 or 3 buckets (blades).

When viewed from above, a two-bucket version features a characteristic 'S'-shaped profile. These buckets are typically arranged with either a central gap between them or, more commonly, with a partial overlap. The rotor may be configured with or without a central shaft, depending on the specific design.

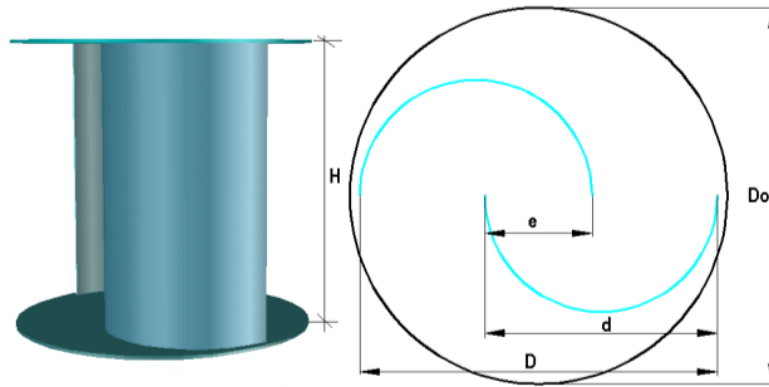


**FIGURE 1.1** – Savonius rotor geometry and main parameters, Adapted from [7].

The Savonius rotor operates on a **differential drag** principle. As wind impacts the rotor, the **concave surface** of the advancing bucket experiences a high positive pressure, generating a strong positive torque ( $M^+$ ). Conversely, the wind flows smoothly around the **convex surface** of the returning bucket, resulting in a lower pressure and a weaker negative torque ( $M^-$ ). The designed overlap ( $e$ ) between buckets promotes this effect by allowing airflow to pass through and further reduce the negative torque on the returning blade. The sum of these torques results in a net driving torque ( $M_{net} = M^+ + M^-$ ) that rotates the system about its vertical axis.

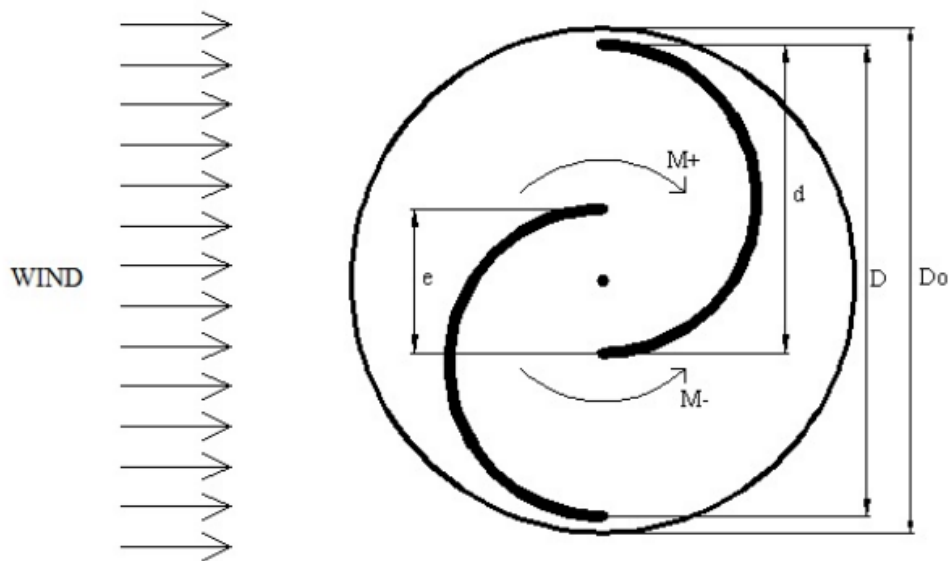


**FIGURE 1.2** – Scheme of the operational principle of Savonius turbine, Adapted from [7].



The real-world aerodynamics that underpin this principle are complex. The operation is best understood by examining the specific flow patterns that develop, as visualized in Figure 1.3. These flows explain both the source of the driving torque and the origins of the rotor's inherent inefficiencies.

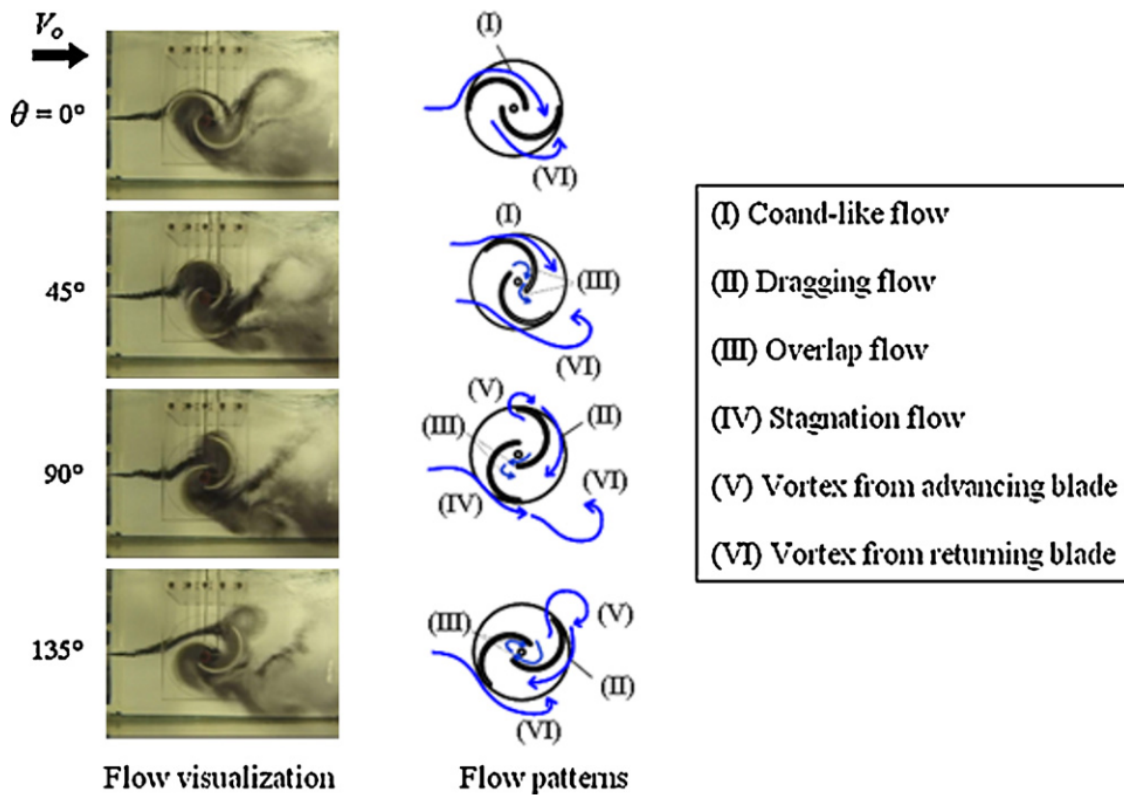


**FIGURE 1.3** – Flows patterns on a Savonius rotor, Adapted from [8].

The operation can be broken down by the following dominant flow patterns:

#### Flows that Generate Positive Torque:

- **Coanda-like Flow (I):** At low angular positions, the airflow attaches to the convex side of the advancing blade, contributing to a favorable pressure distribution.
- **Dragging Flow (II) & Overlap Flow (III):** These flows reduce the negative pressure on the returning bucket, thereby decreasing the opposing drag force and increasing the net torque.

#### Flows that Cause Negative Torque:

- **Stagnation Flow (IV):** This flow impinges directly on the returning bucket, creating a high-pressure zone that forcefully opposes the rotor's motion.
- **Vortex from Advancing Blade (V) & Vortex from Returning Blade (VI):** The shedding of vortices from the blade tips represents a significant energy loss and is a major contributor to the pulsating nature of the torque.

In summary, the net torque is governed by the rotor's specific geometry, which dictates the complex interplay between these competing flows. This interplay fundamentally explains the Savonius rotor's characteristic pulsating torque and moderate efficiency, leading directly to the structural challenges discussed in the next section.

### 1.1.2 Aerodynamic Challenges and Structural Implications

Before delving into the specific aerodynamic limitations and their structural consequences, it is crucial to recognize that rotor performance is not determined by aerodynamics alone. The operational behavior emerges from a complex interplay of design decisions, as illustrated in Figure 1.4.

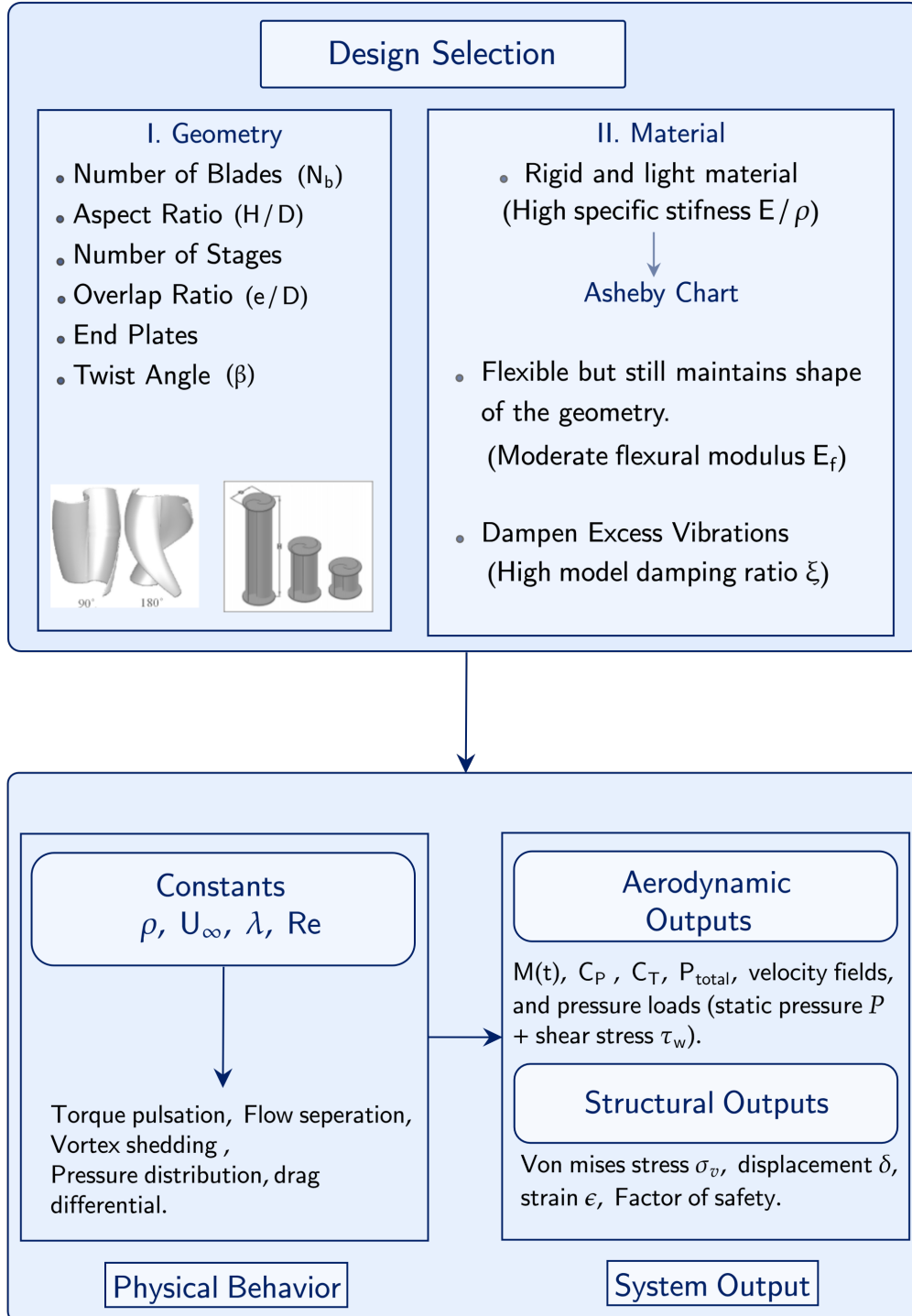


**FIGURE 1.4** – Design Methodology Flowchart.

For the first facet of this analysis, we examine the geometry-driven characteristics that influence the aerodynamics of the flow. A comprehensive understanding requires examining how these

aerodynamic characteristics fundamentally constrain structural design choices, while simultaneously recognizing that material selection actively influences aerodynamic performance through structural deformation and dynamic response.

### Aerodynamic Limitations and Structural Implications

Three interconnected aerodynamic phenomena dominate Savonius rotor behavior and impose significant structural constraints:

1. **Torque Pulsations:** The rotor experiences significant torque fluctuations throughout each revolution due to periodic variations in drag and lift forces. These pulsations create cyclic stresses that drive material fatigue and structural degradation. Multi-staging effectively mitigates these fluctuations by distributing aerodynamic loads more evenly, as demonstrated by the smoothed combined torque profile in Figure 1.5. The same study notes that helical blade twisting produces equivalent smoothing effects, with both approaches reducing peak stresses and improving operational lifetime [26].

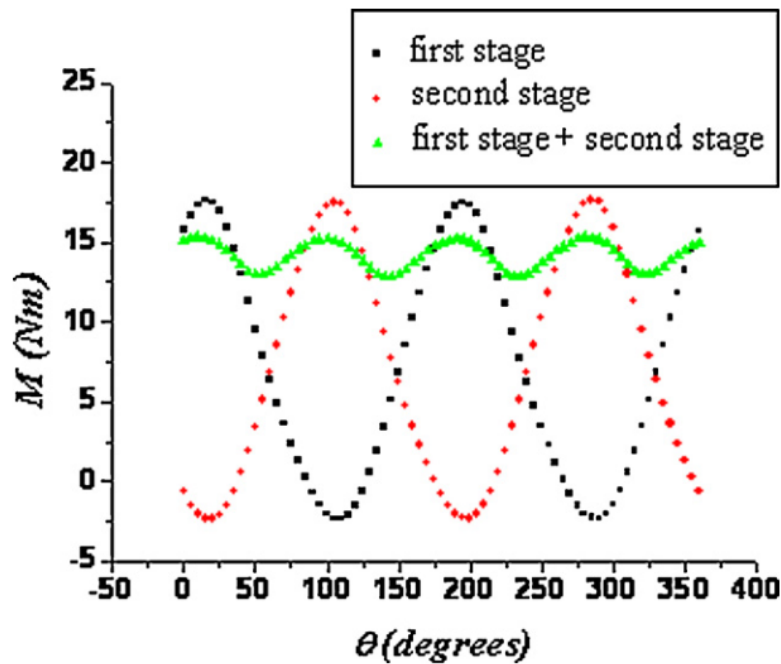


**FIGURE 1.5** – Sum of moment cycles on a different stage rotors, Adapted from [8].

2. **Vortex Shedding:** Low overlap ratios induce strong flow separation at blade edges, generating the alternating vortices identified in studies by Fujisawa and Gotoh (1992). This phenomenon, computationally confirmed by González Madina *et al.* (2021), creates unsteady pressure loads that directly excite structural vibrations. These vibrations dissipate energy and are a primary driver of high-cycle fatigue, critically compromising the turbine's long-term structural integrity.
3. **3D Flow Effects:** The absence of end plates allows significant flow leakage around blade tips, dramatically increasing turbulence kinetic energy and power loss. Research by Kassab *et al.* (2020) quantified that turbines without end plates exhibit twice the TKE at blade tips, directly linking this leakage to the formation of powerful tip vortices. Structurally,

containing this flow is critical, as it reduces the high-frequency vibrations and bending moments induced by tip vortices. The addition of optimally-sized end plates (1.1D) is therefore essential to maintain the pressure differential that generates useful torque and ensures stable structural loading [27].

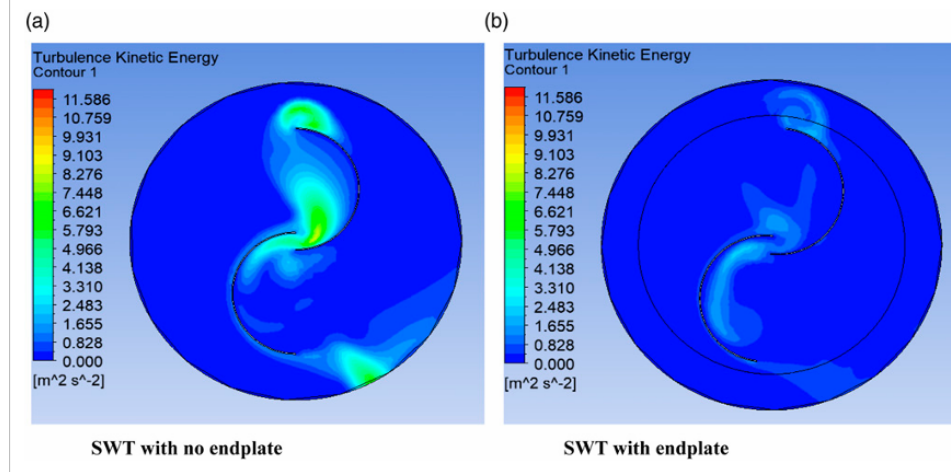


**FIGURE 1.6** – Turbulent kinetic energy (TKE) contours at TSR of 0.8.

From the previously discussed geometric optimization parameters—such as the overlap ratio, end plates, twist angle ( $\beta$ ), and multi-staging—it is clear that a significant body of research has focused on this approach to mitigate aerodynamic challenges like torque pulsations and vortex shedding. However, these geometric strategies represent one facet of the solution and encounter inherent limits:

- Performance gains from one parameter can be offset by compromises in another
- Geometric optimization cannot fully resolve the fundamental issue of cyclic stress accumulation
- Vibrational energy dissipation within the structure requires material-level solutions

This inherent limitation necessitates the second critical facet of the design methodology: material selection. The physical behaviors of torque pulsation, vortex shedding, and unsteady pressure distribution directly inform three key material requirements:

- **High specific stiffness ( $E/\rho$ ):** A rigid and lightweight material, selectable through Ashby charts, is essential to minimize inertial resistance while maintaining geometric integrity under aerodynamic loads. This property directly influences performance outputs including torque ( $C_T$ ) and power ( $P_{total}$ ) by preserving the optimal blade shape during operation.
- **High damping capacity ( $\xi$ ):** The cyclic nature of torque fluctuations demands a material capable of dissipating vibrational energy, thereby reducing the amplitude of von Mises stress ( $\sigma_v$ ) and extending fatigue life.
- **Moderate flexural modulus:** The material must withstand repetitive bending from pressure differentials without accumulating permanent displacement ( $\delta$ ) or critical strain ( $\epsilon$ ) that would compromise the aerodynamic profile over time.

These material criteria are validated through Fluid-Structure Interaction (FSI) studies, which quantify the system's structural response. Research applying one-way FSI to Savonius turbines has demonstrated that the front portion of the advancing blade experiences the most severe

loading, manifesting as a localized zone of minimum Factor of Safety and elevated strain concentrations [9].

As shown in Figure 1.7, the Factor of Safety reaches critical values (as low as 1.63) at specific rotor angles ( $0^\circ$ ,  $180^\circ$ , and  $360^\circ$ ), particularly for configurations with duct augmentation. This finding directly links the aerodynamic loads to the critical structural outputs in the design methodology.

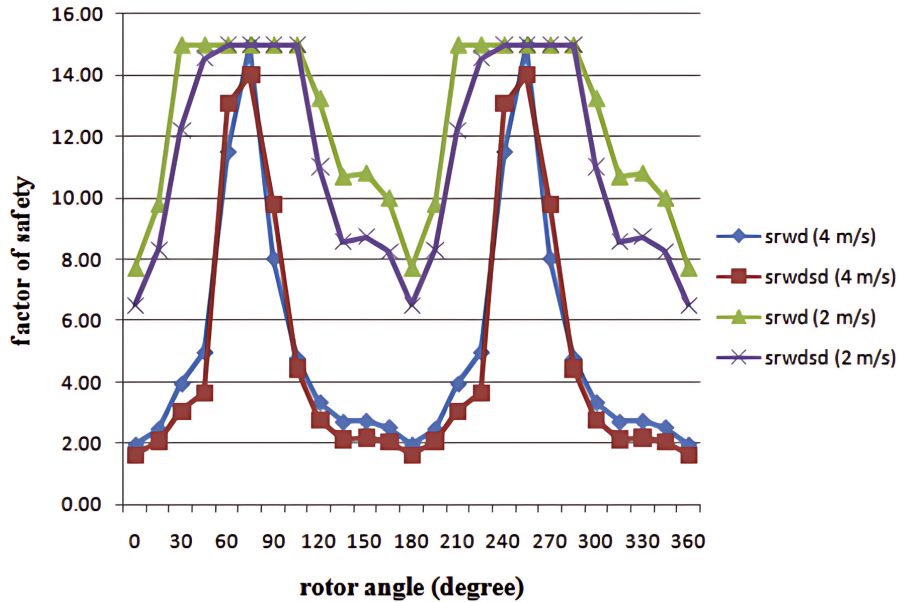


**FIGURE 1.7** – Variation of Factor of Safety with rotor angle for Savonius rotor with duct augmentation at 4 m/s (adapted from [9])

This stark performance-structure trade-off demonstrates that optimizing for metrics like torque ( $C_T$ ) and power ( $P_{\text{total}}$ ) alone is insufficient and can critically compromise structural integrity. The design objective must, therefore, be redefined to balance performance with structural-integrity outputs: von Mises stress ( $\sigma_v$ ), displacement ( $\delta$ ), strain ( $\epsilon$ ), and Factor of Safety.

This balanced philosophy, ensuring both high performance and long-term durability, fundamentally guides the subsequent investigation into advanced composite materials as a necessary solution.

## 1.2 Aerodynamic and Structural Analysis: A Coupled Approach

The performance-structure trade-off established in the previous section necessitates a methodology capable of simultaneously capturing both aerodynamic loading and structural response. For the Savonius rotor, this interaction can be examined through both *experimental* and *numerical* approaches, each offering distinct advantages and limitations.

Experimental validation via wind tunnel testing remains the benchmark for measuring aerodynamic coefficients such as torque ( $C_T$ ) and power ( $C_P$ ). However, studies that also quantify the structural response—including stress, strain, and deformation under operational loads—are

comparatively limited. This gap is being narrowed by the adoption of advanced measurement techniques:

- **Digital Image Correlation (DIC)** is a non-contact optical technique that measures surface displacement fields, from which deformation ( $\delta$ ) and strain ( $\epsilon$ ) are derived. For example, [28] employed 3D-DIC to capture full-field dynamic deformation of wind turbine blades under realistic conditions, providing essential validation data for numerical models.
- **Strain gauge arrays** provide direct, high-frequency measurements of surface stresses and vibrational modes but are limited by wiring complexity, potential signal noise, and calibration challenges on rotating systems.

While these approaches provide valuable experimental insight, their practical implementation on spinning rotors remains challenging and resource-intensive.

To overcome these challenges, **Fluid–Structure Interaction (FSI)** has become the predominant computational framework for analyzing the coupled aerodynamic and structural behavior of the Savonius rotor. FSI integrates two well-established solvers:

- **Computational Fluid Dynamics (CFD)**, typically based on the *Finite Volume Method (FVM)*, solves the Navier–Stokes equations to predict aerodynamic loads.
- **Finite Element Analysis (FEA)** solves the structural equilibrium equations to evaluate the rotor’s deformation and mechanical response.

The two solvers are integrated at their shared interface: pressure and shear forces from the fluid domain act on the structure, while the resulting deformations are fed back into the flow field, enabling a fully coupled aeroelastic simulation.

FSI analysis resolves the coupled system through three interconnected domains, as summarized in Table 1.1:

**TABLE 1.1** – Fluid–Structure Interaction (FSI) framework components

Fluid–Structure Interaction (FSI) Framework		
Fluid Domain	FSI Interface	Structural Domain
<i>Governing Equations:</i> <ul style="list-style-type: none"> <li>• Continuity: <math>\nabla \cdot \mathbf{u} = 0</math></li> <li>• Navier–Stokes equations</li> <li>• Turbulence model</li> </ul>	<i>Coupling Conditions:</i> <ul style="list-style-type: none"> <li>• Velocity continuity</li> <li>• Traction equilibrium</li> </ul> <i>Methods:</i> <ul style="list-style-type: none"> <li>• Monolithic / Partitioned</li> <li>• One-way / Two-way coupling</li> </ul>	<i>Governing Equations:</i> <ul style="list-style-type: none"> <li>• Equilibrium: <math>[K]\{\mathbf{u}\} = \{\mathbf{F}\}</math></li> <li>• Constitutive relations</li> <li>• Compatibility conditions</li> </ul>
Information Exchange Across the FSI Interface		
<b>Fluid → Structure:</b> Pressure ( $p$ ), Shear stress ( $\tau_w$ ) <b>Structure → Fluid:</b> Displacement ( $\mathbf{u}$ ), Velocity ( $\dot{\mathbf{u}}$ )		

### 1.2.1 Principles of CFD Investigations

#### I. Pre-Processing:

##### 1. Geometry Creation:

The computational model is developed in either 2D or 3D, depending on the study objectives. 2D simulations provide faster results and are computationally efficient but neglect three-dimensional effects such as *tip vortices* and *secondary flow structures*.

##### 2. Computational Domain Setup & Boundary Conditions:

The domain geometry and dimensions are typically designed based on wind tunnel dimensions to ensure consistency between CFD and real-world testing and to position the inlet and outlet boundaries far enough to minimize flow distortion.

- For the Savonius rotor, the computational domain is divided into two regions—rotating and stationary. The rotating region (a circle in 2D or a cylinder in 3D) represents the turbine, using the **Multiple Reference Frame (MRF)** approach.
- Many CFD studies include a **body of influence (BoI)** to refine mesh resolution in zones of high turbulence intensity.
- Typical boundary conditions: **velocity inlet**, **pressure outlet**, **symmetry** on domain sides, and **wall** for blade surfaces.

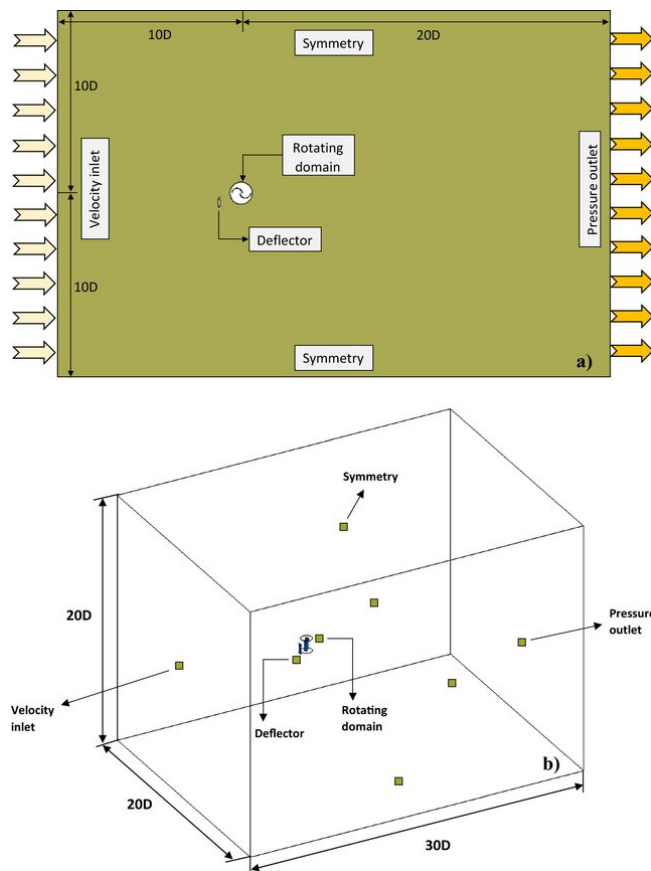


**FIGURE 1.8** – Boundary conditions and computational domains for (a) 2D and (b) 3D Savonius simulations. Adapted from [10].



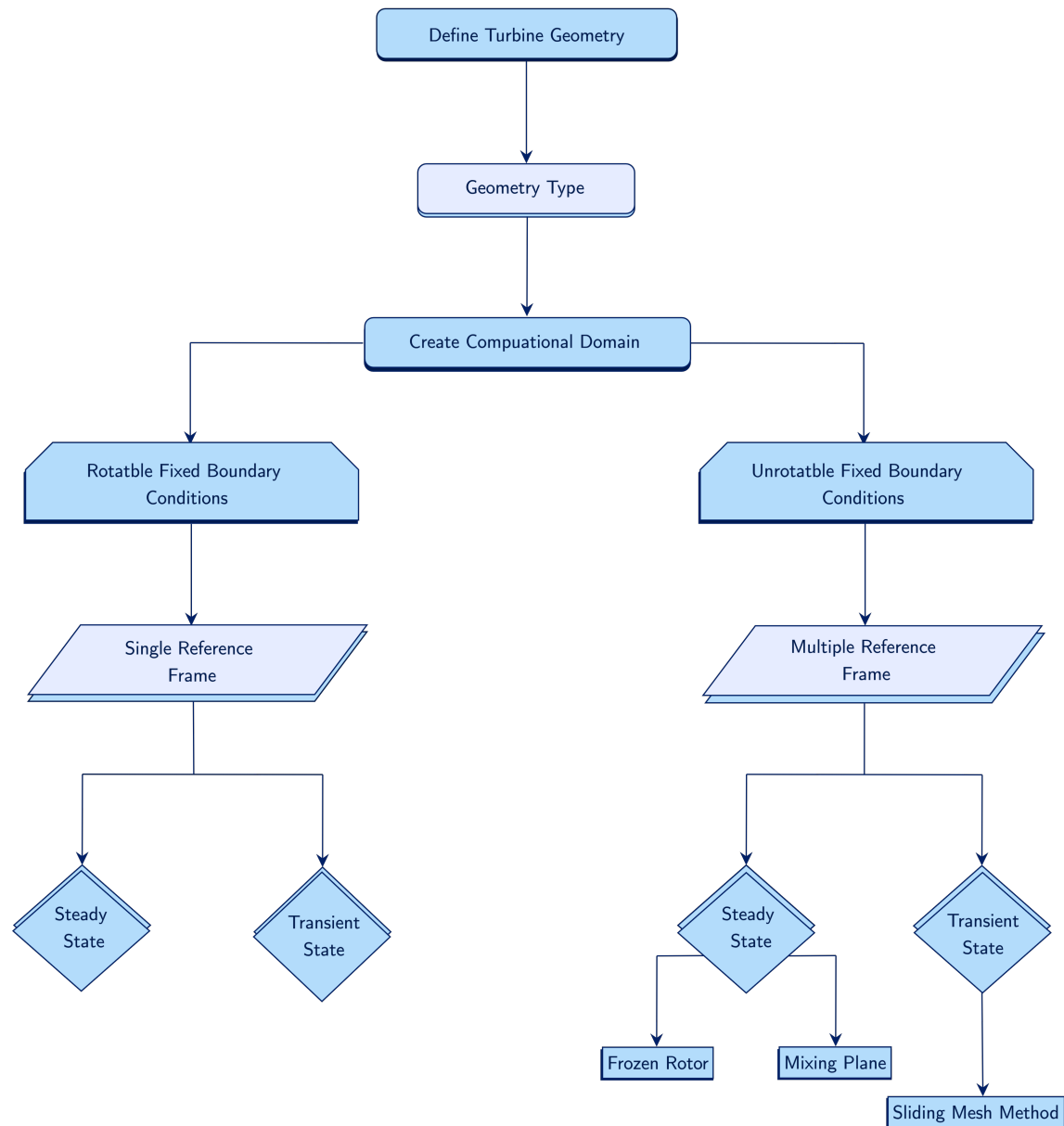


**FIGURE 1.9** – CFD methodology selection framework based on turbine geometry and boundary conditions.

The methodology selection process follows a systematic approach based on geometric and flow characteristics:

- **Single Reference Frame (SRF):** The entire domain rotates as one body (e.g., pumps). Applicable to steady or transient flows.
- **Multiple Reference Frame (MRF):** Stationary and rotating domains coexist—common in turbines.
  - *Steady-state:* Frozen rotor and mixing-plane methods.
  - *Transient:* Sliding mesh method for explicit rotor–stator interactions.
- **Savonius Rotors:** Require MRF with a **Sliding Mesh Method** to capture vortex shedding and dynamic stall.



### 3. Meshing:

Meshing divides the domain into discrete control volumes where governing equations are numerically solved. Savonius rotor studies typically use **unstructured triangular meshes** for flexibility around curved geometries.

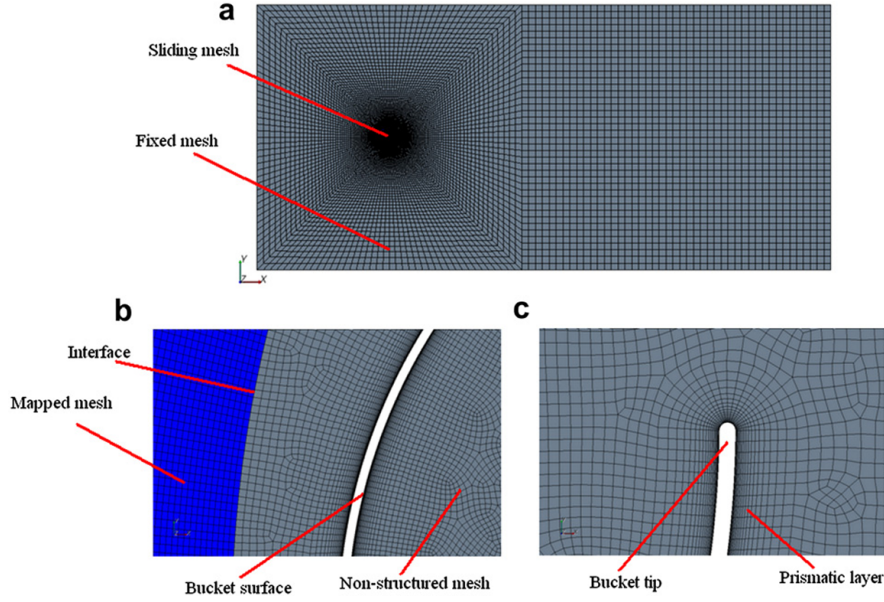


**FIGURE 1.10** – Mesh topology around the S-rotor: (a) overview of the discretized domain; (b) near the interface; and (c) prismatic boundary layers. Adapted from [11].

To resolve near-wall regions—where velocity and turbulence gradients are steep—**inflation layers** (boundary-layer refinement) are applied. These ensure  $y^+ < 1$  for accurate wall treatment.

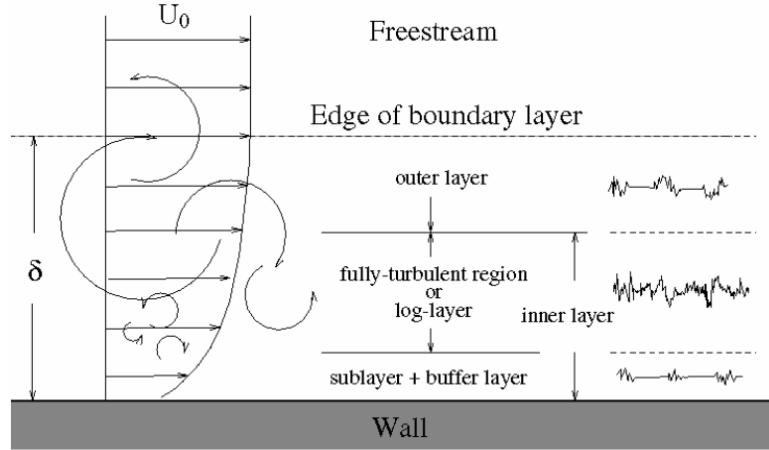


**FIGURE 1.11** – Schematic representation of the near-wall boundary layer.

The first-layer height is calculated to achieve target  $y^+$  values using:

$$y^+ = \frac{u_\tau y}{\nu}, \quad (1.1a)$$

$$u_\tau = U \sqrt{\frac{C_f}{2}}, \quad (1.1b)$$

$$C_f = 0.0576 \text{Re}^{-1/5}, \quad (1.1c)$$

where:

- $U$  : freestream velocity [m/s]
- $\nu$  : kinematic viscosity [m<sup>2</sup>/s]
- $Re = \frac{UD}{\nu}$  : Reynolds number
- $u_\tau$  : friction velocity [m/s]
- $C_f$  : skin friction coefficient
- $y^+$  : non-dimensional wall distance

For typical Savonius turbine conditions, the first-layer height is on the order of  $10^{-5}$  m to resolve the viscous sublayer accurately.

## II. Solver Setup:

In this stage introduces how the numerical solver approximates the conservation laws of mass and momentum for a given flow regime.

### 1. Governing Equations:

CFD simulations solve the continuity and Navier–Stokes equations to model mass and momentum conservation.

#### • Continuity equation:

$$\frac{\partial \rho}{\partial t} + \nabla \cdot (\rho \mathbf{u}) = 0 \quad (1.2)$$

#### • Momentum equation (vector form):

$$\frac{\partial(\rho \mathbf{u})}{\partial t} + \nabla \cdot (\rho \mathbf{u} \otimes \mathbf{u}) = -\nabla p + \nabla \cdot (\mu \nabla \mathbf{u}) + \mathbf{F} \quad (1.3)$$

#### • Expanded form in Cartesian coordinates:

$$\frac{\partial u}{\partial t} + u \frac{\partial u}{\partial x} + v \frac{\partial u}{\partial y} + w \frac{\partial u}{\partial z} = -\frac{1}{\rho} \frac{\partial p}{\partial x} + \nu \left( \frac{\partial^2 u}{\partial x^2} + \frac{\partial^2 u}{\partial y^2} + \frac{\partial^2 u}{\partial z^2} \right) + F_x, \quad (1.4a)$$

$$\frac{\partial v}{\partial t} + u \frac{\partial v}{\partial x} + v \frac{\partial v}{\partial y} + w \frac{\partial v}{\partial z} = -\frac{1}{\rho} \frac{\partial p}{\partial y} + \nu \left( \frac{\partial^2 v}{\partial x^2} + \frac{\partial^2 v}{\partial y^2} + \frac{\partial^2 v}{\partial z^2} \right) + F_y, \quad (1.4b)$$

$$\frac{\partial w}{\partial t} + u \frac{\partial w}{\partial x} + v \frac{\partial w}{\partial y} + w \frac{\partial w}{\partial z} = -\frac{1}{\rho} \frac{\partial p}{\partial z} + \nu \left( \frac{\partial^2 w}{\partial x^2} + \frac{\partial^2 w}{\partial y^2} + \frac{\partial^2 w}{\partial z^2} \right) + F_z. \quad (1.4c)$$

### 2. Turbulence Modeling:

Turbulence is modeled using the Unsteady Reynolds-Averaged Navier–Stokes (URANS) approach, which balances accuracy and computational cost for unsteady flows like the Savonius turbine.

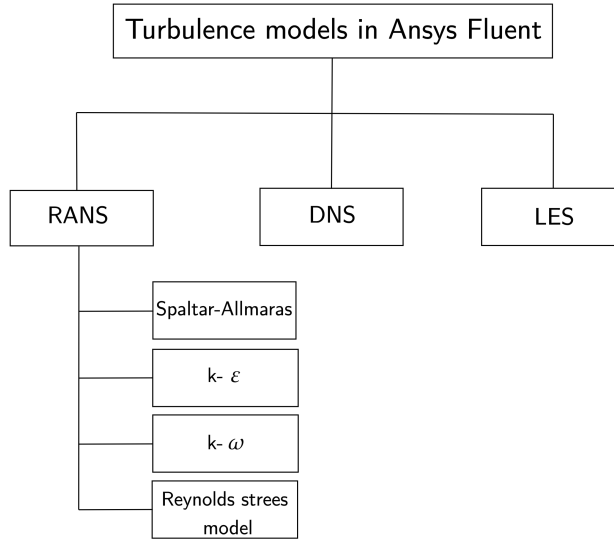


**FIGURE 1.12** – Classification of turbulence models in ANSYS Fluent.

In the Unsteady Reynolds-Averaged Navier–Stokes (URANS) framework, the instantaneous velocity field is decomposed into mean and fluctuating components as:

$$u_i = \bar{u}_i + u'_i$$

Substituting this decomposition into the Navier–Stokes equations and applying a time-averaging operator yields the URANS form:

$$\frac{\partial(\rho \bar{u}_i)}{\partial t} + \frac{\partial(\rho \bar{u}_i \bar{u}_j)}{\partial x_j} = -\frac{\partial \bar{p}}{\partial x_i} + \frac{\partial}{\partial x_j} \left[ \mu \frac{\partial \bar{u}_i}{\partial x_j} - \rho \overline{u'_i u'_j} \right]$$

Here,  $\overline{\rho u'_i u'_j}$  represents the **Reynolds stress tensor**, which introduces additional unknowns—giving rise to the well-known *closure problem*. This issue is resolved using the **SST  $k$ – $\omega$  turbulence model**, widely adopted in Savonius rotor analyses due to its reliable prediction of *flow separation*, *dynamic stall*, and *vortex shedding*.

Once the governing equations and turbulence models are defined, the next step involves their **numerical discretization**. Among the various numerical approaches, the **Finite Volume Method (FVM)** combined with the **SIMPLE** pressure–velocity coupling is most commonly applied in CFD analyses of Savonius rotors for transient, incompressible flows.

### III. Post-Processing:

- **Flow Visualization:** Visualization of vortex shedding, wake interaction, and pressure distribution.
- **Performance Metrics:** Extraction of torque ( $T$ ), power coefficient ( $C_P$ ), and moment coefficient ( $C_M$ ) to evaluate turbine performance.

## 1.2.2 Principles of FEA Structural Analysis

Finite Element Analysis (FEA) predicts the structural response under mechanical or fluid-induced loads by discretizing the domain into finite elements. In Fluid–Structure Interaction (FSI) simulations, FEA provides displacement, strain, and stress data exchanged with the fluid solver, depending on the coupling approach (one-way or two-way). The analysis process is generally divided into three main stages:

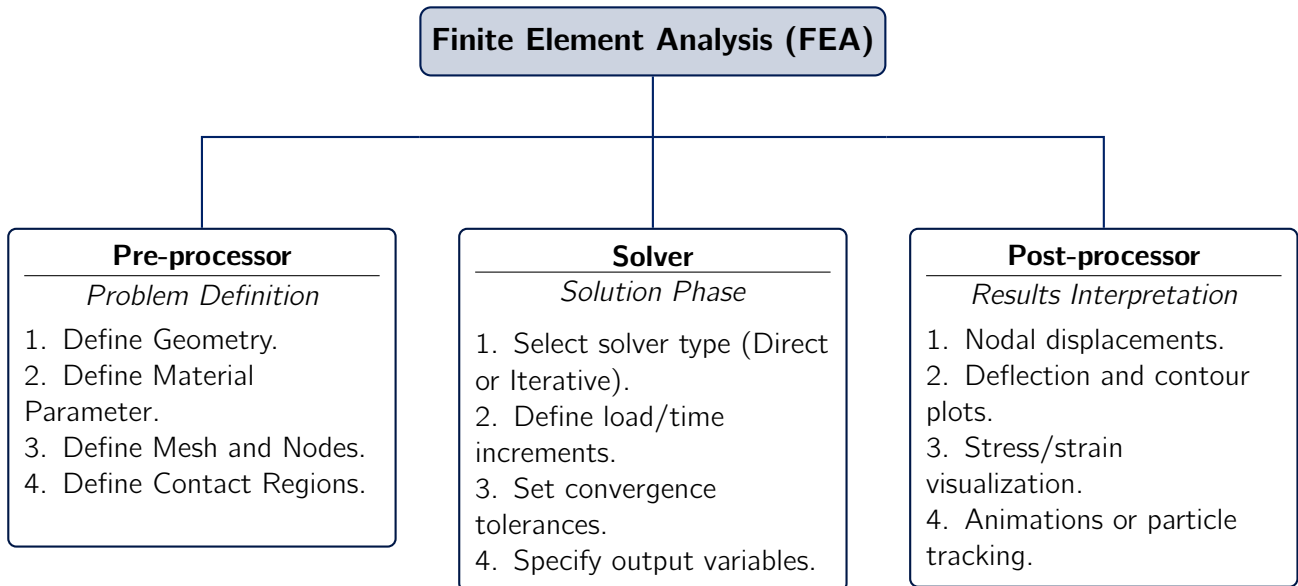


**FIGURE 1.13** – Schematic of Finite Element Analysis (FEA) process.

## I. Pre-Processing:

### 1. Geometry:

For Fluid–Structure Interaction (FSI) simulations, the geometry is shared between the fluid and structural domains to allow consistent definition of the common interface where pressure and displacement data will be exchanged during the coupled analysis.

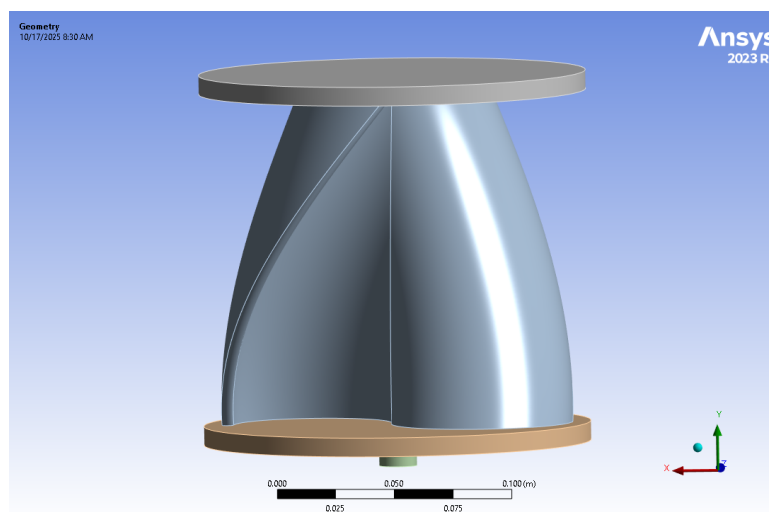


**FIGURE 1.14** – 3D CAD geometry of the rotor model used in the FSI analysis.

When configuring the structural model, the fluid domains are **suppressed**, retaining only the solid components for subsequent meshing and material assignment.

## 2. Material & Boundary Conditions:

In this stage, materials are defined either by selecting from the Fluent material library or by specifying custom properties in the *Engineering Data* section of the Transient Structural module. Once defined, materials are updated and assigned to each solid component individually.

Most recent FSI studies on Savonius rotors adopt a similar setup for structural boundary conditions [29, 12]. The common definitions are as follows:

- **Fixed constraint** applied at the base or shaft interface to restrict all translational and rotational motion.
- **Pressure loads** imported from the Fluent solver at the fluid–structure interface to represent aerodynamic forces.
- **Rotational effects** applied through an angular velocity boundary condition, representing turbine rotation. This automatically includes centrifugal and Coriolis effects within the transient solution.
- **Contact behavior** is specified at interfaces between different materials to ensure accurate load transfer, commonly using a *bonded* condition to maintain full structural continuity.

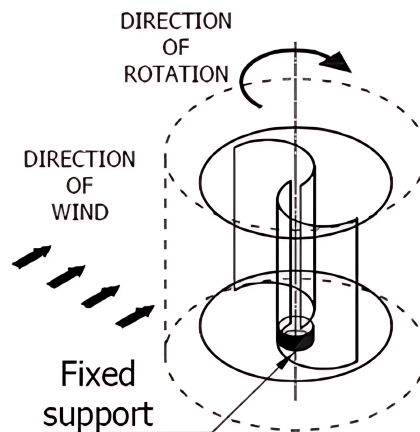


**FIGURE 1.15** – Boundary condition setup for the Savonius rotor [12].

## 3. Define Mesh:

Accurate FSI modelling requires compatible meshing between the fluid and structural domains to ensure stable and realistic load transfer across the interface. As highlighted by Kalita and Rao [30], two meshing strategies are generally employed:

- **Conformal meshing**: both domains share identical nodes along the interface, providing direct load transfer without interpolation but requiring identical mesh topology.
- **Non-conformal meshing**: the fluid and structural meshes differ but are coupled through interpolation functions that map pressure and displacement data across the interface.

ANSYS employs the **non-conformal approach**, where independent fluid and structural meshes are coupled through *System Coupling* using interpolation-based mapping. To reduce interpolation errors, most FSI studies—including Marzec *et al.* [12]—recommend maintaining similar mesh densities along the interface (typically within  $\pm 30\%$ ) for accurate pressure and displacement exchange.

Figure 1.16 illustrates this interpolation process, where the pressure loads from Fluent are transferred to the structural domain through the *Mechanical-Based Mapping* option in ANSYS Transient Structural.

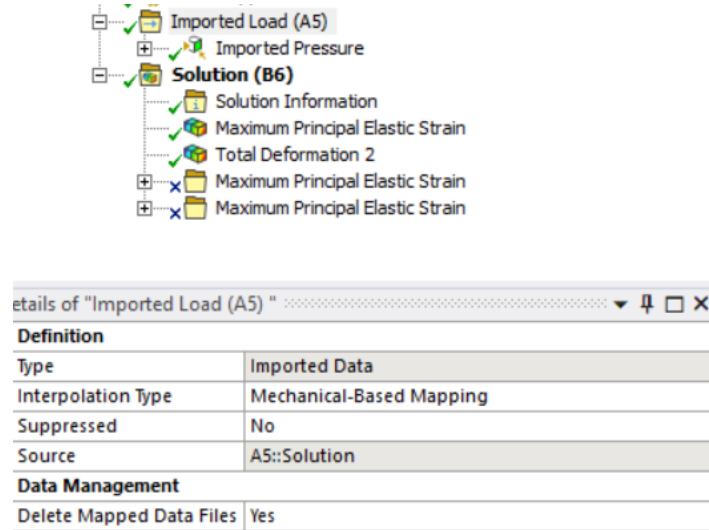


**FIGURE 1.16** – ANSYS interface showing pressure load interpolation using *Mechanical-Based Mapping* between fluid and structural meshes.

## II. Solver Setup:

The solver setup runs the calculations without any interference from the user. In this stage we could define the governing equations, material constitutive behaviour, and the coupling methodology used to integrate the fluid and structural domains.

### 1. Governing Equations:

The specific formulation of the governing equations depends on the assumed material model—*isotropic*, *orthotropic*, or *anisotropic*—as it determines the stress–strain relationship and the number of elastic constants involved.

For the structural domain, the general equation of motion expressing conservation of linear momentum is:

$$\rho_s \frac{\partial^2 \mathbf{u}}{\partial t^2} = \nabla \cdot \boldsymbol{\sigma}_s + \mathbf{f}_s \quad (1.5)$$

where  $\rho_s$  is the solid density,  $\mathbf{u}$  the displacement vector,  $\boldsymbol{\sigma}_s$  the Cauchy stress tensor, and  $\mathbf{f}_s$  the body force per unit volume.

For rotating systems, such as the Savonius rotor, the equation of motion is expressed in a rotating reference frame to account for additional inertial effects. Consequently, the body force

term  $\mathbf{f}_s$  in Eq. 1.5 includes contributions from both centrifugal and Coriolis accelerations, and is written as [12]:

$$\mathbf{f}_s = -\rho_s \left( 2 \boldsymbol{\omega} \times \frac{\partial \mathbf{v}_s}{\partial t} + \boldsymbol{\omega} \times (\boldsymbol{\omega} \times \mathbf{r}) \right) \quad (1.6)$$

where:

- $\boldsymbol{\omega}$ : angular velocity vector of the solid relative to the global inertial frame;
- $\frac{\partial \mathbf{v}_s}{\partial t}$ : rate of deformation of the solid in the rotating reference frame;
- $\mathbf{r}$ : position vector in the rotating reference frame.

The stress tensor  $\sigma_s$  is defined through the constitutive relationship, which varies with material type:

**For isotropic linear-elastic materials:**

$$\sigma_s = \lambda(\nabla \cdot \mathbf{u})\mathbf{I} + 2G\boldsymbol{\varepsilon} \quad (1.7)$$

where  $\lambda$  and  $G$  are Lamé's constants,  $\mathbf{I}$  is the identity tensor, and  $\boldsymbol{\varepsilon}$  is the infinitesimal strain tensor:

$$\boldsymbol{\varepsilon} = \frac{1}{2}(\nabla \mathbf{u} + \nabla \mathbf{u}^T)$$

The Lamé parameters are related to Young's modulus  $E$  and Poisson's ratio  $\nu$  as:

$$\lambda = \frac{E\nu}{(1+\nu)(1-2\nu)}, \quad G = \frac{E}{2(1+\nu)}$$

**For orthotropic materials:**

$$\begin{bmatrix} \sigma_x \\ \sigma_y \\ \sigma_z \\ \tau_{xy} \\ \tau_{yz} \\ \tau_{zx} \end{bmatrix} = [\mathbf{C}] \begin{bmatrix} \varepsilon_x \\ \varepsilon_y \\ \varepsilon_z \\ \gamma_{xy} \\ \gamma_{yz} \\ \gamma_{zx} \end{bmatrix} \quad (1.8)$$

where  $[\mathbf{C}]$  is the  $6 \times 6$  stiffness matrix containing nine independent elastic constants:

Let  $\Delta = 1 - \nu_{xy}\nu_{yx} - \nu_{yz}\nu_{zy} - \nu_{zx}\nu_{xz} - 2\nu_{xy}\nu_{yz}\nu_{zx}$

$$[\mathbf{C}] = \begin{bmatrix} \frac{E_x(1-\nu_{yz}\nu_{zy})}{\Delta} & \frac{E_x(\nu_{yx}+\nu_{zx}\nu_{yz})}{\Delta} & \frac{E_x(\nu_{zx}+\nu_{yx}\nu_{zy})}{\Delta} & 0 & 0 & 0 \\ \frac{E_y(\nu_{xy}+\nu_{zy}\nu_{xz})}{\Delta} & \frac{E_y(1-\nu_{zx}\nu_{xz})}{\Delta} & \frac{E_y(\nu_{zy}+\nu_{xy}\nu_{zx})}{\Delta} & 0 & 0 & 0 \\ \frac{E_z(\nu_{xz}+\nu_{xy}\nu_{yz})}{\Delta} & \frac{E_z(\nu_{yz}+\nu_{xz}\nu_{yx})}{\Delta} & \frac{E_z(1-\nu_{xy}\nu_{yx})}{\Delta} & 0 & 0 & 0 \\ 0 & 0 & 0 & G_{xy} & 0 & 0 \\ 0 & 0 & 0 & 0 & G_{yz} & 0 \\ 0 & 0 & 0 & 0 & 0 & G_{zx} \end{bmatrix}$$

Here  $E_x, E_y, E_z$  are the moduli of elasticity in the principal material directions,  $\nu_{ij}$  the Poisson's ratios, and  $G_{ij}$  the shear moduli, with the symmetry relations  $\nu_{ij}/E_i = \nu_{ji}/E_j$ . In the finite element formulation, the conservation of momentum is discretized over the model domain to yield the global equation of motion:

$$[\mathbf{M}] \ddot{\mathbf{U}} + [\mathbf{C}] \dot{\mathbf{U}} + [\mathbf{K}] \mathbf{U} = \{\mathbf{F}(t)\} \quad (1.9)$$

where  $[M]$  is the global mass matrix,  $[C]$  the damping matrix,  $[K]$  the stiffness matrix,  $U$ ,  $\dot{U}$ , and  $\ddot{U}$  are the nodal displacement, velocity, and acceleration vectors, and  $\{F(t)\}$  is the time-dependent external load vector.

This system of equations is solved incrementally over time using implicit or explicit integration schemes to obtain the transient structural response under fluid-induced loading.

## 2. FSI Coupling Methodology:

Regardless of whether one-way or two-way coupling methods are used, these two general approaches are commonly used:

- **Monolithic coupling:** solves the governing equations of the fluid and structure simultaneously as one unified system. Although this approach provides high numerical accuracy, it is computationally expensive and difficult to implement for large, rotating geometries such as the Savonius turbine.
- **Partitioned coupling:** the more widely adopted method—solves the fluid and structural domains separately using their respective solvers (e.g., Fluent and Transient Structural in ANSYS). At each time step, interface data are transferred iteratively until convergence of forces and displacements is achieved.

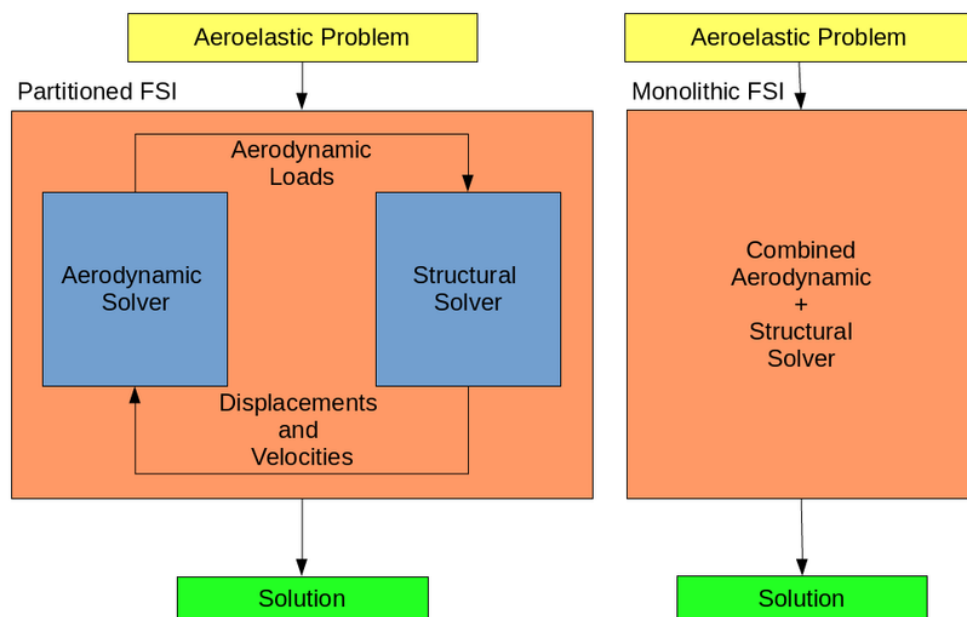


**FIGURE 1.17** – Schematic representation of the partitioned FSI coupling process. Adapted from [13].

In the partitioned approach, the following iterative procedure is generally applied within each time step:

- The **fluid solver** computes pressure and shear forces at the interface and passes them to the structural solver.
- The **structural solver** calculates the resulting displacements and stresses, then returns the updated geometry (or displacement field) to the fluid solver.



- The fluid mesh is updated according to the new deformed interface.
- This exchange repeats until convergence criteria for pressure and displacement are met.

The coupling between the two solvers enforces both **kinematic** and **dynamic** equilibrium at the fluid–structure interface  $\Gamma_{FSI}$ , given by the following relations:

$$\mathbf{u}_f = \mathbf{u}_s \quad \text{on} \quad \Gamma_{FSI} \quad (\text{kinematic continuity}) \quad (1.10)$$

$$\sigma_f \cdot \mathbf{n} = \sigma_s \cdot \mathbf{n} \quad \text{on} \quad \Gamma_{FSI} \quad (\text{dynamic equilibrium}) \quad (1.11)$$

### III. Post-Processing:

Post-processing involves interpreting the numerical results to evaluate the structural integrity and longevity of the rotor.

Commonly extracted quantities include displacement, deformation fields, and equivalent stress distributions such as von Mises or composite failure criteria (Tsai–Hill, Tsai–Wu), along with the *factor of safety* (FoS).

**Tsai–Hill Criterion:** Based on the distortion energy theory, this criterion predicts failure in anisotropic or orthotropic materials as:

$$\left(\frac{\sigma_1}{X_t}\right)^2 - \frac{\sigma_1\sigma_2}{X_t^2} + \left(\frac{\sigma_2}{Y_t}\right)^2 + \left(\frac{\tau_{12}}{S}\right)^2 = 1 \quad (1.12)$$

where  $\sigma_1$  and  $\sigma_2$  are the principal stresses in the material axes,  $X_t$  and  $Y_t$  are the tensile strengths, and  $S$  is the in-plane shear strength.

**Tsai–Wu Criterion:** A more general criterion accounting for both tension and compression asymmetry is expressed as:

$$F_i\sigma_i + F_{ij}\sigma_i\sigma_j = 1 \quad (1.13)$$

where  $F_i$  and  $F_{ij}$  are experimentally determined strength tensors depending on the material properties. Failure is predicted when the left-hand side of Eq. 1.13 exceeds unity.

**Factor of Safety (FoS):** The FoS quantifies the margin between the material strength and the applied stress:

$$\text{FoS} = \frac{\sigma_{\text{allowable}}}{\sigma_{\text{max}}} \quad (1.14)$$

A value greater than one indicates that the structure can withstand the applied load safely, while values close to unity suggest potential failure under extreme conditions.

Visual outputs such as stress contours, safety-factor plots, and deformation animations provide intuitive insight into the regions most susceptible to damage.

## 1.3 Date Palm Fiber Characterization for Composite Applications

To identify the optimal fiber source for composite reinforcement, it is first necessary to understand the anatomical structure of the date palm, as different parts yield fibers with distinct mechanical properties. This anatomical assessment establishes a fundamental basis for determining

which components of the date palm are best suited for composite applications, emphasizing the unique value of this biomass compared to other bio-sourced alternatives.

### 1.3.1 Anatomy of Date Palm and Fiber-bearing Parts

The date palm (*Phoenix dactylifera* L.) stands out among more than 2,600 palm species due to its extensive cultivation across arid regions, spanning from Saharan oases to the Persian Gulf and southern United States. Characterized by a slender stipe reaching up to 30 m in height, this monocotyledon exhibits fundamental structural differences from conventional woody trees. The trunk retains persistent leaf sheaths from abscised fronds, while the crown typically supports 20–30 pinnate leaves, each extending up to 6 m in length.

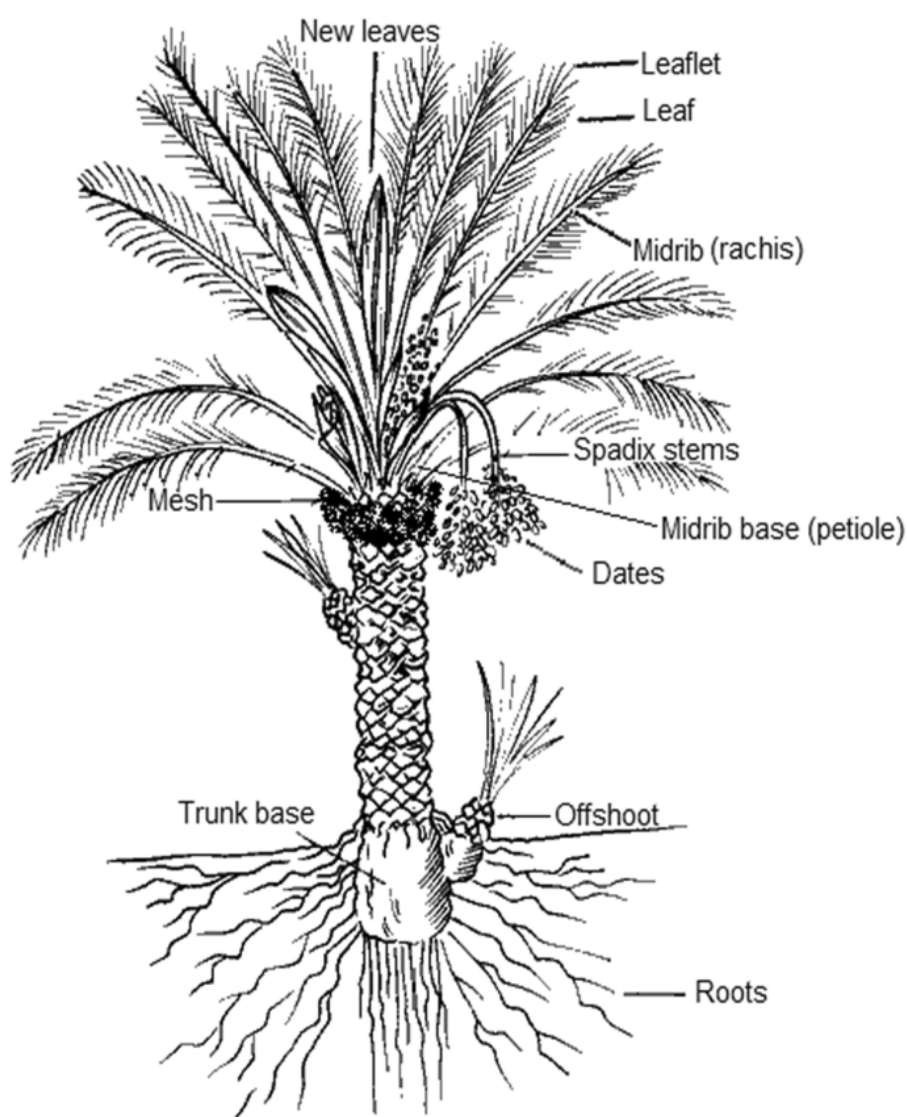


**FIGURE 1.18** – Schematic representation of date palm morphology.

In addition to its role in fruit production, *Phoenix dactylifera* L. also provides a promising source of natural fibers for composite manufacturing. Annual pruning operations, essential for palm maintenance, generate large quantities of fibrous residues.

Figure 1.19 illustrates the four principal fiber sources generated during routine palm maintenance: the *midribs*, *mesh*, *spadix stems*, and *leaflets*. The *midribs* (also called the *rachis*) form the

central axis of the frond and produce coarse, stiff fibers. The *mesh* (or *sheath/coir*) is the fibrous layer surrounding the trunk and leaf bases. The *spadix stems* are the fruit-bearing branches, while the *leaflets* yield finer and more flexible fibers.



**FIGURE 1.19** – Principal date palm fiber sources: spadix stems, leaflets, midribs, and mesh.

From this initial identification, these components can be further organized according to their *length* and *aspect ratio* (fiber length relative to diameter). This parameter is widely used as a standard criterion in natural fiber classification.

In this context, fiber *length* is a primary indicator for selecting the appropriate processing and extraction method, whereas the *aspect ratio* is a critical determinant of the composite's mechanical performance, as it directly affects stress transfer and reinforcement efficiency within the matrix.

Based on these parameters, following established ranges reported for natural fibers, the date palm sources can therefore be grouped into long fibers (midribs and mesh) and short fibers (spadix stems and leaflets), as illustrated in Figure 1.20.

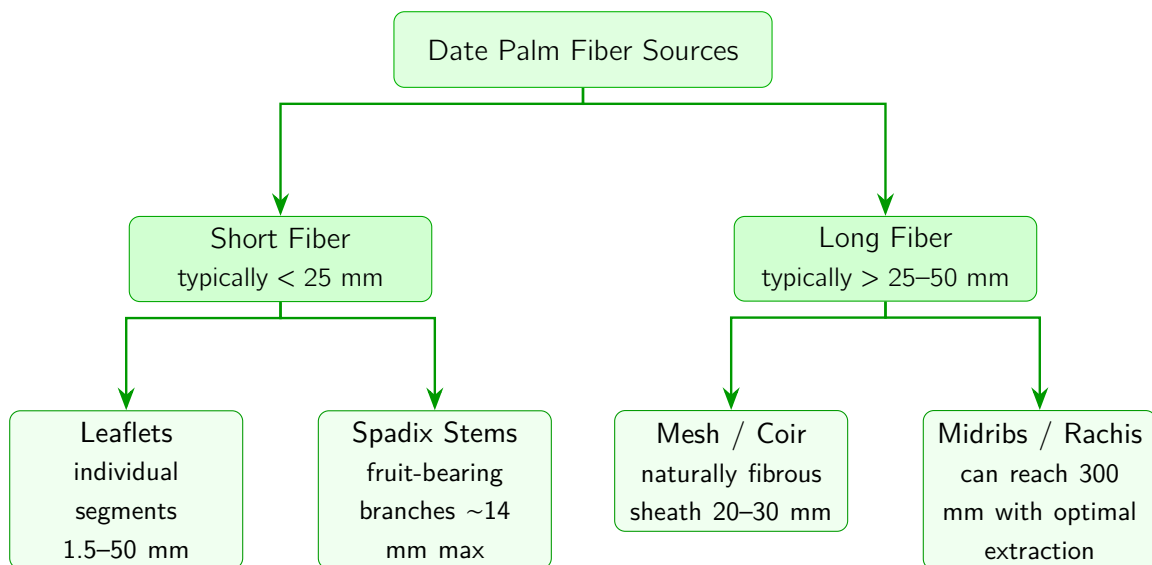


**FIGURE 1.20** – Classification and locations of date palm fiber sources

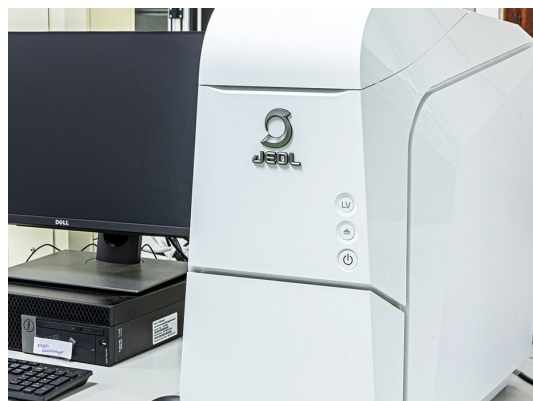
## I. Physical Properties of Date Palm Fibers

Having classified the four primary fiber sources—midribs, mesh, spadix stems, and leaflets—based on their length and aspect ratio, the next step is to examine their intrinsic physical properties as reported in literature. These include diameter, length, density, and aspect ratio presented in Table 1.3.

Among these properties, fiber diameter can be determined using Scanning Electron Microscopy (SEM) with image analysis software. For instance, in the study on maguey (*Agave cantala*) fibers, [31] utilized a benchtop SEM model JCM-7000 operated at 10.0 kV. Uncoated samples were mounted on specimen stubs and imaged using **low-vacuum mode**.



(a) Raw maguey fiber sample observed using SEM



(b) Benchtop SEM model JCM-7000 used for fiber analysis

**FIGURE 1.21** – SEM analysis of maguey fibers showing (a) fiber morphology and (b) the instrumentation used.

**Analysis of the compiled data** in Table 1.3 reveals several key trends regarding fiber properties and extraction methods:

- The extraction technique significantly influenced the fiber dimensions. Mechanically extracted fibers from midribs, spadix stems, and leaflets typically showed shorter lengths due to chopping or rolling processes involved. These shorter fibers resulted in lower aspect ratios, which can limit their processability into yarns, woven preforms, or nonwoven mats.
- In contrast, mesh fibers extracted mechanically exhibited the longest fiber lengths (20–300 mm) and highest aspect ratios (29–3000) among all mechanically extracted fibers. This is attributed to the natural mesh structure requiring minimal processing, primarily involving separation and trimming rather than intensive cutting or milling.
- Chemical extraction methods generally produced fibers with higher aspect ratios compared to mechanical methods for non-mesh fibers, particularly evident in midrib fibers where chemical treatment yielded aspect ratios of 45–3000 compared to 66.3–95 for mechanical extraction. This suggests chemical treatments more effectively isolate individual fibrils while maintaining fiber length.
- The absolute density of date palm fibers was found to range between 1.178 and 1.45 g/cm<sup>3</sup> for chemically treated fibers. The density measurement is typically performed using the Archimedes method according to ASTM D8171-18 standard, where fiber samples are compressed into disks under high pressure and temperature (35 bars and 180°C) to eliminate

air voids. The density is then automatically calculated using a densometer (Elseify et al. 2020) as shown in Fig. 1.22 by measuring the weight difference in air and in liquid.

- , the low bulk density of mesh fibers ( $0.6\text{--}0.7\text{ g/cm}^3$ ) reflects a highly porous structure with significant air space between fibers, making them advantageous for use in lightweight composite materials. The higher absolute density ( $1.30\text{--}1.45\text{ g/cm}^3$ ) confirms that the solid cell wall material itself is dense. The considerable difference between bulk and absolute density underscores the material's high porosity, which can enhance matrix adhesion through mechanical interlocking while contributing to overall composite lightweighting.



**FIGURE 1.22** – Density samples preparation and measurement (adapted from Elseify et al. 2018)

**Comparative analysis with established natural fibers** provides important context for evaluating date palm fibers. Table 1.2 shows how date palm properties position themselves among common natural fiber reinforcements used in composite applications.

**TABLE 1.2** – Physical properties of common natural fibers used in composites

Fiber Type	Density ( $\text{g/cm}^3$ )	Diameter ( $\mu\text{m}$ )	Length (mm)	Category
Flax	1.4–1.5	40–600	5–900	Bast
Jute	1.3–1.5	25–200	1.5–120	Bast
Sisal	1.2–1.5	8–200	900	Leaf

- **Firstly**, the density range of date palm fibers ( $0.13\text{--}1.45\text{ g/cm}^3$ , Table 1.3) is notably lower than bast fibers like flax ( $1.4\text{--}1.5\text{ g/cm}^3$ ) and jute ( $1.3\text{--}1.5\text{ g/cm}^3$ , 1.2), offering significant advantages for lightweight composite design.
- **Additionally**, the morphological diversity across different date palm components provides a wider property spectrum than single-source fibers. For instance, mesh fibers achieve lengths (20–300 mm, Table 1.3) comparable to jute (1.5–120 mm, Table 1.2), while chemically extracted midrib fibers can reach aspect ratios (up to 3000) that compete with premium bast fibers.
- **Furthermore**, compared to sisal—another leaf fiber—date palm offers more consistent diameter control and broader processing flexibility through different extraction methods, as evidenced by the extensive data in 1.3.

**TABLE 1.3** – Physical properties of date palm fibers from different parts and extraction techniques

Date palm part	Extraction Technique	Diameter ( $\mu\text{m}$ )	Length (mm)	Aspect Ratio	Density ( $\text{g}/\text{cm}^3$ )	References
Midribs	Mechanical	13.7–510	1.1–1.69	66.3–95	0.13–0.3	Khristova et al. (2005) [32], Saadaoui et al. (2013), Mirmehdi et al. (2014) [33], Abdel-Aal et al. (2015)
	Chemical	10–100	1.01–300	45–3000	–	Agoudjil et al. (2011) [34], Hegazy and Ahmed (2015) [35], Jaber et al. (2016), Midani (2017)
		Cross-sectional area = $0.046\text{--}0.138\text{ mm}^2$			1.178–1.324	Elseify et al. (2018, 2020)
		Length = 300 mm			(abs.)	
Spadix Stems	Mechanical	23.4	0.61–0.81	26–34.6	–	Hassan et al. (2014)
	Biological (Enzymatic)	20.3–20.6	0.56–0.74	27–36.45	–	Hassan et al. (2014)
	Chemical	$196 \pm 120$	$13.8 \pm 6.5$	70–70.4	$1.37 \pm 0.009$	Ibrahim et al. (2014, 2017)
Leaflets	Mechanical	460	3.42	7.43	–	Mirmehdi et al. (2014)
	Biological (Retting)	Cross-sectional area = $0.4105\text{--}0.5167\text{ mm}^2$			0.99 (bulk)	Rao and Rao (2007)
	Chemical	8–10,000	1.5–50	150–190	–	Pandey and Ghosh (1995), Abu-Sharkh and Hamid (2004), Mohanty et al. (2014), Mohanty (2017)
Mesh	Mechanical	100–2,000	20–300	29–3000	0.6–0.7 (bulk)	Abdal-hay et al. (2012), Alajmi and Shalwan (2015), Al-Rifaie and Al-Niami (2016), Boukhattem et al. (2017), Boumahout et al. (2017)
	Water separation	100–800	10–30	12.5–300	–	Tioua et al. (2017)
	Chemical	200–800	15–60	18.75–300	0.51–1.09 (bulk); 1.30–1.45 (abs.)	Kriker et al. (2005), Abdal-hay et al. (2012)



## II. Morphological Properties of Date Palm Fibers

The morphological characteristics of date palm fibers, including their *cross-sectional geometry* and *surface morphology*, are typically examined using field emission scanning electron microscopy (FESEM) at accelerating voltages up to 30 kV. Sample preparation involves gold sputtering and mounting on metallic stubs using conductive adhesive to ensure high-resolution imaging, as illustrated in Figure 1.23.

### 1. Midribs

Midrib fibers exhibit vascular bundles with circular cross-sections up to 1 mm in diameter, containing two large hollow lumens and microfibrillar elements of approximately 12  $\mu\text{m}$  in diameter.

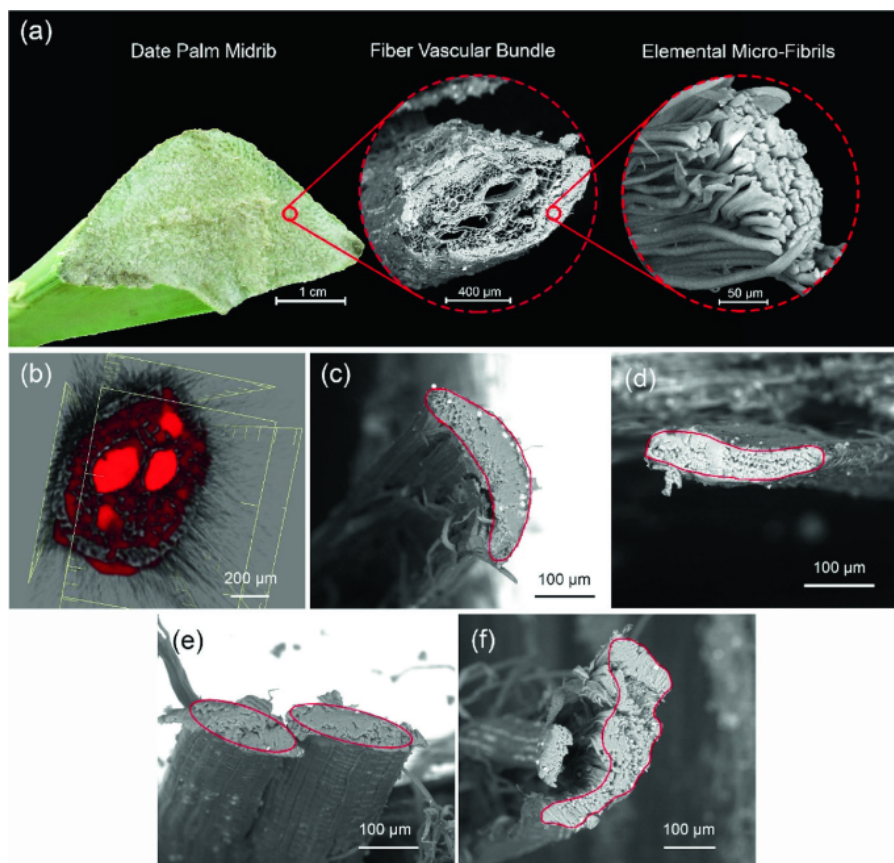


**FIGURE 1.23** – Morphological variations in date palm midrib (DPM) fiber cross-sections: (a) vascular bundle and microfibril structure, (b) CT scan showing lumen distribution, (c) C-shaped fibers, (d) flaky fibers resulting from processing, (e) elliptical fibers, and (f) irregular-shaped fibers (Elseify et al., 2020).

Their cross-sectional configuration is strongly influenced by treatment severity and the degree of fibrillation, varying from C-shaped to flaky, elliptical, or irregular morphologies. The transition from C-shaped to flaky geometries under chemical treatment indicates fiber splitting and structural loosening caused by aggressive alkaline processing.

Additionally, longitudinal analysis reveals that untreated fibers contain surface impurities and parenchyma cells, whereas alkaline-treated fibers retain some parenchyma cells and exhibit silica crystals—evidence of incomplete removal of non-cellulosic components (Figure 1.24).

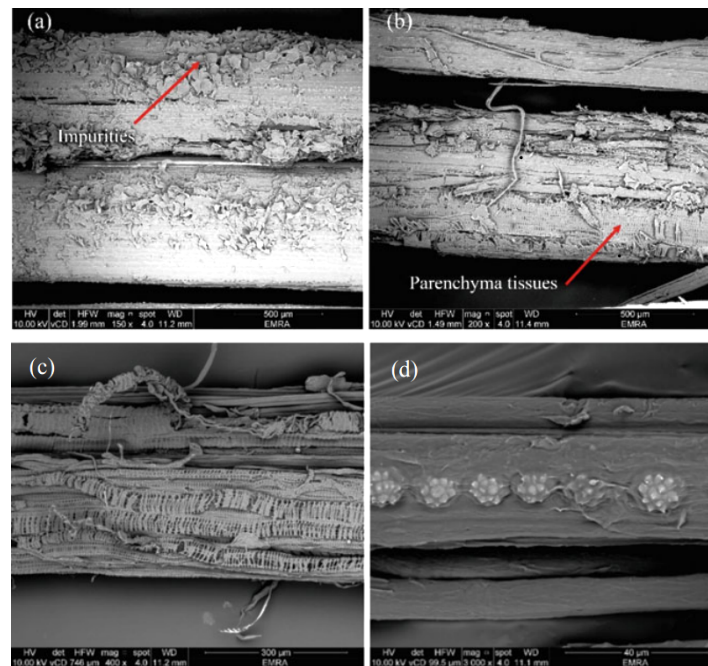


**FIGURE 1.24** – SEM micrographs of date palm midrib fibers in the longitudinal direction: (a, b) untreated fibers showing surface impurities and parenchyma cells; (c, d) NaOH-treated fibers showing partial removal of parenchyma and presence of silica crystals [14].

## 2. Spadix Stems

Spadix stem fibers show similar vascular bundle structure but with smaller lumen-to-bundle diameter ratios (0.1) compared to midrib fibers (0.28). Alkaline treatment effectively cleans fiber surfaces while maintaining the fundamental bundle structure. Cross-sectional views show unfibrillated fiber vascular bundles in untreated specimens. The smaller lumen proportion indicates a denser and more compact internal structure, whereas the larger lumens of midrib fibers make them lighter and more porous, which can enhance flexibility but reduce stiffness.

## 3. Leaflet Fibers

Leaflet fibers feature large lumens surrounded by elemental fibers bound by lignin, with alkaline treatment successfully removing surface impurities and enhancing fiber cleanliness in longitudinal views. The cross-sectional shape of leaflet fibers is similar to those of midribs and spadix stems, consisting of large lumens surrounded by elemental fibers bounded together with lignin.

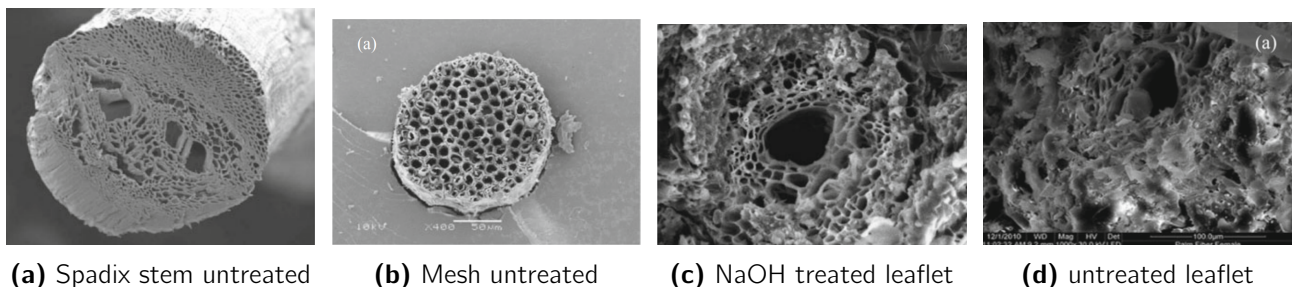


**FIGURE 1.25** – Representative cross-sections of different date palm fiber types

## 4. Mesh Fibers

Mesh fibers display distinct morphology characterized by **multiple small equal-size lumens**



rather than the large lumens found in other date palm fibers. This natural sheath structure facilitates easier extraction compared to other fiber types. Chemical treatments with NaOH and plasma effectively remove surface impurities, while HCl treatment causes surface deterioration due to vigorous acidic attack. Mesh fibers are the most frequently studied variety due to their natural form which requires minimal processing.

### III. Hierarchical Microstructure of Date Palm Fibers

To better grasp how the different components shape the physical structure of date palm fibers, a microstructural diagram is provided in Figure 1.27 [36].

In this hierarchical model, plant fibers can be schematically depicted as **tubular structures** containing a central **lumen**—a hollow channel facilitating sap and water transport—surrounded by four concentric walls. The **primary wall** consists of loosely organized cellulose bundles, while the **secondary layers** (L1, L2, L3) are composed of semi-crystalline microfibrils arranged in helical patterns [37, 38].

These microfibrils, embedded in a matrix of **hemicellulose** and **lignin**, contribute significantly to the fiber's **mechanical integrity**. Lignin, being hydrophobic, protects against microbial degradation and reinforces the cellulose framework, while hemicellulose serves as a binding agent between lignin and cellulose. Minor constituents such as **waxes**, **pectins**, and **minerals** also play a role in fiber organization and are present in trace amounts.

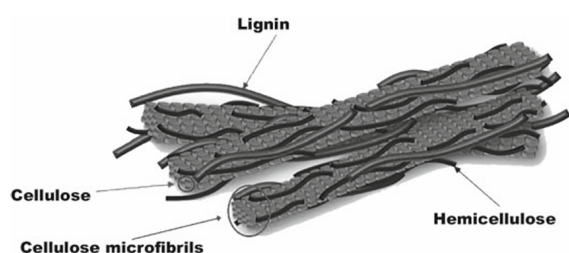


**FIGURE 1.26** – Diagram showing the structural arrangement of lignin, hemicellulose and cellulose microfibrils [1].

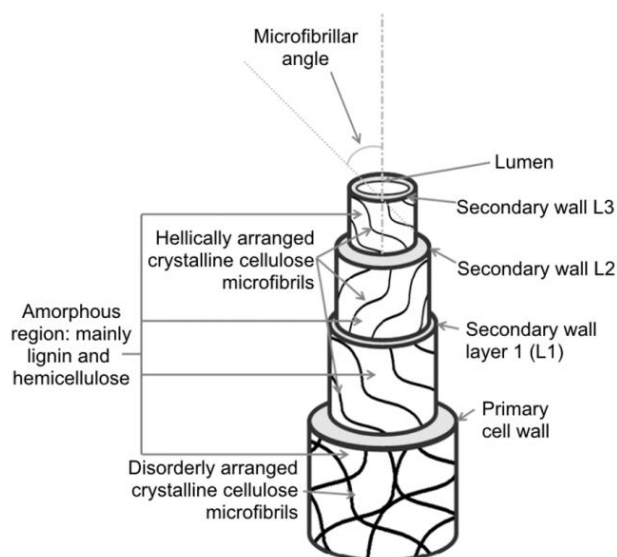


**FIGURE 1.27** – Microstructural organization of plant fibers

In the secondary cell walls, particularly the **L2 layer** which is the thickest and most structurally significant, cellulose is organized in bundles of microfibrils arranged in helical patterns. The cellulose content, its **degree of polymerization**, and the **helical angle (microfibril angle)** of these microfibrils vary across plant species and directly affect the **mechanical performance** of the fibers. Higher cellulose levels combined with smaller spiral angles generally result in stronger fibers.

Figure 1.26 schematically illustrates the spatial organization and interaction of lignin, hemicellulose, and cellulose microfibrils within the plant cell wall structure, complementing the structural overview.

## IV. Date Palm Fiber Chemical Composition

The chemical composition of lignocellulosic fibers from date palm leaflets, as shown in Figure 1.28, is based on averaged results from multiple tests ([39]). It was found that cellulose was the predominant constituent with 35% of dry matter comparable to that found in alfa or other fibers such as flax, kenaf, and jute. Hemicellulose ranks second as a major component, with a content of 28% that is similar to wheat straw fibers. Lignin ranks almost as same as hemicellulose, with the levels close to those observed in bamboo and sugarcane fibers.

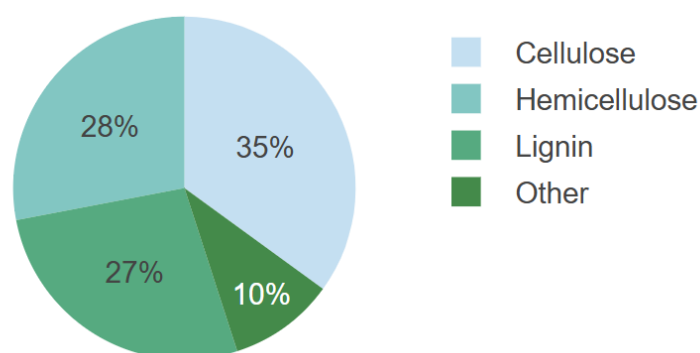


**FIGURE 1.28** – Chemical composition profile of date palm fibers (% by weight)

### 1.3.2 Fiber Extraction Methods

Fiber extraction methods could be categorized as four main families: **physical**, **mechanical**, **chemical**, and **biological**. The selection of an appropriate method depends on factors such as plant species, its maturity, and the specific organ being processed. In some cases, combining multiple methods may be necessary to achieve optimal results.

#### 1. Physical Methods

The pressure explosion by steam, where high pressure steam induces micro-explosions within the plant's most fragile cells (Sotton, 1991 [40]; Kessler et al., 1998 [41]). This cycle is typically repeated 8 to 11 times, leading to rupture of the middle lamella, an intercellular adhesive. Final fiber separation is achieved through rinsing with running water.

Other physical methods, include ultrasound based and microwave assisted treatments, which facilitate detachment.

#### 2. Mechanical Methods

For mechanical extraction methods it could be performed either manually or with machinery. For example, in bamboo processing

- **Manual Methods:** Fibers are separated using knives and metallic combs after initial beating (Rao Rao, 2007 [42]).

- **Rolling or pressing:** Fibers are crushed using rollers or presses, or a combination of both. This process is repeated multiple times to maximize separation (Tokoro et al., 2008 [43]).

### 3. Chemical Methods

Chemical extraction typically involves **alkaline solutions** such as sodium hydroxide (NaOH) or potassium hydroxide (KOH). These treatments are responsible for partially reducing fiber diameter and help break down the binding.

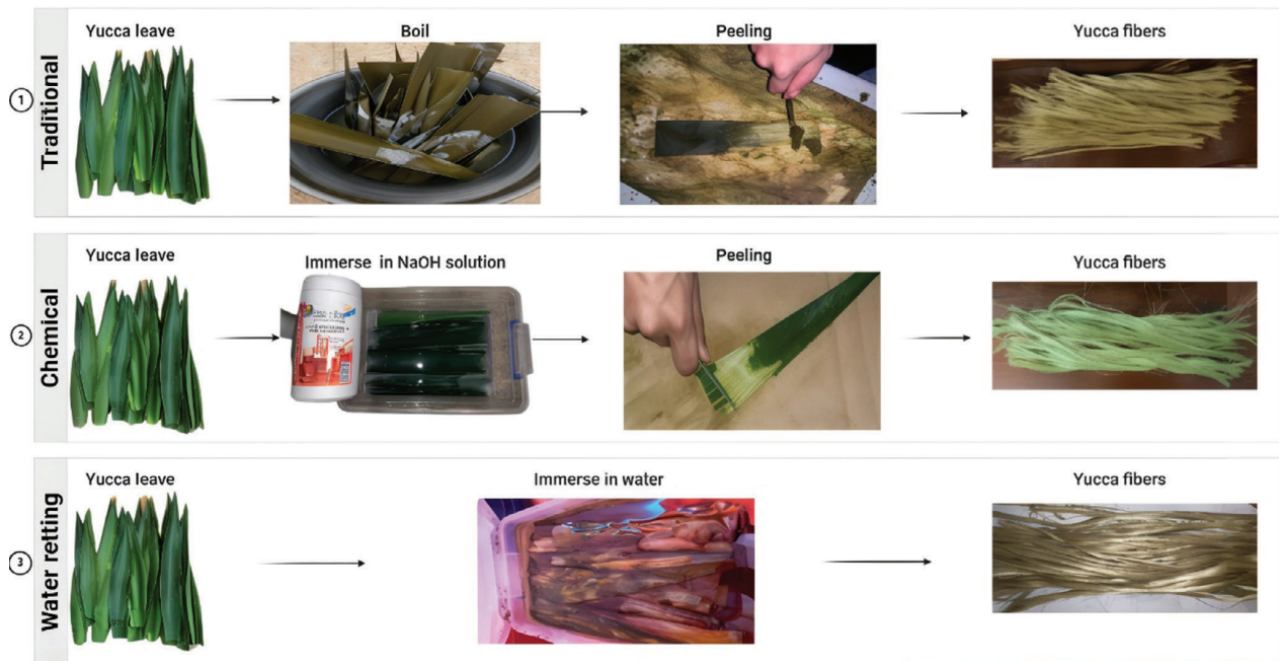


FIGURE 1.29 – Yucca fiber extraction methods comparison (adapted from [15])

### 4. Biological Methods (Retting)

Biological extraction, known as retting, relies on microbial activity and generally requires more time than other methods. Several variants exist:

- **Field retting:** Plants are uprooted and left on the ground for several weeks (e.g., flax), exposed to sun, rain, and wind. Microorganisms degrade pectic substances that bind fiber bundles, facilitating easier separation. The process is low-cost and labor-efficient but requires large areas and is sensitive to weather conditions.
- **Pond retting:** Plant parts are submerged in water, allowing anaerobic bacteria to develop and enzymatically break down macromolecules binding the fibers. Despite its effectiveness, this method is largely abandoned due to environmental and health concerns, as it consumes large volumes of water.
- **Enzymatic retting:** A modern alternative that uses enzyme mixtures to extract fibers with minimal impact on cellulose. It offers reduced treatment time, reproducibility, and lower environmental impact, making it attractive for industrial applications (Ali et al. 2018 [44]).

### 1.3.3 Treatment and Surface Modification of Plant Fibers

Pretreatment and surface modification of cellulose-based plant fibers aims to enhance *fiber-matrix adhesion*, limit moisture absorption, and reduce internal stresses. These treatments are essential due to the inherent limitations of natural fibers, such as poor compatibility with synthetic polymer matrices and low thermal stability (Mohanty et al., 2002 [45]; Yao et al., 2009 [46]).

Consequently, several pretreatment approaches—**chemical**, **physical**, and **biological**—have been explored to enhance the functional properties of plant fibers and ensure their compatibility with polymer matrices. In addition, pretreatment should ensure the removal of impurities to enhance the uniformity of the fiber structure. It is also important to note that the effectiveness of pretreatment techniques depends largely on the nature of the fiber being processed.

**TABLE 1.4** – Summary of surface modification techniques for plant fibers

Treatment Type	Purpose	Mechanism & Effects	Notes
Alkaline Treatment	Enhance fiber-matrix contact and facilitate fiber extraction	Fibers are soaked in a sodium hydroxide (NaOH) solution (2–10%) to remove unwanted materials such as waxes, oils, hemicellulose, and part of lignin. This cleaning roughens the surface and exposes more cellulose, which helps the matrix stick better. It also reduces moisture absorption and slightly improves the fiber's thermal stability.	Control of time, temperature, and concentration is crucial for fiber integrity.
Acetylation Treatment	Increase <b>hydrophobicity</b> and dimensional stability	Hydroxyl groups (–OH) react with acetyl groups (CH <sub>3</sub> CO–), reducing water absorption and swelling.	Improves interfacial shear strength by ~20%.
Silane Treatment	Improve <b>fiber-matrix bonding</b> and mechanical performance	Silane molecules graft onto fiber surfaces, enhancing <b>chemical compatibility</b> with <b>polymer matrices</b> .	Effective on flax, wood, and loofah fibers.
Chemical Bleaching	Prepare fibers for dyeing and improve surface uniformity	Uses hydrogen peroxide, sodium hypochlorite, or sodium chlorite to remove residual components and whiten fibers.	Increases surface area and fiber-matrix interaction.

### 1.3.4 Mechanical Properties of Date Palm Fibers

The tensile strength ( $\sigma$ ), Young's modulus ( $E$ ), and strain at break of individual fibers can be evaluated using the single-fiber tensile test, following the ASTM D3822-01 standard. In this method, a single fiber is mounted between two paper frames.

Each frame measures 3 × 5 cm, with a centered window of 2.5 × 1 cm, providing a gauge length of 10 mm, as illustrated in Figure 1.30. The test is performed using a tensile testing machine at a strain rate of 0.5 mm/min, with no initial load applied. The load cell used must have a capacity below 1 kN, and a minimum of 10 specimens should be tested per sample.

Although numerous studies have examined the mechanical properties of date palm fibers from

all four fiber sources, many did not specify the testing standard used. Without this specification, the trustworthiness of the data remains uncertain.

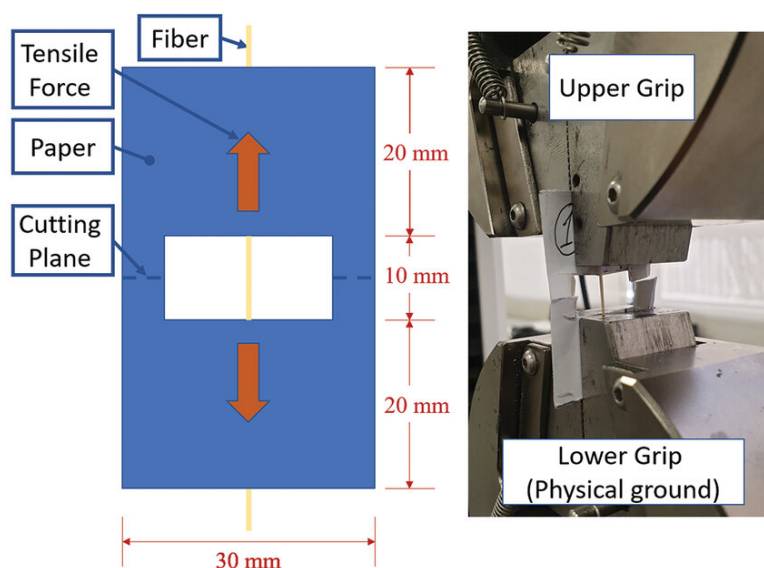


**FIGURE 1.30** – Schematic of the single fiber tensile test specimen setup according to ASTM D3822, showing the paper frame and the gauge length.

Table 1.5 presents the tensile strength and modulus of elasticity values obtained from various studies. It is evident that fiber treatment significantly influences mechanical performance.

According to Table 1.6, the tensile strength of date palm midrib fibers reached a maximum of 452.8 MPa when treated with NaOH, compared to a maximum of 208 MPa for untreated fibers. Spadix stem fibers exhibited even higher tensile strength, with values up to 680 MPa, although their modulus of elasticity was relatively lower.

For date palm leaflet fibers, tensile strength varied considerably depending on the treatment method. Some researchers reported values ranging from 32 to 309 MPa [42, 47, 48], while others observed tensile strength as high as 1250 MPa [49].

**TABLE 1.5** – Mechanical properties of common natural fibers used in composites

Fiber Type	Tensile Strength (MPa)	Young's Modulus (GPa)	Specific Strength (MPa/gm/cm <sup>3</sup> )	Elongation (%)
Flax	345–1830	27–80	227–1220	2.7–3.2
Jute	393–800	10–55	300–610	1.16–1.5
Sisal	468–855	9.4–28	349.3–610	3–7

When compared to established natural fibers (Table 1.5), date palm fibers demonstrate competitive mechanical performance. The tensile strength of treated midrib and spadix stem fibers (up to 680 MPa) falls within the range of jute and sisal, while their lower density offers advantages for specific strength in composite applications. This positions date palm fibers as viable alternatives to conventional natural fibers in various composite formulations.

**TABLE 1.6** – Comparison between mechanical properties of date palm fibers from different parts with different treatment techniques, Adapted from [1].

Date Palm Part	Tensile Strength (MPa)	Young's Modulus (GPa)	Treatment Technique	References
Midribs	11.4–208	10–30	Untreated	Abdel-Rahman et al. (1988) [50], Ghulman et al. (2017) [51]
	105–452.8	1.59–10.5	NaOH	Elesify et al. (2020) [14]
Spadix Stems	117 ± 35	–	Untreated	Amroune et al. (2015) [52]
	195–680	8.81–19	NaOH	Taha et al. (2007) [53], Amroune et al. (2015) [52], Ibrahim et al. (2017) [54]
Leaflets	32.43 ± 2.23	6.48 ± 0.89	Untreated	Mohanty et al. (2014) [48]
	33.33 ± 3.49 to 1246.7 ± 444.7	5.5 to 26.1 ± 11.2	NaOH	AlMaadeed et al. (2013) [47], Mohanty et al. (2014) [48], Tahri et al. (2016) [49]
	309	11.32	Water Retting	Rao and Rao (2007) [42]
	70.72 ± 5.64	16.34 ± 1.72	Acrylic acid	Mohanty et al. (2014) [48]
Mesh	233 ± 27.1 to 5359	0.1782 to 7.15 ± 2.0	Untreated	Taha et al. (2006) [55], Abdalhay et al. (2012) [56]
	215.8 ± 80 to 7073	2.75–11	NaOH	Taha et al. (2006) [53], Abdalhay et al. (2012) [56], Alsaeed et al. (2013) [57], Elbadry (2014) [58], Shalwan and Yousif (2014) [59], Tahri et al. (2016) [49]
	459	1.91	Water Retting	Rao and Rao (2007) [42]
	204.7 (55.1)	4.43 (1.43)	NaC <sub>12</sub> H <sub>25</sub> SO <sub>4</sub>	Taha et al. (2006) [55]
	180.6 (65.7)	5.244 (1.53)	CCl <sub>4</sub>	Taha et al. (2006) [55]
	226.8 (18.1)	4.46 (1.66)	Toluene/methanol/acetone	Taha et al. (2006) [55]

## 1.4 Date Palm Fiber Polymer Composites

After the comprehensive fiber characterization in the last sections above we have shown that date-palm fibers (DPF) possess a higher cellulose-to-hemicellulose ratio, superior tensile modulus, and a distinctive micro-fibrillar architecture compared with common bast or leaf fibers, granting them a unique combination of stiffness and inherent hydrophilicity. These attributes position DPF as a viable reinforcement rather than a mere filler in polymer composites.

### 1.4.1 Matrix Selection: Thermosets vs Thermoplastics

To effectively utilize DPF as reinforcement, appropriate matrix selection is crucial. The accompanying flowchart classifies polymer matrices into two primary origins—petroleum-based and bio-based—each subdivided into thermoplastic and thermoset families (see Figure 1.31). This visual taxonomy provides a systematic framework for selecting matrices compatible with DPF-reinforced systems.

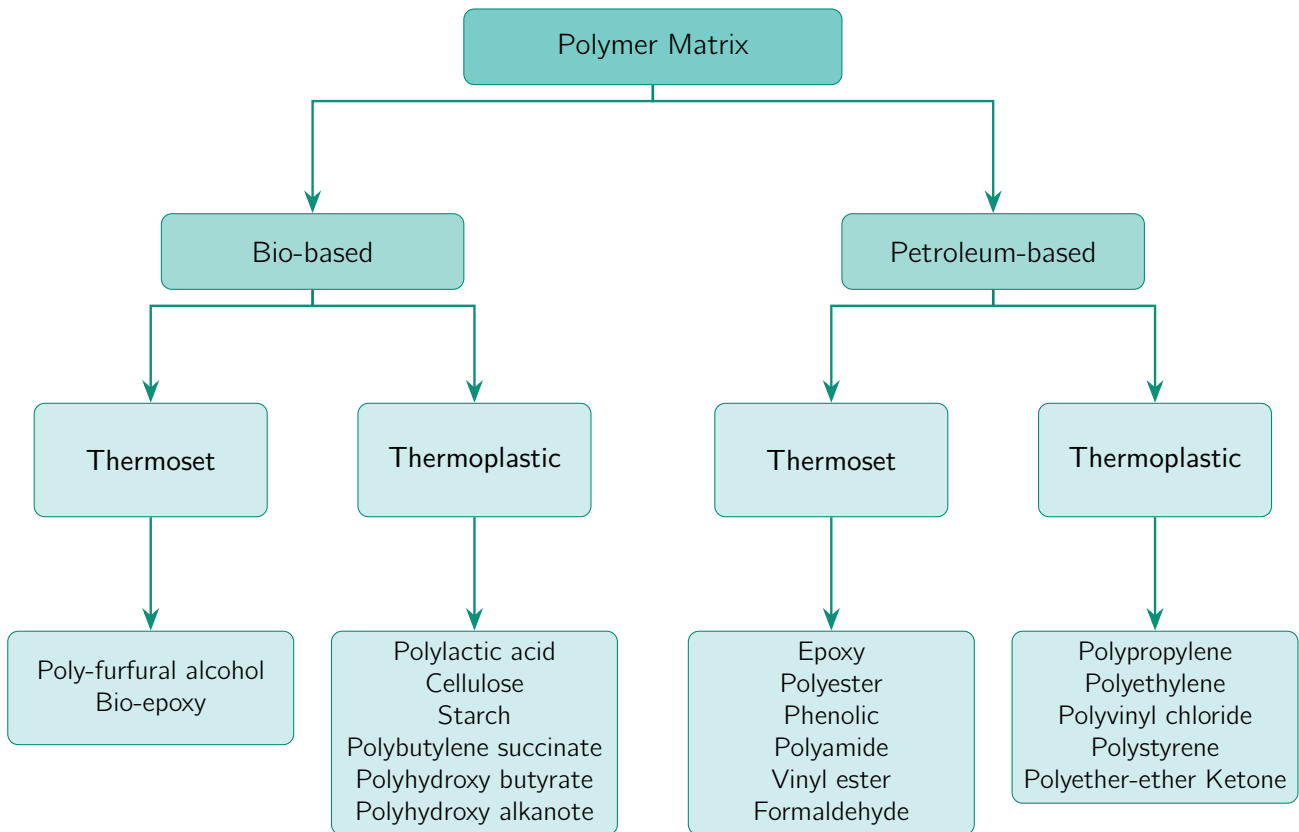


**FIGURE 1.31** – Classification of polymer matrices for natural fiber composites

By definition, a polymer is a macromolecule consisting of repeating monomeric units covalently linked to form long molecular chains. The architecture of these chains—whether linear, branched, or crosslinked—governs the polymer’s thermal and mechanical response.

Polymers with linear or weakly branched chains exhibit mobility upon heating, whereas those with extensive crosslinking form permanent, infusible networks. This molecular distinction forms the basis for the classification of polymers into **thermoplastics** and **thermosets**.

*In the context of natural-fiber composites, understanding the thermal behavior of these polymer matrices is crucial, as the processing and service conditions of the matrix must remain compatible with the thermal stability of the reinforcing fibers.*

For instance, in **date-palm fiber (DPF)**, thermal degradation refers to the breakdown of hemicellulose, cellulose, and lignin components, detectable as mass loss in thermogravimetric analysis (TGA).

It is important to note that DPFs employed in composite systems are typically alkali-treated to improve surface roughness, reduce moisture absorption by removing hydrophilic hemicellulose groups, and eliminate weak amorphous constituents. These modifications enhance fiber–matrix



adhesion and thermal stability, resulting in delayed degradation onset compared to untreated fibers. Most studies report significant mass loss for treated DPF within the 200–300 °C range, with the primary decomposition peak typically near 290 °C [60].

Untreated date-palm fibers, by comparison, exhibit markedly different thermal behavior. Thomason and Rudeiros-Fernández [61] identified four distinct degradation stages in untreated stem and mesh fibres: moisture loss below 150 °C; hemicellulose and pectin decomposition between 150–300 °C (DTG peak 286 °C); cellulose breakdown between 300–400 °C (DTG peak 324 °C); and lignin oxidation above 400 °C.

Both air and nitrogen atmospheres yielded similar profiles below 220 °C, confirming limited stability to that point. Weight-loss data (0.12–0.61 %) indicate that untreated fibres begin to degrade soon after 200 °C, losing mechanical strength as hemicellulose and cellulose decompose.

This comparison demonstrates the protective effect of alkali treatment: by removing unstable amorphous fractions, treated DPFs resist earlier degradation and tolerate slightly higher processing temperatures (Fig. 1.32).

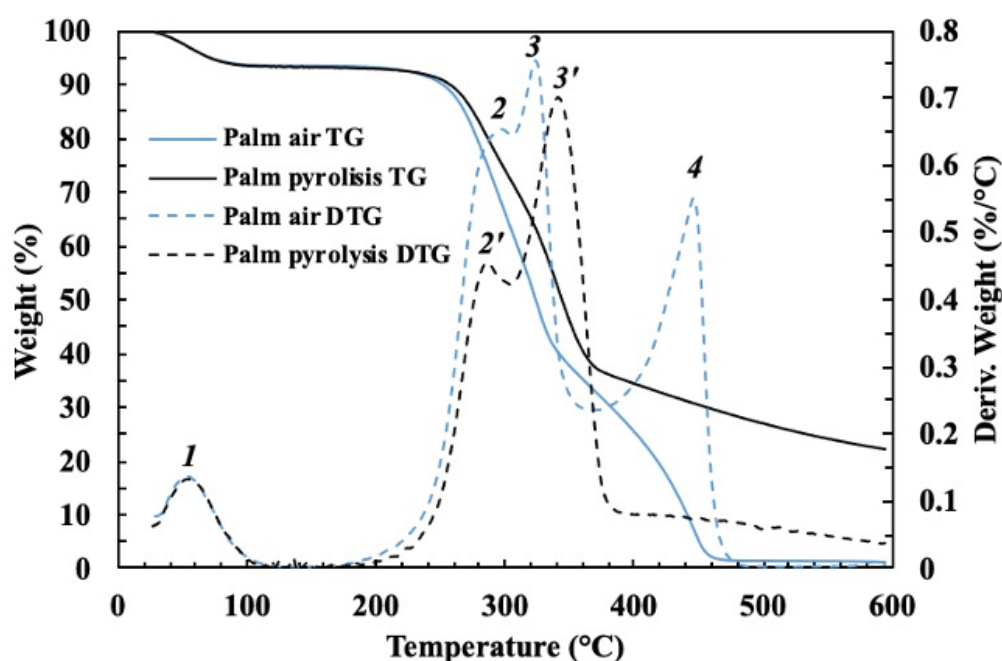


**FIGURE 1.32** – Thermo-gravimetric degradation of coir, under nitrogen and air atmospheres, at the heating rate of 10 °C min<sup>-1</sup>.

This degradation profile establishes a clear constraint for **matrix selection**. To preserve fiber integrity during composite fabrication, the selected matrix must be processable below the degradation onset of DPF.

**Thermoplastics**—which soften and flow when heated above their melting temperature—are generally suitable only if their processing window remains under this limit, typically **below 200 °C**. Low-melting-point polymers such as polypropylene (PP, ~160 °C), polyethylene (PE, ~130 °C), and polybutylene succinate (PBS, ~120 °C) allow adequate flow and interfacial wetting without compromising fiber structure.

**Thermosetting matrices**, in contrast, cure through irreversible crosslinking reactions, usually within **120–180 °C** (e.g., epoxy, bio-epoxy, or unsaturated polyester resins). Once cured, they form rigid, three-dimensional networks that provide excellent dimensional and thermal stability.



Consequently, the classification in Fig. 1.31 serves not only as a compositional taxonomy but also as a practical guide linking DPF's thermal tolerance to the processing and service temperature limits of DPF-based composites.

### 1.4.2 Epoxy Matrix Composites: Fabrication and Performance

Epoxy matrices are **amorphous**, a typical characteristic of thermosetting systems, which enables them to accommodate moderate loads while maintaining good adhesion to natural fibers. They cure at relatively low temperatures, as discussed previously. During curing, the epoxy resin reacts with an amine-based **hardener**, forming a crosslinked network that defines the stiffness and stability of the composite. Although less ductile than thermoplastics, epoxies provide strong interfacial bonding, making them suitable for moderate-load DPF-reinforced applications.

## I. Fabrication techniques

The fabrication of epoxy/date-palm fiber (DPF) composites involves several established techniques that determine fiber distribution, resin infiltration, and overall laminate quality. The most common approaches are outlined below.

### 1. Hand Layup

The most common laboratory method, owing to its simplicity and low cost. Fibers are manually arranged in a mould and impregnated with an epoxy–hardener mixture using brushes or rollers. Curing occurs under ambient or slightly elevated temperatures. Although practical, this process can yield non-uniform fiber distribution and occasional air voids.

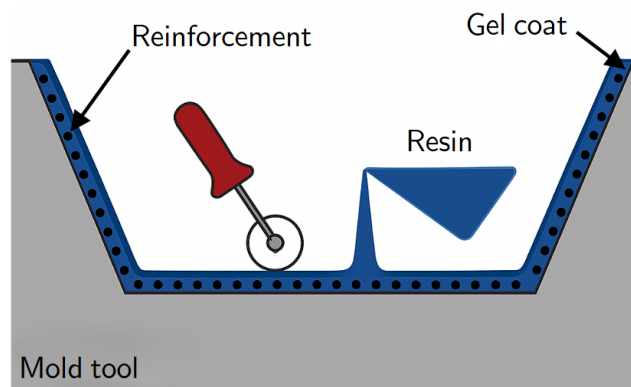


FIGURE 1.33 – Schematic of the hand layup process.

### 2. Compression Moulding

Used mainly with short or mat-type DPF reinforcements pre-impregnated with epoxy resin. The mixture is pressed under heat and pressure until curing is complete. This method yields high dimensional precision and smooth surfaces but may damage fibers if excessive pressure is applied.

### 3. Resin Transfer Moulding (RTM)

In this closed-mould process, dry DPF mats are positioned within a mould cavity, and resin is injected under moderate pressure. RTM allows better control of resin flow and fiber wetting,

producing composites with fewer voids and improved repeatability, suitable for more complex geometries.

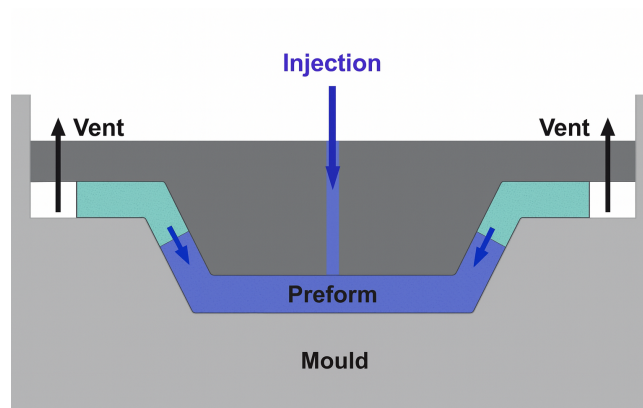


**FIGURE 1.34** – Diagram of Resin Transfer Moulding (RTM) method.

#### 4. Vacuum-Assisted Resin Transfer Moulding (VARTM)

A variant of RTM in which vacuum pressure draws the resin through the fiber preform. This technique improves resin impregnation, minimizes air entrapment, and achieves a consistent fiber–matrix interface. Owing to its balance between cost and quality, VARTM is increasingly used in DPF–epoxy research.

#### 5. Filament Winding

Less common for DPF composites but suitable for cylindrical components. Continuous fibers impregnated with resin are wound onto a rotating mandrel in specific orientations, providing excellent fiber alignment and hoop strength for tubular applications such as pipes and pressure vessels.

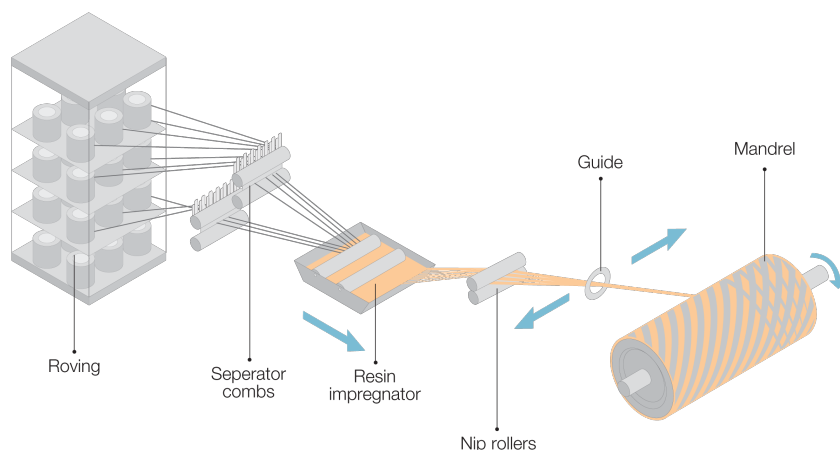


**FIGURE 1.35** – Filaments winding process.

Among these, **hand layup** and **VARTM** dominate reported studies due to their low cost, simplicity, and ability to preserve fiber integrity during fabrication.

## II. Tensile and Flexural Performance of DPF/Epoxy Composites

According to Saba et al. 2019 [2], incorporating date-palm fibers (DPF) into epoxy matrices enhances both tensile strength and stiffness relative to the pure resin. The 50 wt% composite achieves the highest strength (about +25% over pure epoxy) and a threefold increase in modulus, indicating efficient load transfer when fibers are well dispersed. The modest rise in elongation at break (0.91% to 1.41%) suggests improved interfacial bonding that allows limited strain before failure. At 60 wt%, strength and modulus decline, likely due to fiber agglomeration that promotes stress concentrations and disrupts uniform load sharing. Overall, **≈ 50 wt% DPF** yields the most balanced combination of strength, stiffness, and ductility.

**TABLE 1.7** – Mechanical properties of date-palm fiber/epoxy composites [2]

Sample	Tensile strength (MPa)	Tensile modulus (GPa)	Elongation at break (%)
Pure epoxy resin	20.5	0.51	0.91
40% DPF	21.4	0.61	1.16
50% DPF	25.7	1.54	1.41
60% DPF	24.3	1.32	1.34

This optimal fiber loading is further supported by flexural testing. According to Gheith et al. 2019 [3], the flexural strength of epoxy composites increases with the addition of date-palm fibers (DPF), peaking at 50 wt%—about 25% higher than the neat resin. The flexural modulus shows an even stronger improvement, tripling from 2.26 GPa to 3.28 GPa at the same fiber loading, confirming the fibers' efficiency in resisting bending loads. At 60 wt%, both properties decline, mirroring the tensile behaviour and indicating fiber agglomeration and reduced matrix continuity. Therefore, **≈50 wt% DPF** provides the optimal balance between stiffness and load-bearing capacity for both tensile and flexural performance.

**TABLE 1.8** – Flexural properties of date-palm fiber/epoxy composites [3]

Sample	Flexural strength (MPa)	Flexural modulus (GPa)
Pure epoxy resin	26.15	2.26
40% DPF	28.60	2.30
50% DPF	32.64	3.28
60% DPF	27.83	2.94

## 1.5 Sandwich Structures with Lattice Cores

### 1.5.1 Overview of Sandwich Structures

Sandwich structures are widely adopted in high-performance applications requiring a superior strength-to-weight ratio, such as aerospace, automotive, and wind turbine systems. They consist of two strong, stiff face sheets bonded to a lightweight core. This combination offers enhanced flexural rigidity, excellent energy absorption, and tailored deformation responses.

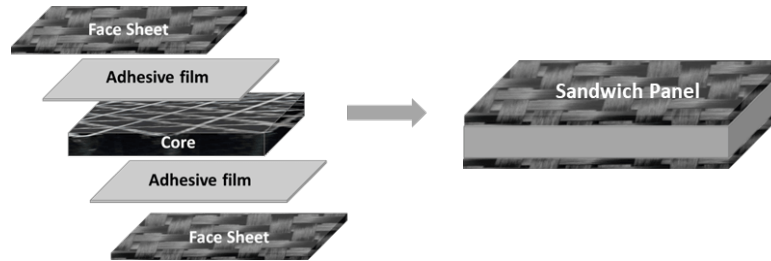


**FIGURE 1.36** – Schematic of a sandwich panel.

The face sheets primarily withstand in-plane tensile and compressive stresses, while the core resists transverse shear loads and contributes to overall out-of-plane stiffness and impact damping.

**TABLE 1.9** – Roles of sandwich structure components

Component	Function	Desired Properties
Face Sheets	Bending, tensile, compressive load-bearing	High strength, stiffness, fatigue resistance
Core	Shear load resistance, energy absorption, spacing	Lightweight, shear rigidity, impact damping
Adhesive Layer	Transfers stresses between components	Strong interfacial adhesion

The effectiveness of sandwich structures has been well established in the literature. Notably, Bitzer (1997) reported that sandwich panels can reduce structural weight by up to 40% while maintaining stiffness.

### 1.5.2 Evolution of Core Architectures: Toward Additive Manufactured Lattices

The performance of a sandwich structure is fundamentally influenced by the mechanical behavior of its core. Traditionally, foams, honeycomb, and balsa wood have been the preferred core materials due to their availability, low cost, and acceptable weight-to-strength ratio. However, these materials often suffer from limitations in directional control, isotropy, and design adaptability, especially when subjected to complex or multi-axial load conditions.

Recent advancements in additive manufacturing (AM) have paved the way for a new generation of architected lattice cores, offering unprecedented control over geometry, anisotropy, and

functionality. These structures, typically designed through periodic topologies, allow engineers to tailor mechanical performance (e.g., stiffness, energy absorption, and failure behavior) to specific applications beyond what conventional cores can achieve.

**TABLE 1.10** – Comparison between traditional and architected lattice cores

Property	Traditional Cores	Lattice Cores
Customization	Fixed shapes	Geometry-tailored via AM
Weight-to-stiffness ratio	Moderate	High
Energy absorption	Moderate	Superior
Directional control	Limited	Tunable anisotropy
Failure behavior	Brittle or unstable	Controlled, progressive
Manufacturing method	Subtractive / Molding	Additive Manufacturing

### 1.5.3 Lattice Structures: Architectures, Properties, and Applications

Lattice structures are spatially periodic cellular materials characterized by interconnected networks of struts, surfaces, or both. Their appeal lies in their high degree of topological controllability, which enables the optimization of macroscopic mechanical and physical properties using a minimal amount of material. They offer several desirable characteristics, such as:

- High specific stiffness and specific strength.
- Low elastic modulus with the possibility of tunability.
- Tailored Poisson’s ratio, including negative values.
- High surface-to-volume ratio and porosity.
- Low thermal expansion and effective damping properties.

These attributes make lattice structures promising candidates for a variety of advanced applications, including:

- **Biomedical scaffolds:** benefiting from porosity and bio-mimetic geometry.
- **Automotive lightweighting:** where strength-to-mass optimization is critical.
- **Energy absorption systems:** such as crash absorbers and packaging.
- **Thermal and acoustic insulation:** through customized conduction paths and wave dissipation.
- **Catalysis and filtration:** owing to their high internal surface area.

For example, Yin et al. [62] developed a composite automotive hood with a pyramidal lattice core, resulting in a 25% weight reduction and improved impact resistance. In another study, Wang et al. [63] introduced a crash box combining a concave shell and a negative-Poisson-ratio (NPR) hexagonal lattice core, which enhanced energy dissipation and stabilized deformation

during impact events. Architecturally, lattice structures are generally categorized into two main families [64] , as shown in Figure 1.37.

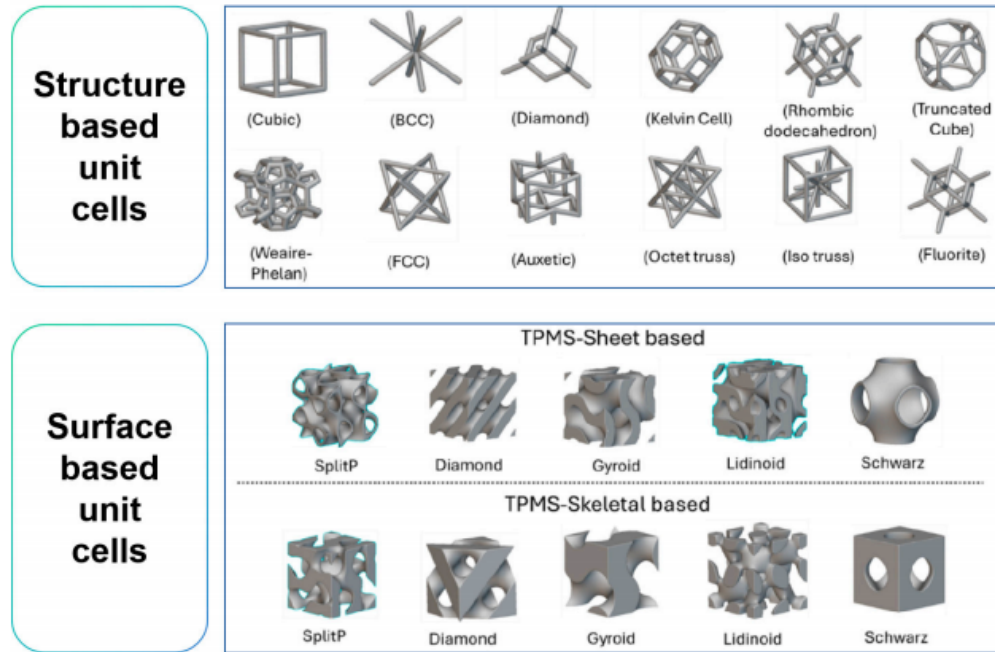


**FIGURE 1.37** – Classification of lattice architectures: strut-based vs. surface-based topologies.

Each class exhibits distinct mechanical responses and energy dissipation mechanisms. The careful selection and design of the unit cell geometry directly influence the global performance of the part, enabling optimization for specific functional goals such as stiffness, damping, thermal conductivity, or failure modes.

#### 1.5.4 Gyroid Lattices: A Special Class of TPMS Structures

The gyroid is a triply periodic minimal surface discovered by Alan Schoen. Its surface is defined by the implicit equation:

$$\sin x \cdot \cos y + \sin y \cdot \cos z + \sin z \cdot \cos x = 0 \quad (1.15)$$

This non-self-intersecting, continuous structure is free of sharp corners, leading to:

- Superior load distribution.
- Smooth stress paths.
- Low stress concentrations.
- Good printability and mechanical resilience.

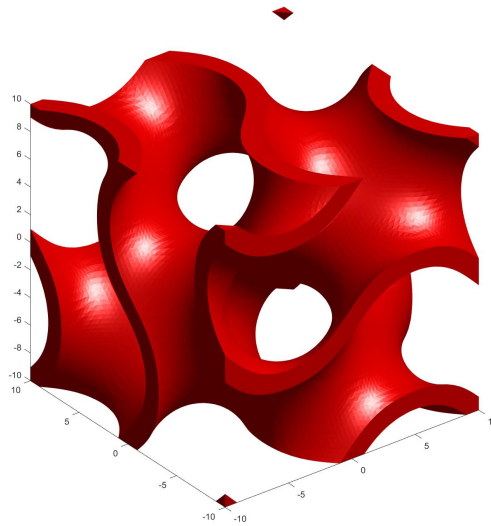


**FIGURE 1.38** – Example of a gyroid unit cell of 40% infill.

## Key Research Findings on Gyroid Structures

### Energy Absorption Performance

In fact, Li et al. [65] investigated the mechanical behavior of gyroid lattice structures fabricated using PLA and ABS via fused deposition modeling (FDM). The study focused on assessing the energy absorption capabilities of these architected structures under compressive loading. A comparative analysis revealed that gyroid lattices can absorb up to twenty times more energy than conventional foam materials of equivalent mass. This significant enhancement was attributed to the controlled deformation mechanisms and distributed load paths intrinsic to the gyroid topology. The study underscores the potential of gyroid lattices for impact mitigation and lightweight protective applications, particularly in automotive and aerospace structures.

### Influence of Cell Size and Wall Thickness on Mechanical Properties

Recent work by Netto *et al.* [66] provides critical insights into how **cell size** and **wall thickness** govern the mechanical behavior of 3D-printed PLA gyroid structures:

- **Cell Size:**

- Smaller cells (4–5 mm) promote plastic deformation and high energy absorption ( $5.34 \text{ MJ/m}^3$ ).
- Larger cells (10 mm) trigger brittle failure via layer collapse, reducing stiffness by 2–3×.

- **Wall Thickness:**

- Thicker walls (0.8 mm) enhance stiffness (165 MPa) but increase material usage.
- Thin walls (0.4 mm) risk defects (e.g., wall holes), lowering reproducibility.

- **Design Priority:** Cell size dominates performance; halving cell size improves stiffness three-fold compared to doubling wall thickness.



Optimal performance is achieved with **4 mm cells and 0.8 mm walls**, balancing strength (6.43 MPa yield stress) and lightweight efficiency (0.46 g/cm<sup>3</sup> apparent density).

### 1.5.5 Sandwich Structures with Lattice Cores: A Synergistic Design

Recent developments in structural design have explored the integration of lattice architectures—particularly triply periodic minimal surfaces (TPMS) such as the gyroid—within sandwich composites to achieve unprecedented stiffness-to-weight ratios, enhanced energy absorption, and damage tolerance.

#### Notable Applications and Findings

- **Yang et al. (2022)** [16] designed and manufactured sandwich panels composed of carbon fiber-reinforced polymer (CFRP) face sheets and gyroid TPMS cores via additive manufacturing. Under three-point bending, the gyroid-core sandwiches exhibited a 40% increase in flexural stiffness and 35% higher energy absorption compared to conventional foam-core sandwiches of equal mass.

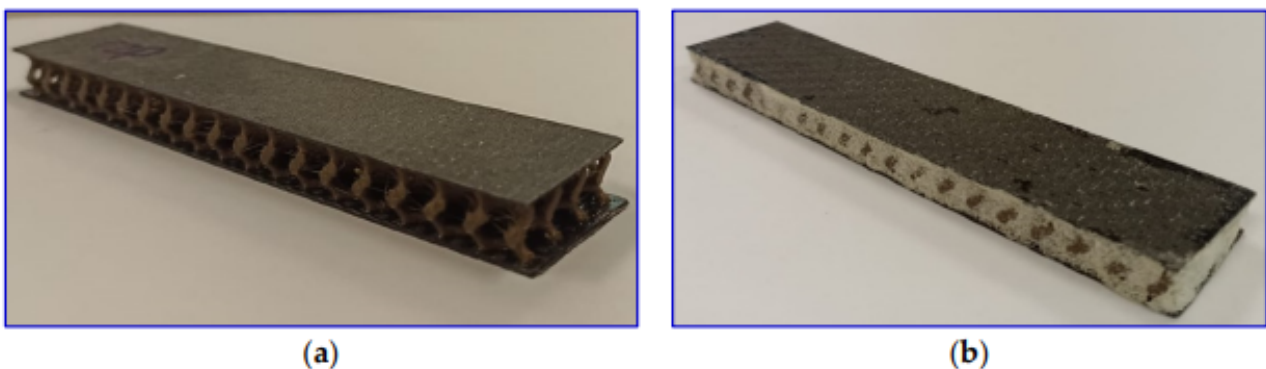


**FIGURE 1.39** – (a) Gyroid sandwich and (b) PUF-filled gyroid sandwich at 20% gyroid core density [16].

- **Zhang et al. (2021)** [67] conducted impact and post-buckling tests on gyroid-based sandwich panels. The results showed a 25% improvement in post-impact load-carrying capacity and a 30% delay in buckling onset compared to honeycomb-core equivalents, demonstrating superior damage resilience and load redistribution under compressive stress.
- **Kolken and Zadpoor (2017)** [68] evaluated TPMS-based lattice cores—including gyroids—in fatigue and dynamic impact scenarios. Sandwich composites using gyroid cores sustained over  $10^6$  cycles at 60% of peak stress without failure, highlighting their suitability for cyclic and high-strain-rate environments such as aerospace and defense applications.



# Design Analysis and Realization Methodology

...

## Overview



This chapter delineates the comprehensive methodology employed for the design, analytical assessment, and fabrication of a structurally optimized Savonius rotor. The systematic approach integrates aerodynamic modeling, structural analysis, and manufacturing techniques to achieve a lightweight, durable composite structure.

- **Aerodynamic Foundation:** Adoption of Kamoji's validated rotor configuration as the reference model
- **Structural Analysis:** Analytical derivation of material requirements through static, deflection, and modal criteria
- **Material Architecture:** Development of hybrid sandwich composite with ABS gyroid core and natural fiber reinforcement
- **Manufacturing Integration:** Sequential fabrication process encompassing additive manufacturing, fiber extraction, and composite layup
- **Performance Validation:** Experimental verification of weight reduction and structural integrity

## 2.1 Rotor Design Configuration

### 2.1.1 Context and Project Goals

Since the main aim of this project is not the aerodynamic optimization of the Savonius rotor but rather developing a lightweight structure that meets stiffness requirements and avoids resonant vibrations, the use of an already validated aerodynamic model was considered more appropriate than the development of a new one.

For this purpose, the work of Kamoji et al. (2009) [4] was selected as the aerodynamic reference. This study addressed a fundamental limitation of conventional Savonius rotors—the presence of negative static torque at specific angular positions ( $135^\circ$ - $165^\circ$  and  $315^\circ$ - $345^\circ$ ) which causes pulsating loads and vibration issues. Kamoji systematically investigated helical configurations with  $90^\circ$  twist, evaluating the effects of overlap ratio ( $a/D$ ), aspect ratio ( $H/D$ ), shaft configuration, and Reynolds number ( $Re$ ) on both static and dynamic performance characteristics.

The comprehensive parametric analysis provides an extensive experimental dataset that enables selection of an optimal configuration balancing torque smoothness with aerodynamic efficiency—essential for structural applications where vibration reduction is critical.

### 2.1.2 Kamoji's Experimental Investigations and Findings

Kamoji *et al.* (2009) conducted a series of open-jet wind tunnel tests on six  $90^\circ$  twisted helical Savonius rotors, each featuring different overlap ratios ( $a/D = 0, 0.10$ , and  $0.16$ ) and three aspect ratios ( $H/D = 0.88, 0.93$ , and  $1.17$ ). The test configurations are summarized in Table 2.1.

**TABLE 2.1** – Configurations of helical Savonius rotors tested

Rotor number	Overlap ratio ( $a/D$ )	Aspect ratio ( $H/D$ )	Rotor diameter $D$ (mm)
1	With shaft	1.0	224
2	0.00	0.88	230
3	0.00	0.93	230
4	0.00	1.20	211
5	0.10	1.00	215
6	0.16	1.00	215

The two helical Savonius rotor configurations investigated are illustrated in Figure 2.1. All rotor blades were fabricated from ABS plastic with a uniform wall thickness of 3 mm.

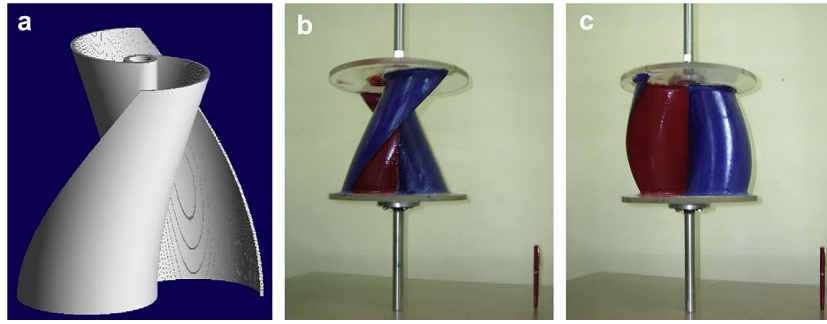


**FIGURE 2.1** – Helical Savonius rotors tested: (a) with shaft between end plates; (b) and (c) two views of helical rotor without shaft between end plates.

Table 2.2 summarizes the key results reported by Kamoji et al. for the different configurations tested, including both conventional and helical rotors. The data are compiled from Tables 3, 6, and 7 of the original publication.

**TABLE 2.2** – Summary of experimental results from Kamoji et al. (2009) for helical Savonius rotor configurations [4].

Configuration	$a/D$	AR	$Re = 1.2 \times 10^5$			$Re = 1.5 \times 10^5$		
			$C_{p,max}$	$C_{t,max}$	$C_{t,min}$	$C_{p,max}$	$C_{t,max}$	$C_{t,min}$
Helical (90°, without shaft)	0.0	0.88	0.165	0.33	+0.08	<b>0.174</b>	<b>0.32</b>	+0.10
Helical (90°, without shaft)	0.0	0.93	0.160	0.33	+0.08	0.170	0.32	+0.10
Helical (90°, without shaft)	0.1	0.88	0.117	0.31	+0.06	0.128	0.32	+0.07
Helical (90°, without shaft)	0.16	0.88	0.110	0.15	+0.05	0.116	0.15	+0.06
Helical (90°, with shaft)	0.0	0.88	0.092	0.09	+0.03	0.095	0.09	+0.03
Conventional Savonius	0.15	1.00	0.170	0.36	<b>-0.12</b>	0.180	0.37	<b>-0.15</b>

### 2.1.3 Selected Rotor Configuration

The helical configuration without shaft, zero overlap ratio and aspect ratio 0.88 shows the highest measured aerodynamic coefficient of performance,  $C_p = 0.174$  at Reynolds number  $Re = 1.5 \times 10^5$  (Table 2.2).

This corresponds to an absolute increase of +0.079 compared with the shafted design ( $C_p = 0.095$ ), and performs within 0.006 of the conventional Savonius rotor ( $C_p = 0.180$ ).

**TABLE 2.3** – Selected reference configuration adopted for the present study.

Parameter	Value / Description
Twist angle	90°
Overlap ratio ( $a/D$ )	0.0
Aspect ratio ( $H/D$ )	0.88
Shaft configuration	Without shaft
Reynolds number (Re)	$1.5 \times 10^5$

Notably, the static torque coefficients at all rotor angles for the helical Savonius rotors tested in this study are positive. However, for the conventional Savonius rotor there exist several rotor angles at which the static torque coefficient is negative.

### 2.1.4 Wind Tunnel Blockage Effects

When a wind turbine rotor is tested inside a wind tunnel, the nearby tunnel walls restrict airflow compared to outdoor (free-stream) conditions. This leads to *blockage effects*, which artificially increase measured wind speeds and affect pressure distributions around the model. Two main types are distinguished:

1. **Solid Blockage:** This blockage arises from the reduction in test-section area available for flow due to the presence (volume and shape) of the rotor. According to the continuity and Bernoulli equations, the flow velocity increases locally near the model compared to unconfined flow.

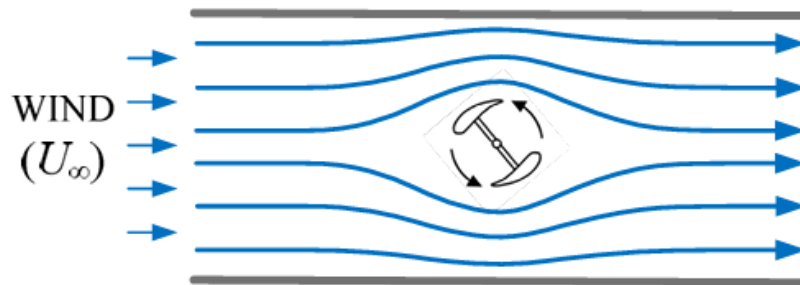


FIGURE 2.2 – Solid blockage, Adapted from [17].

2. **Wake Blockage:** Behind bluff bodies such as a Savonius rotor, the slow-moving turbulent wake region causes the surrounding air to accelerate to maintain mass flow, which also leads to an overestimation of wind speed.

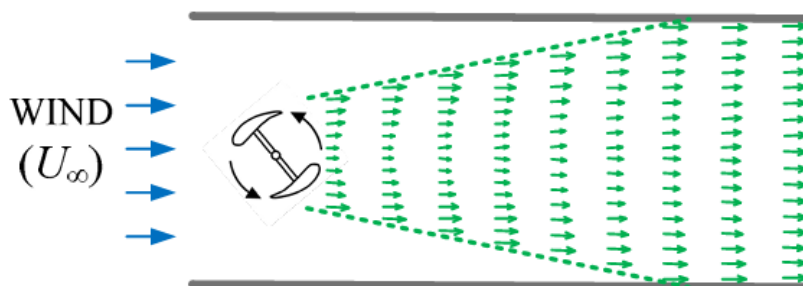
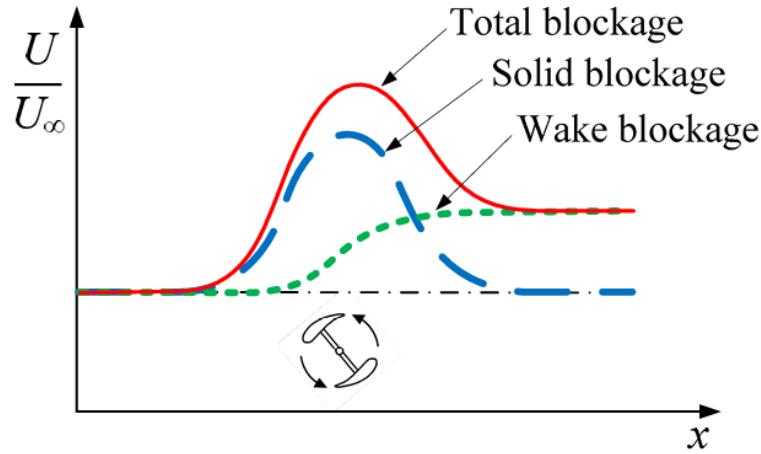


FIGURE 2.3 – Wake blockage, Adapted from [17].

The combined effect can significantly overestimate the rotor's aerodynamic performance unless corrected. Figure 2.4 summarizes the impact of both solid and wake blockage along the tunnel axis.



**FIGURE 2.4** – Combined effects of solid and wake blockage on normalized wind speed along the tunnel axis for a VWAT, *Adapted from [17]*.

### Blockage Ratio and Correction

The degree of blockage is quantified by the blockage ratio:

$$B_R = \frac{A_s}{A_t} \quad (2.1)$$

where:

- $A_s = D \times H$  is the projected frontal area of the rotor,
- $A_t$  is the cross-sectional area of the tunnel test section.

The classification of blockage significance generally follows the criteria proposed by Pope and Harper (1966) and later summarized by Jeong et al. (2018):

**TABLE 2.4** – Blockage ratio thresholds and recommended corrective actions [5? ].

Blockage Ratio $B_R$	Assessment	Recommended Action
$B_R < 5\%$	Negligible blockage	No correction required
$5\% \leq B_R < 10\%$	Moderate blockage	Apply correction using Pope–Harper method
$B_R \geq 10\%$	Significant blockage	Redesign or downscale model

For moderate blockage (5–10%), the corrected wind speed can be expressed as:

$$U_c = U(1 + \epsilon_t), \quad \epsilon_t = \frac{1}{4}B_R \quad (2.2)$$

and the corresponding corrected power coefficient:

$$C_{p,c} = C_p \left( \frac{U}{U_c} \right)^3 \quad (2.3)$$

### 2.1.5 Scaling Calculations for Wind Tunnel Testing

To ensure that blockage effects remained negligible in our experimental setup, the rotor geometry derived from Kamoji's reference model was scaled down according to the dimensions of the wind tunnel test section.

Given a wind tunnel test section area of  $630,000 \text{ mm}^2$  and a scaling factor of  $15/23$ , the following results were obtained:

**TABLE 2.5** – Comparison between the present scaled model and Kamoji's reference configuration.

Parameter	Our Case (Scaled Model)	Kamoji (2009)
Height (mm)	132	202.4
Diameter (mm)	150	230
Thickness (mm)	5	3
Diameter of End-plates (mm)	165	253
Thickness of End-plates (mm)	8	5
Blockage ratio (%) with end plates	3.61	9.64

As the computed blockage ratio  $B_R = 3.61\%$  falls well below the 5% threshold, the flow distortion is negligible, and no blockage correction is necessary. This ensures that the aerodynamic coefficients measured during the experiment can be considered representative of free-stream conditions.

### 2.1.6 Structural Analysis and Minimum Constraint Requirements

This analysis determines the minimum mechanical properties required for the rotor material to withstand aerodynamic loads under demanding operating conditions. The methodology involves:

- Estimating aerodynamic forces from Kamoji's reference torque coefficients
- Translating these forces into equivalent mechanical loads on a simplified structural model
- Deriving required material stiffness and strength from static, deflection, and modal criteria

The analysis uses the selected Kamoji helical Savonius configuration ( $AR = 0.88$ ,  $a/D = 0.0$ , no shaft) scaled  $10\times$  from original dimensions. Conservative parameters include:

- Maximum torque coefficient:  $C_{t,\max} = 0.33$
- Gust wind speed:  $U = 15 \text{ m s}^{-1}$
- Effective density:  $\rho_{\text{eff}} = \frac{1}{2}\rho_{\text{Al}}$  (50% weight reduction target)

Table 2.6 summarizes all input parameters for the structural analysis.

**TABLE 2.6** – Input parameters used for aerodynamic and structural analysis.

Parameter	Symbol	Value
Air density	$\rho$	$1.225 \text{ kg m}^{-3}$
Effective material density	$\rho_{\text{eff}}$	$1350 \text{ kg m}^{-3}$
Wind velocity (gust condition)	$U$	$15 \text{ m s}^{-1}$
Rotor diameter	$D$	$2.024 \text{ m}$
Rotor height	$H$	$2.300 \text{ m}$
Tip speed ratio	$\lambda$	$0.6$
Torque coefficient (maximum)	$C_{t,\text{max}}$	$0.33$
Shell thickness	$t$	$30 \text{ mm}$
Static safety factor	$SF_{\text{stat}}$	$2.0$
Admissible deflection ratio	$\frac{\delta_{\text{adm}}}{R}$	$0.05$
Modal separation factor	$M_{\text{freq}}$	$3.0$
First-mode constant (cantilever)	$\beta_1$	$1.8751$

## I. Structural Modeling Assumptions

The blade structure is idealized with the following simplifications:

- Each blade behaves as a **half-cylindrical thin shell cantilever** (Figure 2.5) with radius  $R = D/2$ , thickness  $t \ll R$ , and height  $H$
- Material exhibits linear elastic, isotropic behavior in this preliminary analysis
- Dynamic and inertial effects of rotation are neglected for static criteria
- The blade is modeled as a **fixed-fixed beam** along the height  $H$
- Aerodynamic loading is represented by an equivalent uniformly distributed pressure wind force

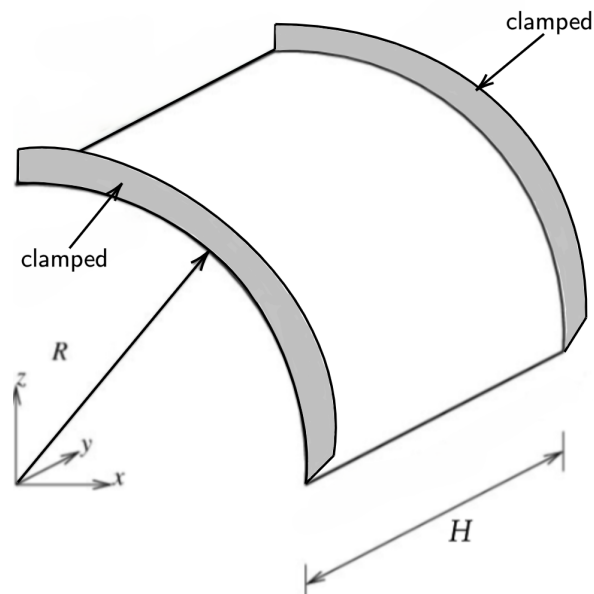


**FIGURE 2.5** – Half-cylindrical shell cantilever model

## II. Analytical Procedure

**Step 1: Aerodynamic Torque and Force** The aerodynamic torque acting on the rotor is expressed using the torque coefficient  $C_t$  as:

$$T = \frac{1}{4}C_t\rho U^2 D^2 H \quad (2.4)$$

The corresponding equivalent normal force transmitted to each blade is approximated by:

$$P_{eq} = \frac{T}{R} \quad (2.5)$$

**Step 2: Section Properties for Half-Cylindrical Shell** For the half-cylindrical shell cross-section:

$$I_{half} = \frac{\pi}{2}R^3t \quad (2.6)$$

$$W_{half} = \frac{I_{half}}{R} \quad (2.7)$$

$$(2.8)$$

**Step 3: Static Strength Criterion** For a fixed-fixed beam with uniformly distributed load:

$$w = \frac{P_{eq}}{H} \quad (2.9)$$

Maximum bending moment at supports:

$$M_{max} = \frac{wH^2}{12} \quad (2.10)$$

Maximum bending stress:

$$\sigma_{max} = \frac{M_{max}}{W_{half}} \quad (2.11)$$

**Step 4: Deflection Criterion** For a fixed-fixed beam, maximum deflection occurs at mid-height:

$$\delta_{max} = \frac{wH^4}{384EI_{half}} \quad (2.12)$$

With admissible deflection  $\delta_{adm}$ , the minimum required Young's modulus is:

$$E_{min}^{(\delta)} = \frac{wH^4}{384I_{half}\delta_{adm}} \quad (2.13)$$

**Step 5: Dynamic Criterion** The first bending natural frequency of a fixed-fixed beam with uniformly distributed mass:

$$f_n = \frac{K_n}{2\pi} \sqrt{\frac{EI_{half}g}{wH^4}} \quad (2.14)$$

Where  $K_n = 22.4$  is the first-mode coefficient for fixed-fixed beams.



Rotational excitation frequency:

$$f_{\text{rot}} = \frac{\lambda U}{\pi D} \quad (2.15)$$

The modal safety multiplier  $M_{\text{freq}} = 3$  ensures:

$$f_n \geq M_{\text{freq}} f_{\text{rot}} \quad (2.16)$$

This defines the minimum required Young's modulus:

$$E_{\text{min}}^{(\text{modal})} = \frac{4\pi^2 \omega H^4 (M_{\text{freq}} f_{\text{rot}})^2}{K_n^2 I_{\text{half}} g} \quad (2.17)$$

**Step 6: Governing Requirement and Shear Modulus** The governing minimum Young's modulus is:

$$E_{\text{min}} = \max(E_{\text{min}}^{(\delta)}, E_{\text{min}}^{(\text{modal})}) \quad (2.18)$$

Minimum shear modulus:

$$G_{\text{min}} = \frac{E_{\text{min}}}{2(1 + \nu)} \quad (2.19)$$

**TABLE 2.7** – Summary of derived aerodynamic and mechanical quantities for the reference gust condition ( $U = 15$  m/s,  $C_{t,\text{max}} = 0.33$ ).

$P_{\text{eq}}$ (N)	$\sigma_{\text{max}}$ (MPa)	$E_{\text{min}}^{(\delta)}$ (MPa)	$E_{\text{min}}^{(\text{modal})}$ (MPa)	$G_{\text{min}}$ (MPa)
211.71	0.000842	0.275	0.0077	0.11

The analytical results reveal a structurally over-conservative design where the maximum bending stress of 0.000842 MPa is negligible compared to typical material strengths, indicating that structural failure is not a concern. The deflection criterion governs the design with a required minimum Young's modulus of 0.275 MPa, which dominates the dynamic requirement of 0.0077 MPa by a factor of 35.7. This means the blade is significantly stiffer than necessary for vibration avoidance, suggesting potential for material reduction while maintaining structural integrity.

## 2.2 Material Selection and Characterization

The material selection for our final rotor followed the workflow detailed in Figure 2.6:

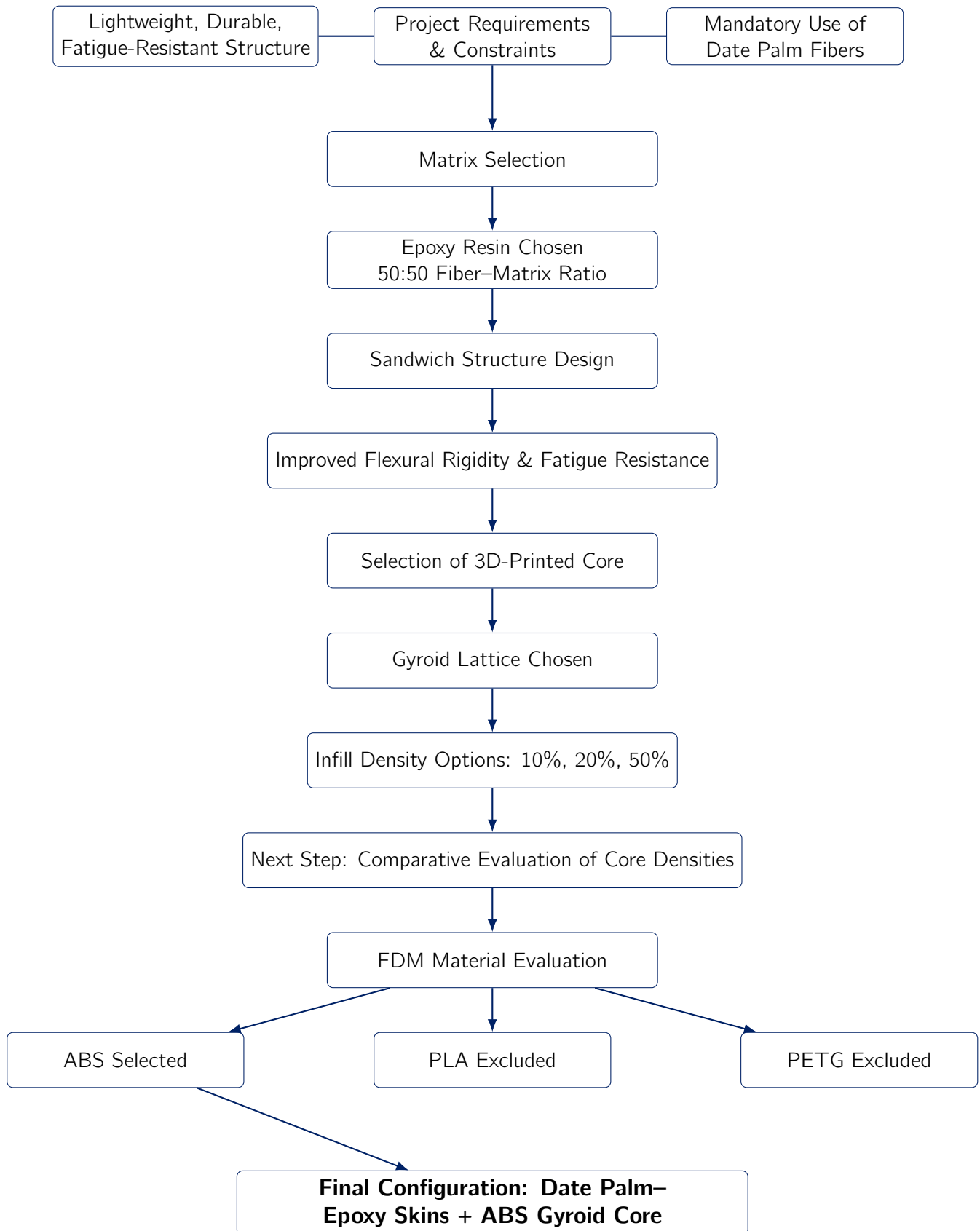


**FIGURE 2.6** – Material selection workflow for the final rotor configuration.

Following the systematic workflow illustrated in Figure 2.6, the design approach focused on combining bio-based reinforcement with a polymeric matrix in a sandwich configuration with a 3D-printed architected core.

### I. Matrix Selection: Epoxy Resin

The project specification mandated the use of natural date palm fibers, necessitating selection of a compatible matrix that ensured both mechanical compatibility and thermal stability. Epoxy resin was selected based on the following advantages:

- Strong interfacial adhesion with lignocellulosic fibers
- Low shrinkage during curing process
- Excellent chemical and fatigue resistance
- Good dimensional stability
- Suitable glass transition temperature (90°C–120°C) compatible with composite curing

A fiber–matrix weight ratio of 50:50 was adopted, representing an optimal compromise between mechanical stiffness, processability, and fiber impregnation quality as established in the literature.

### II. Sandwich Structure Design

To achieve the required high stiffness-to-weight ratio and cyclic durability, a sandwich architecture was implemented, offering:

- **Enhanced flexural rigidity** with minimal mass increase, leveraging the squared dependence of bending stiffness on skin separation distance
- **Improved shear load absorption** through core contribution, reducing local stress concentrations
- **Superior fatigue performance** by distributing cyclic loads more effectively

This configuration is well-established in aerospace and marine applications for its optimal balance of strength, weight, and stability under variable loading conditions.

### III. Core Material Selection

From Table 2.8, the thermal characteristics of candidate FDM materials reveal critical differences that informed the core material selection. The glass transition temperature ( $T_g$ )—the point at which a polymer transitions from a rigid glassy state to a soft rubbery state—was particularly crucial given the 100°C epoxy curing process.

**TABLE 2.8** – Thermal characteristics of candidate 3D-printing materials for the lattice core.

Material	Glass transition $T_g$ (°C)	Remarks
PLA	55–60	Easy printing, poor heat resistance, brittle after curing
PETG	75–85	Good ductility, fair stability, prone to warping
ABS	100–105	Good thermal stability

The material evaluation yielded the following assessments:

- **PLA** exhibits the lowest  $T_g$  (55–60°C), well below the curing temperature. This thermal limitation would cause dimensional instability and potential structural collapse during the 100°C epoxy curing cycle, despite its otherwise favorable printing characteristics.
- **PETG** offers improved thermal resistance ( $T_g = 75\text{--}85^\circ\text{C}$ ) but remains marginal for the curing process. More critically, its pronounced warping tendencies and weak interfacial adhesion with epoxy compromise the skin-core bond integrity essential for sandwich performance.
- **ABS** provides the most suitable thermal profile with a  $T_g$  of 100–105°C, ensuring dimensional stability throughout the curing process. Combined with its proven mechanical strength and reliable printing characteristics, ABS emerged as the optimal choice for the gyroid lattice core.

Building upon the material selection, three gyroid core infill densities—10%, 20%, and 50%—were chosen to investigate the optimal balance between weight reduction and mechanical performance. The final configuration will be selected based on comparative assessment of mass savings, structural properties, printing quality, and adhesion to the composite skin.

In summary, the proposed material architecture consists of two composite skins made of date palm fiber–epoxy bonded to a 3D-printed ABS gyroid lattice core. This configuration ensures low mass, sufficient stiffness, and high resistance to cyclic bending and shear stresses, fully satisfying the requirements of the Savonius rotor design.

## 2.3 Rotor Manufacturing and Realization

The transition from design to physical implementation follows the manufacturing sequence detailed in Figure 2.7:

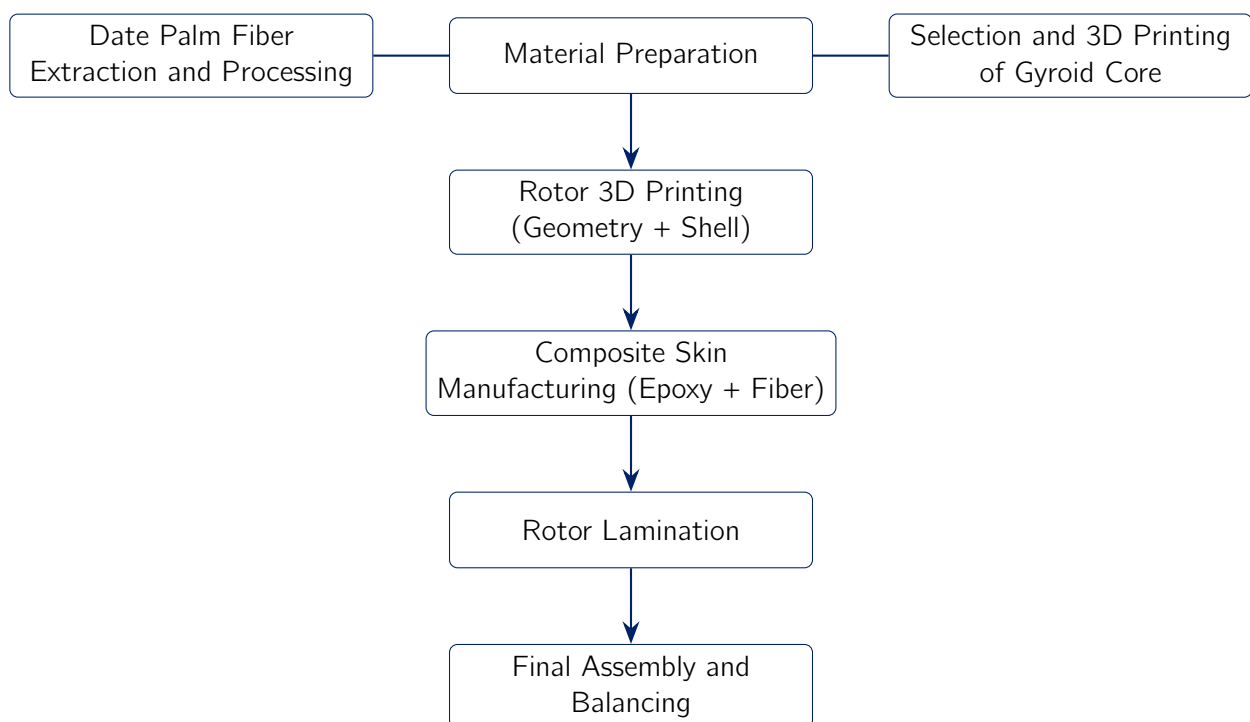


**FIGURE 2.7** – Manufacturing workflow for the rotor realization process.

This comprehensive process integrates natural fiber extraction and preparation, lattice core fabrication, composite skin manufacturing, and final rotor assembly. Each manufacturing step was designed to align with the material and structural constraints established in the design phase, ensuring both optimal performance and practical manufacturability.

The realization begins with date palm fiber extraction and progresses through sequential stages to final assembly, maintaining consistent adherence to the lightweight, durable structural requirements of the Savonius rotor application.

### 2.3.1 Date Palm Fiber Extraction Protocol

The **structural integrity** of natural fibers critically influences the mechanical performance of composite structures. For this reason, the extraction method must ensure minimal damage to fiber morphology while maximizing purity and interfacial compatibility with the matrix. In this work, an optimized extraction protocol was developed for fibers from date palm **midribs**, following multiple iterations and observations to tailor the process to the material's unique anatomical and chemical characteristics.

#### I. Preliminary Trials and Observations:

Initial experimental trials highlighted several critical limitations in conventional extraction practices:

- **Insufficient Penetration in Intact Midribs:** When using unpeeled, uncut midribs, the penetration of water and chemical treatments was hindered, leading to incomplete separation of non-cellulosic components.
- **Outer Layer Resistance:** Samples with intact protective layers showed limited degradation during retting and poor chemical diffusion, retaining excessive amounts of hemicellulose and lignin.
- **Degradation under Strong Alkaline Treatment:** Exposure to high-concentration NaOH solutions caused severe fiber embrittlement, likely due to overextraction or partial hydrolysis of cellulose chains, while lignin and hemicellulose remained largely unaffected.

These observations prompted the development of a more refined, four-stage process emphasizing gradual, non-destructive fiber purification.

#### II. Extraction Process presentation:

The finalized protocol, developed in this work, consists of four sequential stages as summarized in (Figure 2.8).

##### Phase 1: Initial Preparation

The extraction process began with manual separation of date palm fronds into their constituent components. The primary structural element—the midrib—was isolated through sequential steps: frond disassembly using cutting tools to remove leaflets, midrib sectioning into standardized 30 cm lengths with an electric saw, longitudinal slicing into 3–4 mm wide strips, and surface preparation by partial removal of the outer epidermal layer to enhance water permeability. This preparatory phase maximized surface area exposure while facilitating effective fluid penetration during the retting stage, ensuring optimal fiber separation efficiency.



**FIGURE 2.8** – Fiber Extraction from Date Palm Midribs (developed in this work)

## Phase 2: Water Retting

The longitudinally cut frond segments were submerged in a plastic container filled with water at 35 °C for a duration of five days. The container was insulated with polystyrene wrapping to minimize heat dissipation and maintain the temperature. The elevated temperature accelerated microbial activity, particularly of naturally occurring cellulolytic and hemicellulolytic bacteria, which selectively degraded hemicellulose and partially broke down lignin. This biological treatment softened the lignocellulosic matrix surrounding the fiber bundles, facilitating subsequent

mechanical separation.

### **Phase 3: Mechanical Extraction**

Following retting, the softened frond segments underwent mechanical fiber extraction. Each segment was passed through a manual roller and brushed using a steel-bristled metal brush. This process physically separated the individual fibers from the plant matrix, removing loosened residues and isolating fiber bundles. The mechanical action enhanced fibrillation while preserving fiber length and structural integrity, yielding clean, separated fibers ready for subsequent treatment.

### **Phase 4: Mild Alkaline Treatment and Neutralization**

To remove residual surface impurities (e.g., waxes, pectins, and lignin remnants), the extracted fibers were immersed in a 1% NaOH solution and heated at 100 °C for 1 hour using a laboratory oven. This low-concentration alkaline treatment avoided cellulose degradation while improving fiber surface roughness and wettability—critical factors for matrix adhesion in composite applications. The samples were then neutralized using 5% acetic acid (CH<sub>3</sub>COOH) and thoroughly rinsed and dried. This neutralization step eliminated alkaline residues that could inhibit epoxy matrix curing and compromise fiber-matrix interfacial bonding.

### **Extraction Results**

The extraction process produced the date palm fibers shown in Figure 2.9.

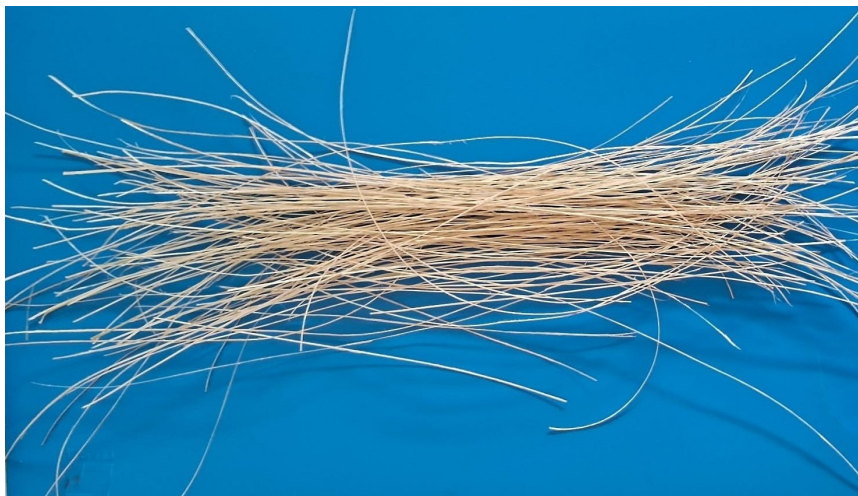


**FIGURE 2.9** – Date palm fibers after extraction.

## **2.3.2 3D Printing Process of the Rotor Components**

The realization of complex geometries, such as gyroid lattice cores, was enabled through fused deposition modeling (FDM) — a widely adopted additive manufacturing technique. This layer-by-layer fabrication method allows for the precise construction of architected materials while offering flexibility in design and optimization of internal features. In the present work, FDM was used for the fabrication of ABS-based gyroid cores and rotor shell geometries.



## 1. Principle of Fused Deposition Modeling:

FDM operates by extruding thermoplastic filament through a heated nozzle. The material is deposited along programmed toolpaths, defined by a slicing algorithm, to form successive layers. Once deposited, the filament rapidly solidifies, adhering to the previous layer through thermal bonding. The platform supporting the printed object typically moves in the vertical ( $z$ ) direction, while the print head translates in the horizontal ( $x$ - $y$ ) plane.

A critical aspect of successful FDM printing is the control of thermal conditions. The nozzle temperature must be sufficient to melt the thermoplastic polymer, while the bed temperature must ensure proper adhesion during the early layers. For example, ABS requires a nozzle temperature of 230–250°C and a heated bed around 90–110°C. Moreover, due to ABS's sensitivity to temperature gradients, printing must be performed in an enclosed build chamber to prevent warping and delamination caused by rapid cooling.

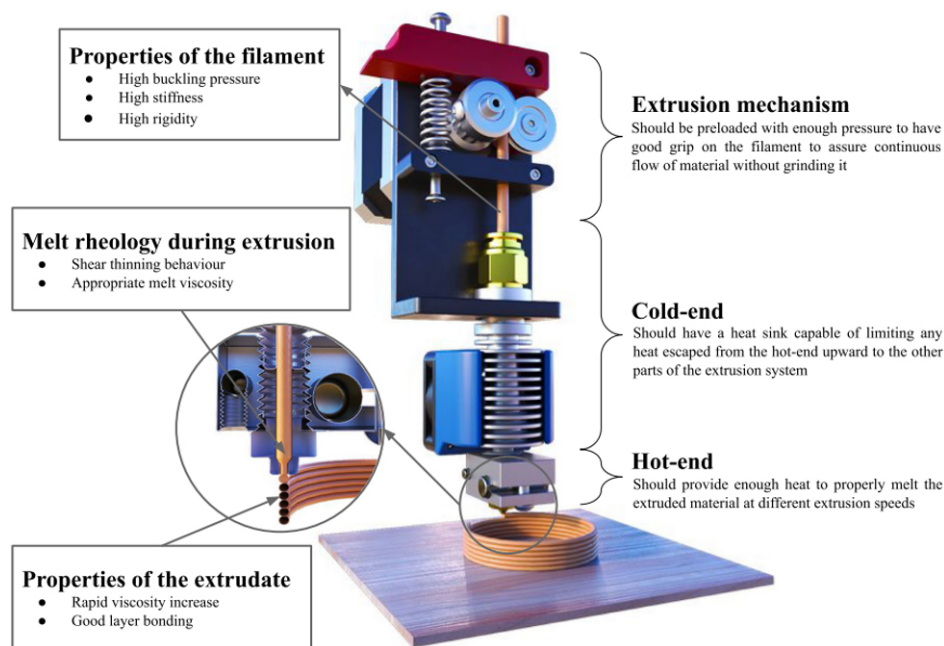


FIGURE 2.10 – Fused deposition modeling diagram

## 2. 3D Printing Parameters and Considerations

FDM manufacturing requires careful parameter optimization to achieve target mechanical properties and dimensional accuracy. Key controllable variables include:

### Raster Angle and Layer Configuration:

- **Raster Angle:** Defines the orientation of deposited filaments within each layer relative to the printing direction. The common  $\pm 45^\circ$  alternating pattern between successive layers distributes mechanical loads uniformly, reducing anisotropic behavior.
- **Layer Height:** Selection (typically 0.1–0.3 mm) represents a compromise between surface resolution and manufacturing time.

### Adhesion and Support Strategies:

- **Raft Implementation:** For materials with high thermal shrinkage like ABS, a disposable lattice foundation combats warping and ensures consistent first-layer adhesion across the build platform.



- **Support Structures:** Essential for geometries exceeding the printer's self-supporting angle limit (typically  $45^\circ$ ). These temporary frameworks prevent sagging in overhangs and bridges, with removal method dictated by material compatibility and geometric complexity.

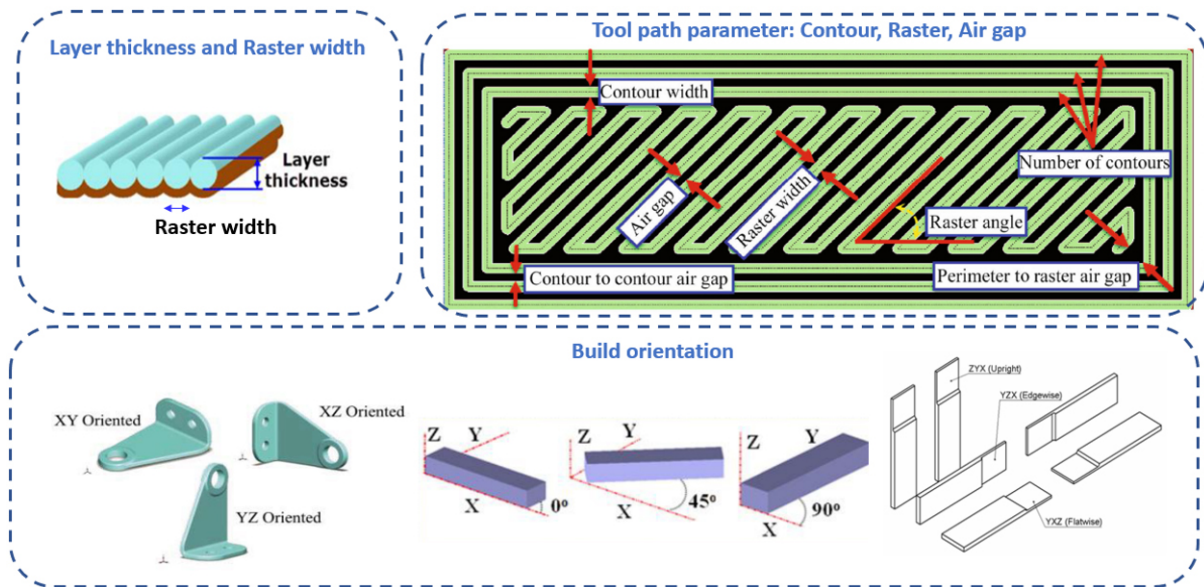


FIGURE 2.11 – Illustrations of process parameters

### Printer Mechanical Considerations:

Printer kinematics fundamentally influence dimensional accuracy, with Cartesian systems distributing linear motion across different axes. Common configurations include moving-bed (Y or Z axis) and moving-extruder designs, each presenting distinct dynamic characteristics and vibration profiles.

Automatic bed leveling compensates for platform deviations, ensuring consistent first-layer deposition critical for print success.

## 3. Gyroid Core Fabrication and Optimization

The fabrication of gyroid cores using Fused Deposition Modeling (FDM) required extensive parameter optimization to balance structural integrity with lightweight objectives.

### 1. Initial Challenges and Solutions:

- **Low-Density Issues:** Insufficient wall thickness led to incomplete deposition and weak interlayer adhesion
- **Medium-Density Problems:** Moderate pore size allowed excessive epoxy infiltration during lamination, compromising weight reduction goals

For these reasons, a balanced configuration was adopted to optimize three competing factors: printability, mechanical integrity, and resin infiltration control. A unit cell of  $5 \times 5 \times 4$  mm with a shell thickness of 1.2 mm at 52% infill density provided sufficient material per gyroid surface to ensure quality printing, while limiting pore diameter enough to prevent deep resin penetration. This ensured effective bonding with the composite skin without sacrificing the lightweight nature of the core.

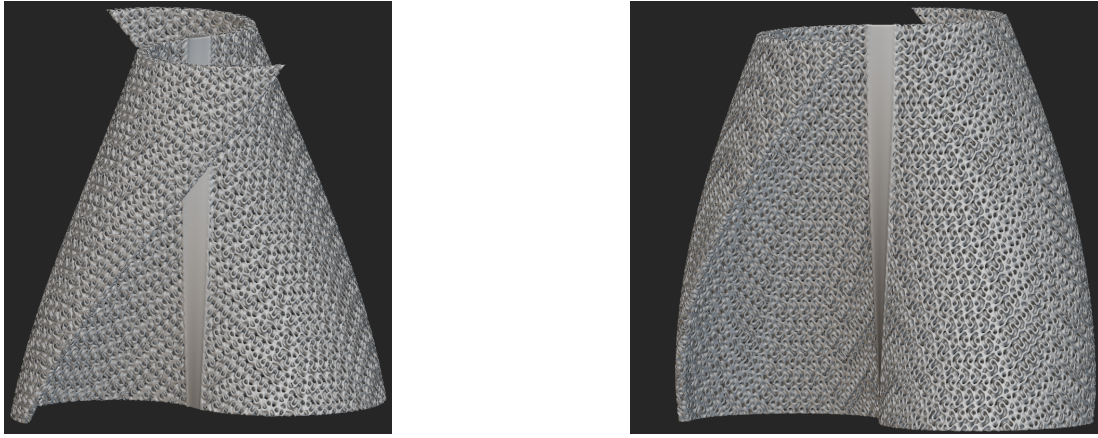


**FIGURE 2.12** – nTopology rotor model.

**TABLE 2.9** – Optimized Gyroid Core Printing Parameters

Parameter	Value
Printing Material	ABS
Nozzle Temperature	240 °C
Bed Temperature	100 °C
Layer Thickness	0.2 mm (surface), 1.2 mm (infill)
Unit Cell Dimensions	5 × 5 × 4 mm
Infill Pattern	Gyroid
Print Environment	Enclosed chamber

## II. Full Rotor Printing Process Development

While the fabrication of gyroid cores proceeded successfully, printing the full rotor geometry introduced a new set of challenges due to its twisted, non-axisymmetric structure. As the print progressed beyond a certain height, significant issues began to arise, including layer shifting and filament entanglement, which ultimately caused the print to fail.



**FIGURE 2.13** – Observed layer shifting at upper rotor heights

### Stage 1: High-Speed Printing — Initial Failure

In the first printing attempt, the print speed was kept high to reduce build time. However, excessive vibrational effects from the fast motion of the print head likely caused instability in the upper layers. Around the mid-height of the rotor, visible misalignment occurred between deposited layers, and filament accumulated around the nozzle due to incomplete adhesion and sudden directional changes. This led to the extrusion head clogging and an aborted print.

### **Stage 2: Speed Reduction — Partial Success**

To address the vibrational sensitivity, the printing speed was reduced. This modification improved the layer alignment and allowed us to reach a greater height before failure. However, the issue persisted in the final third of the rotor, where complex curvature intensified overhang effects and instability of unsupported regions became critical.



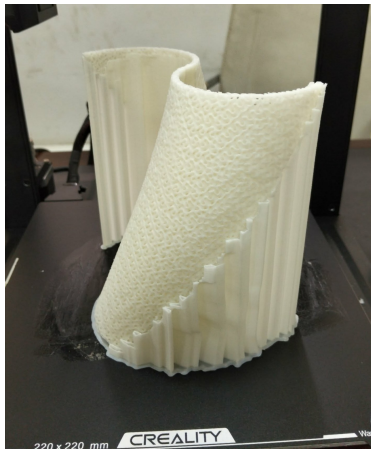
**FIGURE 2.14** – Print improvement with reduced speed, but premature failure remains

### **Stage 3: Use of Adaptive Bed-Leveling Printer — Improved Output**

A more advanced printer with bed-tilt compensation was employed to correct for mechanical misalignment and dynamic shifts. This adjustment significantly stabilized the deposition path, allowing the rotor to be printed almost entirely. Nonetheless, a minor deformation near the top layers was still observed, attributed to insufficient support of the cantilevered final layers.

### **Stage 4: Support Implementation — Final Resolution**

The final issue was the lack of support in the topmost regions, where the material began to curl or sag due to gravity and reduced layer anchoring. Enabling automated support structures in the slicer software provided a stable scaffold for overhanging areas, fully resolving the deformation and layer shift issues. A clean and dimensionally accurate rotor was obtained.



(a) Successful rotor print with support



(b) Support structure used during printing

**FIGURE 2.15** – Final printing with support structures

Table 2.10 summarizes the different rotor printing configurations tested and their corresponding results.

**TABLE 2.10** – Rotor Printing Configurations and Results

Configura- tion	Speed (mm/s)	Duration (h)	Support	Max Height Achieved (mm)	Rotor Mass (g)
High speed, no support	100	11:30 min	No	~70 (failure)	–
Reduced speed, no support	50	22	No	~130 (par- tial)	–
Adaptive bed- leveling	50	21	No	142 (full)	65.98
Final: With support	100	15:48 min	Yes	142 (full)	136.94

### 2.3.3 Composite Lamination and Rotor Assembly

#### 1. Woven fabric preparation:

Due to limitations in the available quantity of calibrated natural fibers, a pragmatic adaptation was made during the skin fabrication phase. A commercial woven fiberglass fabric was employed—not as a mechanical enhancement, but as a practical alternative to ensure the completion of the composite layer. Selected fiberglass yarns were removed and replaced with the extracted date palm fibers, maintaining a hybrid configuration. This substitution was driven purely by material constraints and availability. Had a sufficient amount of natural fibers been accessible, the fabrication would have proceeded exclusively with palm-based reinforcement.





**FIGURE 2.16** – Hybrid reinforcement fabric showing date palm fiber yarns integrated with fiberglass fabric

## 2. Surface Preparation and Treatment:

Effective adhesion between the epoxy resin and the ABS substrate is limited by the inherently low surface energy and chemical inertness of ABS. To overcome this, a surface activation protocol based on acetone wiping was implemented, optimized to enhance mechanical interlocking and interfacial bonding.

Prior to lamination, the 3D-printed ABS rotor was subjected to the following surface activation steps:

1. **Initial Cleaning:** The surface was first cleaned with a dry lint-free cloth to remove any loose particles or contaminants.
2. **Acetone Wipe:** A 100% acetone solution was gently applied using a lint-free cloth in a circular motion. This procedure induces partial surface dissolution and increases micro-roughness at the polymer interface, promoting mechanical interlocking during curing.
3. **Exposure Time:** The acetone was allowed to act for 3 minutes under ambient conditions. This short contact time ensures effective surface activation without inducing structural deformation or excessive softening of the ABS.
4. **Drying Step:** After the exposure period, the surface was wiped again with a clean dry cloth to eliminate any acetone residue. Full evaporation was ensured before applying the composite resin.

## 3. Lamination Process:

The hybrid fiber mat was manually draped over the prepared rotor surface. A hand lay-up process was employed using a two-part epoxy system with a 1.86:1 resin-to-hardener ratio by weight. The resin was evenly distributed across the surface using a hand roller to ensure full wetting of the fibers and to minimize air entrapment.

Lamination was performed under ambient conditions without vacuum assistance. The composite was left to cure at room temperature for 24 hours.

#### 4. Final Assembly:

The final assembly of the hybrid Savonius rotor involved integrating the individual 3D-printed components with the composite blades and mechanical housings. The sequence is illustrated in Figure 2.17.



(a) Rotor bonded between upper and lower end plates.



(b) Lower housing with bearing and spacer insertion.



(c) Final assembled hybrid Savonius rotor.

**FIGURE 2.17** – Sequential assembly process of the hybrid Savonius rotor.

The final assembly of the hybrid Savonius rotor involved integrating the individual 3D-printed components with the composite blades and mechanical housings.

First, the rotor was positioned between the two end plates (upper and lower), which were bonded using silicone adhesive to ensure sealing and prevent detachment during rotation. After securing the end plates, the upper housing was aligned with the lower end plate and fastened using four bolts.

Next, two roller bearings were press-fitted into the lower housing. A spacer was placed between the two bearings to maintain axial alignment and minimize friction. Once the bearing assembly was completed, the shaft was inserted through the upper housing. An elastic pin was then

inserted through aligned holes in both the shaft and upper housing to lock them together mechanically.

Finally, the lower end of the shaft was inserted into the lower housing assembly, completing the structural integration of the rotor, shaft, and bearing system.

## 2.4 Final Outcome and Performance Assessment

The final rotor prototype was successfully fabricated using the developed sandwich structure combining a 3D-printed gyroid ABS core and hybrid fiber-reinforced composite skins. This lightweight structural concept aimed to minimize mass while preserving the mechanical integrity and aerodynamic functionality required for rotational operation.

A comparative evaluation was conducted between the developed rotor, a conventional machined aluminum rotor, and a fully 3D-printed PLA rotor (100% infill). The results, summarized in Table 2.11, highlight the effectiveness of the proposed design in achieving substantial weight reduction while maintaining competitive manufacturing costs.

**TABLE 2.11** – Comparison of final rotor mass and cost with respect to reference rotors.

Rotor Type	Mass (g)	Relative mass reduction of developed rotor w.r.t references (%)	Approx. Cost (DZD)
Developed Hybrid Sandwich Rotor	127.3	–	4 000
Aluminum Rotor [69]	444.07	71.3	40 000
100% Infill PLA Rotor	247.5	48.6	2 000

The results clearly demonstrate that the machining of aluminum rotors is not only significantly more expensive but also results in a much heavier component, unsuitable for low-inertia wind systems. The fully 3D-printed PLA rotor, while more economical, remains substantially heavier due to its full infill density, limiting its dynamic performance.

The proposed hybrid sandwich rotor successfully met the design target of about 50% weight reduction, achieving a total mass of 127.3 g. Although the inclusion of bio-composite skins slightly increases material cost relative to pure PLA, the gain in structural efficiency and aerodynamic responsiveness justifies the marginal cost difference. Moreover, the additive–composite hybrid approach offers superior adaptability for future optimization in stiffness, damping, and sustainability compared with both conventional machining and monolithic polymer printing.

# Material Characterization

...

## Overview

...

This chapter presents the integrated numerical and experimental approach adopted to determine the equivalent elastic properties of the hybrid sandwich material developed in this study. The methodology combines micro-scale characterization, numerical homogenization, and experimental validation to establish accurate orthotropic material parameters for structural simulation.

The chapter is structured as follows:

- **Theoretical Background of Homogenization:** Introduces the fundamental principles and workflow used to obtain equivalent material properties.
- **Characterization of the Woven Skin:** Describes the experimental tensile testing of individual fibers and the numerical homogenization of the woven composite in ANSYS.
- **Characterization of the Gyroid Core:** Details the mechanical testing of the ABS core and the corresponding numerical modeling performed in nTop for validation.
- **Final Homogenization of the Sandwich Structure:** Presents the integration of skin and core equivalent properties to derive the global orthotropic behavior of the full sandwich panel.



### 3.1 Background and scope

Our goal was to obtain a representative stiffness tensor for the structure (namely the components  $E_{ij}$ ,  $\nu_{ij}$ , and  $G_{ij}$ ) to be used in subsequent simulations of the rotor's aeroelastic behavior.

Due to limited access to testing equipment, a complete mechanical characterization could not be conducted experimentally. In particular, we lacked the necessary resources to perform shear tests for determining the shear modulus, as well as the lateral and longitudinal extensometers required to evaluate Poisson's ratio. Consequently, only tensile tests were carried out, allowing us to determine the Young's modulus experimentally. These limitations prompted us to seek an alternative approach to overcome the technical constraints. We therefore adopted a hybrid strategy, combining experimental work with data extracted from the literature when available, complemented by numerical simulations using the homogenization method.

Given the complexity of our sandwich structure, which includes woven natural fiber composite skins, a gyroid-structured ABS core, and their assembly, we opted for a sequential homogenization methodology. This approach simplifies the problem by characterizing each component separately before estimating the overall properties of the composite structure.

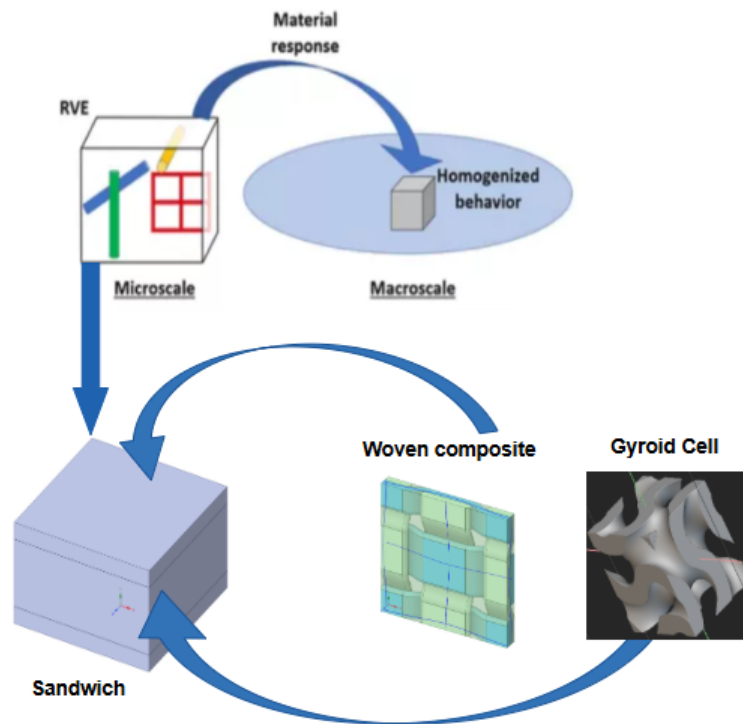


**FIGURE 3.1** – Schematic representation of the material characterization workflow.

## 3.2 Theory of Homogenization

### 3.2.1 Introduction and Motivation

Numerical simulation of composite structures is challenging due to the differences in involved length scales.

Consider a wind turbine rotor blade made of glass fiber reinforced composite materials: the

diameter of the glass fibers is a few micrometers, while the diameter of the turbine is 100 meters. This is a scale difference of roughly eight orders of magnitude.

While the finite element method could be used to simulate the structural mechanics of this system (resolving all length scales), it is not practical. The number of elements required would be astronomically large, and computing the finite element solution would be infeasible, both on modern and near-future computing hardware.

This scale difference is also a problem in additive manufacturing. 3-D printing allows the generation of parts on the meter scale, with complex microstructures. The ratio of the involved length scales is smaller than in the example of the composite blade, but still presents a significant computing challenge with a single finite element model resolving all length scales.

The standard approach to eliminate this problem of scale in finite element analysis for composite materials is homogenization. Material properties for a composite material are averaged, rather than simulating the full complex microstructure. With homogenized material data, structures only require simulation at the macroscopic scale, making composite analysis significantly less computationally intensive. This efficiency motivated our choice of the homogenization method.

### 3.2.2 Fundamental Assumptions and Scope

Homogenization methods are predicated upon the following assumptions:

- **Scale Separation:** Microscale features (e.g., fibers, pores, or unit cells) are significantly smaller than the macroscale structure.
- **Linear Elasticity:** Small strain, linear material response is assumed for most practical formulations.
- **Perfect Bonding:** Interfaces between constituents are ideally bonded, excluding debonding or sliding effects.
- **Microstructure Periodicity or Statistical Homogeneity:** The microstructure must be periodic or sufficiently uniform to justify the use of Representative Volume Elements (RVEs).

Particularly for composites, unless stated otherwise, all the models share the following assumptions:

- The matrix is isotropic and the inclusions are either isotropic or transversely isotropic in the x-direction.
- Inclusions are axially symmetric and identical in size and shape. ..

### 3.2.3 Homogenization Workflow

The homogenization methodology proceeds through three main phases to determine effective material properties from microstructural analysis, as illustrated in Figure 3.2.

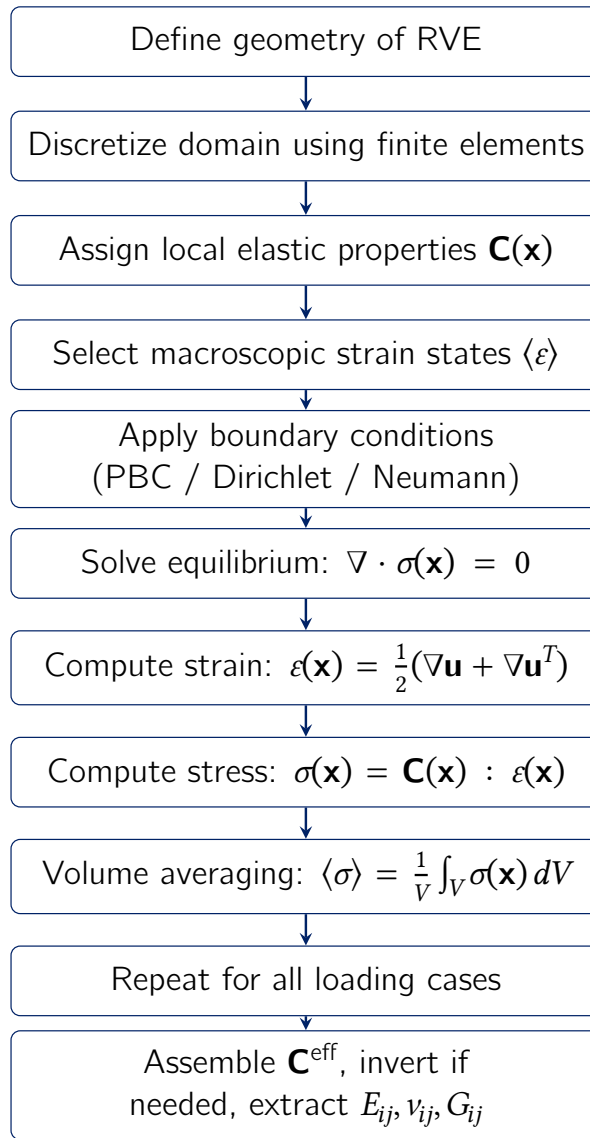


**FIGURE 3.2** – Finite element-based homogenization workflow.

As shown in Figure 3.2, the two principal stages are: first, RVE modeling and meshing; second, extraction of homogenized material properties.

## I. Initial Stage: RVE Modeling and Discretization

### 1. Representative Volume Element (RVE)

The Representative Volume Element (RVE) is a small portion of a material that is sufficiently large to exhibit the correct macroscopic behavior while accurately representing its microstructural characteristics. It serves as a bridge between the microscopic and macroscopic scales.

- **Periodic materials:** The RVE can be easily identified in such materials as one unit cell. In these materials, the microstructure repeats itself in all three coordinate directions. Therefore, this single unit cell contains all the necessary information about the material.
- **Non-periodic materials:** Determining the appropriate RVE size for non-periodic materials is more complex. One approach is to incrementally increase the size of the considered volume and observe whether the resulting macroscopic properties change significantly. If

the macroscopic properties remain constant with further increases in volume size, the volume can be considered a valid RVE.

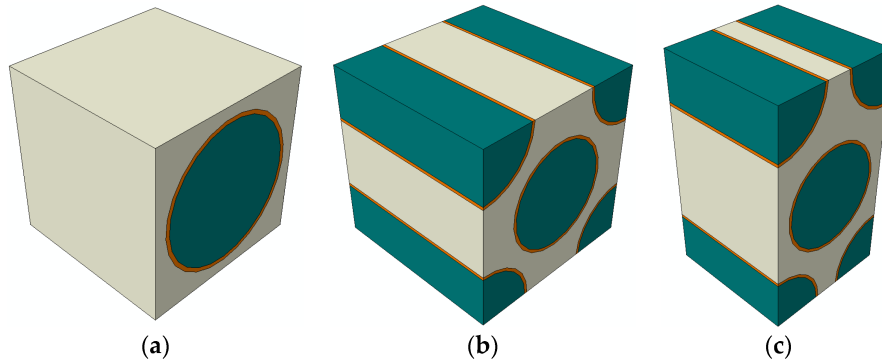


**FIGURE 3.3** – Different RVE configurations showing fiber–matrix disposition.

## 2. Mesh Generation and Material Assignment

The RVE geometry undergoes finite element discretization to enable numerical analysis:

- **Mesh Generation:** The domain is discretized using appropriate element types (tetrahedral, hexahedral) with sufficient refinement to capture microstructural features
- **Material Assignment:** Local elastic properties  $\mathbf{C}(\mathbf{x})$  are assigned to each constituent phase based on their respective material characteristics
- **Mesh Quality:** Element quality metrics are verified to ensure numerical stability and accuracy in subsequent analyses.

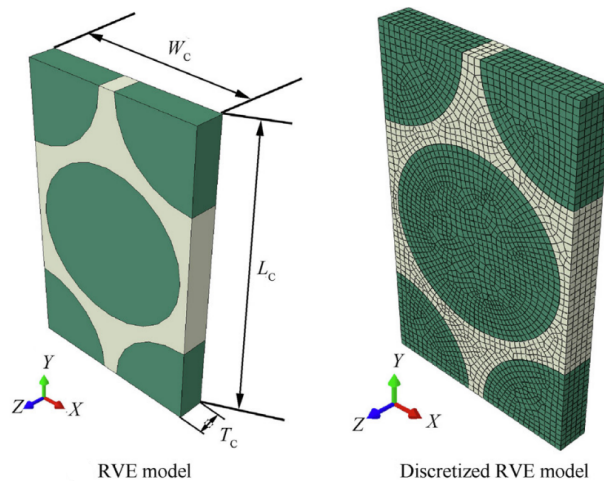


**FIGURE 3.4** – Meshing of representative volume elements (RVE).

## II. Homogenized Property Evaluation

### 1. Orthotropic Material Characterization

To explain the remaining steps of the homogenization workflow, we consider the example of a periodic orthotropic unit cell. To perform the computation of orthotropic elasticity constants, six independent load cases are required: three tensile tests in the X, Y, and Z directions, and three shear tests in the XY, YZ, and XZ planes.

This computational procedure is performed by applying a corresponding macroscopic strain in each of the six cases. After selecting the appropriate macroscopic strain state, we apply boundary conditions such that the reaction forces on the boundary faces of the RVE are used to assemble the stiffness matrix  $\mathbf{C}$ , from which we extract the engineering constants  $E_{ij}$ ,  $\nu_{ij}$ , and  $G_{ij}$ .

The applied boundary conditions are classified into two categories: *periodic* and *non-periodic*. Periodic conditions ensure strain compatibility between opposite faces of the RVE, while non-periodic (Dirichlet-type) conditions impose fixed displacements directly. The corresponding formulations are summarized below.

#### (a) Periodic Boundary Conditions (PBCs)

In each load case, one strain component among  $\varepsilon_x$ ,  $\varepsilon_y$ ,  $\varepsilon_z$ ,  $\gamma_{xy}$ ,  $\gamma_{yz}$ ,  $\gamma_{xz}$  is prescribed (typically  $\varepsilon = 0.001$ ), while all others are set to zero. Periodic displacement relations are imposed on opposite faces of the RVE to maintain kinematic continuity:

$$\begin{aligned} u_x(L_x, y, z) &= u_x(0, y, z) + \varepsilon_x L_x, & u_y(L_x, y, z) &= u_y(0, y, z) + \gamma_{xy} L_x, \\ u_z(L_x, y, z) &= u_z(0, y, z) + \gamma_{xz} L_x, & u_x(x, L_y, z) &= u_x(x, 0, z), \\ u_y(x, L_y, z) &= u_y(x, 0, z) + \varepsilon_y L_y, & u_z(x, L_y, z) &= u_z(x, 0, z) + \gamma_{yz} L_y, \\ u_x(x, y, L_z) &= u_x(x, y, 0), & u_y(x, y, L_z) &= u_y(x, y, 0), \\ u_z(x, y, L_z) &= u_z(x, y, 0) + \varepsilon_z L_z. \end{aligned} \quad (3.1)$$

To eliminate rigid body motion, one node on each coordinate plane is fixed as:

$$u_x(x=0) = 0, \quad u_y(y=0) = 0, \quad u_z(z=0) = 0. \quad (3.2)$$

#### (b) Non-Periodic Boundary Conditions (Dirichlet-type)

For verification, fixed (non-periodic) boundary conditions were also applied. In this case, displacements are directly prescribed on opposing faces of the RVE.

For uniaxial tensile loading:

$$\begin{aligned} u_x(0, y, z) &= 0, & u_x(L_x, y, z) &= \varepsilon_x L_x, \\ u_y(x, 0, z) &= 0, & u_y(x, L_y, z) &= \varepsilon_y L_y, \\ u_z(x, y, 0) &= 0, & u_z(x, y, L_z) &= \varepsilon_z L_z. \end{aligned} \quad (3.3)$$

For shear deformation in the XY-plane ( $\gamma = 0.01$ ):

$$\begin{aligned} u_y(0, y, z) &= 0, & u_y(L_x, y, z) &= \gamma L_x, \\ u_x(x, 0, z) &= 0, & u_x(x, L_y, z) &= 0, \\ u_z(x, y, 0) &= 0, & u_z(x, y, L_z) &= 0. \end{aligned} \quad (3.4)$$

These boundary conditions provide the required macroscopic strain fields to solve the equilibrium equation  $\nabla \cdot \boldsymbol{\sigma}(\mathbf{x}) = 0$  and compute the stress–strain response for each load case.

This extraction follows the sequential application of macroscopic strain loading, equilibrium solution, stress–strain field computation, and volume averaging for each load case.

## 2. Load Case Implementation and Matrix Assembly

Consider the tensile test in the X-direction as a representative example. For an orthotropic material, the stress–strain relationship is governed by:

$$\begin{bmatrix} \sigma_x \\ \sigma_y \\ \sigma_z \\ \tau_{xy} \\ \tau_{yz} \\ \tau_{zx} \end{bmatrix} = \begin{bmatrix} C_{11} & C_{12} & C_{13} & 0 & 0 & 0 \\ C_{12} & C_{22} & C_{23} & 0 & 0 & 0 \\ C_{13} & C_{23} & C_{33} & 0 & 0 & 0 \\ 0 & 0 & 0 & C_{44} & 0 & 0 \\ 0 & 0 & 0 & 0 & C_{55} & 0 \\ 0 & 0 & 0 & 0 & 0 & C_{66} \end{bmatrix} \begin{bmatrix} \varepsilon_x \\ \varepsilon_y \\ \varepsilon_z \\ \gamma_{xy} \\ \gamma_{yz} \\ \gamma_{zx} \end{bmatrix} \quad (3.5)$$

When applying a strain  $\varepsilon_x = 0.001$  with all other strain components set to zero, the first column of the stiffness matrix is determined from the stress response:

$$\begin{bmatrix} C_{11} \\ C_{12} \\ C_{13} \\ 0 \\ 0 \\ 0 \end{bmatrix} = \frac{1}{0.001} \begin{bmatrix} \sigma_x \\ \sigma_y \\ \sigma_z \\ \tau_{xy} \\ \tau_{yz} \\ \tau_{zx} \end{bmatrix} \quad (3.6)$$

## 3. Engineering Constants Extraction

The complete stiffness matrix  $[\mathbf{C}]$  is assembled by repeating this procedure for all six load cases. The compliance matrix  $[\mathbf{S}] = [\mathbf{C}]^{-1}$  is then computed through matrix inversion, enabling extraction of the engineering constants:

$$[\mathbf{S}] = \begin{bmatrix} \frac{1}{E_x} & -\frac{\nu_{yx}}{E_y} & -\frac{\nu_{zx}}{E_z} & 0 & 0 & 0 \\ -\frac{\nu_{xy}}{E_x} & \frac{1}{E_y} & -\frac{\nu_{zy}}{E_z} & 0 & 0 & 0 \\ -\frac{\nu_{xz}}{E_x} & -\frac{\nu_{yz}}{E_y} & \frac{1}{E_z} & 0 & 0 & 0 \\ 0 & 0 & 0 & \frac{1}{G_{xy}} & 0 & 0 \\ 0 & 0 & 0 & 0 & \frac{1}{G_{yz}} & 0 \\ 0 & 0 & 0 & 0 & 0 & \frac{1}{G_{zx}} \end{bmatrix} \quad (3.7)$$

This systematic approach yields the complete set of orthotropic engineering constants:

$$(E_x, E_y, E_z, G_{xy}, G_{yz}, G_{zx}, \nu_{xy}, \nu_{yx}, \nu_{xz}, \nu_{zx}, \nu_{yz}, \nu_{zy}) \quad (3.8)$$

These parameters are required for macroscopic structural analysis.

#### 4. Macroscopic Averaging and Effective Property Computation

For each loading case, the local stress and strain fields  $\sigma(\mathbf{x})$  and  $\varepsilon(\mathbf{x})$  are obtained from the finite element solution. The macroscopic (homogenized) response is then determined through volume averaging according to:

$$\langle \sigma \rangle = \frac{1}{V} \int_V \sigma(\mathbf{x}) dV, \quad \langle \varepsilon \rangle = \frac{1}{V} \int_V \varepsilon(\mathbf{x}) dV \quad (3.9)$$

where  $V$  denotes the RVE volume. The effective stiffness tensor  $\mathbf{C}^{\text{eff}}$  is defined by the constitutive relation:

$$\langle \sigma \rangle = \mathbf{C}^{\text{eff}} : \langle \varepsilon \rangle \quad (3.10)$$

This final averaging step ensures that the derived engineering constants represent the equivalent homogeneous behavior of the heterogeneous microstructure, consistent with the Hill–Mandel energy equivalence principle.

### 3.3 Material Characterization Procedure and Results

To determine the effective elastic properties of the developed sandwich material, a sequential characterization approach was adopted. First, the constituent materials—palm-date fibres and 3D-printed ABS—were individually characterized through mechanical testing and microstructural analysis. This was followed by the evaluation of the sandwich subcomponents: the woven composite skin and the gyroid-structured core. Finally, the complete sandwich structure was characterized using the previously introduced homogenization method to extract its global orthotropic properties.

#### 3.3.1 Date Palm Fibres (DPF) Characterization

Comprehensive morphological and mechanical analyses were carried out to characterize DPF, including diameter measurement and evaluation of mechanical properties.

##### I. Morphological Characterization

To visualize the effect of alkaline treatment, scanning-electron micrographs (SEM) were taken at 250× magnification (Fig. 3.5).

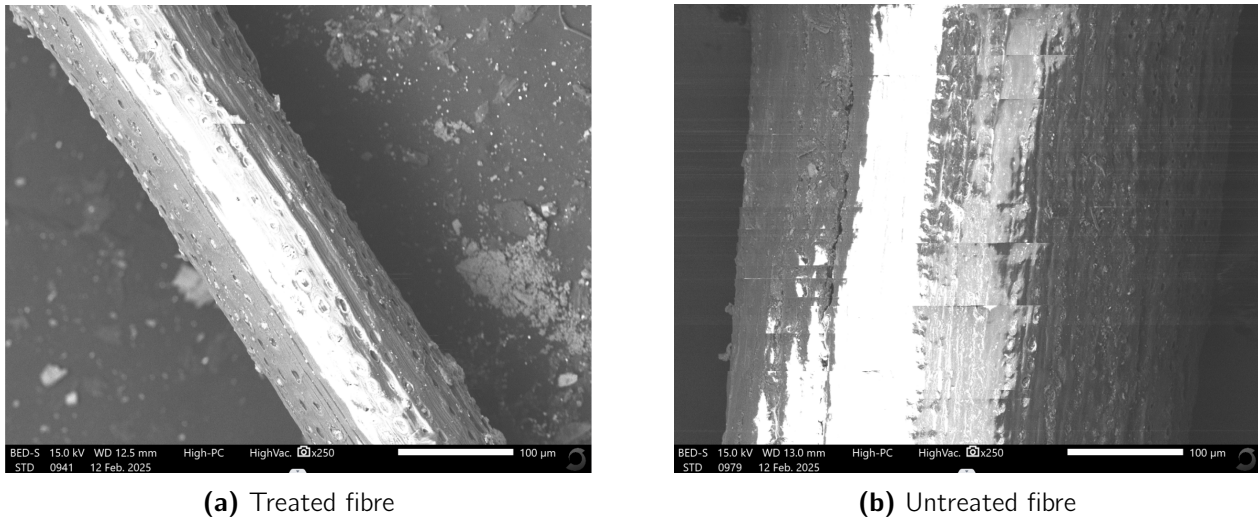


**FIGURE 3.5** – SEM micrographs showing surface morphology of (a) treated and (b) untreated date palm fibres at 250× magnification

The treated fibres exhibit clear fibrillation and surface pores that act as mechanical keys, whereas the untreated fibres retain a smooth, lignin-rich outer layer. This confirms the efficiency of the low-temperature NaOH process in removing surface impurities and enhancing fibre–matrix adhesion.

The data in Table 3.1 show a broad diameter distribution among the analysed fibre bundles, with values ranging from 138 to 385 µm. Statistical analysis was performed to quantify fibre diameter variability using the following equations:

$$\bar{d} = \frac{1}{n} \sum_{i=1}^n d_i \quad (3.11)$$



$$s = \sqrt{\frac{1}{n-1} \sum_{i=1}^n (d_i - \bar{d})^2} \quad (3.12)$$

$$CV = \frac{s}{\bar{d}} \times 100\% \quad (3.13)$$

where  $\bar{d}$  is the mean diameter,  $s$  is the standard deviation,  $n = 11$  is the sample size, and CV is the coefficient of variation.

The calculated mean diameter of approximately 270  $\mu\text{m}$  and coefficient of variation of 31.5% indicate natural heterogeneity, characteristic of lignocellulosic fibres. Such variability originates from differences in fibre maturity, extraction conditions, and cross-sectional irregularities within the palm-date fronds.

**TABLE 3.1** – Descriptive statistics for fibre bundle diameter ( $n = 11$ )

Statistic	$d$ ( $\mu\text{m}$ )
Mean	269.45
Standard deviation	84.79
Coefficient of variation (%)	31.47
Minimum	138.00
Maximum	385.00

Our measured mean diameter lies within the range reported in Table 1.3 for mechanically extracted date-palm midrib fibres (13.7–510  $\mu\text{m}$ ), confirming that the adopted extraction and preparation method effectively corresponds to mechanical processing as commonly described in the literature.

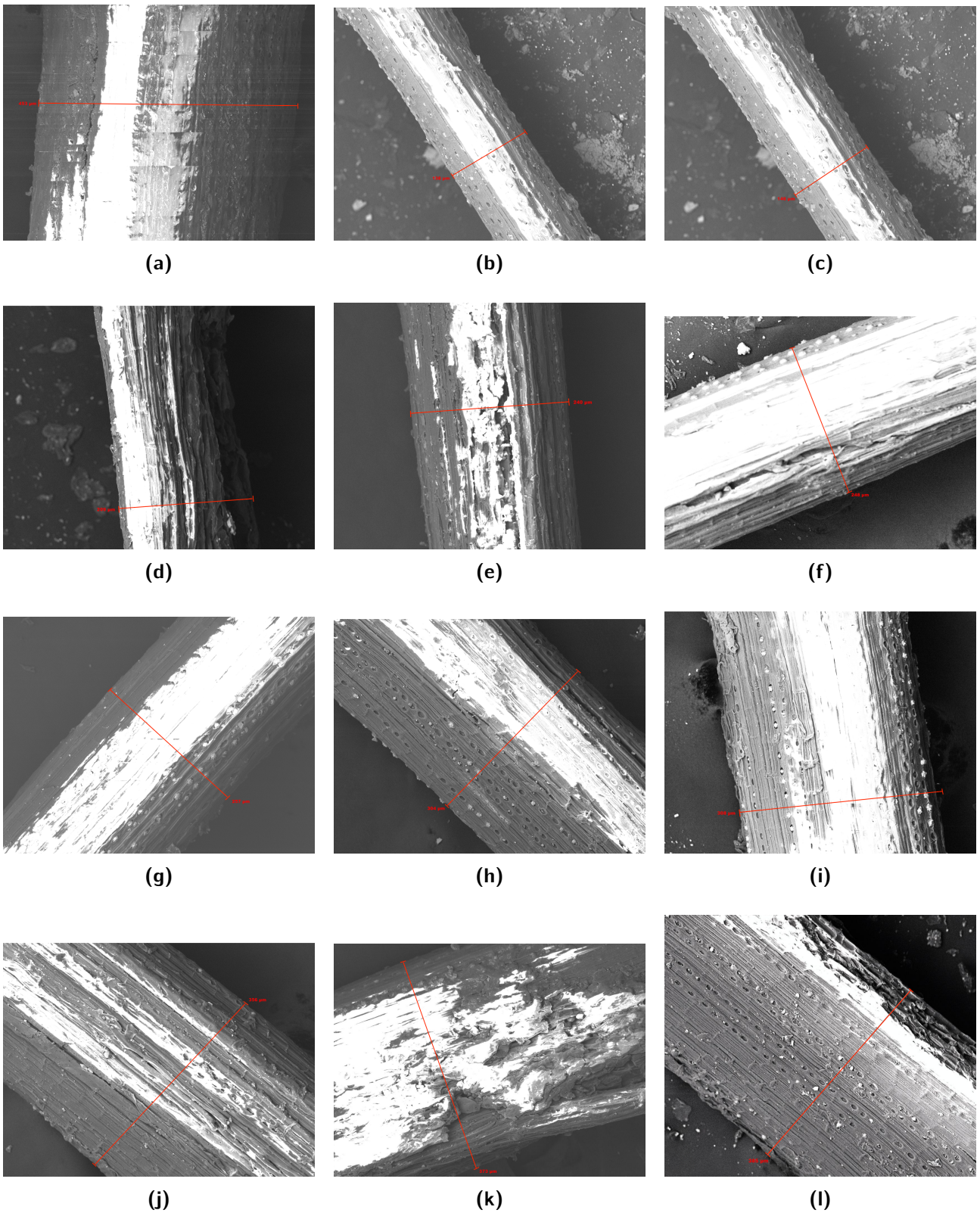


**FIGURE 3.6** – SEM cross-sections of twelve representative date midrib fibres showing diameter variability. Subfigures (a–l) correspond to individual fibres measured at magnifications ranging from 150× to 250×.

## II. Mechanical Characterization

The tensile properties of individual DPF bundles were evaluated following morphological characterization, in accordance with ASTM D3822-01. Tests employed a universal testing machine with a 1 kN load cell at  $0.5 \text{ mm min}^{-1}$  displacement rate across eleven specimens.

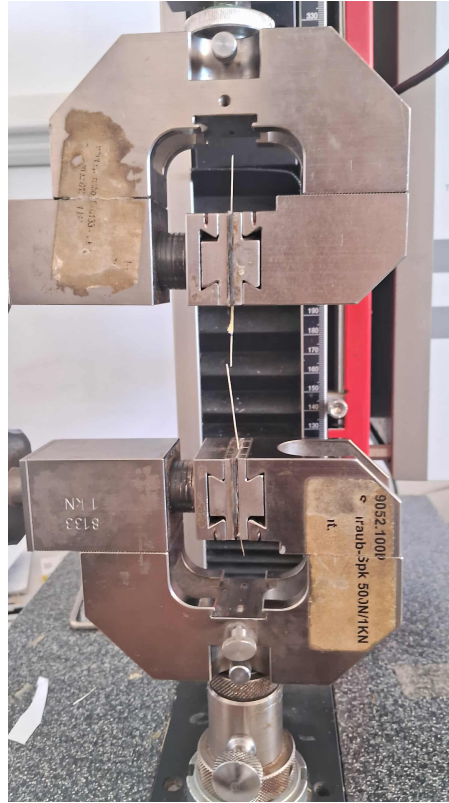


**FIGURE 3.7** – Experimental setup for single-fibre tensile testing according to ASTM D3822.

Table 3.2 summarizes the mechanical properties, with corresponding stress-strain responses in Figure 3.8.

**TABLE 3.2** – Mechanical properties of individual palm-date fibre bundles.

Ref.	$d$ ( $\mu\text{m}$ )	$E$ (GPa)	$\sigma_{\text{max}}$ (MPa)
b	138	14.87	306.9
c	146	13.28	274.2
d	209	13.42	128.9
e	240	8.52	195.8
f	248	8.22	188.8
g	257	8.12	175.7
h	304	7.03	137.4
i	308	6.55	148.1
j	356	5.97	161.0
k	373	5.85	153.2
l	385	5.36	62.4

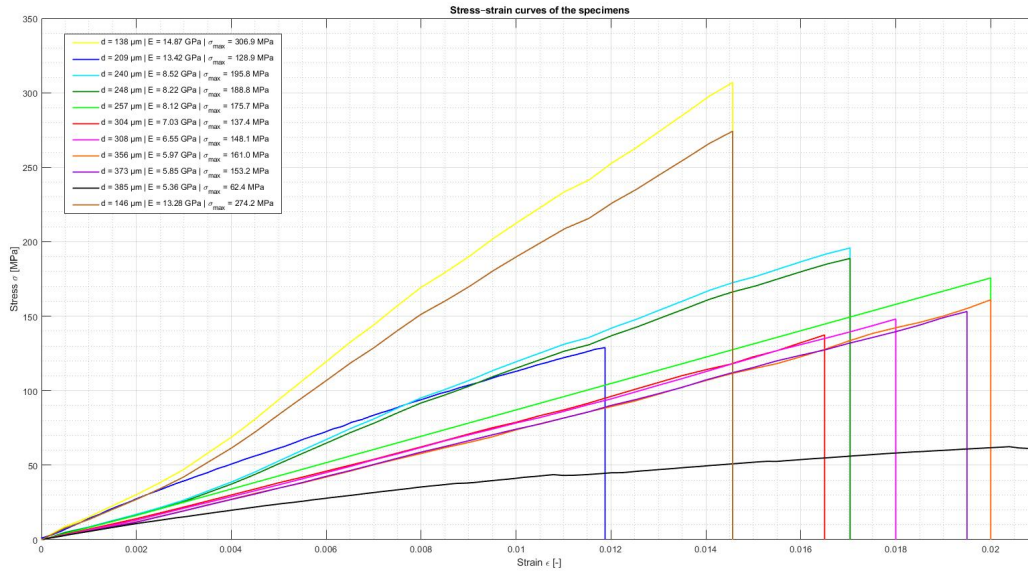


**FIGURE 3.8** – Stress-strain curves for the eleven tested fibre bundles.

## I. Experimental Results

The stress-strain responses reveal a clear inverse trend between fibre diameter and both Young's modulus and tensile strength. Thinner bundles exhibit higher stiffness and strength, attributed to:

- Higher cellulose content fraction,
- Lower microfibril angles promoting improved axial alignment, and
- Fewer surface defects or internal voids.

Table 3.3 compares our results with literature values from Elseify *et al.* Despite our lower mean fiber diameter (269.45  $\mu\text{m}$  versus 340  $\mu\text{m}$ ), their reported mechanical properties are significantly higher ( $E = 16.1$  GPa,  $\sigma_{\text{max}} = 453$  MPa). This discrepancy primarily stems from variations in fiber source, maturity, and alkali treatment conditions including NaOH concentration, soaking duration, and rinsing procedures, which influence fibril alignment and matrix removal.

**TABLE 3.3** – Comparison of average mechanical properties with literature data (Elseify *et al.*).

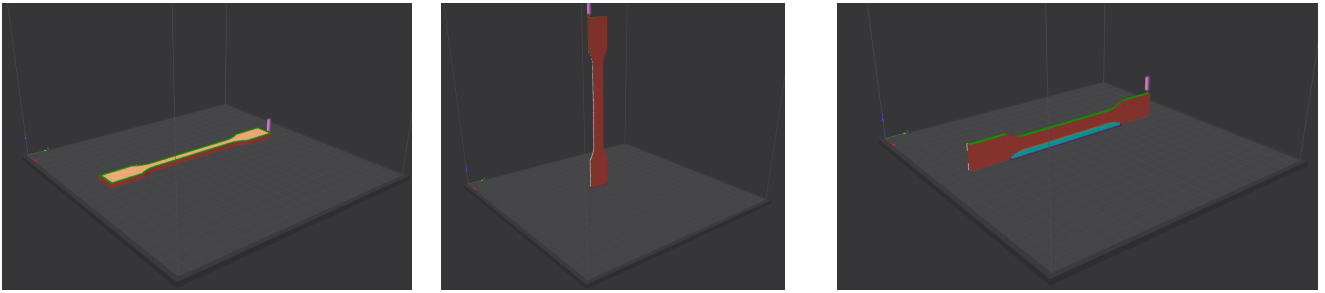
Parameter	This Work	Elseify <i>et al.</i>
$d$ ( $\mu\text{m}$ )	269.45	340
$E$ (GPa)	8.84	16.1
$\sigma_{\text{max}}$ (MPa)	175.67	453
Density ( $\text{kg m}^{-3}$ )	1420	1324

### 3.3.2 ABS Characterization

The inherent anisotropy in fused filament fabrication (FFF) arises from the layer-by-layer deposition process, which induces direction-dependent mechanical properties due to variations in interlayer bonding quality, raster orientation, and thermal history.

To characterize the mechanical behavior, **full-density** tensile specimens were fabricated using a standard FFF printer to establish baseline mechanical properties. Three batches were printed with their main axis aligned along the principal Cartesian directions—X, Y, and Z (Fig. 3.9)—corresponding to horizontal width, printing bed movement, and vertical build directions, respectively.

The printing orientation was modified at the slicing stage to maintain identical specimen geometry across all batches, varying only the material deposition direction. This approach enabled direct comparison of stiffness and strength variations along each principal axis under identical uniaxial tensile testing conditions.



(a) Specimen aligned along X-axis    (b) Specimen aligned along Y-axis    (c) Specimen aligned along Z-axis

**FIGURE 3.9** – Full-density ABS tensile specimens printed along different orientations.

Three specimens were prepared for each printing orientation, following the ISO 527-2 standard for thermoplastic materials. The Type 1A specimen geometry is illustrated in Fig. 3.10, and the corresponding nominal dimensions and testing parameters are summarized in Table 3.4.

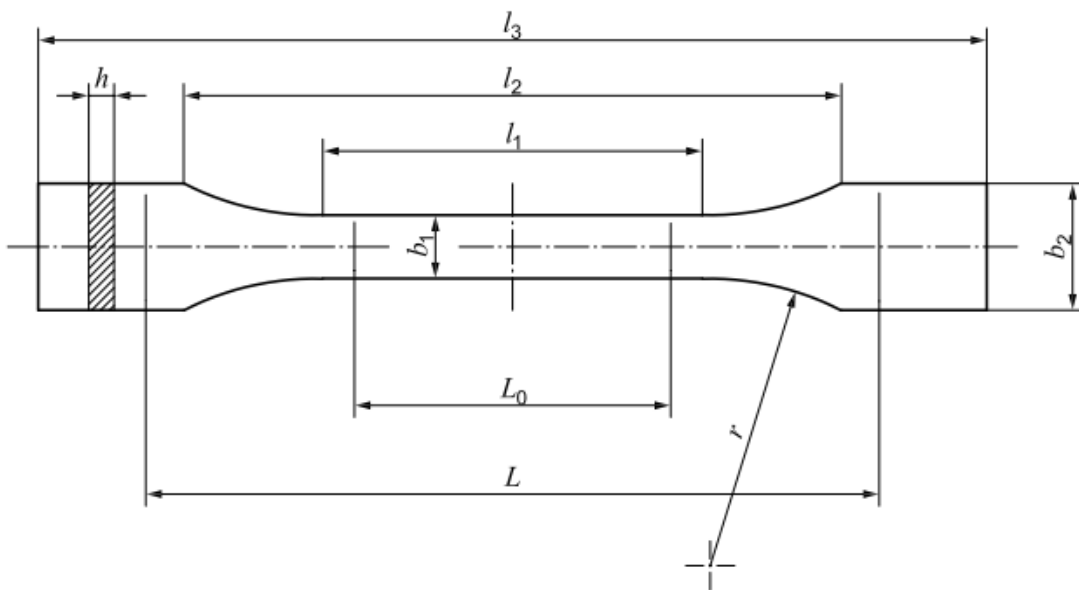


**FIGURE 3.10** – ISO 527-2 Type 1A specimen geometry used for uniaxial tensile tests.



**TABLE 3.4** – Nominal dimensions and testing parameters for ISO 527-2 Type 1A specimens.

Parameter	Value
Total length ( $I_3$ )	170 mm
Narrow parallel portion length ( $I_1$ )	$80 \pm 2$ mm
Fillet radius ( $r$ )	$24 \pm 1$ mm
Distance between wide portions ( $I_2$ )	$109.3 \pm 3.2$ mm
Width at ends ( $b_2$ )	$20.0 \pm 0.2$ mm
Width of narrow portion ( $b_1$ )	$10.0 \pm 0.2$ mm
Recommended thickness ( $h$ )	$4.0 \pm 0.2$ mm
Gauge length ( $L_0$ )	$75.0 \pm 0.5$ mm
Alternative gauge length ( $L_0$ )	$50.0 \pm 0.5$ mm
Initial grip separation ( $L$ )	$115 \pm 1$ mm
Tensile test speed	$1 \text{ mm min}^{-1}$

### I. Brittle Fracture of 3D-Printed ABS

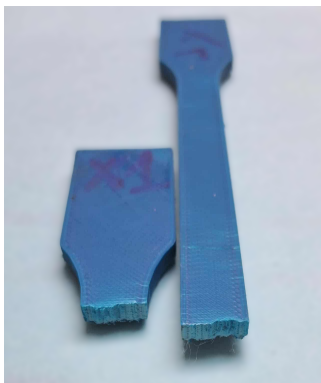
Figure 3.11 shows that specimens failed via brittle fracture. This failure is attributed to weak interlayer bonding and stress concentrations from internal voids, both inherent to the FDM process.



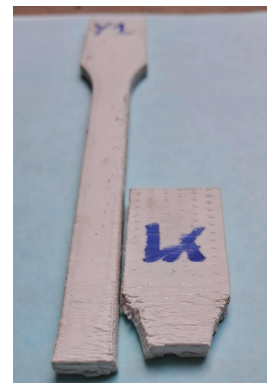
(a) X1 specimen before tensile testing



(b) Y1 specimen before tensile testing



(c) X1 specimen after tensile failure



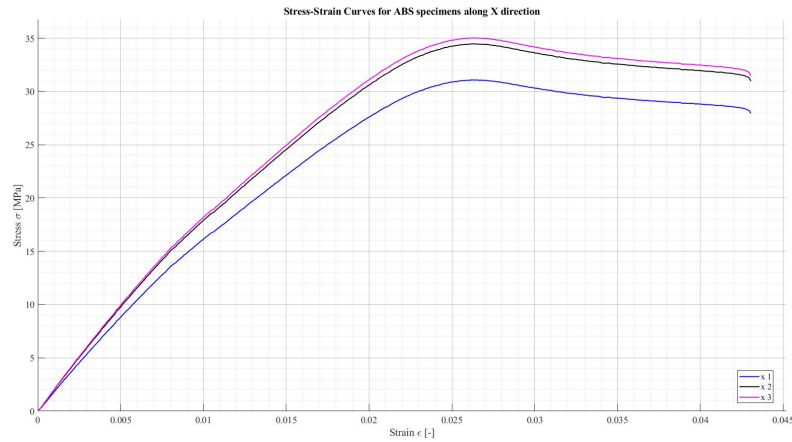
(d) Y1 specimen after tensile failure

**FIGURE 3.11** – Full-density ABS tensile specimens illustrating characteristic FDM failure modes: inter-layer delamination, intralayer separation, and void-induced stress concentrations

### II. Experimental Results

The stress-strain responses of the full-density ABS specimens printed along the three principal directions (X, Y, and Z) are presented in Figures 3.12, 3.13, and 3.14, with corresponding

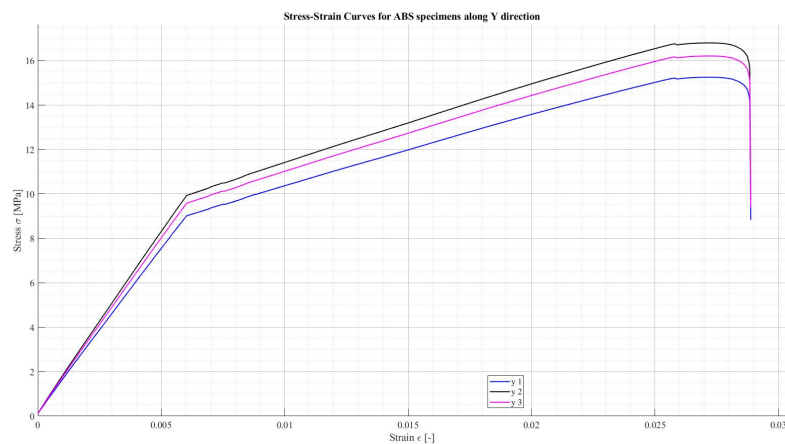
mechanical properties—Young’s modulus ( $E$ ) and ultimate tensile strength ( $\sigma_{UTS}$ )—summarized in Tables 3.5, 3.6, and 3.7. The  $\sigma_{UTS}$  values correspond to the maximum stress attained before fracture, following ISO 527-2 guidelines.



**FIGURE 3.12** – Stress-strain curves for full-density ABS specimens printed along the X-axis.

**TABLE 3.5** – Mechanical properties of full-density ABS specimens printed along the X-axis.

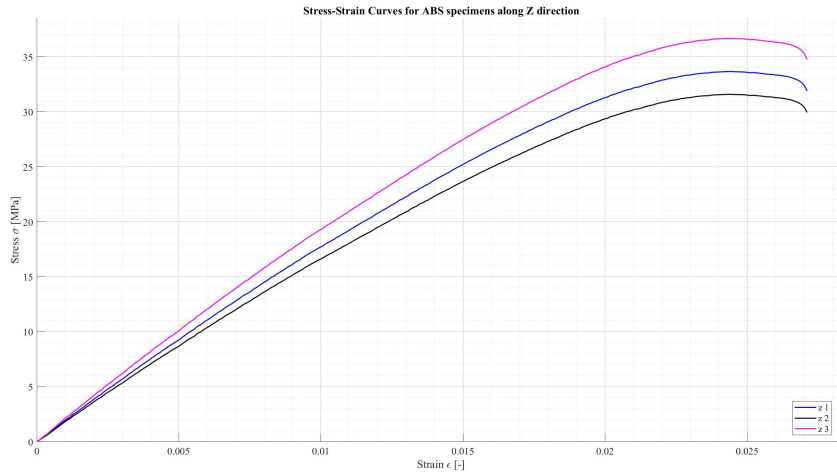
Specimen	$E_x$ (GPa)	$\sigma_{UTS}$ (MPa)
1	1.77	31.09
2	1.98	34.47
3	2.01	35.03
<b>Mean</b>	<b>1.92</b>	<b>33.53</b>



**FIGURE 3.13** – Stress-strain curves for full-density ABS specimens printed along the Y-axis.

**TABLE 3.6** – Mechanical properties of full-density ABS specimens printed along the Y-axis.

Specimen	$E_y$ (GPa)	$\sigma_{UTS}$ (MPa)
1	1.47	15.26
2	1.63	16.80
3	1.57	16.21
<b>Mean</b>	<b>1.56</b>	<b>16.09</b>

**FIGURE 3.14** – Stress-strain curves for full-density ABS specimens printed along the Z-axis.**TABLE 3.7** – Mechanical properties of full-density ABS specimens printed along the Z-axis.

Specimen	$E_z$ (GPa)	$\sigma_{UTS}$ (MPa)
1	1.87	33.67
2	1.75	31.59
3	2.05	36.68
<b>Mean</b>	<b>1.89</b>	<b>33.98</b>

### III. Interpretation of Results

The tensile test results reveal a **transversely isotropic** behavior in 3D-printed ABS:

- The **Y-direction** exhibited the weakest mechanical response, with an average Young's modulus of  $E_y = 1.56$  GPa and an ultimate tensile strength of  $\sigma_{UTS} = 16.09$  MPa. These values are approximately 18% lower in stiffness and more than 50% lower in strength compared to the mean of the X- and Z-directions.
- In contrast, the **X- and Z-directions** showed nearly identical performance, with  $E_x = 1.92$  GPa and  $E_z = 1.89$  GPa, and corresponding tensile strengths of  $\sigma_{UTS} = 33.53$  MPa and  $\sigma_{UTS} = 33.98$  MPa, respectively. These comparable results indicate consistent interlayer adhesion and filament fusion in both orientations.



- Since shear moduli and Poisson's ratios could not be derived from uniaxial tensile tests, the complete orthotropic elastic tensor ( $E_{ij}$ ,  $\nu_{ij}$ ,  $G_{ij}$ ) could not be experimentally reconstructed.
- For subsequent numerical simulations and homogenization, ABS was therefore modeled as an **isotropic material** using the mean tensile properties of the weakest orientation (Y-axis), i.e.,  $E = 1.56$  GPa and  $\sigma_{UTS} = 16.09$  MPa. This conservative approach ensures a lower-bound estimate of the material's overall behavior.

### 3.3.3 Sandwich Characterization

#### I. Woven Composite Skin

The woven composite skin was characterized numerically using the finite element-based homogenization technique implemented in *ANSYS Material Designer*. Since the RVE model in Material Designer requires yarn-level properties rather than raw fiber inputs, the fabric was represented as a system of orthogonally interlaced warp and weft yarns embedded in a polymer matrix. Each of these yarns was modeled as an equivalent unidirectional (UD) composite, whose orthotropic properties were determined using a semi-analytical micromechanical model.

#### 1. Equivalent Yarn Properties

The mechanical behavior of impregnated yarns—composed of natural fibers and epoxy—was estimated by combining the Halpin–Tsai model with classical rule-of-mixtures formulations. The Halpin–Tsai equations were applied to compute the transverse modulus ( $E_2$ ) and in-plane shear modulus ( $G_{12}$ ), while the longitudinal modulus ( $E_1$ ) and density ( $\rho$ ) were obtained using the Voigt model. The out-of-plane shear modulus ( $G_{23}$ ) and Poisson’s ratios ( $\nu_{12}$ ,  $\nu_{23}$ ) were determined through inverse mixture rules (Reuss-type) or empirical averaging.

#### Assumptions

- (a) Fibers are continuous, aligned, and uniformly distributed.
- (b) Perfect bonding and full impregnation (no porosity or voids) are assumed.
- (c) Effects of fiber waviness, misalignment, and interfacial defects are neglected.

#### 2. Input Parameters and Data

Material parameters were extracted from literature and representative experimental data. The fiber volume fraction was set to  $V_f = 0.55$ , corresponding to a 45% matrix volume content. The Halpin–Tsai geometry parameter  $\xi = 2$  was adopted, representing the typical assumption for circular fibers in unidirectional composite configurations.

**TABLE 3.8** – Constituent material properties used in the micromechanical model.

Parameter (unit)	Symbol	Value
Fiber Young’s modulus (GPa)	$E_f$	8.836
Fiber Poisson’s ratio (–)	$\nu_f$	0.30
Fiber density (kg/m <sup>3</sup> )	$\rho_f$	1420
Matrix Young’s modulus (GPa)	$E_m$	3.78
Matrix Poisson’s ratio (–)	$\nu_m$	0.35
Matrix density (kg/m <sup>3</sup> )	$\rho_m$	1160
Fiber volume fraction (–)	$V_f$	0.55
Halpin–Tsai geometry parameter (–)	$\xi$	2

### 3. Governing Equations

The equivalent orthotropic elastic properties of the impregnated yarn were computed using a combination of mixture laws and the Halpin–Tsai relations as summarized below:

■ **Longitudinal modulus (Voigt model):**

$$E_1 = E_f V_f + E_m (1 - V_f)$$

■ **Transverse modulus (Halpin–Tsai):**

$$E_2 = E_m \cdot \frac{1 + \xi \eta_E V_f}{1 - \eta_E V_f}, \quad \text{where } \eta_E = \frac{(E_f/E_m) - 1}{(E_f/E_m) + \xi}$$

■ **Shear moduli (Halpin–Tsai and inverse rule of mixtures):**

$$G_{12} = G_m \cdot \frac{1 + \xi \eta_G V_f}{1 - \eta_G V_f}, \quad \eta_G = \frac{(G_f/G_m) - 1}{(G_f/G_m) + \xi}$$

$$G_{23} = \frac{1}{\frac{V_f}{G_f} + \frac{1 - V_f}{G_m}}$$

■ **Poisson's ratios (mixture rules):**

$$\nu_{12} = \nu_f V_f + \nu_m (1 - V_f), \quad \nu_{23} = \nu_m$$

■ **Density (volume average):**

$$\rho = \rho_f V_f + \rho_m (1 - V_f)$$

### 4. Computed Equivalent Properties

The resulting orthotropic constants of the impregnated yarn are summarized in Table 3.9. These equivalent properties were used as material inputs for mesoscale modeling within *ANSYS Material Designer*.

**TABLE 3.9** – Equivalent orthotropic properties of impregnated yarn ( $V_f = 0.55$ ).

Property (unit)	Symbol	Value
Longitudinal modulus (GPa)	$E_1$	6.561
Transverse moduli (GPa)	$E_2 = E_3$	6.096
In-plane shear moduli (GPa)	$G_{12} = G_{13}$	2.305
Out-of-plane shear modulus (GPa)	$G_{23}$	2.069
Poisson's ratio (–)	$\nu_{12} = \nu_{13}$	0.323
	$\nu_{23}$	0.350
Density (kg/m <sup>3</sup> )	$\rho$	1303.0

## 5. Finite Element Homogenization Procedure

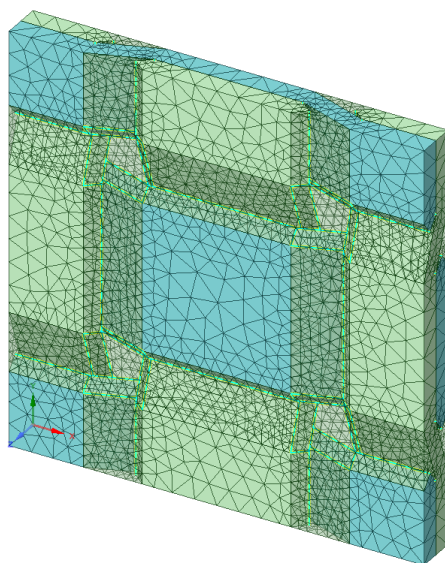
The woven composite homogenization was conducted using the built-in Woven Composite RVE (Representative Volume Element) model in *ANSYS Material Designer*. The step-by-step methodology is outlined below.

- i. **RVE Generation:** The RVE geometry was automatically generated based on the fabric architecture and the equivalent yarn properties (Table 3.10). A plain weave (1/1) configuration was assumed, with warp yarns aligned along the X-axis.

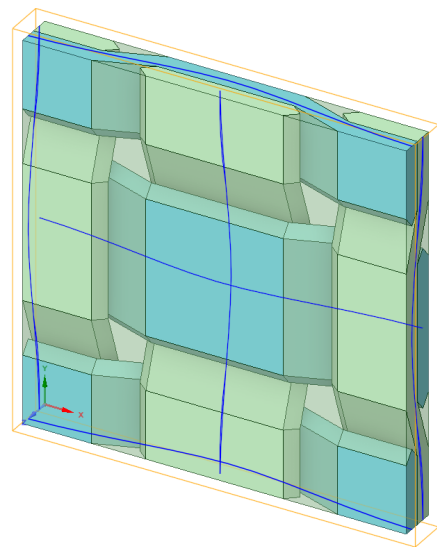
**TABLE 3.10** – Input parameters for woven composite RVE in *ANSYS Material Designer*.

Parameter	Symbol	Value	Unit	Description
Weaving type	–	Plain	–	1/1 pattern
Fiber volume fraction	$V_f$	0.43	–	Total fiber content
Yarn fiber volume fraction	$V_{f,y}$	0.55	–	Fiber content within yarn
Yarn spacing	$s_y$	5	mm	Center-to-center distance
Fabric thickness	$t_f$	1	mm	Single woven layer thickness
Shear angle	$\gamma$	0	°	No draping
Algorithm	–	Simplified	–	Default geometry generator
Repeat count	–	1	–	Single periodic unit cell
Alignment	–	X-direction	–	Warp yarn orientation

- ii. **Meshing:** Conformal tetrahedral meshing was used to ensure compatibility between yarn and matrix interfaces. Two mesh densities were evaluated to check for mesh sensitivity effects.



(a) Woven composite mesh.



(b) Woven composite RVE geometry.

**FIGURE 3.15** – Numerical model setup for woven composite homogenization.

- iii. **Boundary Conditions:** Periodic Boundary Conditions (PBCs) were applied to ensure displacement and traction continuity across opposing faces of the RVE.
- iv. **Loading Scenarios:** Six independent unit strain states—three normal and three shear—were applied to compute the effective stiffness tensor  $\mathbf{C}^{\text{eff}}$ .
- v. **Postprocessing:** Volume-averaged stress components were extracted and used to construct the stiffness matrix, which was subsequently inverted to obtain the compliance matrix. The homogenized engineering constants are summarized in Table 3.11. Results from both mesh configurations showed negligible variation, confirming mesh independence.

**TABLE 3.11** – Homogenization results for woven composite under different mesh densities.

Property	Mesh 1	Mesh 2
$E_x$ (GPa)	5.694	5.694
$E_y$ (GPa)	5.694	5.694
$E_z$ (GPa)	5.499	5.499
$G_{xy}$ (GPa)	2.052	2.052
$G_{yz}$ (GPa)	1.977	1.977
$G_{zx}$ (GPa)	1.977	1.977
$\nu_{xy}$ (–)	0.317	0.317
$\nu_{xz}$ (–)	0.340	0.340
$\nu_{yz}$ (–)	0.340	0.340
Density (kg/m <sup>3</sup> )	1270.778	1270.778
Max element size (mm)	3	2

### 3.3.4 Gyroid Characterization

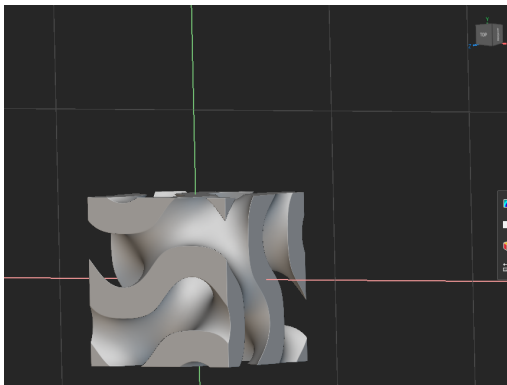
The gyroid core was characterized using a finite element-based homogenization approach implemented in *nTopology* to determine the effective elastic properties of an ABS-based triply periodic minimal surface (TPMS) gyroid structure. The process followed the same methodology introduced earlier for the woven composite, adapted to capture the periodic geometry of the gyroid cell.

#### 1. Modeling Parameters

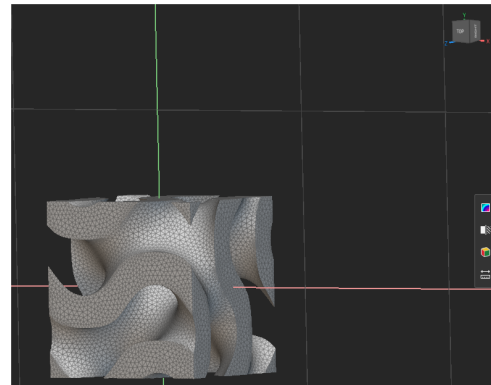
The gyroid RVE model was constructed and analyzed based on the parameters summarized in Table 3.12. The geometry comprised multiple gyroid unit cells arranged periodically to ensure representative behavior under homogenization.

**TABLE 3.12** – Modeling parameters used for gyroid core homogenization.

Parameter	Value / Description
Cell geometry	TPMS Gyroid
RVE block size	$5 \times 5 \times 4$ unit cells
Surface thickness	1.2 mm
Mesh type	Quadratic ( $2^{\text{nd}}$ -order) tetrahedral elements
Mesh refinement	Multiple levels tested until convergence of $E_z$
Boundary conditions	Periodic Boundary Conditions (PBCs)
Material model	Isotropic ABS
Young's modulus, $E$ (GPa)	1.56
Poisson's ratio, $\nu$	0.35
Homogenization method	FE-based with six independent load cases



**(a)** Gyroid RVE geometry.



**(b)** Gyroid mesh ( $2^{\text{nd}}$ -order elements).

**FIGURE 3.16** – Finite element setup for gyroid core homogenization.

## 2. Mesh Convergence Study

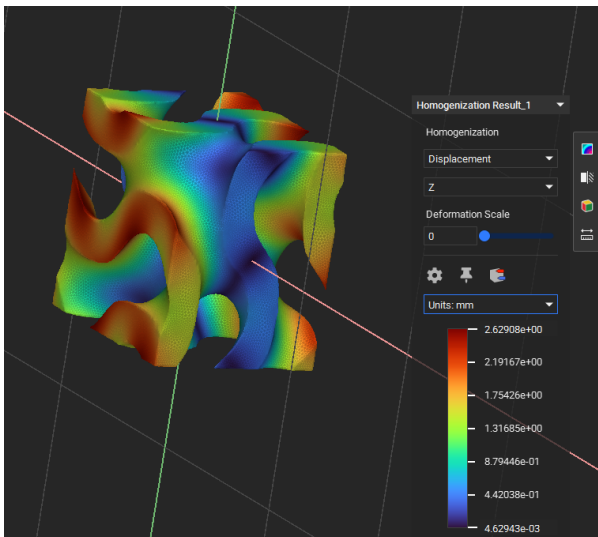
A mesh sensitivity study was performed by refining the finite element mesh until the computed effective modulus along the  $z$ -direction ( $E_z$ ) reached numerical convergence. Table 3.13 summarizes the results, demonstrating negligible change beyond approximately 600,000 elements.

**TABLE 3.13** – Mesh convergence study for gyroid core homogenization.

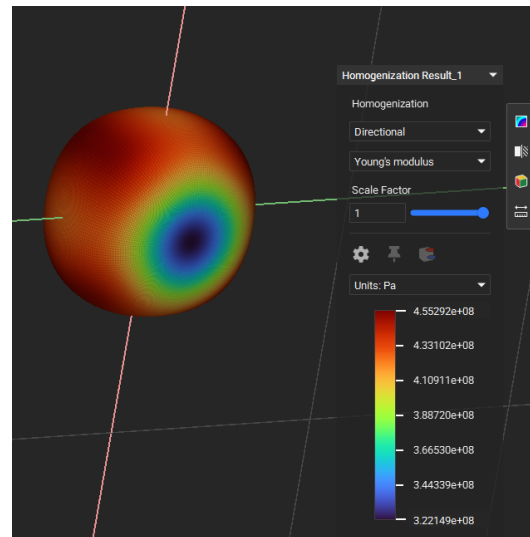
Mesh ID	Element Count	$E_z$ (GPa)
Mesh 1	24,376	0.325
Mesh 2	57,005	0.324
Mesh 3	601,899	0.322
Mesh 4	619,264	0.322

## 3. Homogenized Material Properties

The homogenized elastic constants obtained from the converged mesh are summarized in Table 3.14.



(a) Displacement contours along  $z$ -axis.



(b) Directional modulus distribution.

**FIGURE 3.17** – Representative homogenization results for the gyroid core.

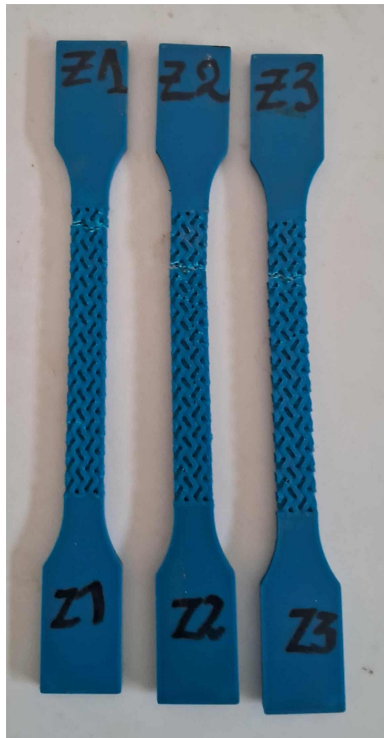
From Table 3.14, the homogenized results reveal that the gyroid core exhibits nearly identical elastic behavior along the in-plane directions, with  $E_x = E_y = 423.5$  MPa, while the out-of-plane modulus is notably lower at  $E_z = 322.2$  MPa. This reduction of approximately 24% reflects the intrinsic anisotropy of the gyroid architecture, as it arises from the geometry of the unit cell, which has a smaller dimension along the  $z$ -axis.

**TABLE 3.14** – Homogenized elastic properties of the ABS gyroid structure.

Property	Value
$E_x, E_y$ (MPa)	423.5
$E_z$ (MPa)	322.2
$G_{xy}$ (MPa)	180.7
$G_{xz}, G_{yz}$ (MPa)	165.6
$\nu_{xy}$ (–)	0.302
$\nu_{xz}, \nu_{yz}$ (–)	0.353
$\rho$ (kg m <sup>-3</sup> )	526.0

Furthermore, the displacement field visualization (Fig. 3.17a) confirms this behavior: minimal displacements occur in the core region, while larger deformations develop toward the outer cell boundaries. This gradient highlights the gyroid’s intrinsic potential for energy dissipation and shock absorption.

To validate the numerical predictions, uniaxial tensile tests were conducted on gyroid specimens along the  $z$ -direction. The specimen geometry was adapted from the ISO 527-2 standard for thermoplastics such as ABS, maintaining equivalent gripping and boundary dimensions. The effective gauge length ( $L_0$ ) was filled with an even number of gyroid unit cells to preserve periodicity and ensure representative behavior.

**FIGURE 3.18** – Gyroid tensile test specimens oriented along the  $z$ -axis.

The experimental tensile results, summarized in Table 3.15, indicate a brittle fracture behavior. The measured average Young’s modulus ( $E_z = 0.29$  GPa) is in close agreement (within 10%) with the numerically predicted value ( $E_z = 0.32$  GPa), confirming the accuracy of the FE-based



homogenization approach. This correspondence validates that the numerical model reliably captures the mechanical response of the gyroid structure. The observed brittle failure mode is consistent with the material's low cross-sectional connectivity along the  $z$ -axis, as predicted by the anisotropic stiffness distribution.

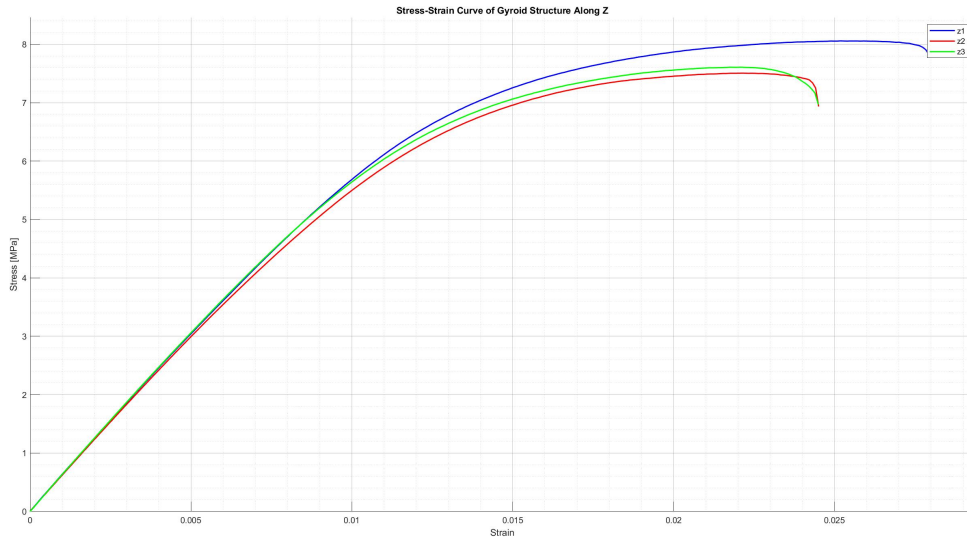


**FIGURE 3.19** – Experimental stress–strain curves for gyroid specimens along the  $z$ -direction.

**TABLE 3.15** – Experimental tensile test results for gyroid specimens along the  $z$ -direction.

Sample	$E_z$ (GPa)	$\sigma_{\max}$ (MPa)	$\sigma_b$ (MPa)
1	0.31	8.06	7.82
2	0.28	7.51	6.93
3	0.28	7.61	6.97
<b>Mean</b>	<b>0.29</b>	<b>7.72</b>	<b>7.24</b>

### 3.3 Full Sandwich Structure

The full sandwich structure comprising two woven composite skins and a central ABS gyroid core was homogenized using *ANSYS Mechanical*. A sequential multiscale strategy was followed, combining the previously homogenized properties of the woven skins and gyroid core.

#### 1. Modeling Configuration

A representative three-layer RVE was built, consisting of:

- Top woven composite skin: 1 mm
- Gyroid core: 3 mm
- Bottom woven composite skin: 1 mm

Each layer was assigned its respective homogenized orthotropic or transversely isotropic material properties. Perfect bonding was assumed at the interfaces. The total sandwich thickness was thus 5 mm, consistent with the physical configuration.

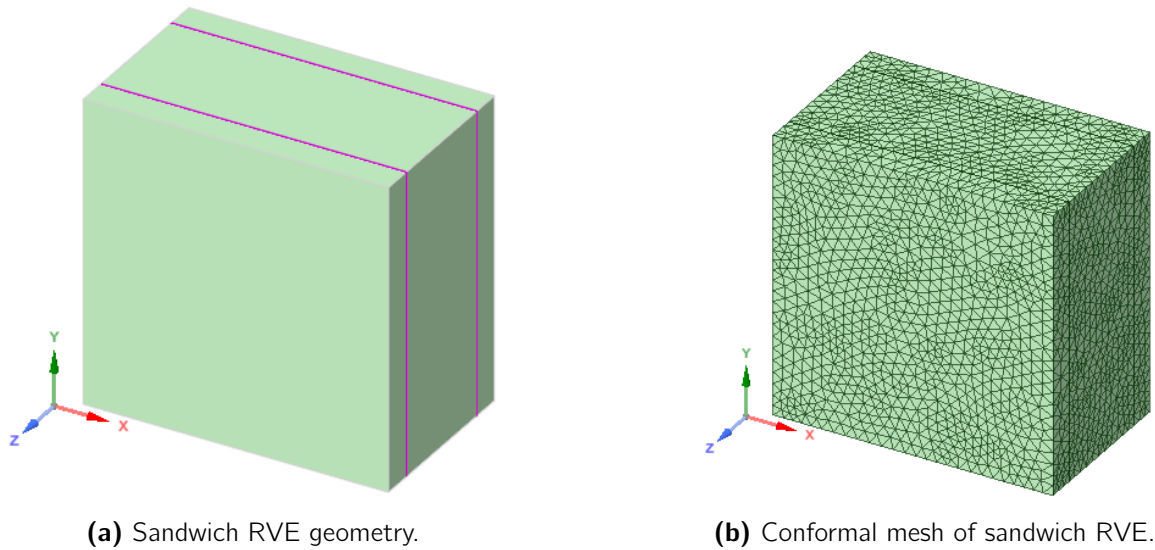


**FIGURE 3.20** – Finite element model of the sandwich structure used for homogenization.

## 2. Homogenization and Mesh Convergence

The built-in periodic homogenization tool in *ANSYS Material Designer* was used to derive the overall sandwich elastic properties. Two mesh densities (0.7 mm and 0.45 mm) were analyzed to confirm numerical stability, with results summarized in Table 3.16.

**TABLE 3.16** – Homogenized properties of the full sandwich structure.

Property	Mesh 1 (0.7 mm)	Mesh 2 (0.45 mm)
$E_x$ (GPa)	2.18	2.18
$E_y$ (GPa)	2.18	2.18
$E_z$ (GPa)	0.585	0.585
$G_{xy}$ (GPa)	0.805	0.805
$G_{yz} = G_{zx}$ (GPa)	0.238	0.238
$\nu_{xy}$ (-)	0.315	0.315
$\nu_{xz} = \nu_{yz}$ (-)	0.345	0.345
Density (kg/m <sup>3</sup> )	774.26	774.26

For comparative analysis, the stiffness-to-weight ratio—defined as the ratio of Young’s modulus to density—was evaluated to assess the mechanical efficiency of the developed material relative to conventional 3D-printed PLA at 100% infill. Considering the orthotropic behavior of the sandwich structure, the modulus used in the comparison corresponds to the  $E_x$  direction, which represents the principal loading direction under wind action.

Reported literature values for fully dense PLA show Young's modulus ranging from 1538 MPa to 2645 MPa and a density of approximately  $1240 \text{ kg/m}^3$  [70], leading to stiffness-to-weight ratios between  $1.24$  and  $2.13 \text{ MPa}\cdot\text{m}^3/\text{kg}$ . In contrast, the developed sandwich material exhibits a modulus of 2180 MPa along the  $x$ -direction and a significantly lower density of  $774.26 \text{ kg/m}^3$ , yielding a stiffness-to-weight ratio of approximately  $2.82 \text{ MPa}\cdot\text{m}^3/\text{kg}$ .

**TABLE 3.17** – Comparison of stiffness-to-weight ratio for different materials.

Material	Young's Modulus (MPa)	Density ( $\text{kg/m}^3$ )	Stiffness-to-Weight Ratio ( $\text{MPa}\cdot\text{m}^3/\text{kg}$ )
3D Printed PLA (Low)	1538	1240	1.24
3D Printed PLA (High)	2645	1240	2.13
<b>Bio-Composite (This Work)</b>	<b>2180</b>	<b>774.26</b>	<b>2.82</b>

The comparison highlights a substantial enhancement in structural efficiency, with an improvement of approximately 32% relative to the upper stiffness-to-weight ratio of fully dense PLA, and over 120% when compared to the lower bound. This improvement directly reflects the optimized combination of the lightweight gyroid core and the bio-based composite skins, which enable superior stiffness while significantly reducing mass.

Beyond stiffness, the developed bio-sourced sandwich material offers additional functional advantages over PLA. Polylactic acid is known to exhibit limited resistance to cyclic loading and is sensitive to elevated temperatures and moisture, leading to degradation in mechanical properties under long-term environmental exposure. In contrast, the hybrid composite architecture—consisting of a bio-reinforced skin and an architected core—offers improved dimensional stability and mechanical retention under cyclic and humid conditions, thus providing greater durability for small-scale wind turbine applications.

Overall, the obtained results demonstrate that the proposed material system achieves a higher stiffness-to-weight efficiency than conventional 3D-printed polymers, while maintaining low density and enhanced environmental resilience, making it a promising candidate for lightweight rotating energy structures.

# Rotor Response and Performance Analysis

...

## Overview



This chapter details the integrated experimental and numerical methodology for evaluating the hybrid Savonius rotor's performance. The work is organized as follows:

- **Experimental Methods:** Comprehensive description of wind tunnel testing, including facility specifications, instrumentation (Pitot tube, digital manometer, tachometer, multimeter), test procedures, and uncertainty analysis.
- **Numerical Validation:** Stepwise CFD validation approach progressing through:
  - 2D conventional rotor (Blackwell et al.)
  - 3D conventional rotor (scaled Blackwell)
  - 3D helical rotor (Kamoji et al.)
- **Fluid-Structure Interaction:** One-way FSI setup using validated pressure fields to predict structural deformations and stresses in the rotor assembly.

## 4.1 Experimental Methods

This section outlines the methodology adopted to evaluate the aerodynamic performance of the rotor. All experiments were conducted in the Hydraulic Laboratory's closed-circuit wind tunnel at ENP. The specialized instrumentation employed, along with the fundamental operating principles of each device, are presented below. The section concludes with a description of the data correction procedures implemented during the measurement campaign.

### 4.1.1 Wind Tunnel Description

The National Polytechnic School of Algiers is equipped with a low-speed, closed-circuit wind tunnel [18], featuring:

- A closed test section measuring **900 × 700 mm**,
- A **single-return loop**,
- A maximum airspeed of **15.74 m/s (Mach 0.0458)**, subsonic).

A settling chamber with a honeycomb flow straightener ensures uniform airflow in the test section, allowing for precise aerodynamic measurements in both research and educational projects.

To better understand the internal structure and airflow, the schematic representation of the tunnel is presented in Figure 4.1.



**FIGURE 4.1** – Closed-circuit wind tunnel at the National Polytechnic School of Algiers.<sup>1</sup>

<sup>1</sup>Source: Adapted from the PFE by M. C. Boudehane, *Étude numérique et expérimentale de l'écoulement à travers une soufflerie à circuit fermé. Étude de cas: soufflerie de l'ENP.*

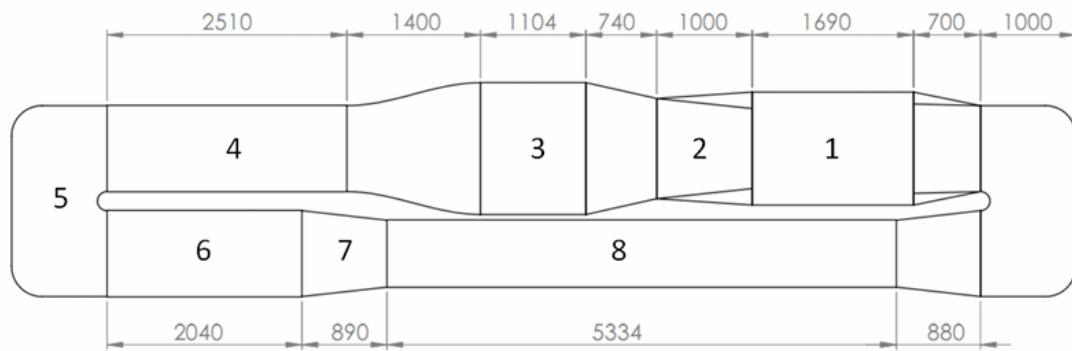


**FIGURE 4.2** – Schematic diagram of the ENP closed-circuit wind tunnel (adapted from [18]).

Each component in the schematic plays a specific aerodynamic role:

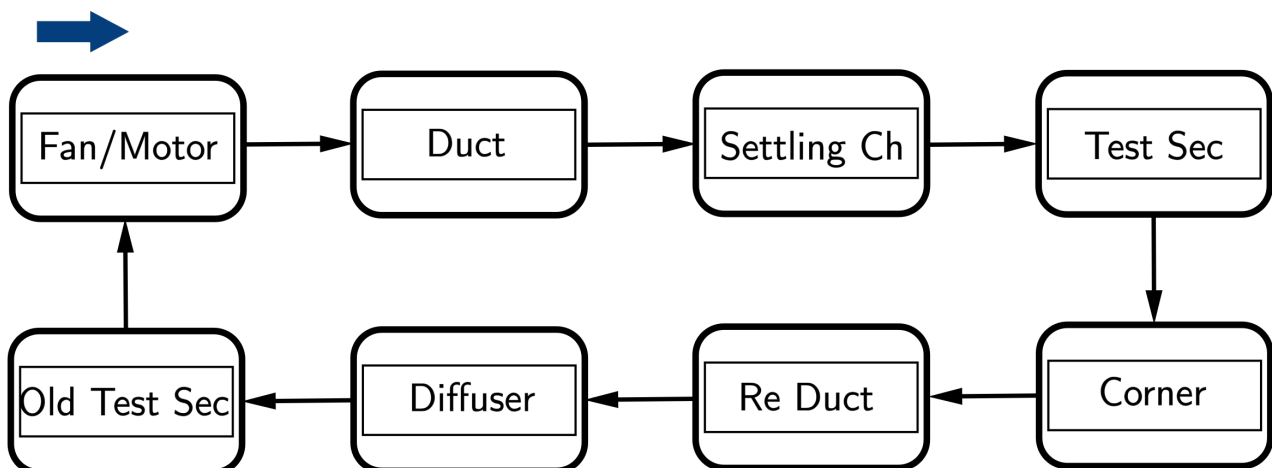


**FIGURE 4.3** – The airflow through the wind tunnel

## Logical Airflow Path in the Wind Tunnel

### 1. Motor Cylinder [1]:

*Start Point:* The fan (or blower) driven by a motor pushes air into the system, creating airflow.

### 2. Duct [2]:

The air passes through a duct that transitions from the round motor cylinder to the rectangular section. This helps reduce pressure losses and directs airflow smoothly into the next section.

### 3. Settling Chamber [3]:

The airflow enters the settling chamber, which usually contains honeycomb and screens to straighten and smoothen the flow, removing turbulence.

**4. Test Section [4]:**

*Main Experiment Zone:* This is where the model (e.g., wind turbine rotor) is placed. Here, the flow is as uniform as possible for accurate measurements.

**5. Corner Turning Vanes [5]:**

After the test section, the air hits the first major corner. Turning vanes guide the flow smoothly around the bend to reduce pressure loss and keep the flow attached.

**6. Return Duct [6]:**

The air continues along the long return duct to the other side of the wind tunnel, maintaining flow direction and energy.

**7. Nozzle/Diffuser [7]:**

The diffuser slows down the air and recovers pressure, while the nozzle re-accelerates and re-straightens the airflow before it re-enters the settling chamber.

**8. Old Test Section [8]:**

In this specific wind tunnel, this section is used as part of the closed-loop to help complete the circuit and maintain continuity.

### 4.1.2 Wind Tunnel Drive System

Airflow in the wind tunnel is generated by a large axial fan directly coupled to an electric motor (see Fig. 4.4). The motor operates on a 380 V AC supply and transmits power to the fan shaft for efficient airflow generation. The assembly is illustrated in Figure 4.4, adapted from Boudhane's PFE [18].



**FIGURE 4.4** – Electric motor and axial fan assembly (adapted from [18]).

The rotational speed of the fan, and thus the airflow velocity in the test section, is precisely regulated by a Variable Frequency Drive (VFD) housed within the main control panel (Fig. 4.5). The VFD enables smooth adjustment of the motor's speed by varying the supply frequency, allowing for stable and repeatable test conditions.



**FIGURE 4.5** – Main control panel with integrated Variable Frequency Drive (VFD) for fan speed regulation.

Operator commands and status feedback are managed through the VFD's digital interface (see Fig. 4.6), which displays key parameters such as operating frequency, current, and system status.



**FIGURE 4.6** – VFD digital interface for controlling and monitoring the fan motor.

The fan speed is controlled via a Variable Frequency Drive (VFD), which adjusts the AC supply frequency to the motor, enabling wind speeds from 0 to 15.7 m/s. The operator selects the desired frequency and monitors key parameters (Hz, current) on the digital interface panel.

### 4.1.3 Instrumentation in the Wind Tunnel

Accurate measurement of airflow is fundamental for wind tunnel experiments. The ENP tunnel is equipped with:

1. **Pitot Tube with KIMO MP200 Digital Manometer**

Air velocity is measured by a stainless steel Pitot tube connected to a **KIMO MP200** digital manometer (see Fig. 4.7 and Fig. 4.8).

The MP200, configured with its differential pressure module, calculates the airspeed from the dynamic pressure measured between the Pitot tube's total and static ports. The



relevant equations are:

$$\Delta P = P_{\text{tot}} - P_{\text{stat}} \quad (4.1)$$

$$u = \sqrt{\frac{2\Delta P}{\rho}} \quad (4.2)$$

where  $\Delta P$  is the pressure difference (Pa) and  $\rho$  is the air density ( $\text{kg/m}^3$ ).

- **Operating range:** 2–100 m/s air velocity, with accuracy  $\pm 0.2$  m/s (per manufacturer manual<sup>2</sup>).

*Note:* The MP200 is a digital manometer, not an anemometer. When used with a Pitot tube, it functions as a complete airspeed measurement system.

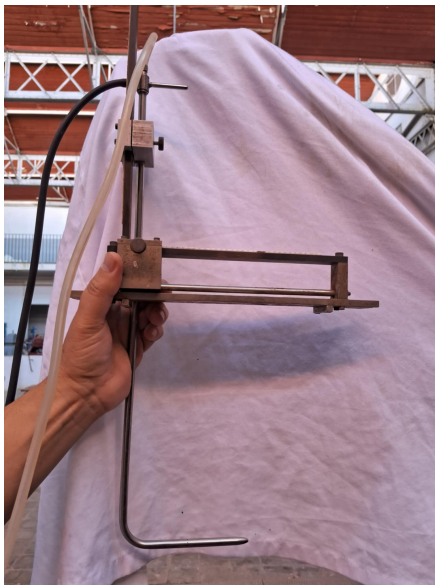


**FIGURE 4.7** – Pitot tube for airspeed measurement.



**FIGURE 4.8** – KIMO MP200 digital manometer.

## 2. Contact/Non-Contact Tachometer (AMPROBE TACH-10)

The rotor's angular speed is measured using an **AMPROBE TACH-10** digital tachometer, which supports both contact and non-contact measurement modes (see Fig. 4.9).

- **Contact mode:** The supplied tip is pressed directly against the rotor shaft, and the device reads rotational speed (RPM) or surface speed (m/min, ft/min).
- **Non-contact mode:** A reflective tape is affixed to the rotating component, and the tachometer optically detects the passage of the tape to measure RPM, at a distance of 5–30 cm.
- **Measurement range:** 10–99,999 RPM (non-contact); 10–19,999 RPM (contact).
- **Surface speed:** 1.000–9,999.9 m/min (contact mode).
- **Accuracy:**  $\pm 0.1\%$  of reading +2 digits.

<sup>2</sup>KIMO MP200 User Manual, Sentronic AG, 2020.

This versatility allows for reliable measurements regardless of the rotor configuration. For further details, see the user manual.<sup>3</sup>



**FIGURE 4.9** – AMPROBE TACH-10 contact/non-contact digital tachometer.

### 3. Voltage and current measurement instrument

A single **CROWN CT44052 digital multimeter** was used to measure both the voltage and current generated by the Savonius rotor. The measurements were taken separately by configuring the multimeter as:

- A **voltmeter**, connected in parallel with the generator terminals to measure the output voltage.
- An **ammeter**, connected in series with the load to measure the generated current.

Each quantity was recorded independently to ensure accurate readings under identical test conditions.



**FIGURE 4.10** – CROWN CT44052 digital multimeter used for voltage and current measurements.

<sup>3</sup>Amprobe Test Tools, *TACH-10 Contact/Non-Contact Tachometer, User Manual*, Rev. 1, 2010.

#### 4.1.4 Generator selection criteria

Generator sizing was based on experimentally measured power-coefficient ( $C_p$ ) data from Kamoji et al. (2009) for **Configuration 2**, which shares geometric similarity with the present rotor design, differing only in scale.

The rated power was calculated at a wind speed of 4 m/s, corresponding to a data point in the referenced study with  $C_{p,\max} = 0.11$ .

$$C_p = \frac{P_{\text{rated}}}{P_{\text{wind}}} \quad (4.3)$$

$$P_{\text{rated}} = C_p P_{\text{wind}} \quad (4.4)$$

N.A:

$$P_{\text{rated}} = 0.11 \times 0.5 \times 0.15 \times 0.132 \times 4^3 = 0.776 \text{ W.}$$

Therefore, the estimated rated power is approximately 0.78 W. For availability we've selected a dynamo of a bicycle of rated power of 3W.



**FIGURE 4.11** – Bicycle dynamo (3 W) selected for power generation

#### 4.1.5 Calculating Measurement Uncertainty

Experimental measurements always have uncertainty. When these measurements appear in calculations, their uncertainties propagate to the final result. For a function  $y = f(x_1, x_2, \dots, x_n)$ , the rule for combining the uncertainties  $\Delta x_1, \Delta x_2, \dots$  depends on the operation. The main rules are:

- **Addition/Subtraction:** Absolute uncertainties add.
- **Multiplication/Division:** Relative uncertainties add.
- **Powers:** The exponent multiplies the relative uncertainty.

The general rules are summarized below for quick reference.

**TABLE 4.1** – Summary of uncertainty rules.

Operation	Formula	Uncertainty rule
Addition / Subtraction	$y = x_1 \pm x_2 \pm \dots$	$\Delta y = \Delta x_1 + \Delta x_2 + \dots$
Multiplication / Division	$y = \frac{x_1 x_2 \dots}{x_3 x_4 \dots}$	$\frac{\Delta y}{ y } = \frac{\Delta x_1}{ x_1 } + \frac{\Delta x_2}{ x_2 } + \dots$
Power	$y = x^\alpha$	$\frac{\Delta y}{ y } =  \alpha  \frac{\Delta x}{ x }$
General power law	$y = x_1^\alpha x_2^\beta \dots$	$\frac{\Delta y}{ y } =  \alpha  \frac{\Delta x_1}{ x_1 } +  \beta  \frac{\Delta x_2}{ x_2 } + \dots$

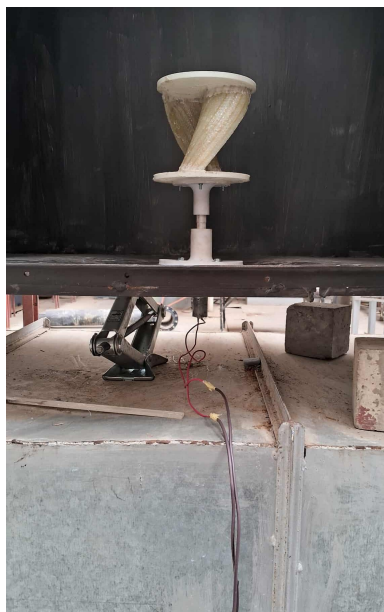
### 4.1.6 Test Procedure

The Pitot tube was installed in the wind-tunnel roof and its pressure lines were connected to the digital manometer prior to mounting the rotor; the manometer directly provided the wind velocity used for each test condition.

The assembled Savonius rotor was placed in the test section. The lower housing was then secured to the test-section floor and the pre-assembled shaft remained in place; the coupling between the turbine shaft and the generator shaft was attached.

A reflective sticker was affixed to the coupling located outside the test section for rotational-speed measurement.

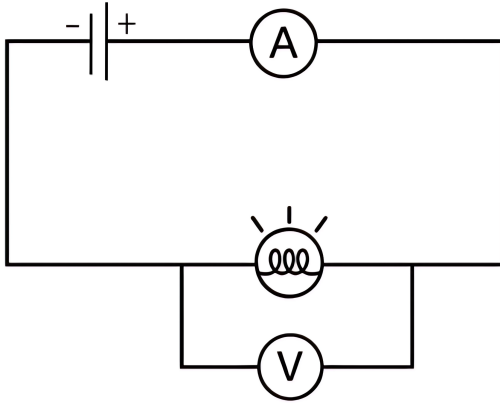
The generator outputs were connected to the measurement instruments. After closing the test-section door, the axial fan was started and the wind speed adjusted with the variable-frequency drive to obtain wind speeds in the 2–8 m/s range. For each test speed, steady-state readings of voltage, current, RPM and the manometer-displayed wind velocity were recorded.

**FIGURE 4.12** – Rotor assembly mounted

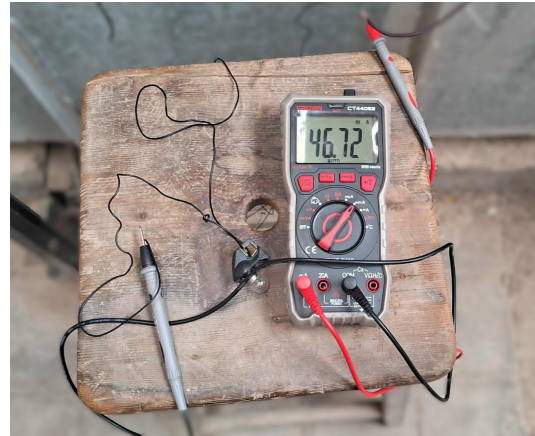
The generator electrical output was connected to a simple load circuit and instrumented for voltage and current measurements. The wiring arrangement used in the tests is shown schematically

in Figure 4.13 and was implemented as follows:

- The voltmeter was connected *in parallel* with the generator terminals to measure the open/load voltage across the generator.
- The ammeter was placed *in series* with the external resistive load so that the current flowing from the generator through the load passed through the meter.
- The load resistor which is a small lamp was connected between the ammeter output and the generator return to complete the circuit.



(a) Schematic representation of the electrical circuit.



(b) Experimental setup with multimeter connection.

**FIGURE 4.13** – Circuit setup used for electrical measurements during testing.

## 4.2 Numerical Setup and Methodology

This section outlines the systematic approach adopted to develop and validate the computational methodology used for analyzing the novel hybrid Savonius rotor.

A stepwise validation strategy was employed to build confidence in the numerical tools incrementally—progressing from simple canonical configurations to the final complex geometry involving fluid–structure interactions.

The computational framework follows four sequential stages:

- **2D Conventional Rotor Validation:** Establish fundamental CFD methodology using Blackwell et al. (1978) in a computationally efficient 2D framework.
- **3D Conventional Rotor Validation:** Extend the methodology to three dimensions using a scaled Blackwell configuration.
- **3D Helical Rotor Validation:** Apply the methodology to Kamoji et al. (2009) helical configuration, which shares geometric similarities with our hybrid design.
- **One-Way Fluid-Structure Interaction (FSI):** Utilize validated aerodynamic loads in ANSYS Workbench 2023 to predict structural deformations and investigate fluid-structure interactions.

### 4.2.1 2D Validation Case Setup

#### 1. Geometry and Parameters for C-S Rotor

The geometry used in the 2-D simulation was reconstructed to replicate the rotor cross-section reported by Blackwell *et al.* [6]. The main geometric parameters are summarized in Table 4.2, and the corresponding cross-sectional shape is shown in Figure 4.14.

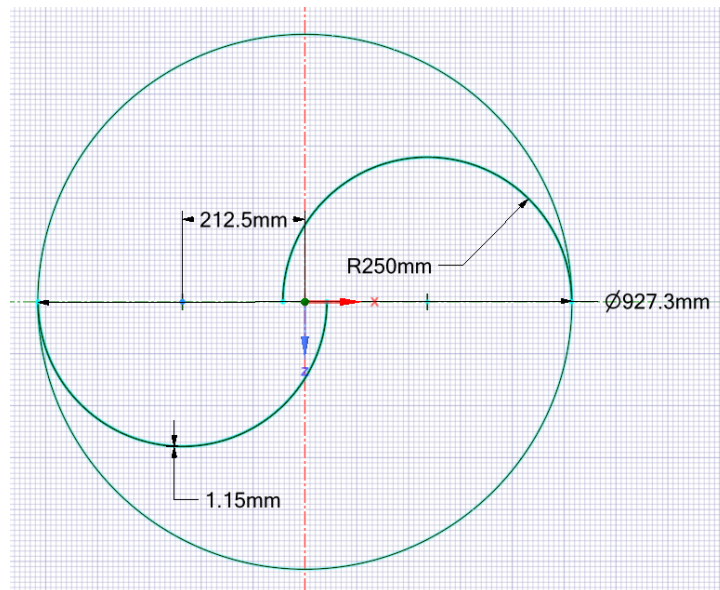


**FIGURE 4.14** – Savonius rotor cross-section.

In their study, several configurations were investigated. For the present validation, **configuration 16** was selected, which corresponds to a Reynolds number of  $4.32 \times 10^5$  based on the rotor diameter and freestream velocity.

**TABLE 4.2** – Geometric parameters of the Savonius rotor used for 2-D validation (adapted from [6]).

Parameter	Value
Number of blades	2
Rotor diameter ( $D$ )	927.3 mm
Rotor height ( $H$ )	1000.0 mm
Bucket diameter ( $d$ )	500.0 mm
Gap ( $s$ )	75.0 mm
Overlap ratio ( $s/d$ )	0.15
Blade thickness ( $t$ )	1.15 mm
Aspect ratio ( $H/D$ )	1.0783

## 2. Computational domain and boundary conditions

The computational domain was designed to replicate the setup used by Tian *et al.* [19], and is subdivided into three regions: the fixed domain, the body-of-influence (Bol), and the rotating domain.

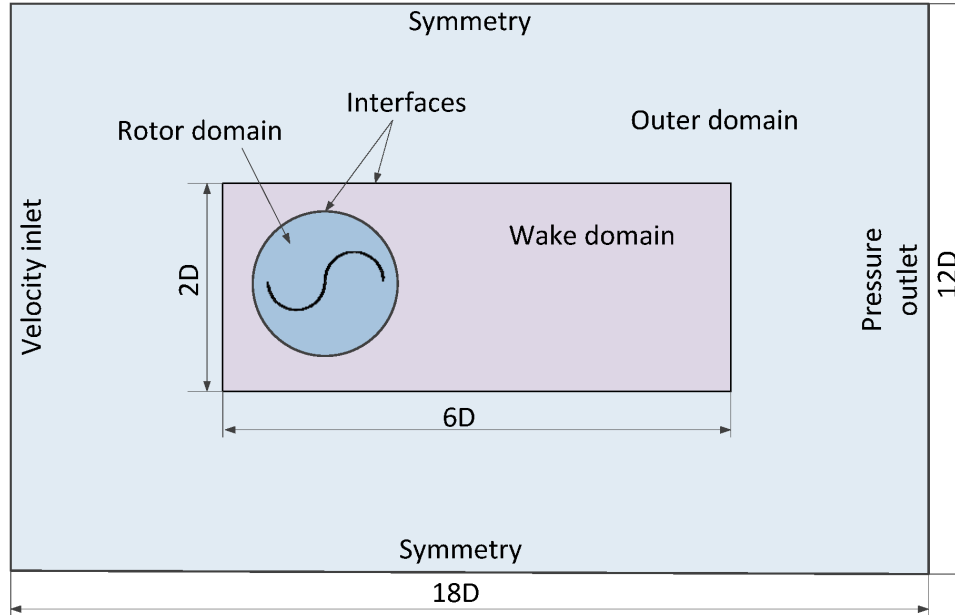


**FIGURE 4.15** – Computational domain layout for 2D simulations (adapted from [19]).

The domain dimensions and functions of each subdomain are summarized in Table 4.3.



**TABLE 4.3** – Computational domain geometry specifications.

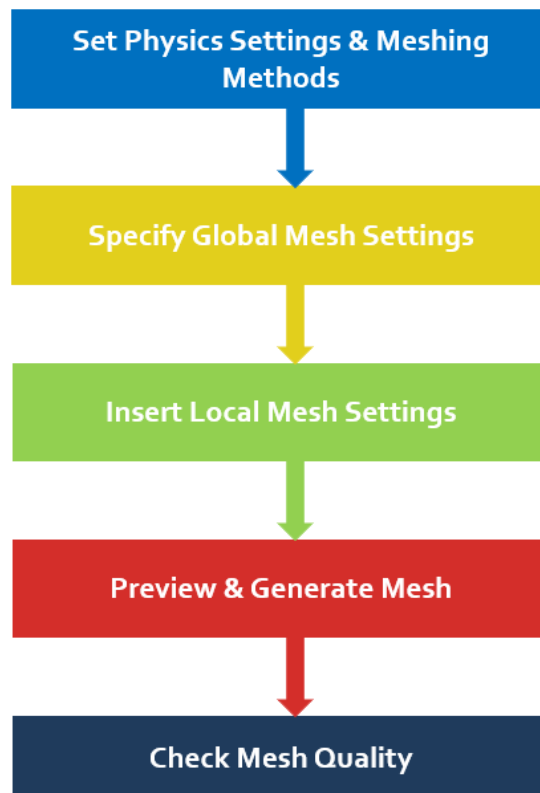
Domain zone	Size (D)	Boundary condition	Purpose
Rotor domain	Diameter = 1.25 D	Rotating wall (sliding mesh)	Contains the rotating turbine.
Wake domain (BoI)	6 D × 2 D	Interface (body of influence)	Captures the developing wake; enables mesh refinement.
Fixed domain	Inlet/Outlet = 12 D; Side = 18 D	Inlet – velocity; Outlet – pressure; Sides – symmetry	Represents the far-field flow and minimises boundary effects.

### 3. Mesh Generation

Mesh generation divides surfaces and volumes into discrete cells to solve the governing equations numerically and obtain results relevant to the type of study being performed. A good mesh should match the geometry well, use quality elements, and not be too dense to avoid long computation times. It should also be refined in key areas where more detail is needed.

For both 2D and 3D simulations in our CFD study, the mesh was generated using a structured and unstructured meshing strategy following the sequential steps illustrated below.

The first step is to set the physics for our case, which is CFD, and to select global mesh sizing and defeaturing.

**FIGURE 4.16** – Mesh generation steps



Local mesh settings can be applied from the **Mesh Control** dropdown menu. These settings allow for precise control over specific parts of the mesh. Local mesh settings (Mesh Control dropdown):

- **Inflation:** 20 prism layers in 2D (growth rate 1.2); first-layer height set from target  $y^+$  of 0.6 (2D) and 0.8 (3D) using  $U = 7$  m/s,  $Re = 4.32 \times 10^5$ .
- **Sizing:** edge/face/body sizing on blades, end plates and wake regions.
- **Bol:** body of influence zones for local refinement.

**Example: First-Layer Height Calculation** The SST  $k-\omega$  turbulence model requires a sufficiently fine mesh near the wall to resolve the viscous sublayer. This is ensured by maintaining a non-dimensional wall distance  $y^+ < 1$ . This calculation finds the first cell height  $y$  for the target  $y^+$ .

$$y^+ = \frac{u_\tau y}{\nu}, \quad (4.5a)$$

$$u_\tau = U \sqrt{\frac{C_f}{2}}, \quad (4.5b)$$

$$C_f = 0.0576 Re^{-1/5}, \quad (4.5c)$$

With  $U = 7$  m/s,  $D = 0.9273$  m, and  $\nu = 1.5 \times 10^{-5}$  m<sup>2</sup>/s, we get

$$Re = 4.33 \times 10^5, \quad C_f = 4.30 \times 10^{-3}, \quad u_\tau = 0.324 \text{ m/s}.$$

$$y = \frac{y^+ \nu}{u_\tau} = 2.8 \times 10^{-5} \text{ m}.$$

For the final step in meshing it's crucial to check element quality so the solution is accurate and, most importantly, does not diverge during runtime. The mesh was checked against standard quality metrics before simulation. In Table 4.4, the metrics are listed together with their ranges and target values.

**TABLE 4.4** – Mesh quality metrics and target values used for mesh acceptance.

Metric	Range	Ideal / Target
Element quality	0 to 1	1
Aspect ratio	0 to $\infty$	1
Jacobian ratio	-1 to 1	0
Parallel deviation	0 to 180°	0°
Skewness	0 to 1	0
Orthogonal quality	0 to 1	1
Warping factor	(problem-specific)	1
Maximum corner angle	—	60° (tri), 90° (quad)

The final 2-D mesh after all local refinement and inflation controls is shown in Figure 4.17.

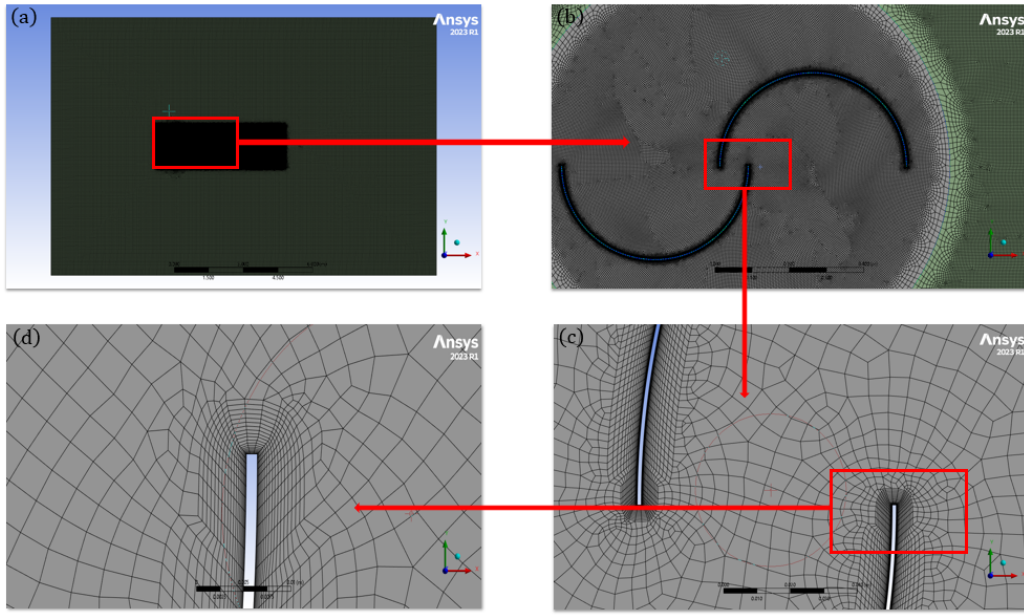


**FIGURE 4.17** – Refined 2D mesh after applying the meshing strategy

## 4. Solver Configuration

Solving the transient, incompressible flow around the Savonius rotor requires resolving four unknowns: the three velocity components  $u_x, u_y, u_z$  and pressure  $p$  governed by the Navier-Stokes momentum equations and the continuity constraint:

$$\frac{\partial \mathbf{U}}{\partial t} + (\mathbf{U} \cdot \nabla) \mathbf{U} = -\frac{1}{\rho} \nabla p + \nu \nabla^2 \mathbf{U}, \quad (4.6a)$$

$$\nabla \cdot \mathbf{U} = 0. \quad (4.6b)$$

1. **Solve Momentum Equations:** Using a pressure field guess  $p^*$ , solve the discretized momentum equation:

$$A \mathbf{U}^* = -\nabla p^* + b.$$

This gives a velocity field  $\mathbf{U}^*$  that satisfies momentum but not mass continuity ( $\nabla \cdot \mathbf{U}^* \neq 0$ ).

2. **Solve for Pressure Correction  $p'$ :** The pressure correction  $p'$  is calculated by solving the Pressure-Poisson equation:

$$\nabla^2 p' = \frac{\rho}{\Delta t} \nabla \cdot \mathbf{U}^*.$$

The source term  $\nabla \cdot \mathbf{U}^*$  is the mass error from step 1. The CFD solver computes  $p'$  numerically by inverting this equation.

3. **Correct the Fields:** Update the pressure and velocity fields using the calculated correction  $p'$ :

$$p^{n+1} = p^* + p', \quad \mathbf{U}^{n+1} = \mathbf{U}^* - \frac{\Delta t}{\rho} \nabla p'.$$

The gradient  $\nabla p'$  acts as a force that corrects the velocity to enforce mass conservation.

4. **Repeat:** Use  $p^{n+1}$  and  $\mathbf{U}^{n+1}$  as the new guesses  $p^*$  and  $\mathbf{U}^*$ . The algorithm repeats steps 1–3 until the solution **converges**.

Convergence is achieved when the scaled residuals for all governing equations fall below a specified tolerance, for example  $1 \times 10^{-5}$ .

## Discretization Schemes

The following spatial discretization schemes were applied:

- **Initialization Phase:** First-order upwind scheme for all equations for the first 100 iterations to damp numerical instabilities and establish a stable flow field.
- **Production Run:** Switched to second-order upwind scheme for momentum, pressure, turbulent kinetic energy ( $k$ ), and specific dissipation rate ( $\omega$ ) to minimize numerical diffusion and capture wake dynamics accurately.

## 5. Turbulence Modeling

The  $k$ - $\omega$  SST model by Menter [71] was selected for **turbulence closure** due to its accuracy in predicting the flow separation and vortex shedding prevalent around the Savonius rotor's curved blades. Its key innovation is a limiter on the turbulent viscosity that provides a more accurate prediction of wall shear stress, which is essential for capturing the onset and extent of flow separation.

The transport equations for turbulent kinetic energy ( $k$ ) and specific dissipation rate ( $\omega$ ) are:

$$\frac{\partial(\rho k)}{\partial t} + \frac{\partial(\rho u_j k)}{\partial x_j} = \tilde{P}_k - \beta^* \rho k \omega + \frac{\partial}{\partial x_j} \left[ (\mu + \sigma_k \mu_t) \frac{\partial k}{\partial x_j} \right], \quad (4.7)$$

$$\frac{\partial(\rho \omega)}{\partial t} + \frac{\partial(\rho u_j \omega)}{\partial x_j} = \alpha \frac{\rho}{\mu_t} \tilde{P}_k - \beta \rho \omega^2 + \frac{\partial}{\partial x_j} \left[ (\mu + \sigma_\omega \mu_t) \frac{\partial \omega}{\partial x_j} \right] + (1 - F_1) \frac{2\rho}{\omega} \sigma_{\omega 2} \frac{\partial k}{\partial x_j} \frac{\partial \omega}{\partial x_j}. \quad (4.8)$$

The turbulent viscosity  $\mu_t$  is calculated as:

$$\mu_t = \frac{\rho a_1 k}{\max(a_1 \omega, S F_2)},$$

$S$ : Invariant strain rate magnitude.  $S = \sqrt{2 S_{ij} S_{ij}}$ .

$$\tilde{P}_k = \min(P_k, 10 \cdot \beta^* \rho k \omega), \quad \text{with} \quad P_k = \tau_{ij} \frac{\partial u_i}{\partial x_j}.$$

$\tilde{P}_k$ : Limited production rate of turbulent kinetic energy.

$P_k$ : Production rate of turbulent kinetic energy.

The constants of the model ( $\phi = \{\sigma_k, \sigma_\omega, \alpha, \beta, \dots\}$ ) are blended between the inner ( $k$ - $\omega$ ) and outer ( $k$ - $\epsilon$ ) models using the function  $F_1$ :

$$\phi = F_1 \phi_1 + (1 - F_1) \phi_2.$$

## Boundary Conditions

The applied boundary conditions were as follows:

- **Inlet:** Velocity inlet with a magnitude of 7 m/s.
- **Outlet:** Pressure outlet with 0 Pa gauge pressure.
- **Top and Bottom Walls:** Symmetry plane.
- **Turbine Blades:** No-slip wall.
- **Interfaces:** Rotor-stator interaction zones were defined as interface boundaries.

## 5. Time-Stepping and Convergence

A fixed time step was used to advance the solution, corresponding to a  $1^\circ$  rotation of the rotor per step. The angular velocity  $\omega$  was calculated from the specified tip-speed ratio ( $\lambda = 0.8$ ), rotor diameter ( $D = 0.9273$  m), and freestream velocity ( $U = 7$  m/s):

$$\omega = \frac{2\lambda U}{D} = 12.08 \text{ rad/s.}$$

The period for one full revolution is therefore:

$$T = \frac{2\pi}{\omega} = 0.52 \text{ s.}$$

The time step was set as:

$$\Delta t = \frac{T}{360} = 1.445 \times 10^{-3} \text{ s.}$$

Each simulation was run for 4000 time steps, equivalent to over 11 full revolutions, to ensure the solution achieved periodicity. The torque on the blades was monitored and recorded at each time step. The torque was time-averaged over the final 5 revolutions (1800 time steps) to obtain a steady performance value.

## 6. Mesh independence study

A mesh-independence study was performed on the 2-D Blackwell configuration using three progressively refined grids. The number of nodes and elements for each mesh are reported in Table 4.5.

**TABLE 4.5** – Mesh statistics for the 2-D mesh-independence study.

Mesh level	Nodes	Elements
Coarse	31 933	31 235
Medium	157 482	155 903
Fine	780 884	779 476

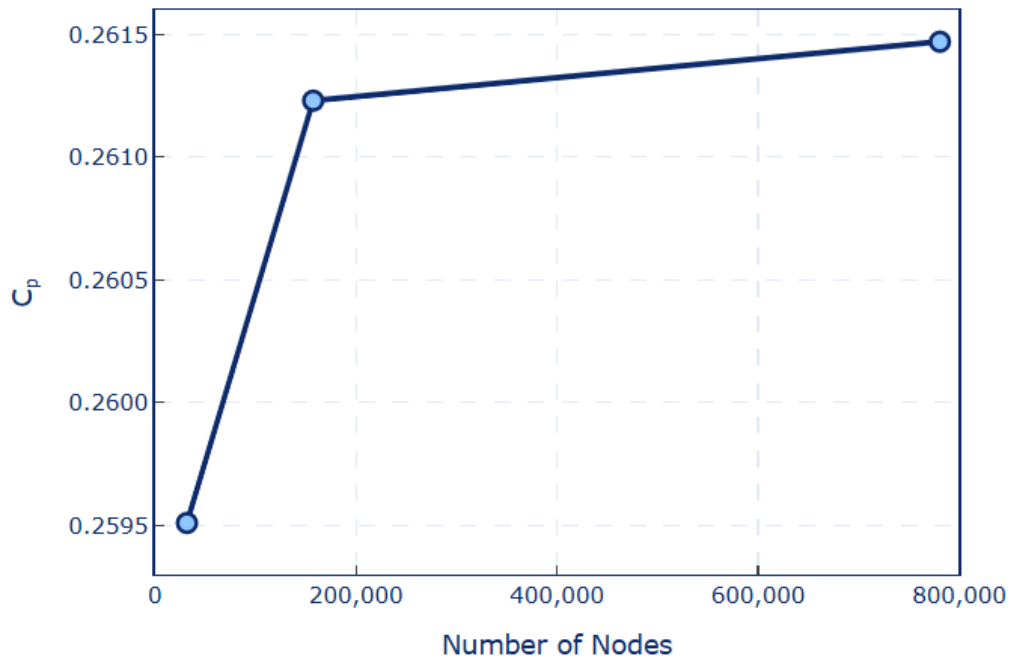


**FIGURE 4.18** – 2D mesh independence study at TSR = 0.8.

The medium mesh was chosen for all subsequent 2-D simulations, as further refinement yielded negligible changes in the predicted coefficient of power ( $C_p$ ).

## 4.2.2 3D Validation Case Setup

### 1. Geometry and Parameters for 3D S-C Rotor

To limit the mesh size, the rotor was modeled at a **1:2 scale** of the reference Blackwell et al (1978), configuration 16. All linear dimensions were reduced by half while preserving the non-dimensional ratios ( $H/D$ ,  $s/d$ ). The Reynolds number is defined as

$$\text{Re}_D = \frac{\rho U_\infty D}{\mu}.$$

Since the rotor diameter  $D$  was halved, the freestream velocity  $U_\infty$  must be doubled to preserve  $\text{Re}_D$ :

$$U'_\infty = \frac{U_\infty}{S} = 2U_\infty, \quad \text{with } S = \frac{1}{2}.$$

Consequently, the angular velocity  $\omega$  was also doubled in order to maintain the same tip speed ratio (TSR), and the simulation time step  $\Delta t$  was scaled accordingly to ensure the same angular resolution per step.

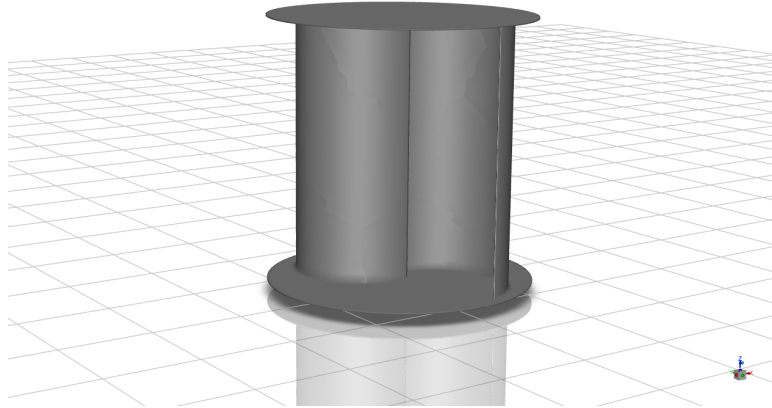


**FIGURE 4.19** – 3D geometry of the Savonius rotor.

**TABLE 4.6** – Geometric parameters for the scaled 3D Savonius rotor validation.

Parameter	Value
Number of blades	2
Rotor diameter ( $D$ )	463.65 mm
Rotor height ( $H$ )	500.0 mm
Bucket diameter ( $d$ )	250.0 mm
Gap ( $s$ )	37.5 mm
Overlap ratio ( $s/d$ )	0.15
Blade thickness ( $t$ )	0.575 mm
Aspect ratio ( $H/D$ )	1.0783

## 2. Computational Domain and Boundary Conditions

For the 3D case, the computational domain cross-section was modified relative to the 2D setup. A trapezoidal wake region combined with a semicircular inlet was adopted, as this layout gave better resolution of vortex shedding and wake development downstream of the rotor during preliminary tests (Fig. 4.20).

For the spanwise direction, the fixed domain depth was set to  $2H = 1000$  mm

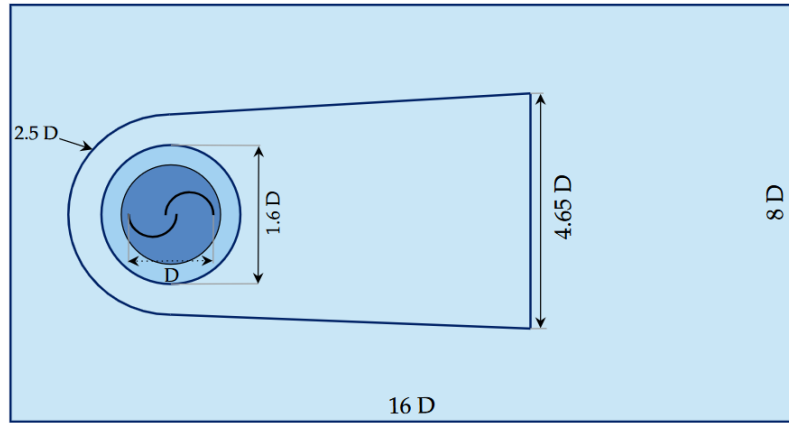


FIGURE 4.20 – Cross-section of the 3D computational domain.

### Boundary Conditions

Boundary conditions were imposed as follows:

- **Inlet:** Uniform velocity,  $U_{\infty} = 14$  m/s.
- **Outlet:** Pressure outlet,  $p = 0$ .
- **Side walls:** Symmetry.
- **Rotor domain:** Rotating region with no-slip walls (blades and endplates).
- **Interface:** Between the rotating domain and the fixed domain.

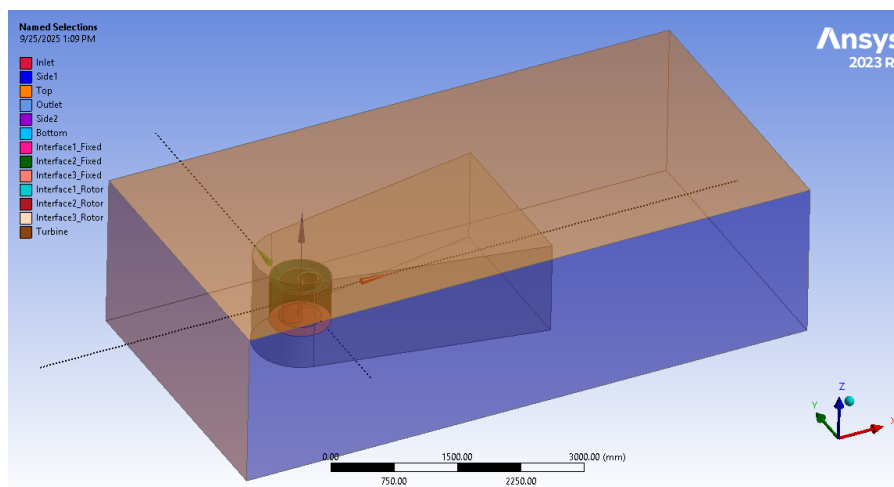


FIGURE 4.21 – 3D computational domain with named selections.

### 3. Mesh Independence Study

A mesh-independence study was carried out for the 3-D validation case of the Savonius rotor. Three progressively refined grids were tested, and the corresponding mesh statistics are reported in Table 4.7.

**TABLE 4.7** – Mesh statistics for the 3-D mesh-independence study.

Mesh level	Nodes	Elements
Coarse	206 850	592 850
Medium	571 818	1 700 905
Fine	1 859 464	5 335 415

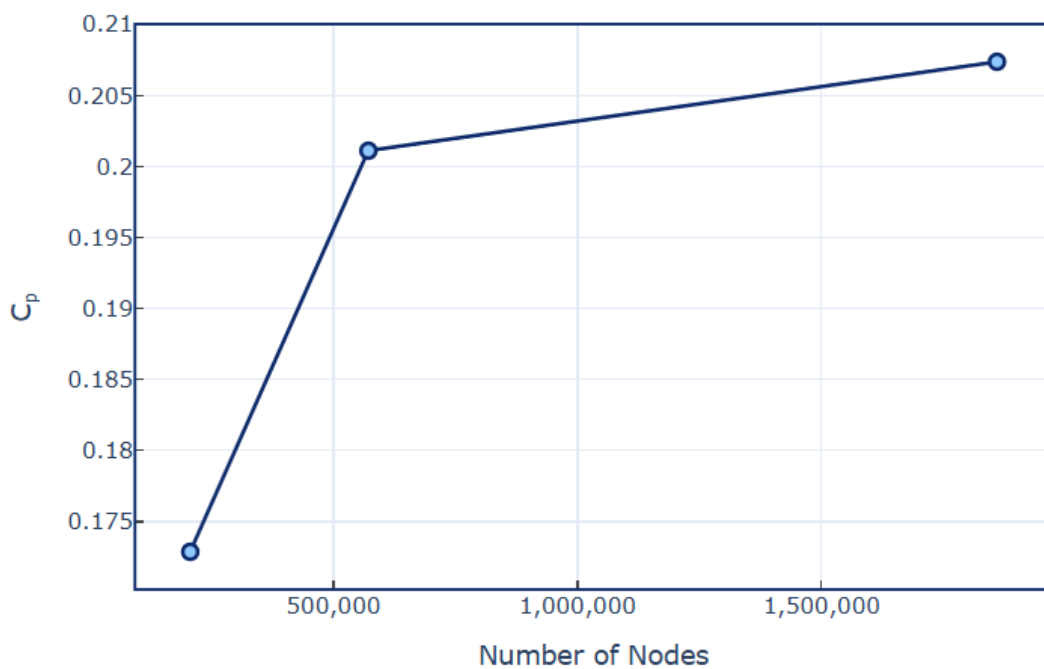


**FIGURE 4.22** – 3D mesh independence study at TSR = 0.8.

The medium mesh was selected for all subsequent 3-D simulations, as further refinement produced negligible differences in the predicted power coefficient ( $C_p$ ).

### Mesh Strategy

The 3-D meshing approach followed the same general methodology as in the 2-D case. An unstructured grid of tetrahedral elements was used in the fluid domain, with enhanced resolution in regions of strong gradients. Figure 4.23 illustrates the mesh distribution around the rotor, emphasizing the overlap region where vortex shedding is most pronounced.

- **Inflation layers:** Twenty prism layers were applied on the blade and endplate surfaces with a moderate growth rate, ensuring a first-cell height corresponding to  $y^+ \approx 0.8$ .
- **Surface refinement:** Blade surfaces employed curvature-based and proximity-based refinements to accurately capture flow separation and vortex development.



- **Quality control:** The mesh maintained acceptable orthogonal quality thresholds suitable for transient rotor simulations.

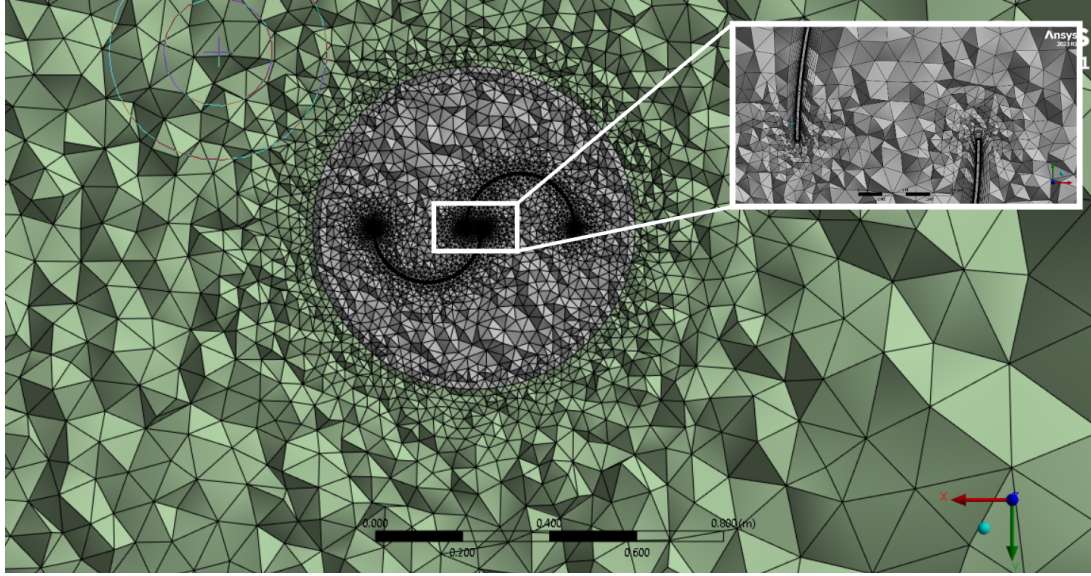


**FIGURE 4.23** – Local mesh refinement around the Savonius rotor and overlap gap region.

### 4.2.3 3D Helical Savonius (S-90) Validation Case

#### 1. Geometric Configuration

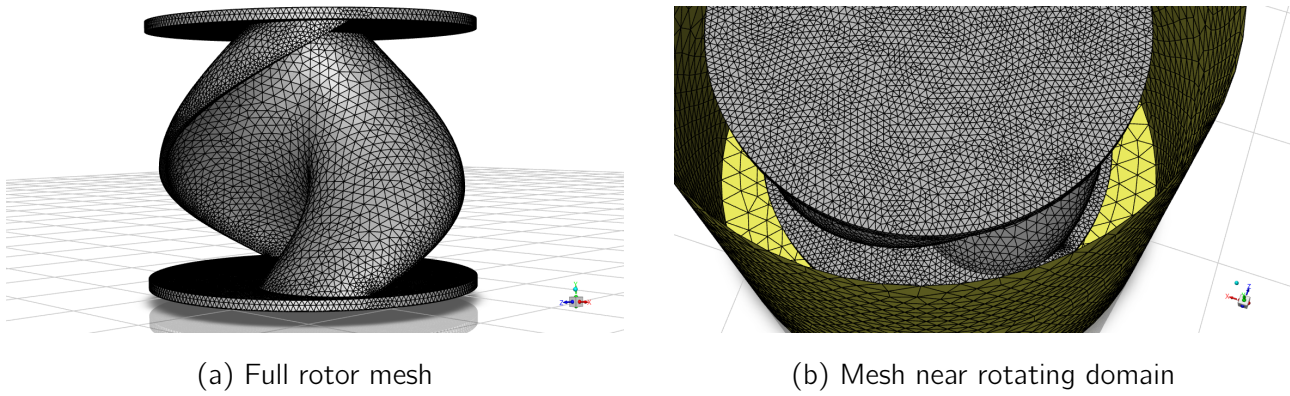
The computational model replicates configuration 2 from Kamoji et al. (2009), which features a shaftless design with zero overlap ratio ( $a/D = 0.00$ ) and aspect ratio ( $H/D = 0.88$ ).

**TABLE 4.8** – Geometric configuration of helical Savonius rotors (Kamoji et al., 2009).

Rotor	Shaft	$a/D$	$H/D$	$D$ (mm)	$H$ (mm)	$a$ (mm)	$D_o$ (mm)
1	With	0.00	1.00	224	224	0	246.4
2	Without	0.00	0.88	230	202.4	0	253.0
3	Without	0.00	0.93	230	213.9	0	253.0
4	Without	0.00	1.17	211	253.2	0	232.1
5	Without	0.10	1.00	215	215	21.5	236.5
6	Without	0.16	1.00	215	215	34.4	236.5

#### 2. Computational Setup

The geometry was scaled to a diameter of 150 mm while preserving the non-dimensional ratios. The computational parameters are summarized below.

**FIGURE 4.24** – Surface mesh of the helical Savonius rotor.**TABLE 4.9** – Computational parameters for validation case.

Parameter	Value
Number of blades	2
Rotor diameter ( $D$ )	150 mm
Rotor height ( $H$ )	132 mm
Aspect ratio ( $H/D$ )	0.88
Overlap ratio ( $a/D$ )	0.00
Reynolds number ( $Re_D$ )	155,500
Inlet velocity ( $U_\infty$ )	12.3 m/s
Tip speed ratio (TSR)	0.65

### 3. Validation Targets

The validation targets the performance characteristics at  $Re_D = 115,500$ , with focus on the power coefficient and torque behavior.

**TABLE 4.10** – Experimental performance targets (Kamoji et al., 2009).

$U_\infty$ (m/s)	$Re_D$	$C_{Pmax}$	TSR
4	57,700	0.11	0.70
6	86,600	0.15	0.72
8	115,500	0.16	0.65
10	144,000	0.17	0.66
12	173,000	0.19	0.72
14	202,000	0.20	0.71

The primary validation focuses on achieving a power coefficient comparable to the experimental target of  $C_P \approx 0.16$ .

## 4.2.4 One-Way Fluid–Structure Interaction (FSI) Simulation

### 1. Geometry Setup

The geometry from the *ANSYS Fluent* simulation was imported into *ANSYS Transient Structural*. The fluid domains (rotating and stationary) were suppressed, retaining only the solid components for structural analysis.

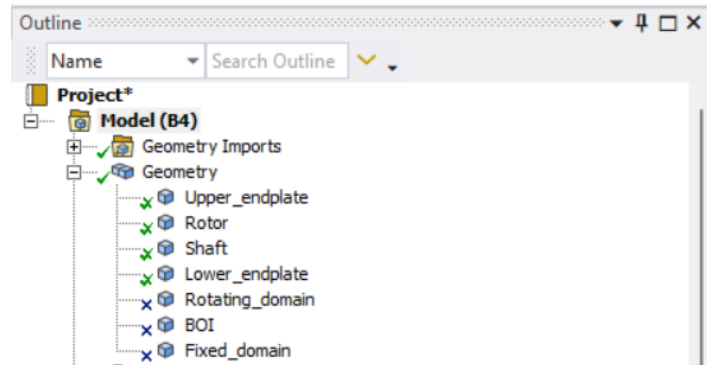


**FIGURE 4.25** – Imported geometry in *ANSYS Transient Structural* showing suppressed fluid domains.

The structural model consists of four solids: upper and lower plates, central shaft, and rotor (Fig. 4.26).

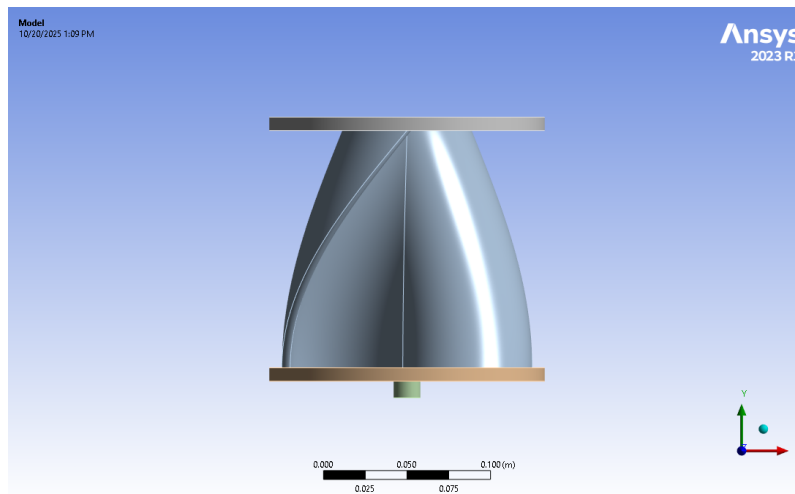


**FIGURE 4.26** – Helical rotor assembly with main solid components.

A *named selection* was created for the external surface of the rotor (**FSI Wall**) to enable pressure load mapping from the CFD solver.

### 2. Material and Boundary Conditions

The rotor was assigned the previously characterized sandwich composite (see Chapter 3), while the upper and lower plates and the central shaft were defined as PLA. All material properties—elastic modulus, Poisson’s ratio, and density—were specified in the *Engineering Data* module (Fig. 4.27).

Outline of Schematic B2: Engineering Data				
	A	B	C	D
1	Contents of Engineering Data		Source	Description
2	Material			
3	PLA		C:\V	
4	Sandwich		C:\V	
*	Click here to add a new material			

Properties of Outline Row 3: PLA				
	A	B	C	D
1	Property	Value	Unit	
2	Material Field Variables	Table		
3	Density	1240	kg m <sup>-3</sup>	
4	Isotropic Elasticity			
5	Derive from	Young's Modulus and Poisson...		
6	Young's Modulus	3.5	GPa	
7	Poisson's Ratio	0.36		
8	Bulk Modulus	4.1667E+09	Pa	
9	Shear Modulus	1.2868E+09	Pa	

FIGURE 4.27 – Material definitions in *ANSYS Engineering Data*.

To ensure structural continuity, **bonded contacts** were defined between all solid interfaces (rotor–plates–shaft). In *ANSYS Mechanical*, a bonded contact constrains the contacting surfaces to act as a single continuous body—preventing sliding, separation, or penetration (Fig. 4.28).

Details of "Contact Region"	
<b>Scope</b>	
Scoping Method	Geometry Selection
Contact	1 Face
Target	1 Face
Contact Bodies	Upper_endplate
Target Bodies	Rotor
Protected	No
<b>Definition</b>	
Type	Bonded
Scope Mode	Automatic
Behavior	Program Controlled
Trim Contact	Program Controlled
Trim Tolerance	9.277e-003 m
Suppressed	No
<b>Display</b>	
Element Normals	No

FIGURE 4.28 – Bonded contact definition between rotor and upper plate.

External boundary conditions were applied. Three main constraints and loads were imposed, as illustrated in Fig. 4.29:

- **Fixed Support:** Applied to the lower face of the shaft, fully constraining all translational and rotational degrees of freedom.
- **Pressure Load:** Imported from the *ANSYS Fluent* simulation and mapped on the rotor's *FSI Wall* surface to represent the aerodynamic loading.
- **Rotational Velocity:** Assigned to all bodies as  $\omega = -106.6$  rad/s.

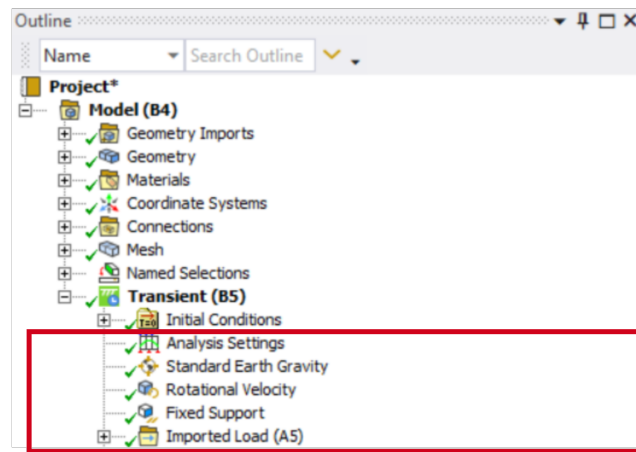
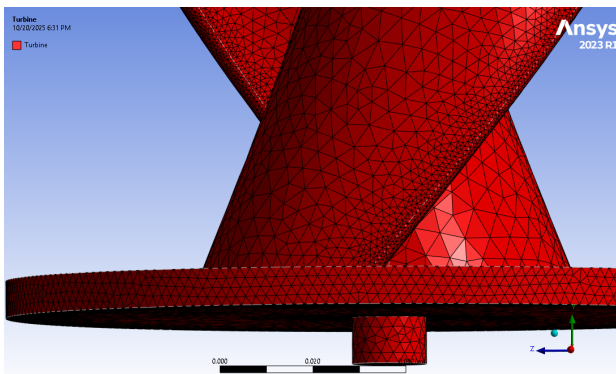


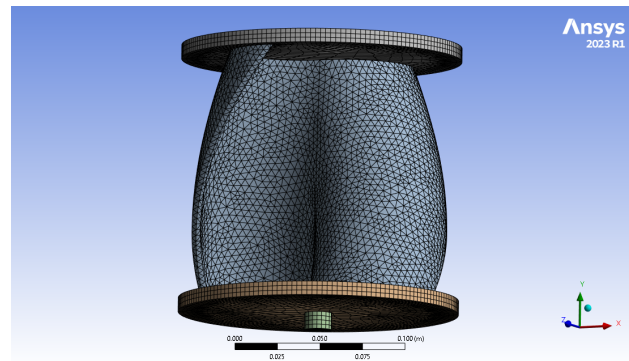
FIGURE 4.29 – Boundary condition setup in the Transient Solver.

### 3. Mesh Generation

As discussed in Chapter 1, ANSYS employs a non-conformal interface for fluid–structure coupling. To ensure accurate data transfer across the FSI boundary, comparable mesh densities were maintained between the CFD and structural domains. The mesh sizing and element type were therefore selected to achieve a consistent discretization at the fluid–solid interface.



(a) CFD mesh applied to the rotating domain in *ANSYS Fluent*.



(b) Structural mesh of the rotor assembly in *ANSYS Transient Structural*.

FIGURE 4.30 – Comparison of mesh discretization between the CFD and structural domains used for one-way FSI coupling.

In the CFD model (*ANSYS Fluent*), the reported mesh statistics include the rotating domain and the Boolean-subtracted solid regions (shaft, rotor, and plates). Therefore, the total element count represents an extrapolated value higher than the actual surface mesh density along the FSI interface. In the structural domain (*ANSYS Transient Structural*), the mesh was refined to maintain a similar node spacing on the rotor surface, ensuring proper one-way load mapping.

TABLE 4.11 – Comparison of mesh statistics for fluid and structural domains.

Domain	Solver	Nodes	Elements
Fluid (rotating + stationary)	<i>ANSYS Fluent</i>	102,250	552,517*
Structural (solid components)	<i>ANSYS Transient Structural</i>	84,227	28,975

## 4. Solver Setup

The structural simulation was performed using the *ANSYS Transient Structural* solver. A single load step was defined with a total simulation time of 0.655 s, corresponding to the duration of the imported aerodynamic pressure field from the CFD analysis. Time integration was activated, and the solver automatically handled inertial effects using implicit time-stepping.

The analysis settings are summarized in Table 4.12. All parameters were kept at their program-controlled defaults, except for the **Large Deformation** option, which was disabled due to the expected small elastic strains. This assumption ensures numerical stability without compromising accuracy.

**TABLE 4.12** – Solver configuration used for the transient structural analysis.

Parameter	Setting	Description
Number of Steps	1	Single load step for one-way FSI
Step End Time	0.655 s	Duration of CFD pressure data
Time Integration	On	Implicit transient formulation
Auto Time Stepping	Off	Fixed step size
Time Step	$1.64 \times 10^{-4}$ s	Constant increment
Solver Type	Program Controlled	Default transient solver (implicit)
Weak Springs	Off	Default
Large Deformation	<b>Off</b>	Small-strain assumption
App.-Based Settings	Moderate Speed Dynamics	Default physical control

The resulting configuration provides a stable implicit transient solution suitable for small-deformation dynamic loading under the aerodynamic pressure field mapped from the CFD domain.

# Results and Discussion

...

## Overview



This chapter presents experimental and computational analysis of Savonius rotor performance, structured as follows:

- **Experimental Performance:** Wind tunnel testing of helical prototype with comprehensive uncertainty analysis.
- **Numerical Validation:** 2D and 3D CFD validation against experimental data from **Blackwell et al. (1978)**.
- **Comparative Analysis:** Torque stability and power coefficient validation for helical vs conventional rotors, with helical validation against **Kamoji et al. (2009)**.
- **Flow Visualization:** Pressure, velocity, and vorticity contour analysis.
- **Structural Assessment:** Fluid-Structure Interaction analysis of deformation patterns.



## 5.1 Experimental Wind Tunnel Performance

The experimental results from the tests done in the wind tunnel are tabulated below:

**TABLE 5.1** – Experimental wind-tunnel results

$U$ (m/s)	RPM	Current (mA)	Voltage (V)	$P$ (W)	TSR	$C_p$
2	272	24	0.773	0.0186	1.07	0.08
3	327	33	1.000	0.033	0.86	0.043
4	347	35	1.060	0.037	0.68	0.02
5	406	41	1.230	0.050	0.64	0.015
6	440	45	1.350	0.0608	0.58	0.01
7	460	49	1.420	0.0696	0.52	0.007
8	490	54	1.480	0.0799	0.48	0.0055

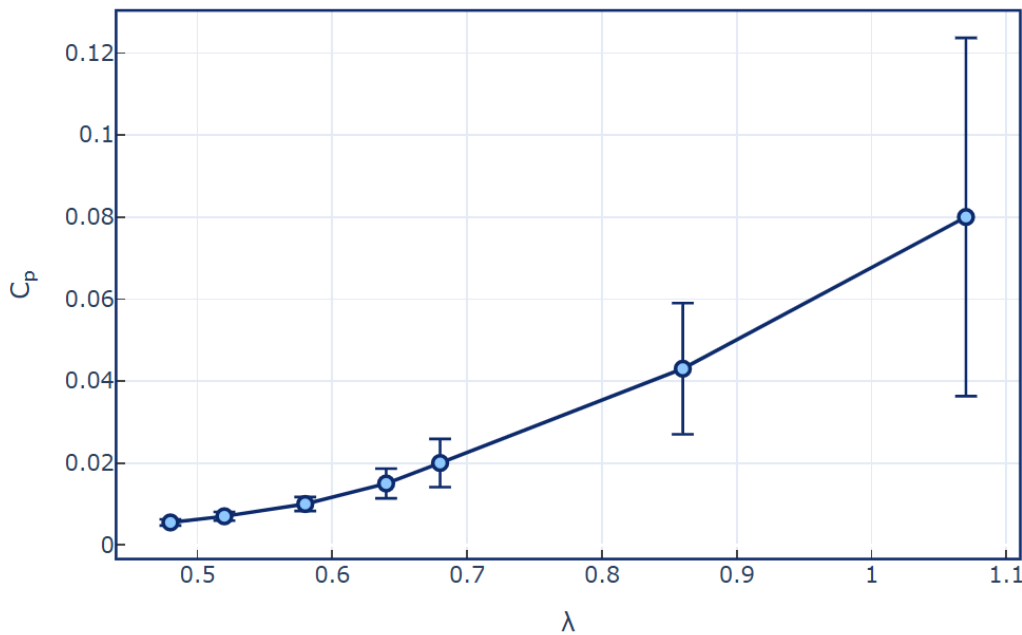


**FIGURE 5.1** – Measured power coefficient  $C_p$  vs. tip-speed ratio (TSR) with uncertainty bars.

The observed performance degradation at higher wind speeds can be primarily attributed to structural vibrations that became significant above 3 m/s. While the rotor successfully achieved self-starting behavior at a cut-in speed of 2.0 m/s, compared to approximately 3.5 m/s reported in the literature [72], this demonstrates enhanced responsiveness resulting from the reduced mass of the developed design. However, the aerodynamic performance was adversely affected at elevated rotational speeds. The measured maximum power coefficient ( $C_p = 0.08$  at  $\text{TSR} = 1.07$ ) was approximately 50% lower than that reported by Kamoji for a similar helical Savonius rotor ( $C_p \approx 0.16$ ) [4]. This deviation is mainly explained by factors related to the manufacturing process and test setup. The hand lay-up fabrication method used for the composite skins introduced non-uniform fiber distribution and variable resin thickness, resulting in local stiffness



inconsistencies and structural imbalance. In addition, imperfect assembly of the external composite cover contributed to dynamic misalignment and vibration during rotation, which led to mechanical energy losses and, consequently, a reduction in aerodynamic efficiency. A secondary but non-negligible source of performance loss was identified in the experimental setup itself: a slight air leak in the wind tunnel blower, which reduced the effective wind velocity and available input power during testing.

### 5.1.1 Measurement uncertainty estimation

Uncertainties were calculated from the instruments' accuracy specs and simple propagation rules.

#### Tip-speed ratio

The tip-speed ratio is given by  $\lambda = \frac{\omega R}{U}$ . The relative uncertainty is

$$\frac{\Delta\lambda}{\lambda} = \frac{\Delta\omega}{\omega} + \frac{\Delta R}{R} + \frac{\Delta U}{U}, \quad (5.1)$$

Instrument accuracies (tachometer, caliper, manometer) from the manufacturers' manuals were used to estimate  $\Delta\omega$ ,  $\Delta R$  and  $\Delta U$ .

**TABLE 5.2** – Tip-speed-ratio uncertainties.

$U \text{ (ms}^{-1}\text{)}$	$\lambda$	$\Delta\omega/\omega \text{ (%)}$	$\Delta U/U \text{ (%)}$	$\Delta\lambda/\lambda \text{ (%)}$	$\Delta\lambda$
2	1.07	0.835	15.0	15.85	0.170
3	0.86	0.712	10.0	10.73	0.092
4	0.68	0.676	7.50	8.19	0.056
5	0.64	0.593	6.00	6.61	0.042
6	0.58	0.555	3.83	4.40	0.025
7	0.52	0.535	3.36	3.90	0.020
8	0.48	0.508	3.00	3.52	0.017

#### Electrical power

Electrical power was calculated as  $P = V \cdot I$ . For products, fractional uncertainties, so

$$\frac{\Delta P}{P} = \frac{\Delta V}{V} + \frac{\Delta I}{I} \implies \Delta P = P \left( \frac{\Delta U}{U} + \frac{\Delta I}{I} \right). \quad (5.2)$$

Absolute errors  $\Delta V$  and  $\Delta I$  were derived from the multimeter specification.

#### Power coefficient

The aerodynamic power coefficient  $C_p$  is defined by  $C_p = P/(0.5 \rho A U^3)$ . Treating density  $\rho$  as constant, differentiating shows

$$\frac{\Delta C_p}{C_p} = \frac{\Delta P}{P} + 3 \frac{\Delta U}{U} + \frac{\Delta H}{H} + \frac{\Delta R}{R}, \quad (5.3)$$

**TABLE 5.3** – Electrical-power uncertainties computed from Table 1.1.

$U$ (m/s)	$P$ (W)	$\Delta P/P$ (%)	$\Delta P$ (W)
2	0.0186	9.59	0.00178
3	0.0330	7.26	0.00240
4	0.0370	6.90	0.00255
5	0.0500	6.04	0.00302
6	0.0608	5.59	0.00339
7	0.0696	5.22	0.00363
8	0.0799	4.84	0.00387

- **Tachometer:**  $\pm(0.1\%$  of reading + 2 rpm).
- **Caliper:**  $\pm 0.02$  mm.
- **Manometer (MP200):**  $\pm 0.3 \text{ m s}^{-1}$  for  $U \leq 5 \text{ m s}^{-1}$ ; otherwise  $\pm(0.5\%$  of reading +  $0.2 \text{ m s}^{-1}$ ).
- **Multimeter:**  $\pm(0.5\%$  of reading + 0.002) (voltage and current).

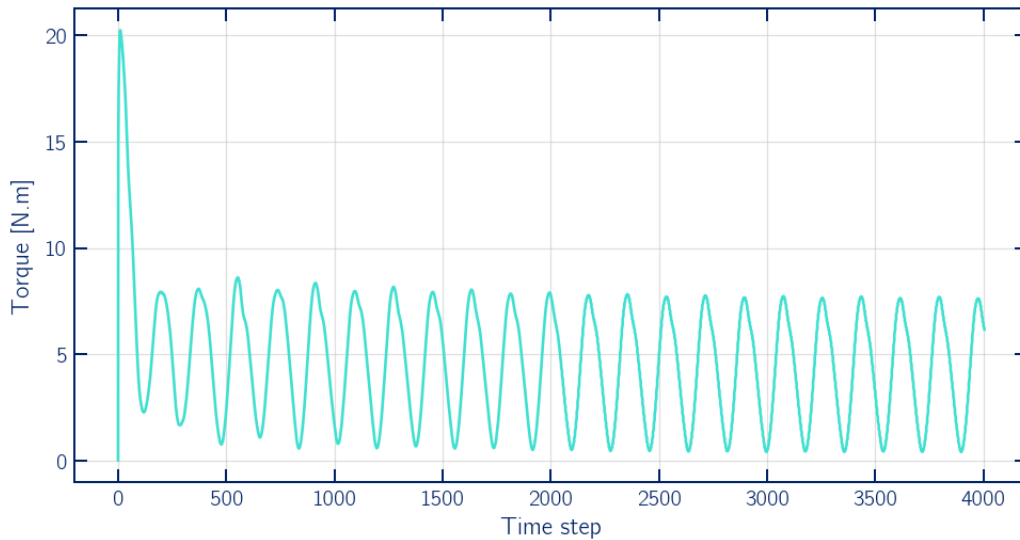
**TABLE 5.4** – Uncertainty in the power coefficient  $C_p$ .

$U$ ( $\text{m s}^{-1}$ )	$C_p$	$\Delta P/P$ (%)	$3\Delta U/U$ (%)	$\Delta C_p$ (abs)
2	0.0800	9.59	45.00	0.0437
3	0.0430	7.26	30.00	0.0160
4	0.0200	6.90	22.50	0.00588
5	0.0150	6.04	18.00	0.00361
6	0.0100	5.59	11.50	0.00171
7	0.0070	5.22	10.07	0.00107
8	0.0055	4.84	9.00	0.00076

## 5.2 Numerical Simulation Results

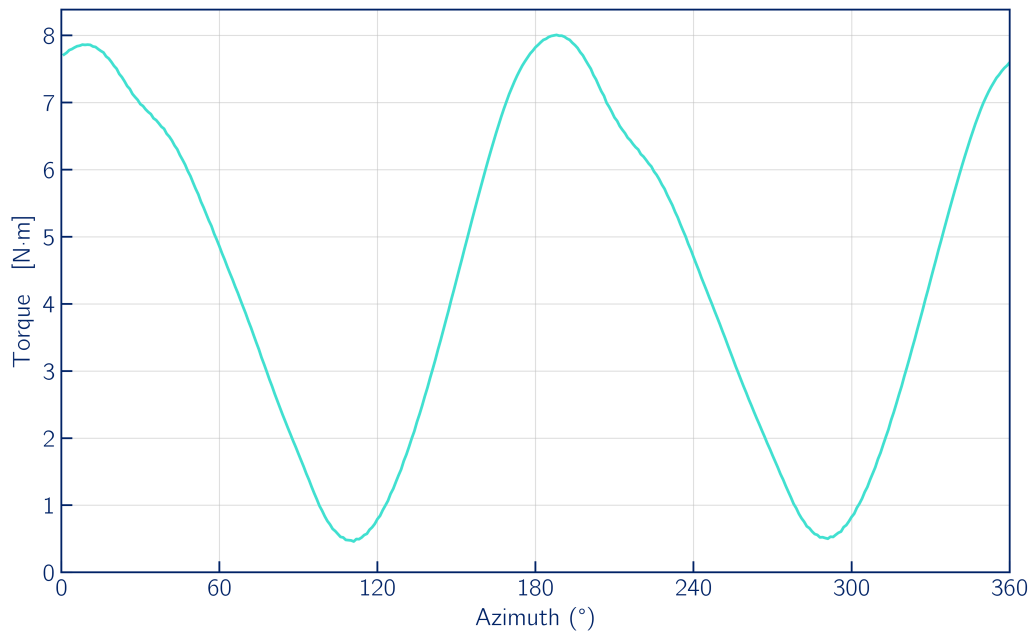
### 5.2.1 2D Conventional Savonius Rotor

Figure 5.2 shows the instantaneous torque output at  $TSR=0.8$ . The initial transient oscillations result from CFD solver initialization, after which the torque exhibits periodic fluctuations. The torque remains positive throughout the simulation.



**FIGURE 5.2** – Instantaneous torque output from 2D CFD simulation at  $TSR=0.8$

Figure 5.3 presents the dynamic torque variation, measured in Newtons-meters, as a function of azimuth angle for the conventional Savonius rotor operating at tip speed ratio of 0.8.



**FIGURE 5.3** – Dynamic torque variation with azimuth angle

Overall, the dynamic torque profile exhibits a strongly periodic pattern with two complete cycles per revolution, characterized by sharp peaks followed by gradual declines. The torque remains strictly positive throughout the operating cycle, confirming continuous unidirectional operation.

In detail, the torque reaches it's first maximum of 7.86 N.m at 7° azimuth that corresponds to the maximum drag generated by the wind on the concave part of the blade, followed by a rapid decline to a minimum of 0.57 N.m at 105°. The second torque cycle mirrors this behavior, achieving a slightly higher peak at 8.01 N.m at 187° before decreasing to 0.52 N.m at 285°. The periodicity of of approximately 180° between successive peaks corresponds directly to the two-bucket configuration of the Savonius rotor.

### 5.2.2 Validation of Two-Dimensional Computational Model

2D numerical simulations were conducted to validate the computational methodology against established experimental data from Blackwell et al. (1978) for a conventional Savonius rotor. This validation serves to verify mesh quality, turbulence modeling, and solver settings while establishing a robust foundation for subsequent three-dimensional analyses of more complex geometries.

Overall, the numerical and experimental curves for both ( $C_p$ ) and ( $C_m$ ) exhibit the same characteristic rise to a mid-range TSR peak followed by a gradual decline at higher TSR.

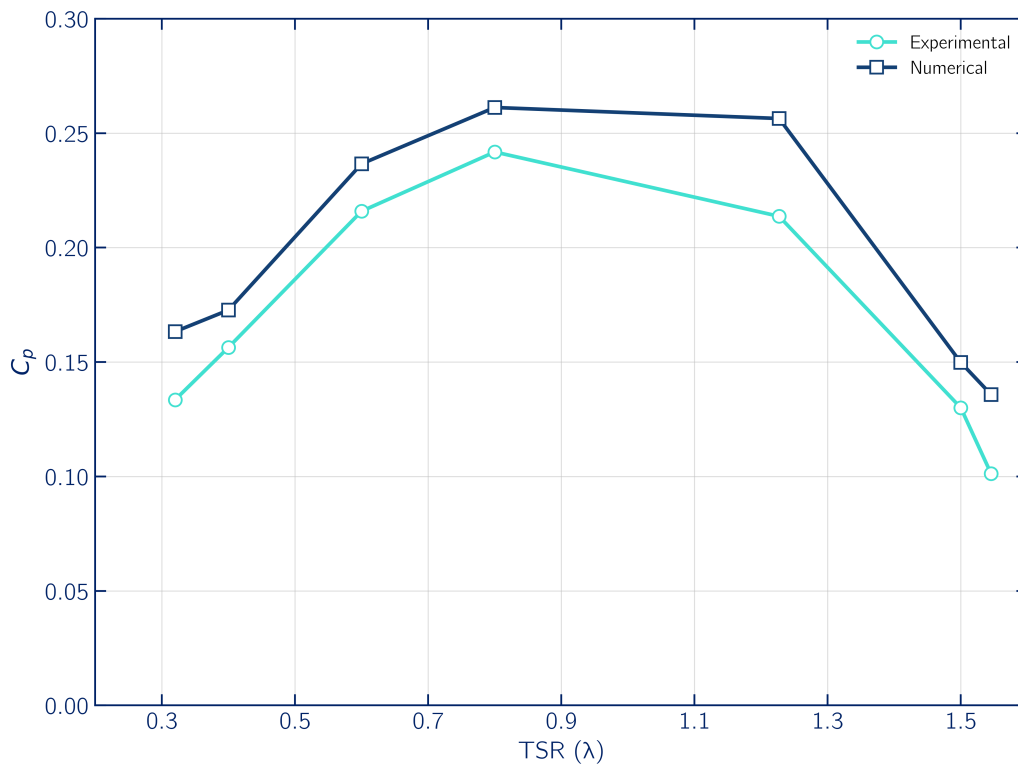


**FIGURE 5.4** – 2D CFD validation: Power coefficient vs tip speed ratio

In Figure 5.4, the experimental ( $C_p$ ) increases from 0.1335 at ( $\lambda=0.32$ ) to 0.2418 at ( $\lambda = 0.80$ ) and then falls to 0.1012 at ( $\lambda = 1.55$ ). The 2D CFD predicts the same peak location but overestimates its magnitude (0.2612), resulting in an 8 % error at the optimum TSR and up to 34 % error at the highest TSR.

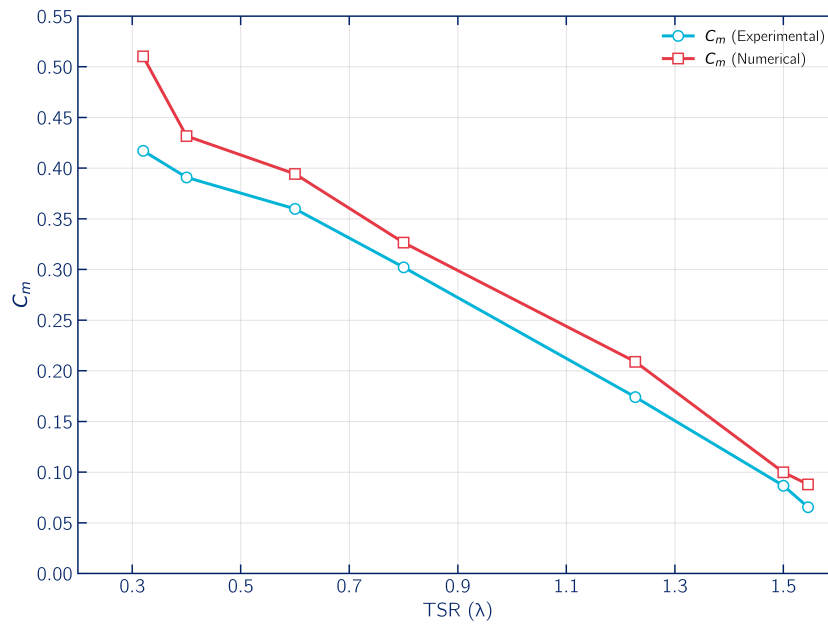


**FIGURE 5.5** – 2D CFD validation: Torque coefficient vs tip speed ratio

Similarly, Figure 5.5 shows that ( $C_m$ ) decreases almost linearly from 0.51 at ( $\lambda=0.32$ ) to 0.09 at ( $\lambda=1.55$ ), with the CFD results again matching the trend but remaining 10–15 % higher in absolute value. These discrepancies grow at the extremes of the TSR range, where three-dimensional tip losses, vortex shedding, and spanwise separation—absent in a planar model—have the greatest impact. Nevertheless, agreement within  $\pm 10$  % around the peak TSR confirms that our medium-mesh 2D CFD setup provides a reliable foundation for subsequent 3D simulations of more complex rotor geometries.

### 5.2.3 Validation of Three-Dimensional Computational Model

3D CFD simulations were performed to extend and refine the 2D results, capturing spanwise flow effects, tip losses, and end-plate vortices. The same experimental dataset from Blackwell et al. (1978) was used for comparison. Figures 5.6 and 5.7 plot the 3D CFD predictions alongside the reference measurements.

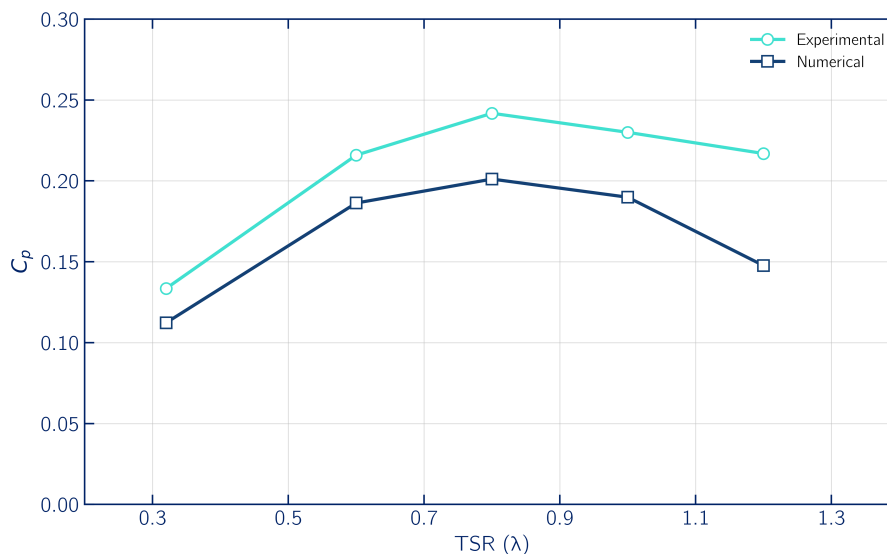


**FIGURE 5.6** – 3D CFD validation: Power coefficient vs. tip-speed ratio

Both coefficients demonstrate systematic underprediction, with power coefficient errors ranging from -13.7% to -31.9% across TSR values. Similar torque coefficient discrepancies reflect the inclusion of three-dimensional flow losses absent in 2D simulations. While indicating remaining modeling limitations, this improved correlation validates the methodology for subsequent helical rotor analysis.

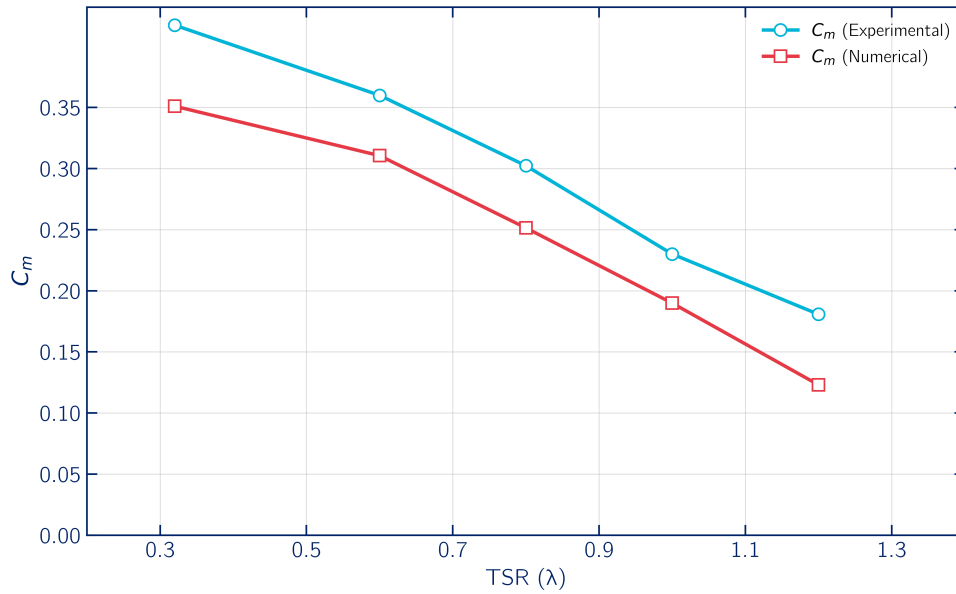


**FIGURE 5.7** – 3D CFD validation: Torque coefficient vs tip speed ratio( $\lambda$ )

### 5.2.4 Quantitative Comparison of Torque Stability for Helical and Conventional Rotors

This section presents a quantitative comparison of torque stability between the 3D conventional and helical Savonius rotors. Both datasets were obtained from 3D CFD simulations, but with geometrical and flow scaling adjustments. Therefore, a normalized representation of the torque profiles is adopted. Both simulations were performed at the tip-speed ratios corresponding to the maximum power coefficient ( $C_p$ ) reported in the reference studies —  $\lambda = 0.8$  for the conventional Savonius rotor [6] and  $\lambda = 0.65$  for the helical configuration [4].

To enable a fair comparison, the instantaneous torque  $T_i$  at each azimuthal position is normalized with respect to the mean torque  $\bar{T}$  over one complete revolution, as expressed in Equation 5.4:

$$T_{\text{norm}} = \frac{T_i}{\bar{T}} \times 100\% \quad (5.4)$$

This normalization provides a dimensionless representation of torque fluctuation intensity, allowing qualitative assessment of the relative pulsations independent of scale or units. Values above 100% indicate torque exceeding the mean, while values below 100% represent torque deficits.

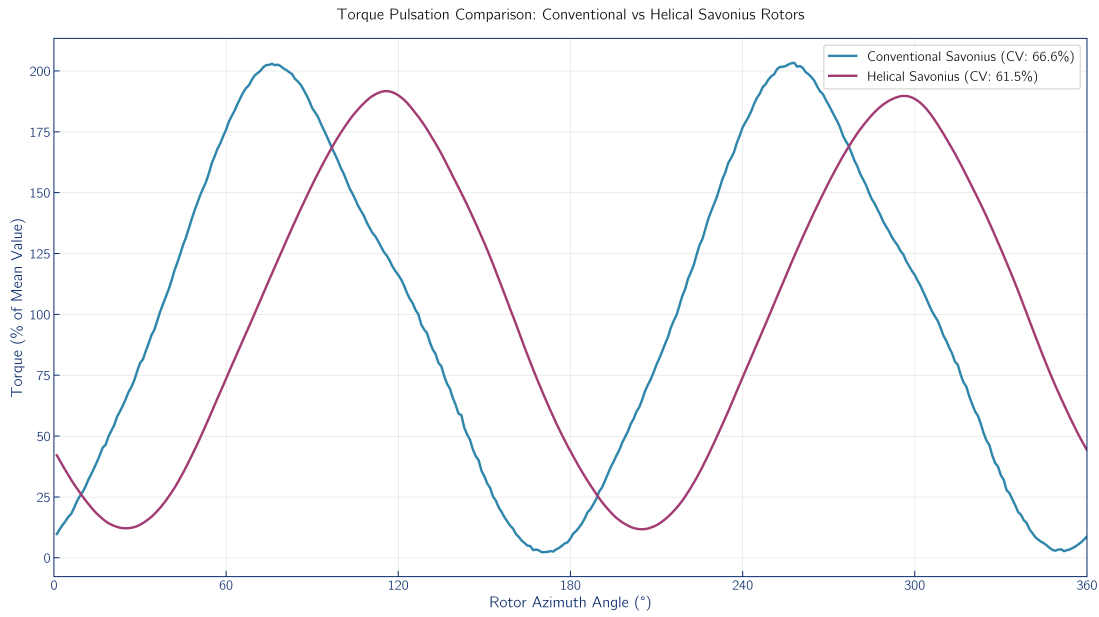


**FIGURE 5.8** – Normalized torque variation over one revolution.

As clearly demonstrated in Figure 5.8, the normalized torque plot reveals that the helical Savonius rotor exhibits significantly reduced torque pulsations compared to the conventional design. The conventional rotor experiences extreme torque variations ranging from 2% to 203% of its mean value, while the helical rotor maintains a more consistent output between 12% and 192% of its mean value. This 10.5% reduction in torque pulsation amplitude validates the fundamental advantage of the helical configuration for smoother power generation.

To quantify these fluctuations, the **coefficient of variation (CV)** was calculated for each torque dataset using Equation 5.5:

$$CV = \frac{\sigma_T}{\bar{T}} \times 100\% \quad (5.5)$$

where  $\sigma_T$  is the standard deviation of the torque signal, and  $\bar{T}$  is the mean torque.

The computed statistical results are summarized below:

**TABLE 5.5** – Statistical analysis of torque variability for the conventional and helical Savonius rotors.

Rotor Type	$\bar{T}$ (N·m)	$T_{\min}$ (N·m)	$T_{\max}$ (N·m)	Range (N·m)	CV (%)
Conventional	1.622	0.037	3.298	3.261	66.6
Helical	0.030	0.004	0.058	0.054	61.5

The conventional Savonius rotor exhibits a coefficient of variation of approximately **66.6%**, compared to **61.5%** for the helical configuration. Although both rotors present significant torque pulsations due to their drag-based operating principle, the helical design demonstrates a reduction of roughly **8%** in relative torque variability. This reduction confirms the theoretical expectation that a twisted geometry mitigates torque pulsations by promoting continuous aerodynamic loading, reducing abrupt pressure gradients and wake-induced instabilities.

### 5.2.5 Validation of Numerical Model through Power Coefficient Analysis

To validate the numerical model used in this study, the power coefficient ( $C_p$ ) was calculated for the scaled helical rotor operating at its optimal tip-speed ratio of  $\lambda = 0.65$ , as established in the previous chapter.

The torque output, where the average torque over five complete rotational cycles was determined to be:

$$\bar{T} = 0.0301 \text{ N·m}$$

Using the angular velocity corresponding to  $\lambda = 0.65$ :

$$\omega = 106.6 \text{ rad/s}$$

the mechanical power output of the turbine was calculated as:

$$P = \bar{T} \times \omega = 3.211 \text{ W}$$

The available wind power was computed for the inlet velocity of 12.3 m/s, with air density  $\rho = 1.225 \text{ kg/m}^3$  and swept area  $A = 0.15 \text{ m} \times 0.132 \text{ m} = 0.0198 \text{ m}^2$ :

$$P_{\text{wind}} = \frac{1}{2} \rho V^3 A = 22.567 \text{ W}$$

The numerical power coefficient was then determined:

$$C_{p,\text{numerical}} = \frac{P}{P_{\text{wind}}} = 0.1423$$

This result was compared with the experimental value  $C_{p,\text{exp}} = 0.16$ . The relative error between numerical and experimental results is:

$$\text{Error} = 11.06\%$$



This error of approximately 11 % falls within acceptable limits for CFD simulations of turbulent flows around rotating machinery. The close agreement between numerical and experimental results validates the computational approach and mesh resolution employed in this study.

## 5.2.6 Flow Field Visualization and Contour Analysis

In this post-processing stage, contour plots were generated from the CFD simulations to visualize the pressure, velocity, and vorticity distributions around the Savonius rotor. The following sections present and analyze these plots for the **conventional rotor** in both two-dimensional (2D) and three-dimensional (3D) cases, followed by the **modified rotor** configuration.

### 1. 2D Flow Field Contour Analysis

In Figure 5.9, the static pressure contours for the conventional Savonius rotor at two tip speed ratios ( $\lambda = 0.6$  and  $\lambda = 0.8$ ) are presented. Overall, both cases exhibit a similar pressure distribution pattern, with high-pressure zones forming on the concave surfaces of the advancing blades and low-pressure regions developing along the convex surfaces of the returning blades. This distribution reflects the drag-driven nature of the Savonius rotor, where torque generation arises primarily from the pressure differential acting between these two sides.

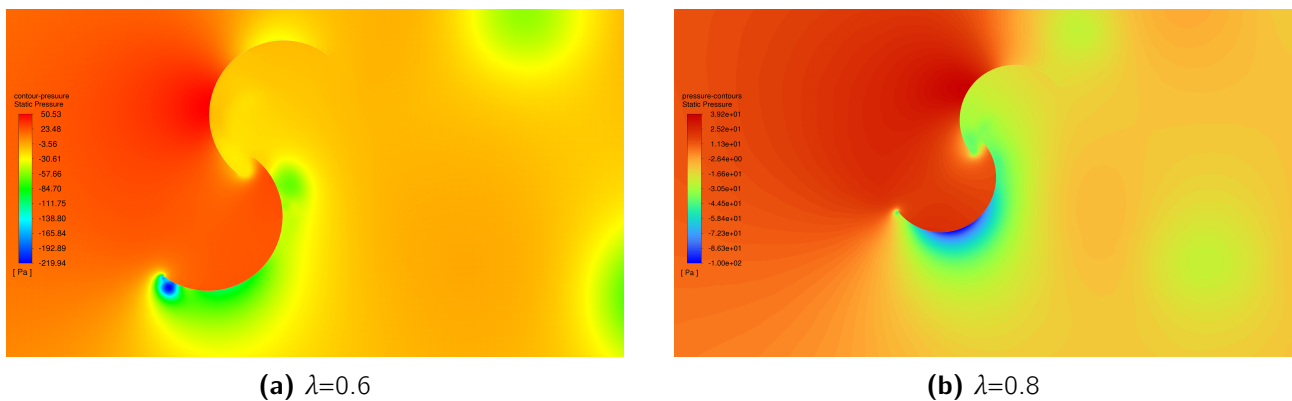


**FIGURE 5.9** – Static pressure contours around the rotor blades at two different tip speed ratios (TSR).

At  $\lambda = 0.6$ , the magnitude of this pressure differential is more pronounced, with peak static pressures reaching approximately 50 Pa on the concave side and minimum values near  $-220$  Pa on the convex side. This marked pressure gradient indicates a strong drag force acting on the advancing blade, resulting in higher instantaneous torque.

As the tip speed ratio increases to  $\lambda = 0.8$ , the overall pressure field becomes smoother, and the difference between the high- and low-pressure regions reduces (from roughly  $\Delta P \approx 170$  Pa at  $\lambda = 0.6$  to about  $\Delta P \approx 61$  Pa at  $\lambda = 0.8$ ). The reduced differential suggests less flow separation and a more stabilized aerodynamic condition.

As shown in Figure 5.10, the velocity contours follow an inverse trend to the pressure distribution. According to Bernoulli's principle, regions of high pressure correspond to low velocity, and vice versa. Thus, the concave sides of the blades—where the static pressure is highest—exhibit reduced flow velocity, approaching near-stagnation along the blade surface, while the convex sides experience accelerated flow due to the local pressure drop. The free-stream velocity corresponding to  $U = 7$  m/s is clearly visible in the far-field region, confirming proper representation of the inlet boundary condition.

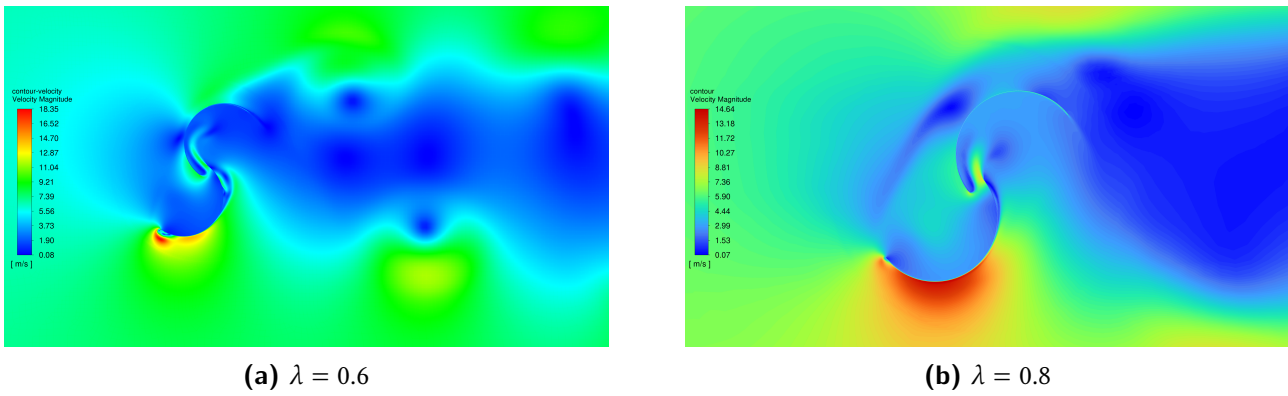


**FIGURE 5.10** – Velocity magnitude contours around the rotor blades.

As shown in Figure 5.11, the vorticity magnitude contours visualize the unsteady wake structure formed behind the rotor blades. At the lower tip speed ratio ( $\lambda = 0.6$ ), strong vortical structures are generated near the blade tips and shed periodically into the wake, indicating highly unsteady flow and stronger interaction between the returning and advancing blades. In contrast, at  $\lambda = 0.8$ , the vorticity distribution appears smoother with weaker vortex formation and reduced wake intensity, suggesting a more stable aerodynamic condition. This trend aligns with the observed reduction in pressure differential and flow separation at higher TSR, confirming a more efficient flow regime around the rotor.

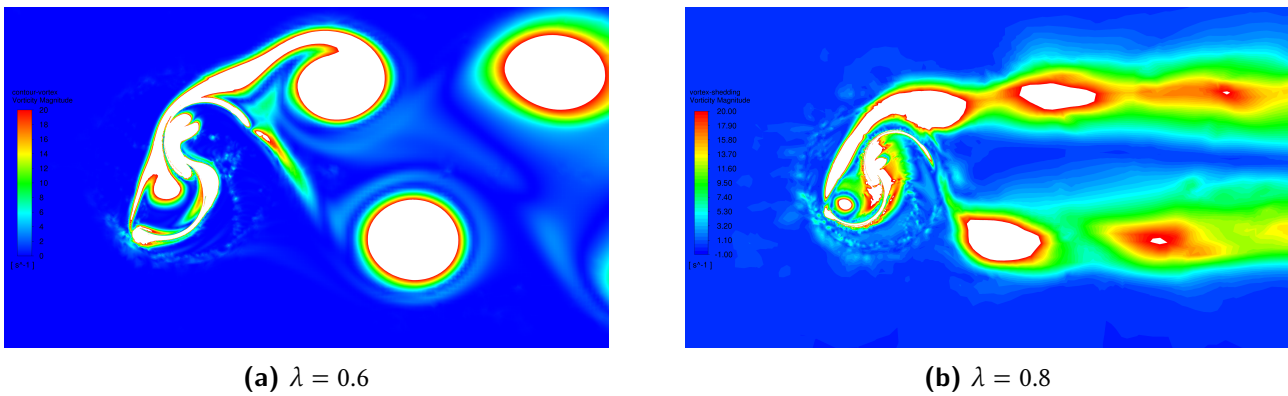


**FIGURE 5.11** – Vorticity magnitude contours.

## 2. 3D Vorticity Contour Analysis

In Figure 5.12, the vorticity magnitude contours are presented for the 3D Savonius rotor at two tip speed ratios ( $\lambda = 0.6$  and  $\lambda = 0.8$ ), using the same vorticity scale range ( $0\text{--}20\text{ s}^{-1}$ ) as in the 2D analysis for consistency. Despite the different viewing angles between the 2D and 3D models, the results clearly show that the 3D simulation captures a greater number of distinct vortical structures and more detailed wake development downstream of the rotor. This indicates that three-dimensional effects significantly enhance the representation of vortex shedding and wake interaction.

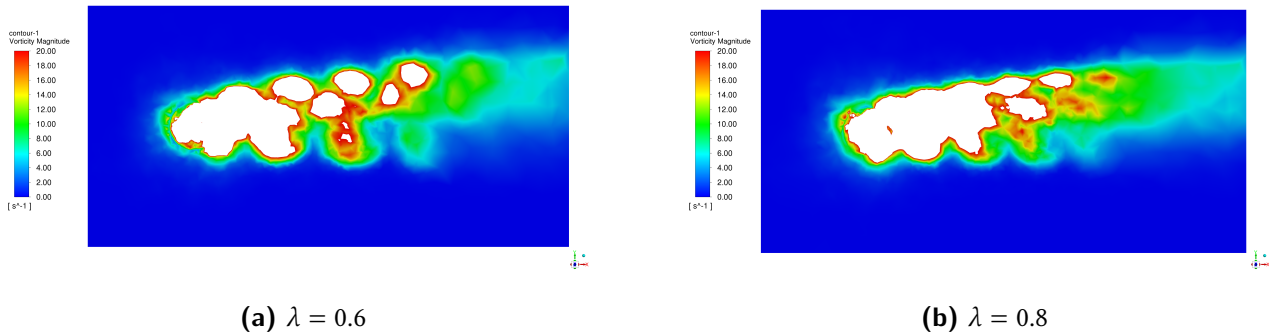


**FIGURE 5.12** – Vorticity magnitude contours for the 3D Savonius rotor.

## 3. 3D Velocity Field Visualization

In Figure 5.13, the velocity magnitude contours and relative velocity vectors are presented to visualize the 3D flow characteristics around the Savonius rotor.

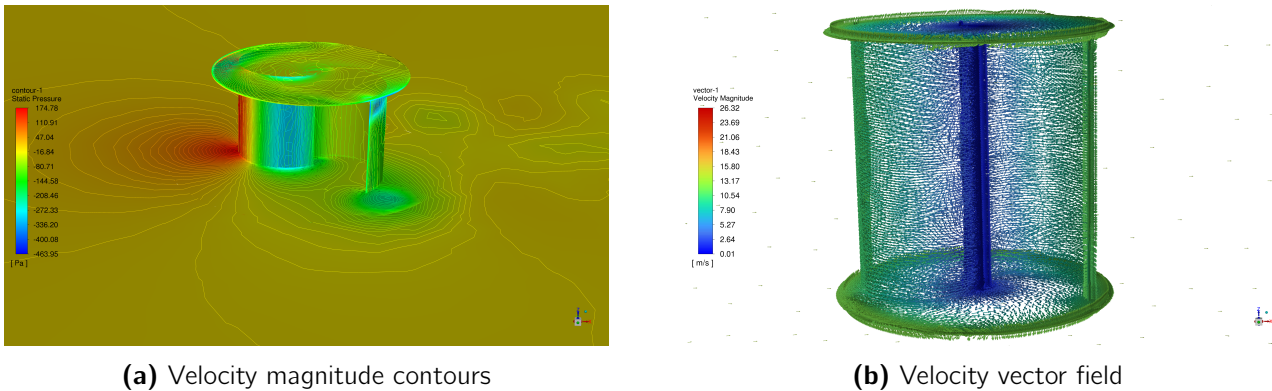


**FIGURE 5.13** – 3D velocity field visualization for the Savonius rotor.

These plots serve primarily for qualitative interpretation, as the blade angular position relative to the inlet flow differs from the 2D case, preventing a direct quantitative comparison between the pressure and velocity fields.

Furthermore, due to the geometric scaling applied in the 3D simulation—where the rotor radius was halved while maintaining the same tip speed ratio—the inlet velocity was doubled to preserve the Reynolds number. Consequently, the absolute velocity and pressure magnitudes differ from the 2D analysis, and the color scale range is not directly comparable.

#### 4. Flow Visualization for the Helical Rotor Configuration

In Figure 5.14, the vorticity magnitude contours are presented for the helical Savonius rotor configuration at a tip speed ratio of  $\lambda = 0.65$ .

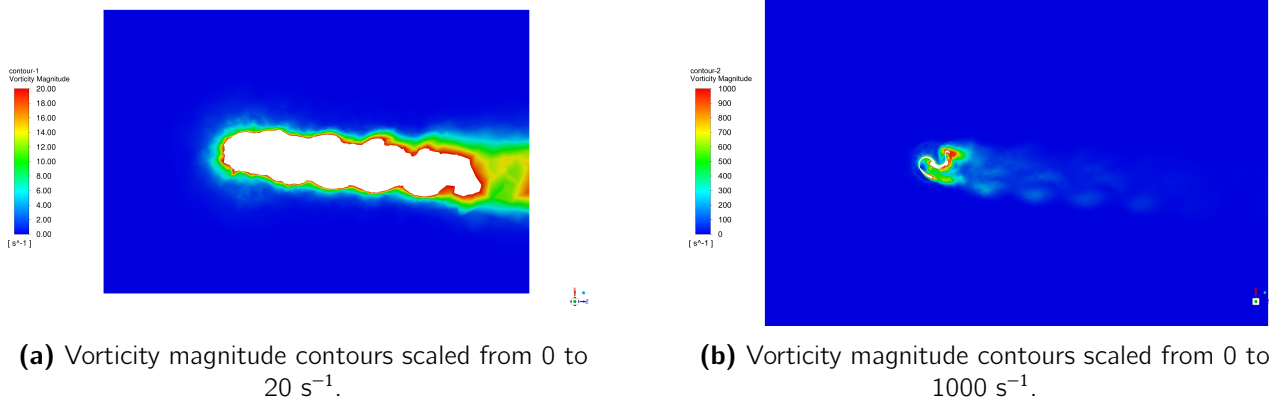


**FIGURE 5.14** – Comparison of vorticity magnitude contours for the helical Savonius rotor at  $\lambda = 0.65$  under two different contour scaling ranges.

Compared to the conventional two-bucket rotor, the helical configuration exhibits a much smoother vortex shedding pattern and a more uniform wake structure. The vorticity field shows continuous and less abrupt transitions between the high- and low-vorticity regions, indicating a reduction in flow separation and unsteady interactions between the blades.

*Note:* The broader vorticity scale (0–1000  $\text{s}^{-1}$ ) provides a more representative visualization of the vortex shedding intensity, avoiding color saturation effects and revealing finer wake details.

Figures 5.15 illustrate the velocity and pressure contours for the helical Savonius rotor at  $\lambda = 0.65$ .

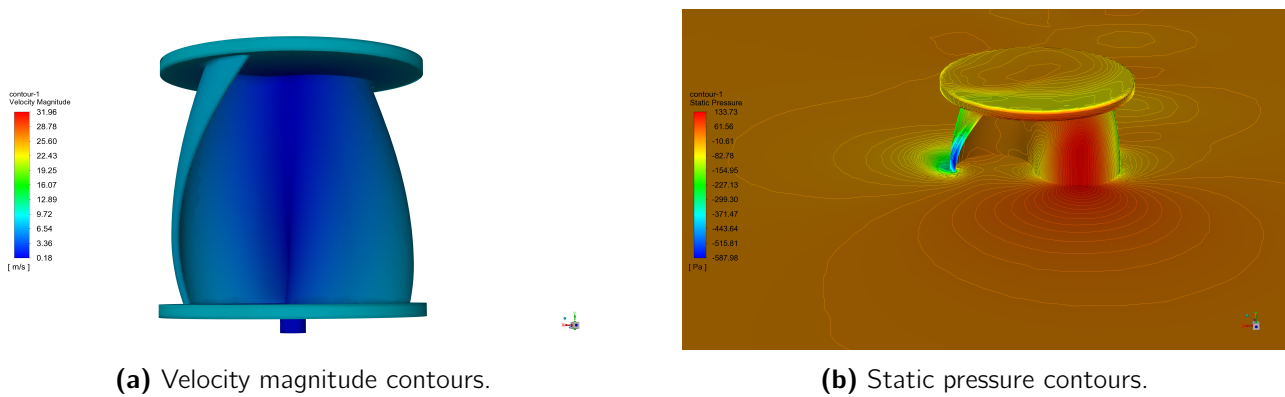


**FIGURE 5.15** – Velocity and static pressure contours for the helical Savonius rotor at  $\lambda = 0.65$ .

### 5.2.7 Fluid–Structure Interaction (FSI) Analysis of the Helical Rotor

The one-way Fluid–Structure Interaction (FSI) simulation results for the helical Savonius rotor at the optimal tip-speed ratio ( $\lambda = 0.65$ ) are presented in Figure 5.16. The total displacements are plotted over one complete rotor revolution.

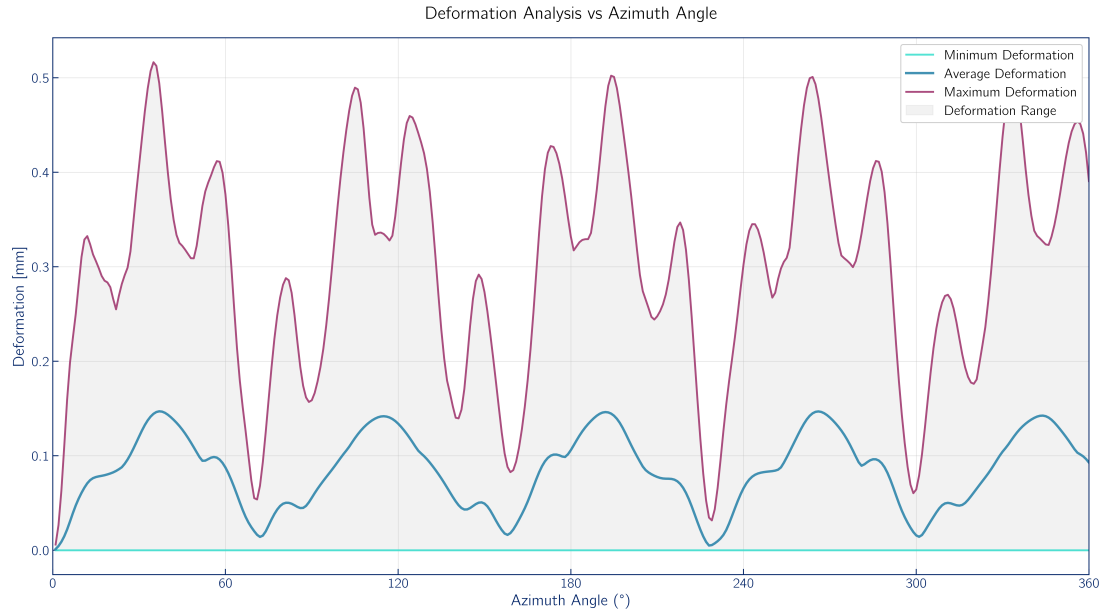


**FIGURE 5.16** – Total displacement of the helical Savonius rotor as a function of azimuth angle.

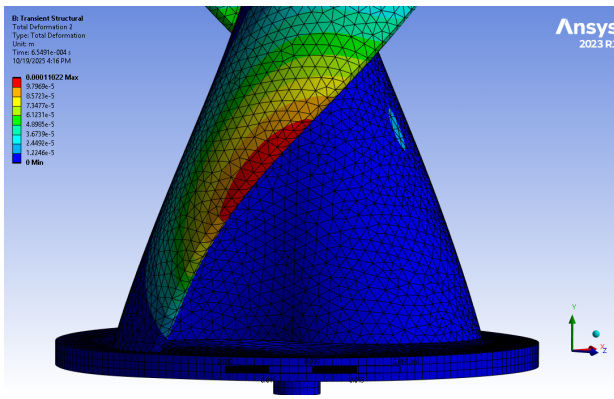
The displacement graph illustrates how structural displacement varies with azimuth angle. The observed 17 displacement peaks indicate cyclic loading effects at specific rotational positions, where the rotor encounters similar aerodynamic conditions.

These displacement patterns result from changing pressure gradients as the blades rotate, with maximum displacement occurring at critical azimuth angles where pressure differentials are most significant.

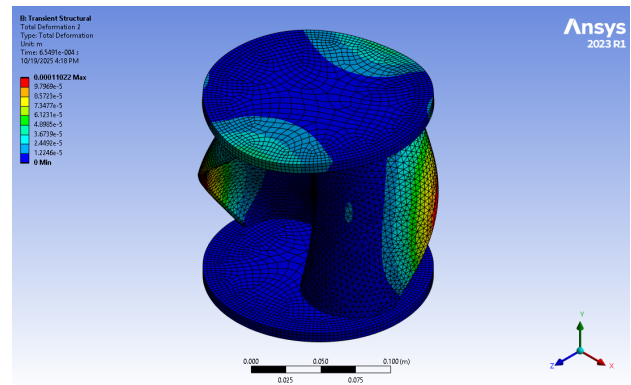
**TABLE 5.6** – Critical displacement peak coordinates

Azimuth Angle (°)	Displacement (mm)
35	0.516
194	0.502
264	0.501
105	0.489
333	0.497

As shown in Figure 5.17, which represents the displacement map at time step  $t = 6.5491e-4$  s, the maximum displacement occurs near the upper half of the rotor along the concave blade surface, where aerodynamic loading and bending moments are most pronounced. The lower region and base remain largely undeformed due to the fixed support constraint. This distribution confirms that the structural response is dominated by aerodynamic forces acting on the upper blade.



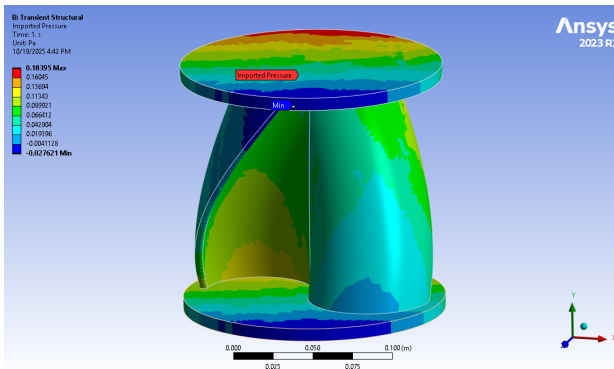
(a) Front view.



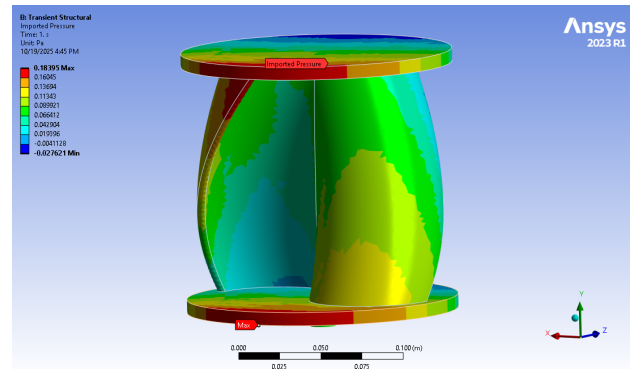
(b) Top view.

**FIGURE 5.17** – Total deformation contours on the helical Savonius rotor.

Figure 5.18 presents the pressure contours imported from the CFD solution and applied to the structural model. The color maps show the spatial distribution of the aerodynamic pressure across the rotor blades.



(a) Minimum pressure regions..



(b) Maximum pressure regions.

**FIGURE 5.18** – Imported pressure loadings applied on the helical Savonius rotor.

# Conclusion

■ ■ ■

This study proposed, designed, and validated both numerically and experimentally a lightweight Savonius vertical-axis wind turbine (SWT) rotor developed from a bio-sourced composite reinforced with date palm fibers and integrated with a 3D-printed gyroid core. The dual objectives were to enhance low-speed aerodynamic performance and promote sustainable material use in small-scale renewable energy systems. A multidisciplinary methodology was employed, combining material processing, composite manufacturing, finite element structural analysis, fluid–structure interaction (FSI) simulations, and wind tunnel experimentation.

The following key findings were obtained:

- The sandwich configuration (composite skin + gyroid core) achieved a Young’s modulus of 2.18 GPa in the wind loading direction, corresponding to a specific stiffness 32% higher than a fully 3D-printed PLA reference. This high specific stiffness resulted in minimal tip deflection under operational loading, with finite element analysis predicting a maximum tip displacement of 0.50 mm, well within admissible limits for Savonius rotor blades and ensuring structural integrity. At the same time, the total rotor mass of 127.3 g—48.6% lighter than the PLA reference, reduced rotational inertia, enhancing start-up dynamics and contributing to a low cut-in wind speed of 2.0 m/s, confirming self-starting capability at low wind speeds.
- Coupled CFD–FEA simulations under a worst-case wind speed of 8 m/s predicted a maximum power coefficient ( $C_p$ ) of 0.14 at a tip-speed ratio of 0.65. The twisted blade geometry reduced torque variability by approximately 8%, mitigating torque pulsations and improving overall energy conversion stability.

**TABLE 5.7** – Summary of main experimental and numerical results.

Parameter	Value (mean)	Observation
Sandwich modulus (load dir.)	2.18 GPa	32% gain over 100% PLA reference.
Rotor mass	127.3 g	48.6% lighter than the 100% PLA reference.
Max tip deflection	0.5 mm	Peak structural displacement within safe limits.
Cut-in wind speed	2.0 m/s	Confirmed self-starting behavior under low wind conditions.

Despite these promising results, several limitations were identified.

- The fiber treatment process remains partially manual, introducing variability in surface quality and alignment.



- From a materials engineering perspective, the long-term durability of the bio-composite under cyclic humidity and temperature variations remains to be investigated. Natural fibers are inherently hydrophilic, which can reduce interfacial bonding and alter stiffness over time. Accelerated aging and fatigue tests will therefore be required to validate the environmental stability and long-term reliability of the material system.
- At the rotor design level, the gyroid topology may be further parametrically optimized to achieve targeted stiffness gradients along the blade span. Variable-density or graded lattice structures could provide enhanced vibration damping and energy absorption without significant mass penalties.

## Perspectives and Future Work

Looking forward, future work should focus on automating and optimizing the fiber extraction process to improve yield, repeatability, and economic viability. Inspiration could be drawn from existing machines developed for banana fiber extraction (an illustrative example of which will be provided in Figure 5.19), allowing mechanized rolling and separation of fibers while minimizing manual intervention.

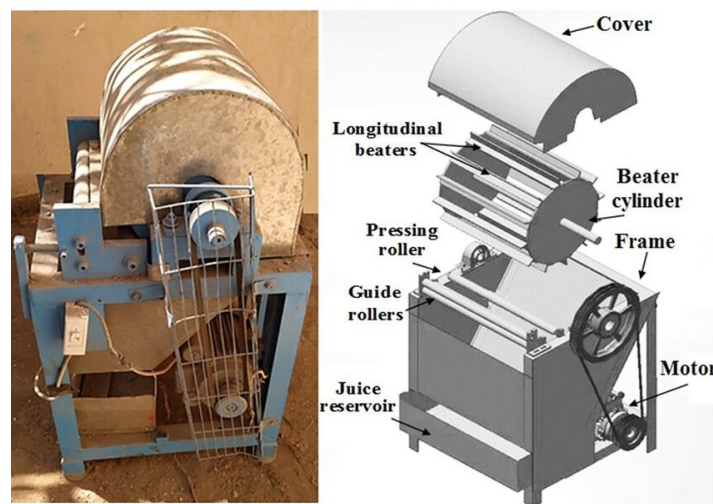


**FIGURE 5.19** – Conceptual mechanization of the fiber extraction process using a banana-fiber type rolling system, Adapted from [73].

Expanded material characterization campaigns would refine numerical models and enable multi-physics simulations addressing skin–core interfacial adhesion, crack propagation, and fatigue response.

The developed bio-composite system demonstrated mechanical capabilities that exceed the load requirements of the present rotor application. This indicates its potential suitability for other lightweight structural systems in the energy and transport sectors. Future research could therefore explore derivative materials by adjusting the fiber architecture or optimizing the relative density of the gyroid core to tailor the stiffness-to-weight ratio for specific functional requirements.

Scaling up the design to full-sized turbines will require careful assessment of manufacturing



reproducibility, cost-effectiveness, and appropriate selection of structural components. For instance, while the present prototype employed a 3D-printed PLA shaft suitable for experimental validation, a full-scale turbine would benefit from a metallic shaft, such as aluminum, to withstand cyclic loads and environmental exposure.

To conclude, beyond its immediate application, this research establishes a methodological framework for designing sustainable, lightweight wind turbines using bio-sourced and architected materials. By integrating material development, structural analysis, aerodynamic simulation, and experimental validation, the study demonstrates how laboratory-scale innovations can inform future turbine design, despite not representing a full-scale industrial implementation. The findings highlight the technical potential of PDF composites to serve not only as environmentally friendly alternatives but also as competitive materials for renewable energy systems. This work opens avenues for further development in fibre extraction, lattice architecture, and graded core design, thereby contributing to localized, sustainable energy solutions.

# Bibliography

■ ■ ■

- [1] Mohamad Midani, Naheed Saba, Othman Y Alothman, et al. Date palm fiber composites. *composites science and technology*. Singapore: Springer Singapore, 2020.
- [2] N Saba, Othman Y Alothman, Zeyad Almutairi, M Jawaidd, and Waheedullah Ghori. Date palm reinforced epoxy composites: tensile, impact and morphological properties. *Journal of Materials Research and Technology*, 8(5):3959–3969, 2019.
- [3] Mohamed Hamdy Gheith, Mohamed Abdel Aziz, Waheedullah Ghori, Naheed Saba, Mohammad Asim, Mohammad Jawaidd, and Othman Y Alothman. Flexural, thermal and dynamic mechanical properties of date palm fibres reinforced epoxy composites. *Journal of Materials Research and Technology*, 8(1):853–860, 2019.
- [4] MA Kamoji, Shireesh B Kedare, and SV Prabhu. Performance tests on helical savonius rotors. *Renewable Energy*, 34(3):521–529, 2009.
- [5] Houigab Jeong, Seungho Lee, and Soon-Duck Kwon. Blockage corrections for wind tunnel tests conducted on a darrieus wind turbine. *Journal of Wind Engineering and Industrial Aerodynamics*, 179:229–239, 2018. ISSN 0167-6105. doi: <https://doi.org/10.1016/j.jweia.2018.06.002>. URL <https://www.sciencedirect.com/science/article/pii/S016761051730702X>.
- [6] Robert E Sheldahl, Bennie F Blackwell, and Louis V Feltz. Wind tunnel performance data for two-and three-bucket savonius rotors. *Journal of Energy*, 2(3):160–164, 1978.
- [7] Tania Rus, Lucian Florin Rus, Dana-Adriana Iluțiu-Varvara, Roxana Mare, Ancuta C. Abrudan, and Florin Vasile Domnița. Experimental investigation on the influence of overlap ratio on savonius turbines performance. *International Journal of Renewable Energy Research*, 2018. URL <https://api.semanticscholar.org/CorpusID:125765344>.
- [8] Joao Vicente Akwa, Horacio Antonio Vielmo, and Adriane Prisco Petry. A review on the performance of savonius wind turbines. *Renewable and sustainable energy reviews*, 16(5): 3054–3064, 2012.
- [9] Dinesh Kumar and Shibayan Sarkar. Numerical investigation of hydraulic load and stress induced in savonius hydrokinetic turbine with the effects of augmentation techniques through fluid-structure interaction analysis. *Energy*, 116:609–618, 2016.
- [10] Esmaeel Fatahian, Farzad Ismail, Mohammad Hafifi Hafiz Ishak, and Wei Shyang Chang. Flow dynamics and performance enhancement of drag-type savonius wind turbine with a novel elliptic-shaped deflector. *Flow, Turbulence and Combustion*, 114(2):643–675, 2025.

- 
- [11] João Vicente Akwa, Gilmar Alves da Silva Júnior, and Adriane Prisco Petry. Discussion on the verification of the overlap ratio influence on performance coefficients of a savonius wind rotor using computational fluid dynamics. *Renewable energy*, 38(1):141–149, 2012.
  - [12] Łukasz Marzec, Zbigniew Buliński, and Tomasz Krysiński. Fluid structure interaction analysis of the operating savonius wind turbine. *Renewable Energy*, 164:272–284, 2021.
  - [13] Yuri Bazilevs, Kenji Takizawa, and Tayfun E Tezduyar. *Computational fluid-structure interaction: methods and applications*. John Wiley & Sons, 2013.
  - [14] LA Elseify, M Midani, A Hassanin, T Hamouda, and R Khiari. Long textile fibers extracted from date palm (phoenix dactylifera l.) midribs: effect of the alkaline treatment on the mechanical properties. *Ind Crops Prod*, 115:112466, 2020.
  - [15] Mohamed Amine Kacem, Moussa Guebailia, Nassila Sabba, Said Abdi, and Mahdi Bodaghi. Assessing extraction methods and mechanical and physicochemical properties of algerian yucca fibers for sustainable composite reinforcement. *Macromolecular Materials and Engineering*, 309(10):2400082, 2024.
  - [16] L. Yang, X. Wang, and Y. Huang. Lightweight sandwich structures with tpms cores: Design and mechanical performance. *Materials & Design*, 213, 2022.
  - [17] M.A. Maulana, C.J.S. Ferreira, G.J.W. van Bussel, et al. Blockage corrections for wind tunnel testing of vertical-axis wind turbines. *Flow Measurement and Instrumentation*, 62: 121–131, 2018.
  - [18] Mohamed Chakib Boudehane. Étude numérique et expérimentale de l'écoulement à travers une soufflerie à circuit fermé. Étude de cas: soufflerie de l'enp. Master's thesis, École Nationale Polytechnique d'Alger, 2021.
  - [19] Wenlong Tian, Baowei Song, James H VanZwieten, and Parakram Pyakurel. Computational fluid dynamics prediction of a modified savonius wind turbine with novel blade shapes. *Energies*, 8(8):7915–7929, 2015.
  - [20] International Renewable Energy Agency. Renewable power generation costs in 2023. Technical report, International Renewable Energy Agency, Abu Dhabi, 2024. URL <https://www.irena.org/publications/2024/Jun/Renewable-power-generation-costs-in-2023>. IRENA (2024).
  - [21] World Wind Energy Association (WWEA). Wwea annual report 2024: A challenging year for wind power. Technical report, World Wind Energy Association, Bonn, Germany, 2024. URL <http://www.wwindea.org/>. Accessed June 2025.
  - [22] Ivan Farozan, Tubagus Ahmad Fauzi Soelaiman, Priyono Soetikno, and Yuli Setyo Indartono. The effect of rotor aspect ratio, stages, and twist angle on savonius wind turbine performance in low wind speeds environment. *Results in Engineering*, 25:104041, 2025. ISSN 2590-1230. doi: <https://doi.org/10.1016/j.rineng.2025.104041>. URL <https://www.sciencedirect.com/science/article/pii/S259012302500129X>.
  - [23] Sanghyeon Kim and Cheolung Cheong. Development of low-noise drag-type vertical wind turbines. *Renewable Energy*, 79:199–208, 2015. ISSN 0960-1481. doi: <https://doi.org/10.1016/j.renene.2014.09.047>. URL <https://www.sciencedirect.com/science/article/pii/S0960148114006120>. Selected Papers on Renewable Energy: AFORE 2013.
-

- 
- [24] Kenza Almi, Adel Benchabane, Said Lakel, and Abdelouahed Kriker. Potential utilization of date palm wood as composite reinforcement. *Journal of Reinforced Plastics and Composites*, 34(15):1231–1240, August 2015. doi: 10.1177/0731684415588356.
- [25] Lobna A. Elseify, Mohamad Midani, Ahmed H. Hassanin, Tamer Hamouda, and Ramzi Khiari. Long textile fibres from the midrib of date palm: Physiochemical, morphological, and mechanical properties. *Industrial Crops and Products*, 151:112466, 2020. ISSN 0926-6690. doi: <https://doi.org/10.1016/j.indcrop.2020.112466>. URL <https://www.sciencedirect.com/science/article/pii/S0926669020303824>.
- [26] J.V. Akwa, H.A. Vielmo, and A.P. Petry. A review on the performance of savonius wind turbines. *Renewable and Sustainable Energy Reviews*, 16(5):3054–3064, 2012.
- [27] Ahmed S Saad, Ibrahim I El-Sharkawy, Shinichi Ookawara, and Mahmoud Ahmed. Performance enhancement of twisted-bladed savonius vertical axis wind turbines. *Energy Conversion and Management*, 209:112673, 2020.
- [28] Jing Jia, Liru Zhang, Wei Gao, Tong Qiu, YuQi Hou, and Jianwen Wang. An experimental study and prediction of dynamic deformation of wind turbine blade based on dic. *Scientific Reports*, 15(1):5106, 2025.
- [29] Muhamad Hasfanizam Mat Yazik, Mohd Hafiz Zawawi, Ali Najah Ahmed, Lariyah Mohd Sidek, Hidayah Basri, and Farzad Ismail. One-way fluid structure interaction analysis of a static savonius hydrokinetic turbine under different velocity and surface roughness with different blade materials. *Ocean Engineering*, 291:116373, 2024.
- [30] Ananya Kalita and TVVLN Rao. An overview of fluid-structure interaction: Modelling, finite element method and applications. *Ann. Multidiscip. Res. Innov. Technol.*, 2(2): 93–105, 2023.
- [31] Erwin C Sumarago, Mary Frahnchezka M dela Cerna, Andrea Kaylie B Leyson, Noel Peter B Tan, and Kendra Felizimarie Magsico. Production and characterization of nanocellulose from maguey (agave cantala) fiber. *Polymers*, 16(10):1312, 2024.
- [32] P Khristova, O Kordsachia, and T Khider. Alkaline pulping with additives of date palm rachis and leaves from sudan. *Bioresource technology*, 96(1):79–85, 2005.
- [33] Seyed Mohammad Mirmehdi, Farhad Zeinaly, and Fatemeh Dabbagh. Date palm wood flour as filler of linear low-density polyethylene. *Composites Part B: Engineering*, 56: 137–141, 2014.
- [34] Boudjemaa Agoudjil, Adel Benchabane, Abderrahim Boudenne, Laurent Ibos, and Magali Fois. Renewable materials to reduce building heat loss: Characterization of date palm wood. *Energy and buildings*, 43(2-3):491–497, 2011.
- [35] Said S Hegazy and Khaled Ahmed. Effect of date palm cultivar, particle size, panel density and hot water extraction on particleboards manufactured from date palm fronds. *Agriculture*, 5(2):267–285, 2015.
- [36] Hon-Meng Ng, Lee Tin Sin, Tiam-Ting Tee, Soo-Tueen Bee, David Hui, Chong-Yu Low, and AR Rahmat. Extraction of cellulose nanocrystals from plant sources for application as reinforcing agent in polymers. *Composites Part B: Engineering*, 75:176–200, 2015.
-

- 
- [37] Min Zhi Rong, Ming Qiu Zhang, Yuan Liu, Gui Cheng Yang, and Han Min Zeng. The effect of fiber treatment on the mechanical properties of unidirectional sisal-reinforced epoxy composites. *Composites Science and technology*, 61(10):1437–1447, 2001.
- [38] Susheel Kalia, BS Kaith, and Inderjeet Kaur. Pretreatments of natural fibers and their application as reinforcing material in polymer composites—a review. *Polymer Engineering & Science*, 49(7):1253–1272, 2009.
- [39] Adil Sbiai, Abderrahim Maazouz, Etienne Fleury, Henry Sautereau, and Hamid Kaddami. Short date palm tree fibers/polyepoxy composites prepared using rtm process: effect of tempo mediated oxydation of the fibers. *BioResources*, 2010.
- [40] Michel Sotton and Marc Ferrari. Adjustment of the steam explosion treatment to extract fibres from plants, usable for textile and related end-uses. *Steam Explos. Tech. Fundam. Ind*, 1991.
- [41] RW Kessler, U Becker, R Kohler, and B Goth. Steam explosion of flax—a superior technique for upgrading fibre value. *Biomass and Bioenergy*, 14(3):237–249, 1998.
- [42] K Murali Mohan Rao and K Mohana Rao. Extraction and tensile properties of natural fibers: Vakka, date and bamboo. *Composite structures*, 77(3):288–295, 2007.
- [43] Ryoko Tokoro, Duc Minh Vu, Kazuya Okubo, Tatsuya Tanaka, Toru Fujii, and Takayasu Fujiura. How to improve mechanical properties of polylactic acid with bamboo fibers. *Journal of materials science*, 43(2):775–787, 2008.
- [44] Azam Ali, Khubab Shaker, Yasir Nawab, Madeha Jabbar, Tanveer Hussain, Jiri Militky, and Vijay Baheti. Hydrophobic treatment of natural fibers and their composites—a review. *Journal of Industrial Textiles*, 47(8):2153–2183, 2018.
- [45] Amar Kumar Mohanty, Manjusri Misra, and LT Drzal. Sustainable bio-composites from renewable resources: opportunities and challenges in the green materials world. *Journal of Polymers and the Environment*, 10(1):19–26, 2002.
- [46] Fei Yao, Qinglin Wu, and Dingguo Zhou. Thermal decomposition of natural fibers: Global kinetic modeling with nonisothermal thermogravimetric analysis. *Journal of Applied Polymer Science*, 114(2):834–842, 2009.
- [47] MA AlMaadeed, Ramazan Kahraman, P Noorunnisa Khanam, and Somaya Al-Maadeed. Characterization of untreated and treated male and female date palm leaves. *Materials & Design*, 43:526–531, 2013.
- [48] Jyoti R Mohanty, Sankar N Das, Harish C Das, and Sarat K Swain. Effect of chemically modified date palm leaf fiber on mechanical, thermal and rheological properties of polyvinylpyrrolidone. *Fibers and Polymers*, 15(5):1062–1070, 2014.
- [49] Ichrak Tahri, Isabelle Ziegler Devin, Julien Ruelle, César Segovia, and Nicolas Brosse. Extraction and characterization of fibers from palm tree. *BioResources*, 11(3):7016–7025, 2016.
- [50] HH Abdel-Rahman, R Al-Juruf, F Ahmad, and I Alam. Physical, mechanical and durability characteristics of date palm frond stalks as reinforcement in structural concrete. *International Journal of Cement Composites and Lightweight Concrete*, 10(3):175–181, 1988.
-

- [51] HA Ghulman, M Nabil Metwally, and MW Alhazmi. Study on the benefits of using the date palm trees residuals in saudi arabia for development of the non-traditional wooden industry. In *AIP Conference Proceedings*, volume 1814, page 020012. AIP Publishing LLC, 2017.
- [52] Salah Amroune, Abderrezak Bezazi, Alain Dufresne, Fabrizio Scarpa, and Abdellatif Imad. Investigation of the date palm fiber for green composites reinforcement: thermo-physical and mechanical properties of the fiber. *Journal of Natural Fibers*, 18(5):717–734, 2021.
- [53] I Taha, L Steuernagel, and G Ziegmann. Optimization of the alkali treatment process of date palm fibres for polymeric composites. *Composite Interfaces*, 14(7-9):669–684, 2007.
- [54] Hamdy Ibrahim, Sherif Mehanny, Lamis Darwish, and Mahmoud Farag. A comparative study on the mechanical and biodegradation characteristics of starch-based composites reinforced with different lignocellulosic fibers. *Journal of Polymers and the Environment*, 26(6):2434–2447, 2018.
- [55] I Taha, L Steuernagel, and G Ziegmann. Chemical modification of date palm mesh fibres for reinforcement of polymeric materials. part i: examination of different cleaning methods. *Polymers and Polymer Composites*, 14(8):767–778, 2006.
- [56] Abdalla Abdal-Hay, Ngakan Putu Gede Suardana, Do Yeon Jung, Kwang-Seog Choi, and Jae Kyoo Lim. Effect of diameters and alkali treatment on the tensile properties of date palm fiber reinforced epoxy composites. *International Journal of Precision Engineering and Manufacturing*, 13(7):1199–1206, 2012.
- [57] T Alsaeed, BF Yousif, and H Ku. The potential of using date palm fibres as reinforcement for polymeric composites. *Materials & Design*, 43:177–184, 2013.
- [58] Elsayed A Elbadry. Agro-residues: Surface treatment and characterization of date palm tree fiber as composite reinforcement. *Journal of Composites*, 2014(1):189128, 2014.
- [59] A Shalwan and BF Yousif. Influence of date palm fibre and graphite filler on mechanical and wear characteristics of epoxy composites. *Materials & Design*, 59:264–273, 2014.
- [60] Sakib Hossain Khan, Hom N Dhakal, Abu Saifullah, and Zhongyi Zhang. Improved mechanical and thermal properties of date palm microfiber-reinforced pcl biocomposites for rigid packaging. *Molecules*, 30(4):857, 2025.
- [61] James L Thomason and Jose L Rudeiros-Fernández. Thermal degradation behaviour of natural fibres at thermoplastic composite processing temperatures. *Polymer Degradation and Stability*, 188:109594, 2021.
- [62] Sha Yin, Haoyu Chen, Yaobo Wu, Yibing Li, and Jun Xu. Introducing composite lattice core sandwich structure as an alternative proposal for engine hood. *Composite Structures*, 201:131–140, 2018.
- [63] Fengxiang Xu, Kejong Yu, Lin Hua, and Xiaoqiang Niu. Crashworthiness design of crash box filled with negative poisson's ratio based on horn structure. *Mechanics of Advanced Materials and Structures*, 29(27):6403–6420, 2022.

- 
- [64] Yuhua Li, Deyu Jiang, Rong Zhao, Xin Wang, Liqiang Wang, and Lai-Chang Zhang. High mechanical performance of lattice structures fabricated by additive manufacturing. *Metals*, 14(10):1165, 2024.
- [65] S Higuera, R Miralbes, and D Ranz. Mechanical properties and energy-absorption capabilities of thermoplastic sheet gyroid structures. *Mechanics of Advanced Materials and Structures*, 29(25):4110–4124, 2022.
- [66] Joaquim Justino Netto, Manuel Sardinha, and Marco Leite. Influence of the cell size and wall thickness on the compressive behaviour of fused filament fabricated pla gyroid structures. *Mechanics of Materials*, 195:105051, 2024.
- [67] Y. Zhang, C. Li, and R. Zhao. Damage and buckling performance of gyroid-core sandwich structures under impact loading. *Thin-Walled Structures*, 162, 2021.
- [68] H.M.A. Kolken and A.A. Zadpoor. Auxetic mechanical metamaterials. *RSC Advances*, 7(9):5111–5129, 2017.
- [69] Aimen Guediri, Abdelhakim Khaldi, and Arezki Smaili. Conception et réalisation d'une éolienne de type savonius hélicoidale et tests de performances en soufflerie/cfd. Mémoire de projet de fin d'Étude, École Nationale Polytechnique, Département Génie Mécanique, Alger, Algérie, 2018. URL <http://repository.enp.edu.dz/jspui/handle/123456789/1194>.
- [70] Aneta Liber-Kneć and Sylwia Łagan. Effect of mass reduction of 3d-printed pla on load transfer capacity—a circular economy perspective. *Materials*, 18(14):3262, 2025.
- [71] Florian R Menter. Two-equation eddy-viscosity turbulence models for engineering applications. *AIAA journal*, 32(8):1598–1605, 1994.
- [72] Senthilvel Santhakumar, Ilamathi Palanivel, and Krishnanand Venkatasubramanian. A study on the rotational behaviour of a savonius wind turbine in low rise highways during different monsoons. *Energy for Sustainable Development*, 40:1–10, 2017. ISSN 0973-0826. doi: <https://doi.org/10.1016/j.esd.2017.05.002>. URL <https://www.sciencedirect.com/science/article/pii/S0973082616311036>.
- [73] Wael Abo El-Magd Mahmoud Mohamed, Ahmed Salah Eissa, Ahmed M Mousa, et al. Mechanical processing of banana slices-stem for fiber extraction. *Agricultural Engineering International: CIGR Journal*, 25(4), 2023.
- [74] Vincenzo Crupi, Gabriella Epasto, and Eugenio Guglielmino. Low-velocity impact strength of sandwich materials. *Journal of Sandwich Structures & Materials*, 13(4):409–426, 2011.
- [75] Albert Forés-Garriga, Giovanni Gómez-Gras, and Marco A. Pérez. Lightweight hybrid composite sandwich structures with additively manufactured cellular cores. *Thin-Walled Structures*, 191:111082, 2023. ISSN 0263-8231. doi: <https://doi.org/10.1016/j.tws.2023.111082>. URL <https://www.sciencedirect.com/science/article/pii/S0263823123005608>.
- [76] MK Khan. Compressive and lamination strength of honeycomb sandwich panels with strain energy calculation from astm standards. *Proceedings of the Institution of Mechanical Engineers, Part G: Journal of Aerospace Engineering*, 220(5):375–386, 2006.
-

- 
- [77] Tamer Ali Sebaey and Harri Junaedi. Bio-inspired 3d-printed gyroid structure core with cfrp laminate face sheet sandwich structures.
- [78] Catarina Silva, Ana Isabel Pais, Gabriela Caldas, Barbara PPA Gouveia, Jorge Lino Alves, and Jorge Belinha. Study on 3d printing of gyroid-based structures for superior structural behaviour. *Progress in Additive Manufacturing*, 6(4):689–703, 2021.
- [79] Albert Forés-Garriga, Giovanni Gómez-Gras, and Marco A Pérez. Lightweight hybrid composite sandwich structures with additively manufactured cellular cores. *Thin-Walled Structures*, 191:111082, 2023.
- [80] Cem Güdür, Türker Türkoğlu, and İlker Eren. Effect of lattice design and process parameters on the properties of pla, abs and petg polymers produced by fused deposition modelling. *Journal of Materials and Mechatronics: A*, 4(2):561–570, 2023.
- [81] Hocine Djemai, Tarek Djoudi, and Adnane Labed. Experimental investigation of mechanical behaviour and damage of bio-sourced sandwich structures based on date palm tree waste and cork materials. *Journal of Composite & Advanced Materials/Revue des Composites et des Matériaux Avancés*, 32(5), 2022.
- [82] A Bouhelal, MN Hamlaoui, A Smaili, S Rechak, Y Belkacemi, M Mahfoud, and S Ouchene. Multi-objective optimization and aeroelastic analysis of small wind turbine blades made of date palm fibers. In *Technological and Innovative Progress in Renewable Energy Systems: Proceedings of the 2024 International Renewable Energy Days (IREN Days' 2024)*., pages 351–355. Springer, 2025.
- [83] Mouna Mahfoud, Abdelhamid Bouhelal, Arezki Smaili, Said Rechak, Yacine Belkacemi, and Samir Ouchene. Development of rotor blades based on date palm fibers for wind turbines: A feasibility study. In *2023 1st International Conference on Renewable Solutions for Ecosystems: Towards a Sustainable Energy Transition (ICRSEtoSET)*, pages 1–4. IEEE, 2023.
- [84] Abderraouf Gherissi, Fahd Alahmari, Mohamed Fadhl, Adnan Asiri, Meshal Alhwiti, Omar Alamri, Metab Alanisi, and Ibrahim Nasri. Wind turbine blades structure based on palm cellulose fibers composite material. *Építőanyag (Online)*, (3):109–114, 2021.
- [85] Abdelkader Bendahou, Youssef Habibi, Hamid Kaddami, and Alain Dufresne. Physico-chemical characterization of palm from phoenix dactylifera–I, preparation of cellulose whiskers and natural rubber–based nanocomposites. *Journal of Biobased Materials and Bioenergy*, 3(1):81–90, 2009.
- [86] Lobna A Elseify, Mohamad Midani, Ayman A El-Badawy, Said Awad, and Mohammad Jawaid. Comparative study of long date palm (phoenix dactylifera I.) midrib and spadix fibers with other commercial leaf fibers. *Cellulose*, 30(3):1927–1942, 2023.
- [87] Alireza Dehghani, Sara Madadi Ardekani, Mariam A Al-Maadeed, Azman Hassan, and Mat Uzir Wahit. Mechanical and thermal properties of date palm leaf fiber reinforced recycled poly (ethylene terephthalate) composites. *Materials & Design (1980-2015)*, 52: 841–848, 2013.
- [88] Mariam A AlMaadeed, Zuzana Nógellová, Ivica Janigová, and Igor Krupa. Improved mechanical properties of recycled linear low-density polyethylene composites filled with date palm wood powder. *Materials & Design*, 58:209–216, 2014.
-

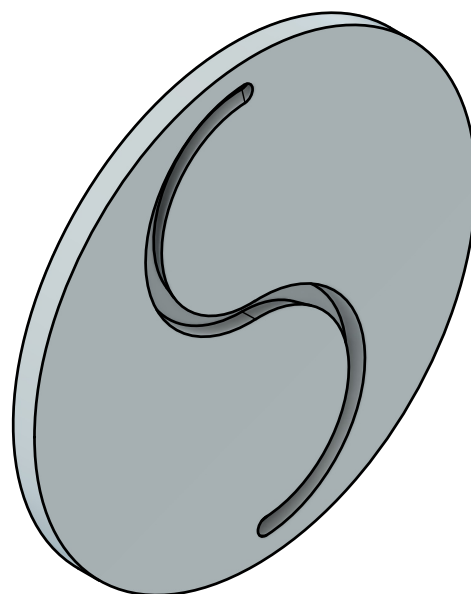
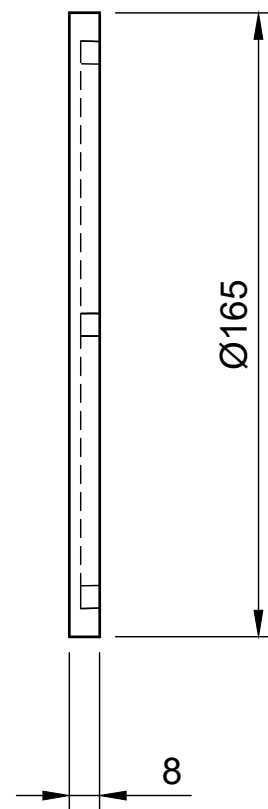
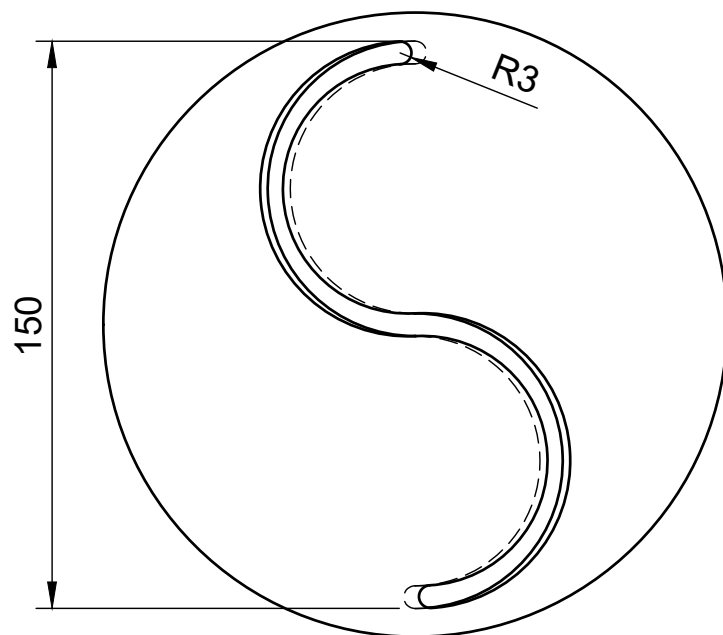


- 
- [89] A Al-Khanbashi, K Al-Kaabi, and A Hammami. Date palm fibers as polymeric matrix reinforcement: fiber characterization. *Polymer composites*, 26(4):486–497, 2005.
- [90] Ahmad Alawar, Ahmad M Hamed, and Khalifa Al-Kaabi. Characterization of treated date palm tree fiber as composite reinforcement. *Composites Part B: Engineering*, 40(7): 601–606, 2009.
- [91] Maryam Gholami, Mohammad Saleh Ahmadi, Mohammad Ali Tavanaie, and Mohammad Khajeh Mehrizi. Effect of oxygen plasma treatment on tensile strength of date palm fibers and their interfacial adhesion with epoxy matrix. *Science and Engineering of Composite Materials*, 25(5):993–1001, 2018.
- [92] KIMO Instruments. *MP200: Multifunction Manometer – User Manual*, 2002. URL [https://www.kimocanada.com/Francais/pdf/Manuels-francais/Portables%20\(2002\)/7\\_Classe%20200/NT%20MP200.pdf](https://www.kimocanada.com/Francais/pdf/Manuels-francais/Portables%20(2002)/7_Classe%20200/NT%20MP200.pdf). NT MP200.
- [93] S. J. Savonius. The s-rotor and its applications: A bi-vane power wheel of s-shaped cross-section working in wind or water. *Mechanical Engineering*, 53(5):333–338, May 1931. Presented at the A.S.M.E. Aeronautic Division meeting, Baltimore, May 12–14, 1931. Source: WRCA-081 archival collection.
- [94] WA El-Askary, Ahmed S Saad, Ali M AbdelSalam, and IM Sakr. Investigating the performance of a twisted modified savonius rotor. *Journal of Wind Engineering and Industrial Aerodynamics*, 182:344–355, 2018.
- [95] Federico González Madina, Alejandro Gutiérrez, and Pedro Galione. Computational fluid dynamics study of savonius rotors using openfoam. *Wind Engineering*, 45(3):630–647, 2021.
- [96] Keum Soo Jeon, Jun Ik Jeong, Jae-Kyung Pan, and Ki-Wahn Ryu. Effects of end plates with various shapes and sizes on helical savonius wind turbines. *Renewable energy*, 79: 167–176, 2015.
- [97] Sadek Z Kassab, Sammy J Chemengich, and Eslam R Lotfy. The effect of endplate addition on the performance of the savonius wind turbine: A 3-d study. *Proceedings of the Institution of Mechanical Engineers, Part A: Journal of Power and Energy*, 236(8): 1582–1592, 2022.
- [98] Jae-Hoon Lee, Young-Tae Lee, and Hee-Chang Lim. Effect of twist angle on the performance of savonius wind turbine. *Renewable Energy*, 89:231–244, 2016.
- [99] Ruzita Sumiati, Uyung Gatot S Dinata, and Dendi Adi Saputra. Enhancing savonius rotor performance with zigzag surface investigated at drag force, pressure, and flow visualization analysis. *TEM Journal*, 13(2):866, 2024.
- [100] A Kriker, G Debicki, A Bali, MM Khenfer, and M Chabannet. Mechanical properties of date palm fibres and concrete reinforced with date palm fibres in hot-dry climate. *Cement and Concrete Composites*, 27(5):554–564, 2005.
- [101] Ramadan A Nasser. An evaluation of the use of midribs from common date palm cultivars grown in saudi arabia for energy production. *BioResources*, 9(3):4343–4357, 2014.
- [102] SN Pandey and SK Ghosh. The chemical nature of date-palm (phoenix dactylifera-l) leaf fibre. 1995.
-

- 
- [103] Matej Gljušćić, Domagoj Lanc, Marina Franulović, and Andrej Žerovnik. Microstructural analysis of the transverse and shear behavior of additively manufactured cfrp composite rves based on the phase-field fracture theory. *Journal of composites science*, 7(1):38, 2023.
- [104] Jack R. Vinson. *Sandwich structures*. Applied Science Publishers, 1999.
- [105] Tom Bitzer. *Honeycomb technology: Materials, design, manufacturing, applications and testing*. Springer Science & Business Media, 1997.
- [106] Ian Maskery, Akinlabi O. Aremu, Chris J. Tuck, Ricky D. Wildman, Ian A. Ashcroft, and Richard J.M. Hague. Mechanical properties of tpms lattices in selective laser sintered pa12. *Additive Manufacturing*, 24:647–656, 2018.
- [107] H.M.A. Kolken, S. Janbaz, and A.A. Zadpoor. Mechanical characterization of additively manufactured meta-biomaterials based on minimal surfaces. *Materials & Design*, 194, 2021.
- [108] J. Wieding, A. Jonitz-Heincke, and R. Bader. Mechanical behavior of a functionally graded porous titanium scaffold designed for load-bearing orthopedic applications. *Materials Science and Engineering: C*, 48:586–593, 2015.
- [109] X. Li, P. Tan, W. Song, and C. Wang. Mechanical performance and energy absorption of 3d printed lattice structures: A comparative study. *Composites Part B*, 223, 2021.
- [110] Harri Junaedi, Marwa A Abd El-baky, Mahmoud M Awd Allah, and Tamer A Sebaey. Mechanical characteristics of sandwich structures with 3d-printed bio-inspired gyroid structure core and carbon fiber-reinforced polymer laminate face-sheet. *Polymers*, 16(12): 1698, 2024.
- [111] Sadek Z Kassab, Sammy J Chemengich, and Eslam R Lotfy. The effect of endplate addition on the performance of the savonius wind turbine: A 3-d study. *Proceedings of the Institution of Mechanical Engineers, Part A: Journal of Power and Energy*, 236 (8):1582–1592, 2022. doi: 10.1177/09576509221098480. URL <https://doi.org/10.1177/09576509221098480>.
- [112] Keum Soo Jeon, Jun Ik Jeong, Jae-Kyung Pan, and Ki-Wahn Ryu. Effects of end plates with various shapes and sizes on helical savonius wind turbines. *Renewable Energy*, 79:167–176, 2015. ISSN 0960-1481. doi: <https://doi.org/10.1016/j.renene.2014.11.035>. URL <https://www.sciencedirect.com/science/article/pii/S0960148114007502>. Selected Papers on Renewable Energy: AFORE 2013.
- [113] Ahmed S. Saad, Ibrahim I. El-Sharkawy, Shinichi Ookawara, and Mahmoud Ahmed. Performance enhancement of twisted-bladed savonius vertical axis wind turbines. *Energy Conversion and Management*, 209:112673, 2020. ISSN 0196-8904. doi: <https://doi.org/10.1016/j.enconman.2020.112673>. URL <https://www.sciencedirect.com/science/article/pii/S0196890420302119>.
- [114] Federico González Madina, Alejandro Gutiérrez, and Pedro Galione. Computational fluid dynamics study of savonius rotors using openfoam. *Wind Engineering*, 45(3): 630–647, 2021. doi: 10.1177/0309524X20924958. URL <https://doi.org/10.1177/0309524X20924958>.
-

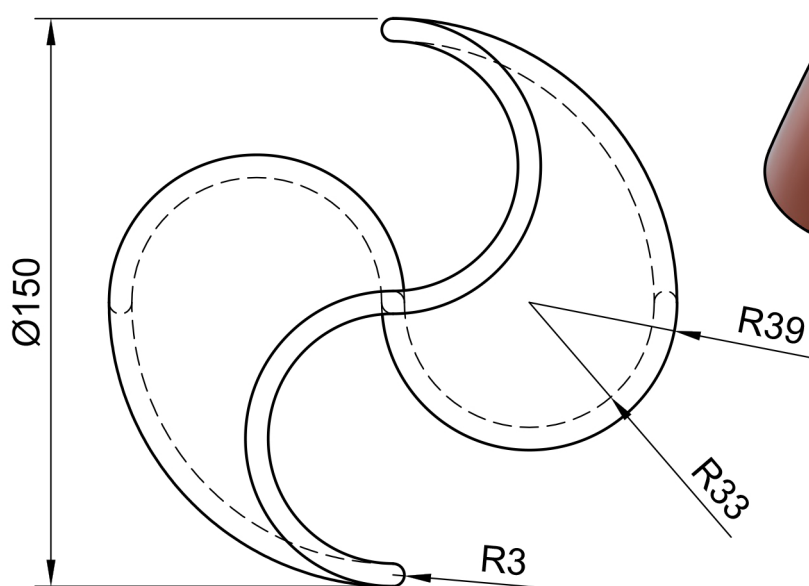
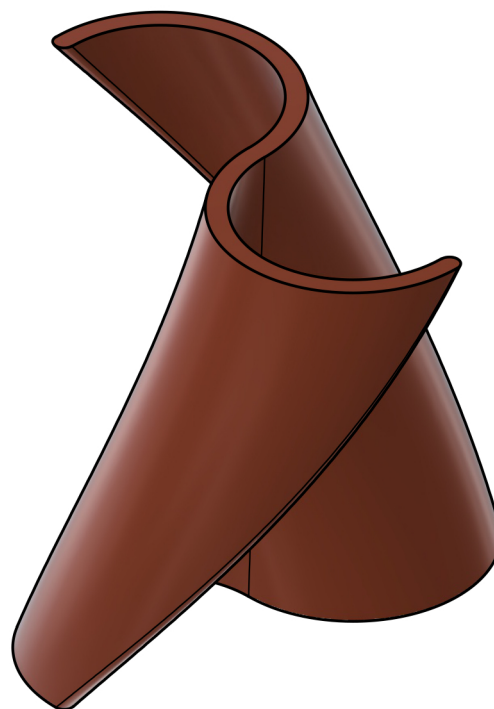
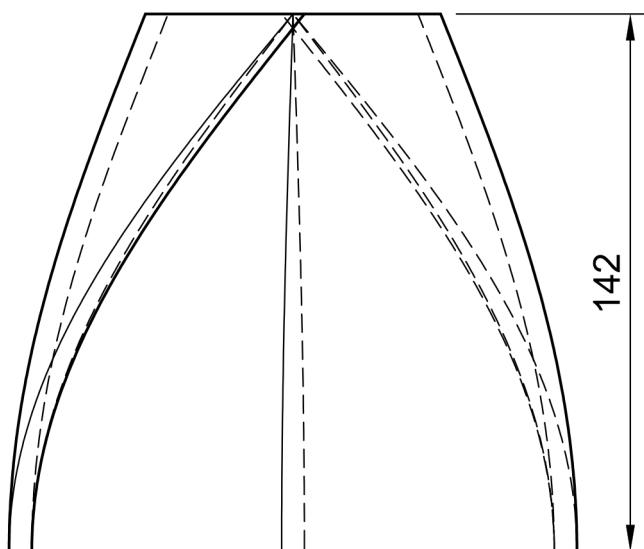
- [115] Jae-Hoon Lee, Young-Tae Lee, and Hee-Chang Lim. Effect of twist angle on the performance of savonius wind turbine. *Renewable Energy*, 89:231–244, 2016. ISSN 0960-1481. doi: <https://doi.org/10.1016/j.renene.2015.12.012>. URL <https://www.sciencedirect.com/science/article/pii/S0960148115305164>.
- [116] W.A. El-Askary, Ahmed S. Saad, Ali M. AbdelSalam, and I.M. Sakr. Investigating the performance of a twisted modified savonius rotor. *Journal of Wind Engineering and Industrial Aerodynamics*, 182:344–355, 2018. ISSN 0167-6105. doi: <https://doi.org/10.1016/j.jweia.2018.10.009>. URL <https://www.sciencedirect.com/science/article/pii/S016761051830254X>.
- [117] Nabila Saadaoui, Antoine Rouilly, Khalid Fares, and Luc Rigal. Characterization of date palm lignocellulosic by-products and self-bonded composite materials obtained thereof. *Materials & Design*, 50:302–308, 2013.
- [118] MA Abdel-Aal, RA Nasser, PR Khan, and HA Al-Mefarrej. Anatomical and physical characterisations of some lignocellulosic residues and their suitability for fibre production. *Journal of environmental biology*, 36(3):543, 2015.
- [119] Mohammed A Jaber, Kadhim J Hammadi, Alyaa A Abdul Kareem, and M Abd-Alrazak. Physical and mechanical properties of medium density fiberboard made of palm fronds and trunks. *Asian journal of applied sciences*, 4(4), 2016.
- [120] M Midani. Date palm fibre composites: a novel and sustainable material for the aerospace industry. *JEC Compos Mag*, 54:45–47, 2017.
- [121] LA Elseify, M Midani, and LA Shihata. Investigating the effect of the chemical treatment on the properties of a novel microfibrillated long date palm fibers. *German University in Cairo (GUC)*, 2018.

**Appendix A — Technical Drawings of Rotor Components**

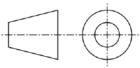


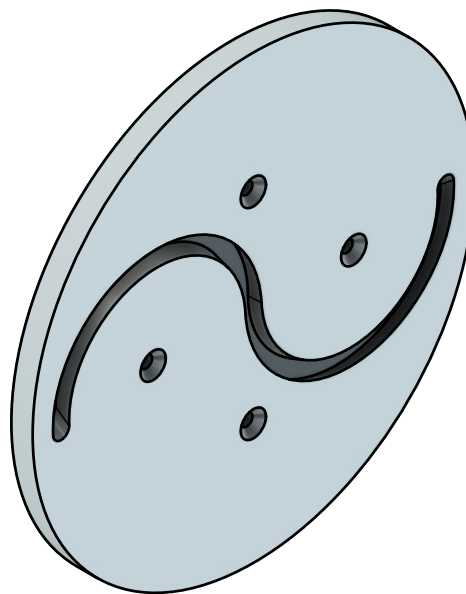
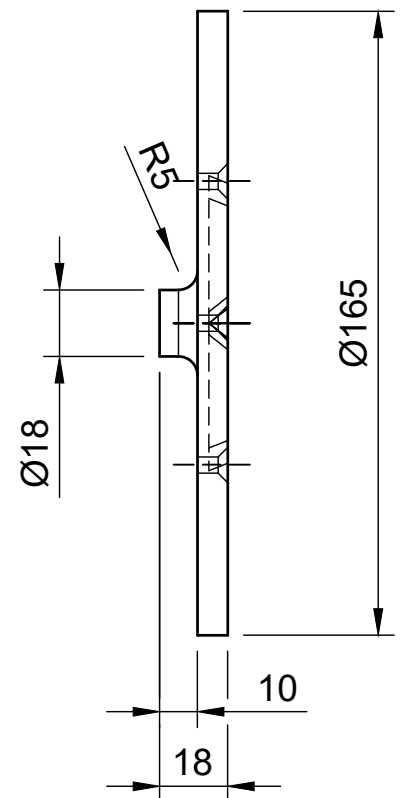
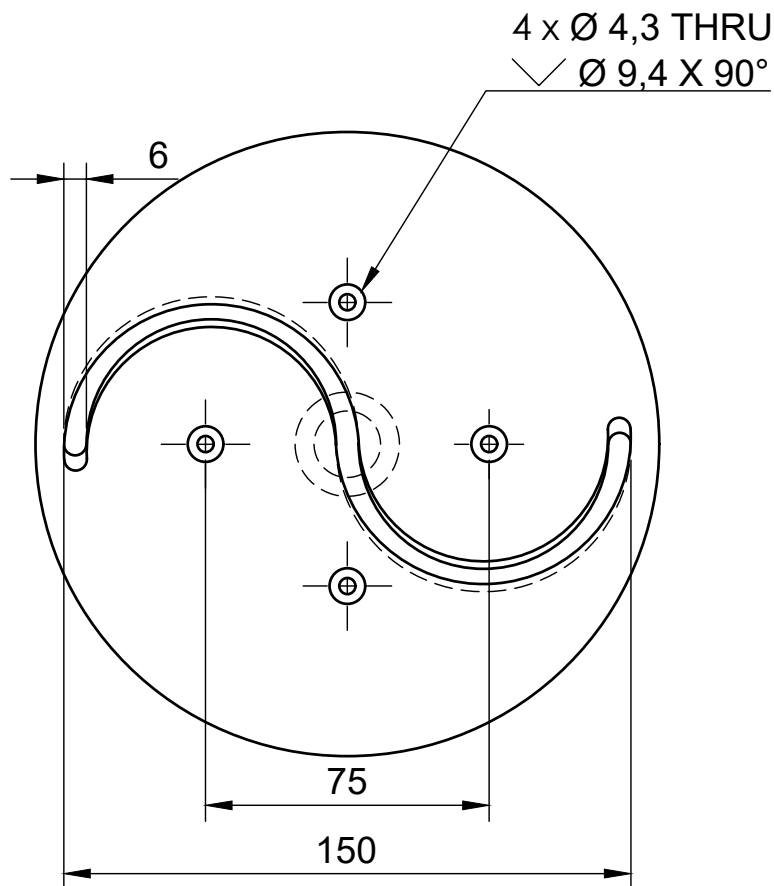
# ECOLE NATIONALE POLYTECHNIQUE

SCALE	MASS			<p>LOWER END PLATE</p>	<p><i>ENP</i> MECHANICAL. DEPT</p>
STUDENT	AIB. M.				
STUDENT	BENSGHIR. I.				
SUPERVISOR	GUERGUEB. B.				
SUPERVISOR				<p>MATERIAL PLA</p>	<p>SRA.10W.005</p>
DEPT. HEAD	BELKACEMI. Y.				

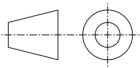


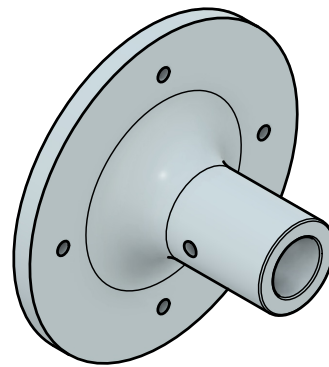
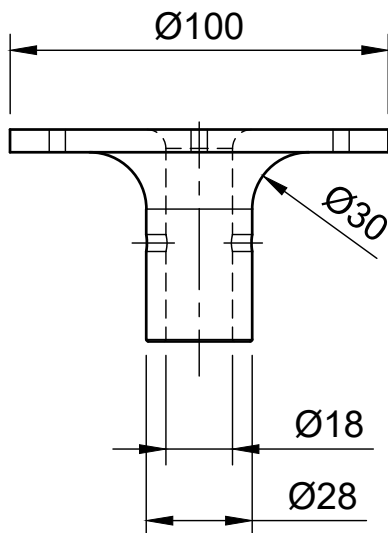
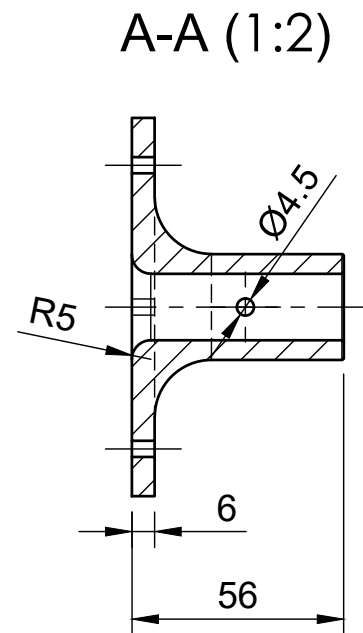
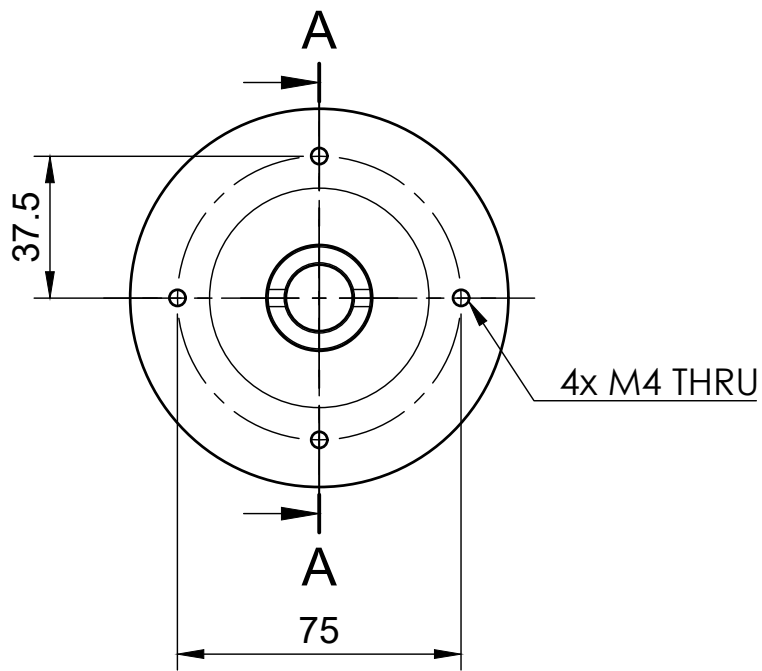
# ECOLE NATIONALE POLYTECHNIQUE

SCALE	MASS			<p>SAVONIUS ROTOR</p>	<p>ENP MECHANICAL. DEPT</p>
1:2					
STUDENT	AIB. M.				
STUDENT	BENSGHIR. I.				
SUPERVISOR	GUERGUEB. B.				
SUPERVISOR				<p>MATERIAL COMPOSIT</p>	<p>SRA.10W.0010</p>
DEPT. HEAD	BELKACEMI. Y.				

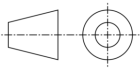


# ECOLE NATIONALE POLYTECHNIQUE

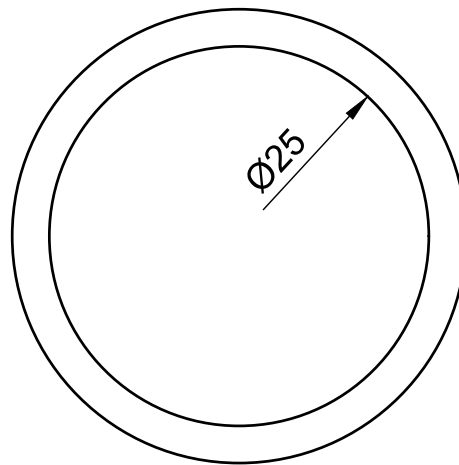
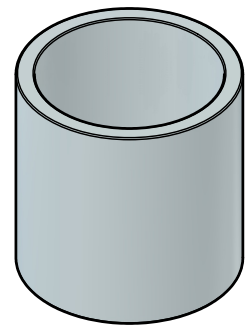
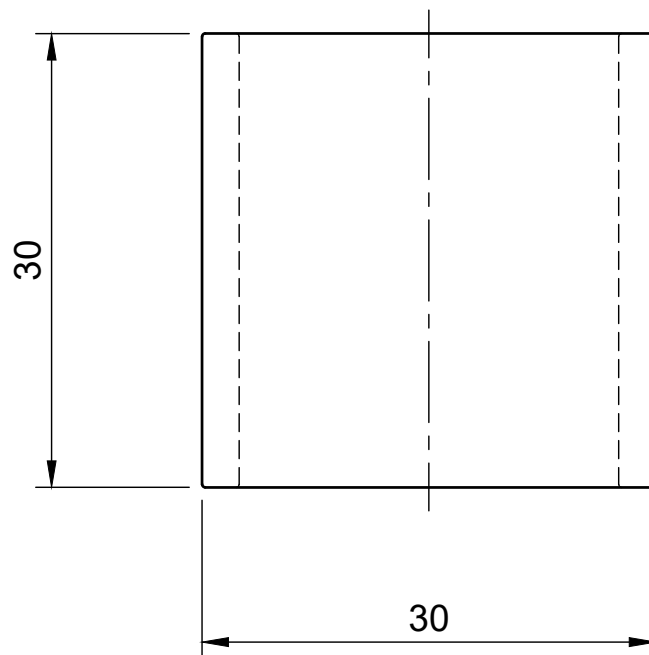
SCALE	MASS			<p>LOWER END PLATE</p>	<p>ENP MECHANICAL. DEPT</p>
1:2					
STUDENT	AIB. M.				
STUDENT	BENSGHIR. I.				
SUPERVISOR	GUERGUEB. B.				
SUPERVISOR				<p>MATERIAL PLA</p>	<p>SRA.10W.005</p>
DEPT. HEAD	BELKACEMI. Y.				



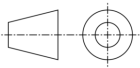
# ECOLE NATIONALE POLYTECHNIQUE

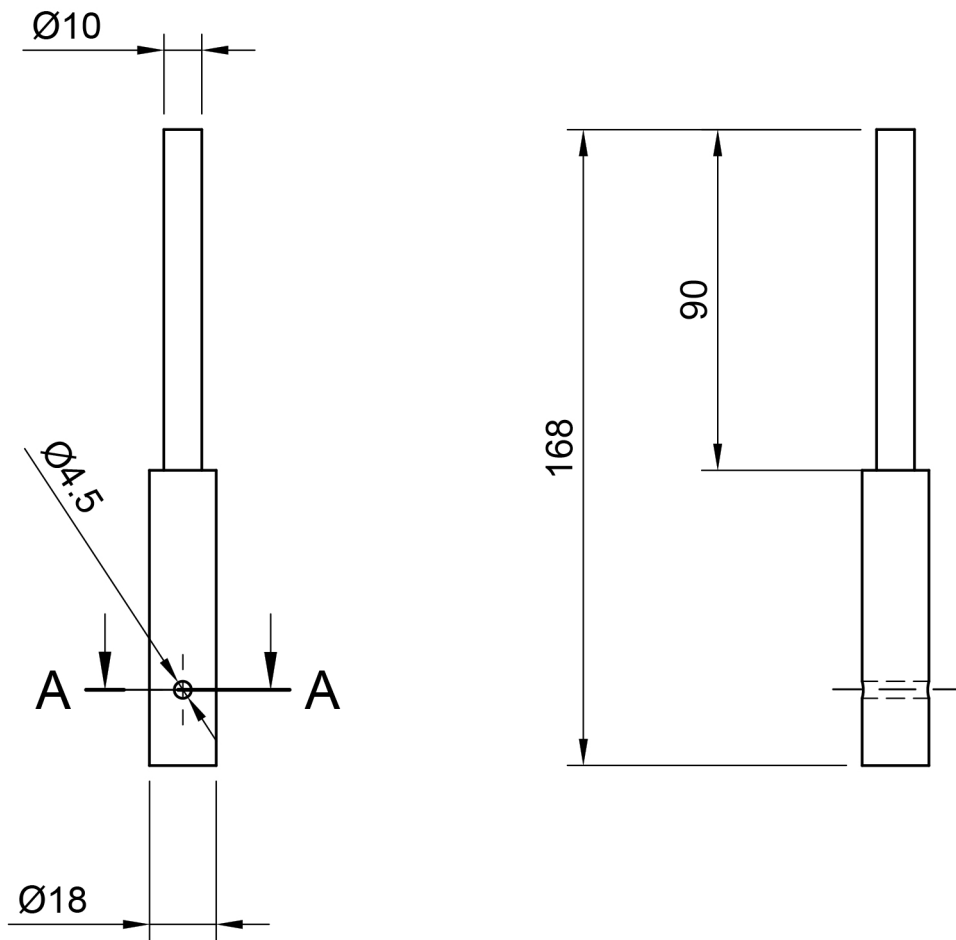
SCALE	MASS			UPPER FLANGE	<p>ENP</p> <p>MECHANICAL. DEPT</p>
1:2					
STUDENT	AIB. M.				
STUDENT	BENSGHIR. I.				
SUPERVISOR	GUERGUEB. B.				
SUPERVISOR				MATERIAL	SRA.10W.004
DEPT. HEAD	BELKACEMI. Y.				
				PLA	





# ECOLE NATIONALE POLYTECHNIQUE

SCALE	MASS			SPACER	<i>ENP</i> MECHANICAL. DEPT
2:1					
STUDENT	AIB. M.				
STUDENT	BENSGHIR. I.				
SUPERVISOR	GUERGUEB. B.				
SUPERVISOR				MATERIAL PLA	SRA.10W.002
DEPT. HEAD	BELKACEMI. Y.				

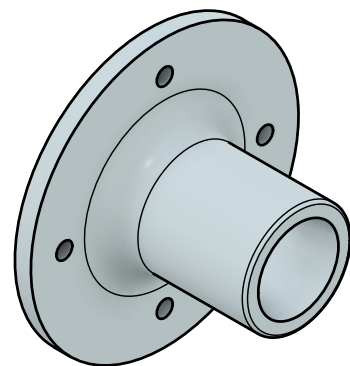
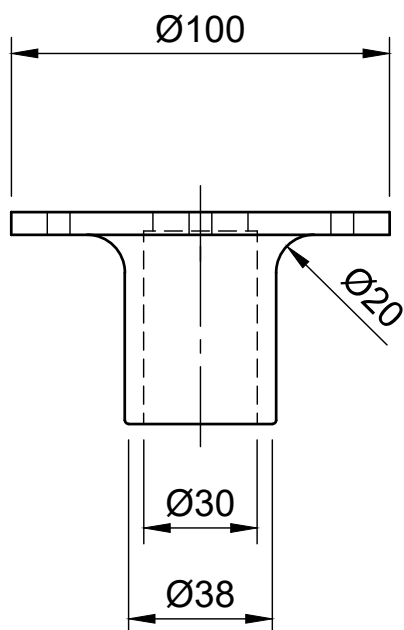
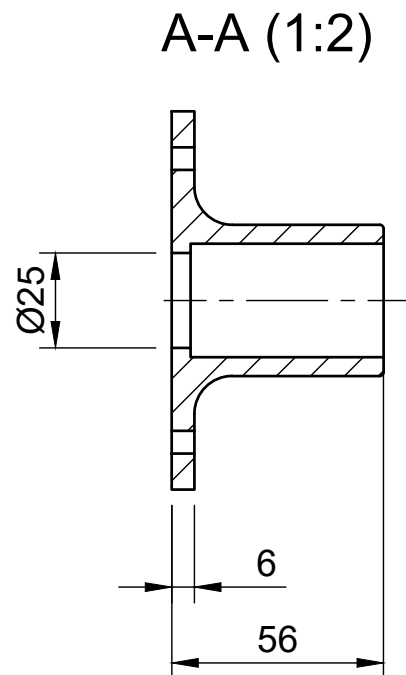
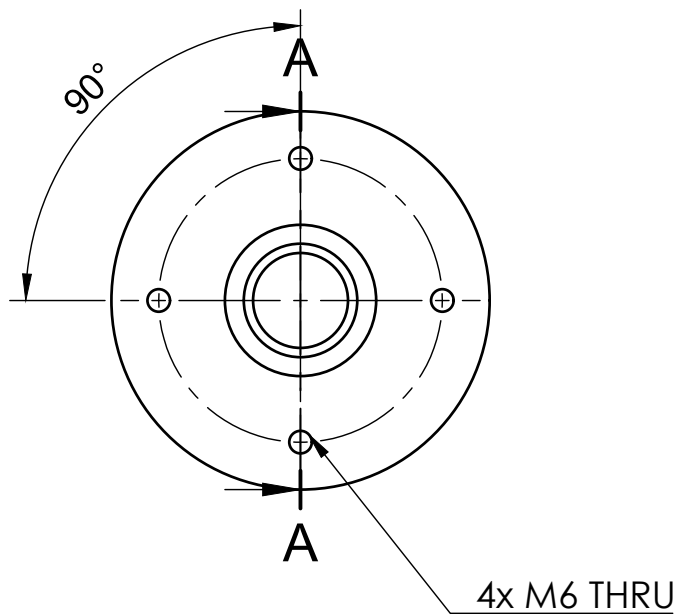


A-A (1:2)



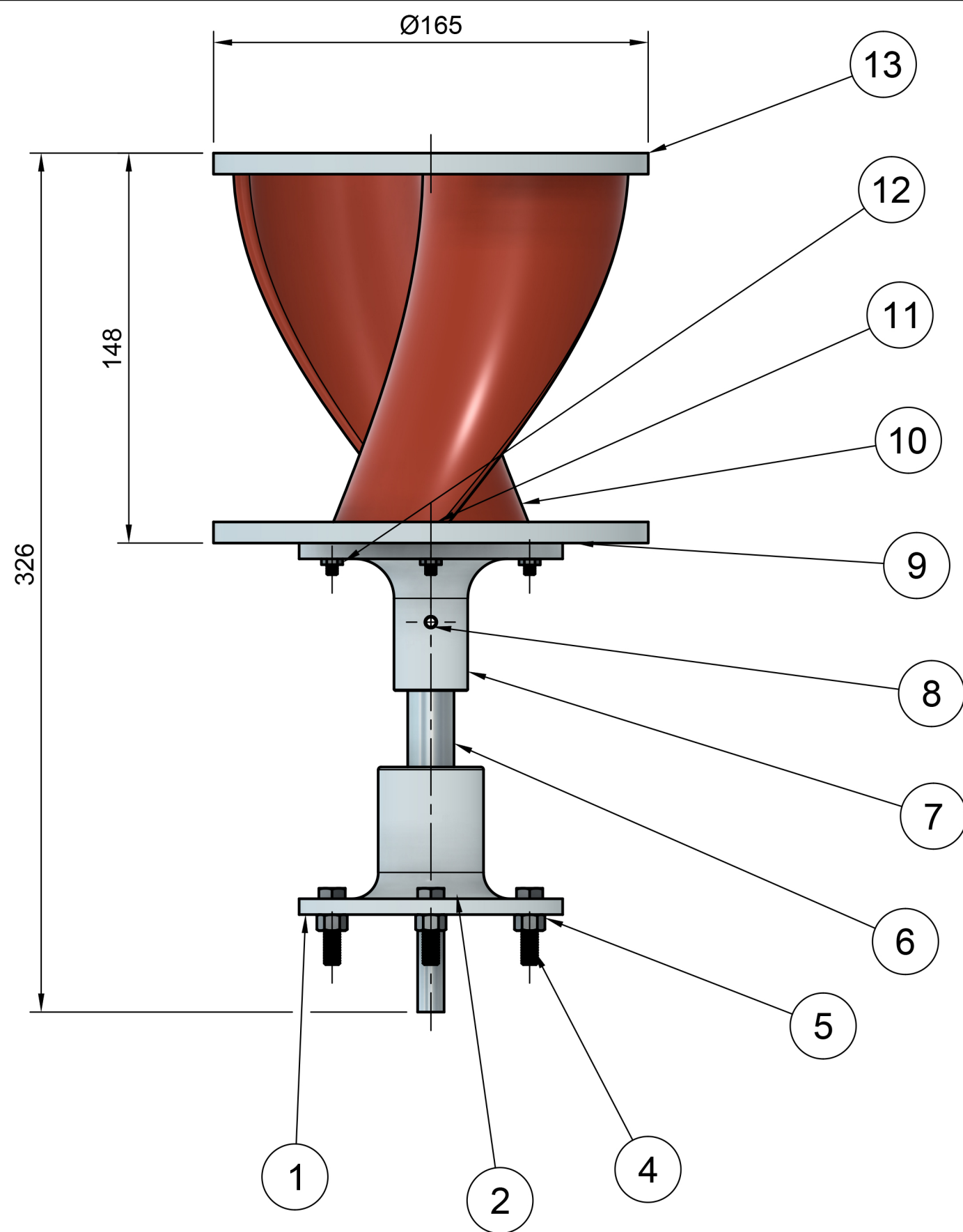
# ECOLE NATIONALE POLYTECHNIQUE

SCALE	MASS			SHAFT	<i>ENP</i> MECHANICAL. DEPT
1:2					
STUDENT	AIB. M.				
STUDENT	BENSGHIR. I.				
SUPERVISOR	GUERGUEB. B.				
SUPERVISOR				MATERIAL PLA	SRA.10W.003
DEPT. HEAD	BELKACEMI. Y.				



# ECOLE NATIONALE POLYTECHNIQUE

SCALE	MASS		LOWER HOUSING	ENP MECHANICAL. DEPT
1:2				
STUDENT	AIB. M.			
STUDENT	BENSGHIR. I.			
SUPERVISOR	GUERGUEB. B.			
SUPERVISOR			MATERIAL PLA	SRA.10W.001
DEPT. HEAD	BELKACEMI. Y.			



13	SRA.10W.008	UPPER END PLATE	1			PLA	
12		THIN HEX NUT – M6 – 5	4			STEEL	
11	SRA.10W.007	COUNTERSUNK SCREW – M4×17 – H	4			STEEL	
10	SRA.10W.006	SAVONIUS ROTOR	1			COMPOSIT	
9	SRA.10W.005	LOWER END PLATE	1			PLA	
8		SPRING PIN – 4.5×28	1			XC38	
7	SRA.10W.004	UPPER FLANGE	1			PLA	
6	SRA.10W.003	SHAFT	1			PLA	
5		HEX NUT – M6 – 5	4			STEEL	
4		HEX BOLT – M6×25 – 8.8	4			STEEL	
3	SRA.10W.002	SPACER	1			PLA	
2		DEEP GROOVE BEARING 6200 2RS	2				
1	SRA.10W.001	LOWER HOUSING	1			PLA	
PR	DRAWING N°	DESIGNATION	NB	UNIT	TOTAL	MAT	OBSERV
				MASS			

ECOLE NATIONALE POLYTECHNIQUE

SCALE	MASS			SAVONIUS ROTOR ASSEMBLY	ENP MECHANICAL. DEPT
1:2	3273.555 g				
STUDENT	AIB. M.				
STUDENT	BENSEGHIR. I.				
SUPERVISOR	GUERGUEB. B.				
SUPERVISOR					SRA.10W.00
DEPT. HEAD	BELKACEMI. Y.				